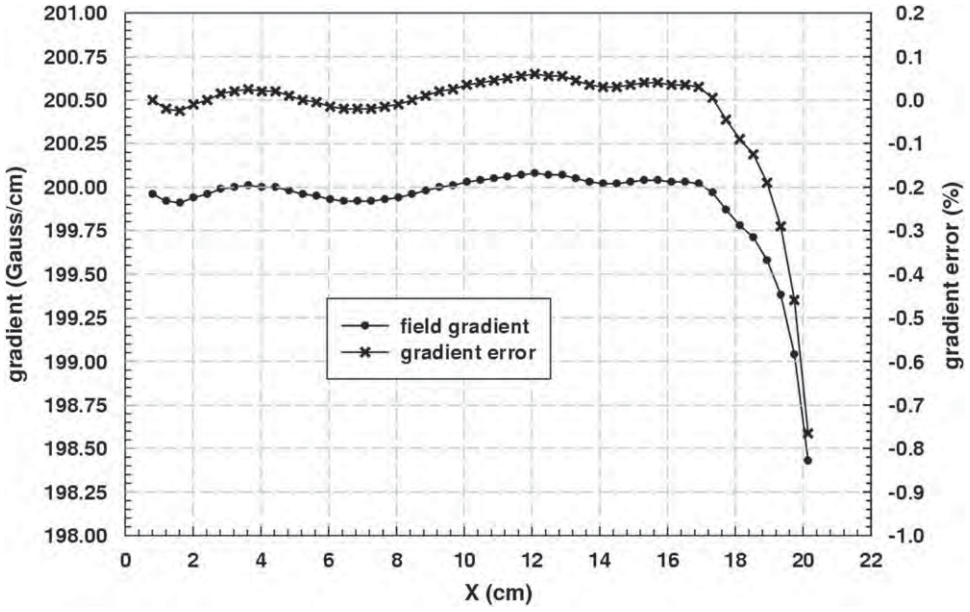

Fig. 5. Magnetic field distribution at midplane from the hyperbola pole compared with the final design.

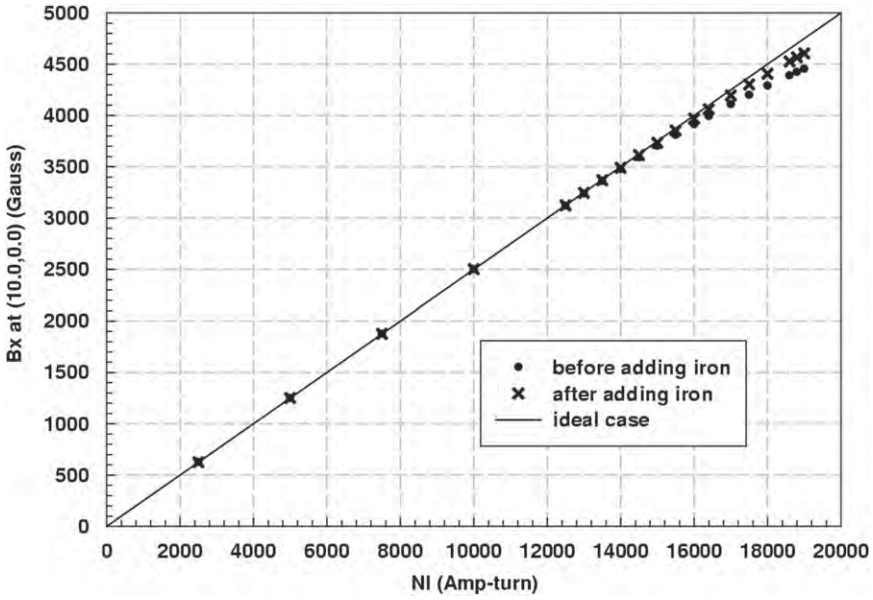

Fig. 6. Magnetic field at x=10 cm as a function of current (NI).

2.2. Magnetic field saturation

Magnetic field saturation [11] occurs at high excitation currents, which causes some regions in the magnet core to have too high of a magnet flux density. Fig. 4 shows that the return yoke and the front plate are the regions that have a high flux density. To reduce this high flux density, the thickness of the front plate and the return yoke are increased. Fig. 6 shows the magnetic field from POISSON before and after adding iron at these two regions. The calculations show that after adding more iron, the saturation occurs at higher currents (from $>$14,000 Ampere-turn to $>$17,000 Ampere-turn).

3. Construction of the alpha magnet

3.1. Construction of the magnet core

The magnet core is constructed from low-carbon steel (0.035% carbon, $\mu_r \sim$2500–3000). The core is composed of two magnet poles and a front plate. Each pole piece was fabricated from nine iron laminations. All components of the magnet core were machined by a computer numerical controlled (CNC) machine. Fig. 7(a) shows a pole piece lamination of the alpha magnet. Nine laminations are stacked and tightened together by long bolts and nuts, as shown in Fig. 7(b). The complete assembly of the magnet core is shown in Fig. 7(c).

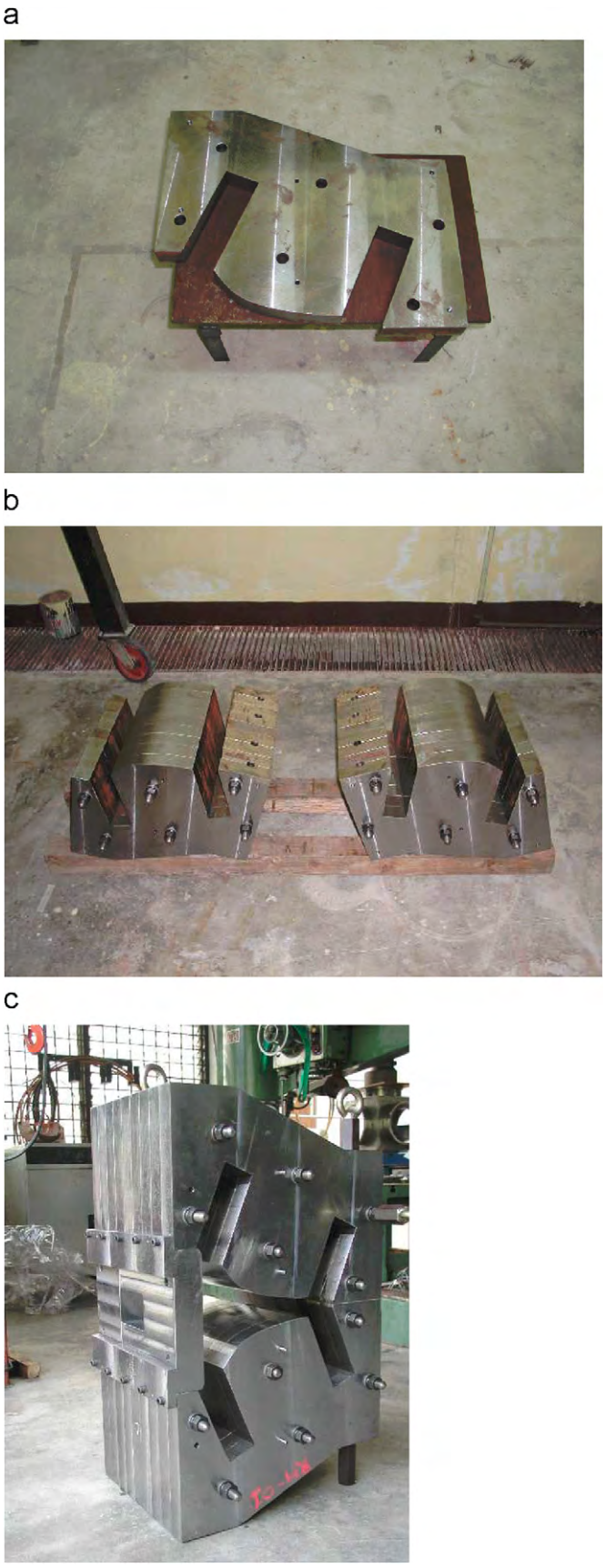

Fig. 7. (a) A pole piece lamination of the alpha magnet, (b) alpha-magnet poles, and (c) alpha-magnet assembly.

3.2. Construction of the magnet coils

The magnet coils are constructed from $1 \times 1\,cm^2$ copper wire, with a 4-mm-diameter cooling hole. The double pancake technique is used to wind the hollow copper wire. The wire is wound by using a winding platform mounted on a rotating table. In this design, one double pancake has two layers of copper wire, and each layer has five turns. Before winding the coil, the wire is wrapped by glass cloth tape as insulation. The wire is wound five turns for the first layer, and it is cut and connected to the other end for the winding of the second layer. The wire is then wound five turns in the opposite direction of the first layer. The water connectors are connected to both ends of one double pancake. Seven double pancakes are connected and stacked together to be one alpha-magnet coil, as shown in Fig. 8(a). The resistance of the two coils is 94 mΩ, resulting in the total power dissipation of 7.9 kW at a current of 290 A. The 10 °C water, with flow rate of 10 l/s, is used to remove most of the heat dissipation. The complete assembly of the alpha magnet is shown in Fig. 8(b).

4. Performance of the magnetic bunch compressor

4.1. Magnetic field measurement

The alpha-magnet field distribution is measured along the X direction at the midplane by using a DMT-130-PS Hall effect Teslameter. The magnetic field gradient is then derived from the field measurement. Fig. 9 shows the excitation curve of the alpha magnet from calculations and measurements. A maximum gradient of 465 G/cm can be achieved, limited by the DC power supply. Saturation was observed at a current higher than 150 A. With sufficient water cooling, there is no significant temperature rise during operation.

4.2. Bunch length measurement

At the experimental station located downstream of the linac, the 8- to 10-MeV electron bunches were used to generate coherent transition radiation for electron bunch length measurement. By placing a 25-μm-thick aluminum foil (Al foil) at 45 degrees with respect to the electron path, the backward transition radiation is emitted perpendicular to the beam axis. A far-infrared Michelson interferometer was employed to measure the electron bunch length by an autocorrelation technique [16]. The coherent transition radiation is collimated by a gold-coated parabolic mirror. The radiation beam exits through a high-density polyethylene window and enters a Michelson interferometer. The interferometer consists of a beam splitter, a fixed mirror, and a movable mirror. In the Michelson interferometer, the radiation is split into two parts by a beam splitter, and it then travels in different directions to be reflected back by the mirrors. After reflection, the two radiation pulses are combined again and detected by a pyroelectric detector for intensity determination. By scanning the movable mirror, the radiation intensity as a function of the optical path difference, called the interferogram, was obtained, as shown in Fig. 10. For a Gaussian bunch distribution, the full width at half maximum (FWHM) of the interferogram is $4\sqrt{\ln 2}\sigma_Z$. The bunch length measurements for various alpha-magnet gradients have been conducted, and the results are shown in Fig. 11.

The measurement results show that short electron bunches can be generated when the alpha-magnet gradient is higher than 300 G/cm. However, the calculation predicted the shortest bunch

a

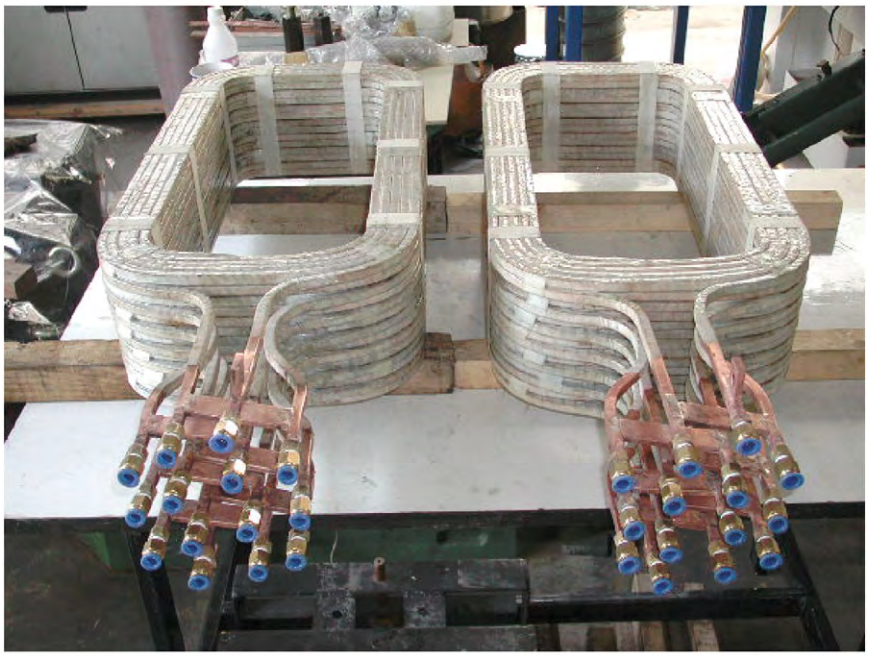

b

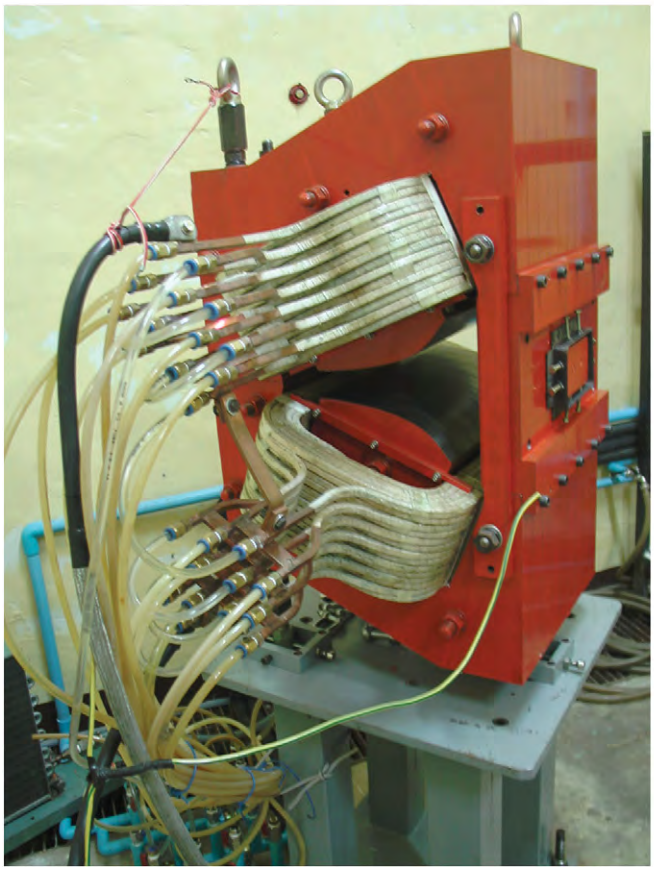

Fig. 8. (a) Two complete coils, and (b) a completed alpha magnet.

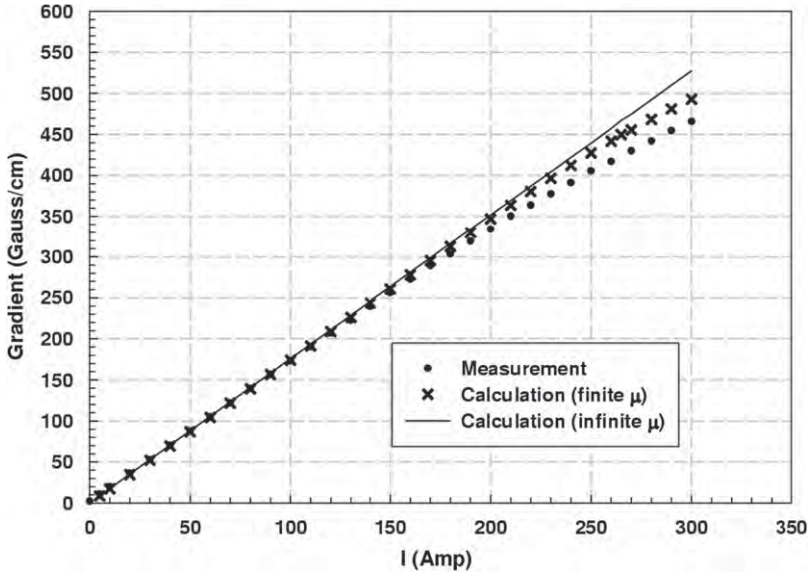

Fig. 9. Excitation curve of the alpha magnet from calculation (infinite μ and finite μ) and measurement.

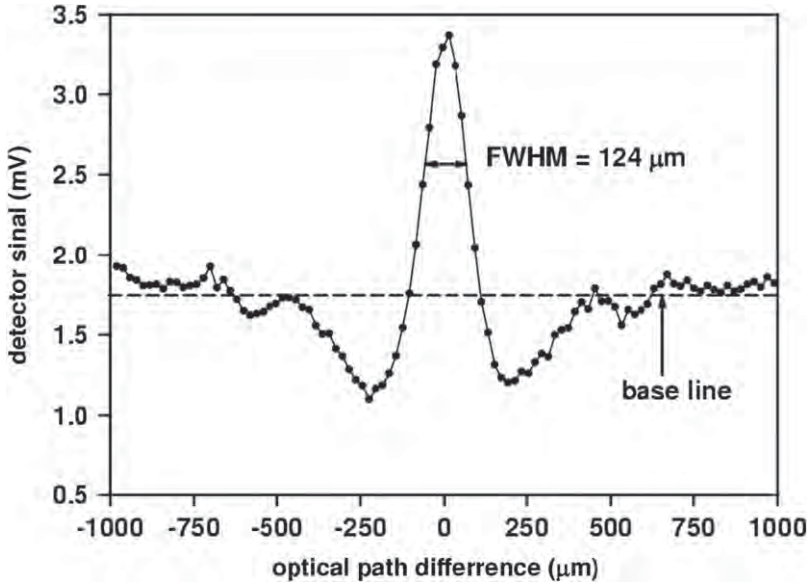

Fig. 10. An interferogram obtained from the bunch length measurement.

when using the alpha-magnet gradient of 328 G/cm for the 10-MeV electron beam (see Table 2). Equally short bunches can be obtained from our system through a broad range of alpha-magnet gradients due to the large energy spread (8–12 MeV). Calculations from the bunch compression program show that different electron beam energies require different alpha-magnet gradients to generate the minimum bunch length, as shown in Table 2. If the electron bunches have a large energy spread, then some electrons are compressed at a specific alpha-magnet gradient, while others are under-compressed or over-compressed, depending on their energy. It is therefore possible that equally short electron bunches of a large energy spread beam can be obtained through a broad range of alpha-magnet gradients.

5. Conclusion

An alpha magnet was successfully designed, constructed, and tested at the Plasma and Beam Physics Research Facility at Chiang Mai University. With this alpha magnet constructed in-house, a few hundred femtosecond electron bunches for THz radiation production can be generated from the thermionic-cathode RF gun. The experimental results show that electron bunches as short as $\sigma_z \sim 200$ fs can be generated from the system. Electron bunch length may be reduced with energy spread and lattice optimization. Our short electron bunches will be used to produce THz radiation for spectroscopy experiments and THz imaging applications.

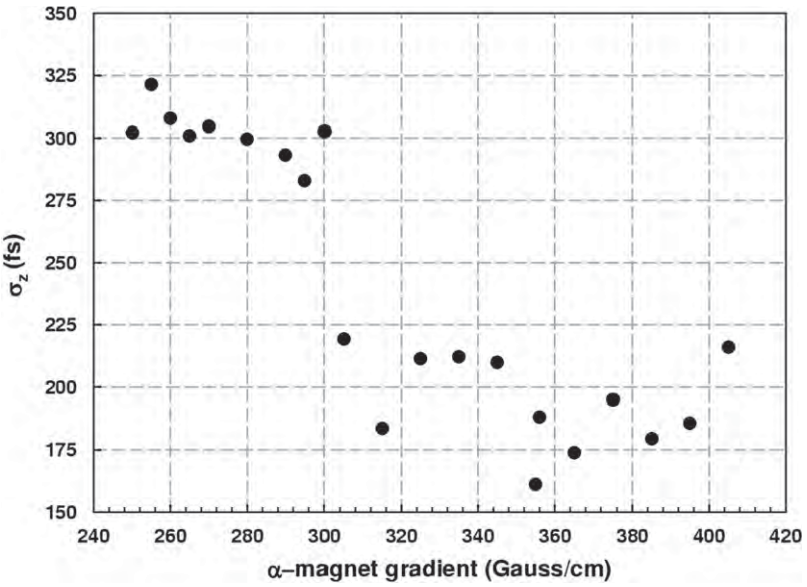

Fig. 11. Bunch length as a function of the alpha-magnet gradient.

Table 2
Alpha-magnet gradient for a minimum electron bunch of different electron energies.

Electron energy (MeV)	Alpha-magnet gradient (G/cm) (for minimum electron bunch)
8.0	298
9.0	315
10.0	329
11.0	342
12.0	352

Acknowledgments

The authors are grateful to Professor Helmut Wiedemann for his comments and suggestions. We would also like to acknowledge the support from the National Research Council of Thailand, the Thailand Research Fund, the (Thailand) Commission on Higher Education, and the graduate school of Chiang Mai University.

References

[1] H. Ihee, et al., Science 291 (2001) 458.
[2] M. Bauer, et al., Phys. Rev. Lett. 87 (2001) 025501.
[3] D.A. Reis, et al., Phys. Rev. Lett. 86 (2001) 3072.
[4] P. Kung, et al., Phys. Rev. Lett. 73 (1994) 967.
[5] I. Endo, et al., Phys. Rev. E 51 (1995) 6305.
[6] R. Bonifacio, et al., Opt. Commun. 50 (1985) 313.
[7] H. Wiedemann, et al., J. Nucl. Mater. 248 (1997) 374.
[8] H. Linh, et al., Phys. Rev. E 53 (1996) 6413.
[9] S. Rimjaem, et al., Nucl. Instr. and Meth. A 533 (2004) 258.
[10] H. Wiedemann, Computer Code Bunch Compression, Stanford University, Stanford, CA, 2000.
[11] H.A. Enge, Rev. Sci. Instr. 34 (1963) 385.
[12] H. Wiedemann, Particle Accelerator Physics I, 2nd edition, Springer, 1999.
[13] G.E. Fischerm, Iron Dominated Magnet, Stanford Linear Accelerator Center (SLAC)-PUB-3726, 1985.
[14] M. Borland, A High-brightness Thermionic Microwave Electron Gun, Ph.D. Thesis, Stanford University, Stanford, CA, 1991.
[15] L.M. Young, J.H. Billen, Los Alamos National Laboratory Technical Note, LA-UR-96-1834, Los Alamos, NM, 1999.
[16] C. Thongbai, et al., Nucl. Instr. and Meth. A 587 (2008) 130.

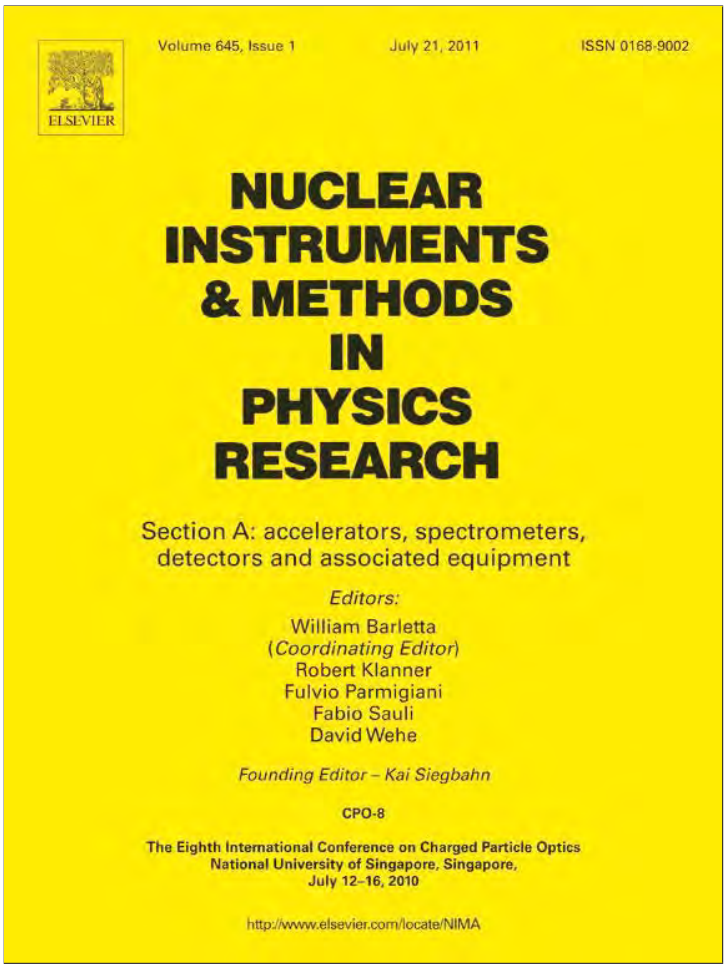

Nuclear Instruments and Methods in Physics Research A 645 (2011) 187–190

Contents lists available at ScienceDirect

Nuclear Instruments and Methods in Physics Research A

journal homepage: www.elsevier.com/locate/nima

Bunch compression efficiency of the femtosecond electron source at Chiang Mai University

C. Thongbai [a,b], K. Kusoljariyakul [a,b,*], J. Saisut [a,b]

[a] Department of Physics and Materials Science, Chiang Mai University, Chiangmai 50200, Thailand
[b] ThEP Center, Commission on Higher Education, Ministry of Education, Bangkok 10400, Thailand

ARTICLE INFO

Available online 17 December 2010

Keywords:
Bunch compression
Femtosecond electron bunch
RF-gun

ABSTRACT

A femtosecond electron source has been developed at the Plasma and Beam Physics Research Facility (PBP), Chiang Mai University (CMU), Thailand. Ultra-short electron bunches can be produced with a bunch compression system consisting of a thermionic cathode RF-gun, an alpha-magnet as a magnetic bunch compressor, and a linear accelerator as a post acceleration section. To obtain effective bunch compression, it is crucial to provide a proper longitudinal phase-space distribution at the gun exit matched to the subsequent beam transport system. Via beam dynamics calculations and experiments, we investigate the bunch compression efficiency for various RF-gun fields. The particle distribution at the RF-gun exit will be tracked numerically through the alpha-magnet and beam transport. Details of the study and results leading to an optimum condition for our system will be presented.

1. Introduction

Bunch compression can be considered as the exchange of longitudinal phase-space parameters [1] and generally requires two steps. First, an accelerating system creates a correlation between particle energy and position. Then, a non-isochronous magnetic transport line is used to rotate the particle distribution in phase-space until the desired bunch length is reached. The accelerating section is phased such that the center of the relativistic particle bunch does not see any field (zero-phase) while the particles ahead of the bunch center are accelerated and the particles behind the bunch center are decelerated. Following the accelerating section, the particles travel through an asynchronous curved beam transport system (chicane). Early particles within a bunch, having been accelerated, follow a longer path than the reference particles at the center of the bunch while the decelerated particles being late with respect to the bunch center follow a shorter path. All particles are considered highly relativistic and therefore bunch compression works by way of path variation rather than velocity.

The first step can be eliminated in the case of an electron beam generated in an RF-gun [1,2], in which the electron emerges from a cathode, which is inserted into an RF-cavity. The electrons are accelerated immediately where the acceleration is a strong function of time because of the rapidly oscillating field. An RF-gun with a thermionic cathode can produce an electron bunch with a correlation between energy and time such that higher energy particles are at the head of the bunch followed by lower energy particles. Bunch compression for this case can be achieved using an alpha-magnet [3], which got its name from the alpha-like shape of the particle trajectories. In the alpha-magnet, higher energy electrons follow longer paths, while lower energy electrons follow shorter ones and thereby leading to bunch compression.

A femtosecond electron source, as shown in Fig. 1, has been developed at the Plasma and Beam Physics Research Facility (PBP), Chiang Mai University (CMU), Thailand. Ultra-short electron bunches can be produced with the bunch compression system consisting of a thermionic cathode RF-gun, an alpha-magnet as a magnetic bunch compressor, and a linear accelerator as a post acceleration section. With a specific RF-gun design and alpha-magnet gradient, the electron bunch can be compressed down to sub-picosecond scale [4,5]. To obtain effective bunch compression, it is crucial to provide a proper longitudinal phase-space distribution at the gun exit matched to the subsequent beam transport system. Via beam dynamics calculations and experiments, we investigate the bunch compression efficiency for various RF-gun fields. The particle distribution will be tracked numerically from the RF-gun exit through the alpha-magnet and beam transport. Details of the study and results leading to an optimum condition for our system will be presented.

2. Electron source

The PBP-CMU RF-gun consists of 1½ S-band cavities and a thermionic cathode attached to one wall of the first half cell as indicated in Fig. 1. The full cell and the half cell are coupled through

* Corresponding author at: Department of Physics and Materials Science, Chiang Mai University, Chiangmai 50200, Thailand. Tel.: +66 53943379; fax: +66 53222776.
E-mail address: zartparz@gmail.com (K. Kusoljariyakul).

0168-9002/$ - see front matter © 2010 Elsevier B.V. All rights reserved.
doi:10.1016/j.nima.2010.12.068

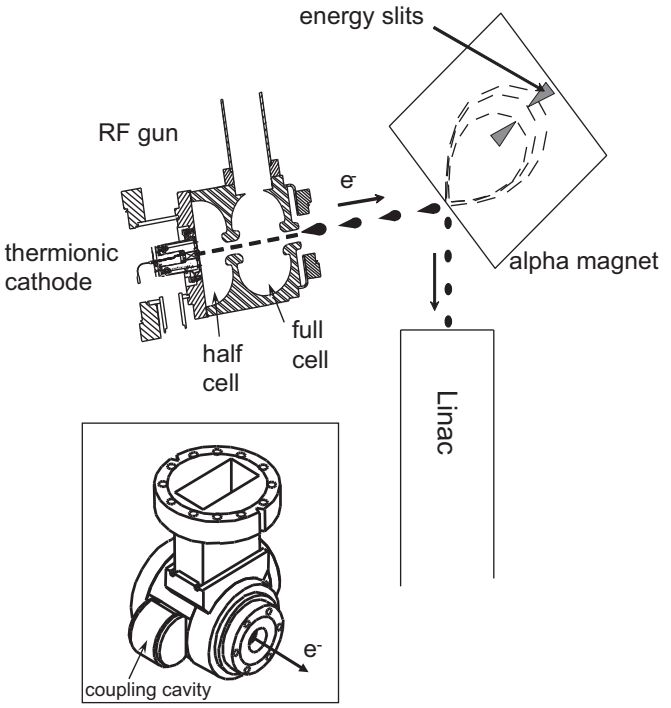

Fig. 1. Femtosecond electron source at the Plasma and Beam Physics Research Facility (PBP), Chiang Mai University (CMU).

a side coupling cavity, which can be seen in the 3D drawing of the RF-gun in Fig. 1. The dimensions and fields are specially optimized for ultra-short bunch generation. Systematic simulation studies were carried out to investigate the fundamental and practical limits in reducing the electron bunch lengths and details of RF-gun optimization as well as beam dynamic studies for generating femtosecond electron bunches have been described in Ref. [6]. Electron distribution at the RF-gun exit depends greatly on the RF field in each cell. The optimum ratio of the RF field in each cell as well as the field intensities play important roles in the bunch compression. For very high RF-field in the half cell, the bunch head can become quasi-monochromatic and thus not suitable for bunch compression [2,6]. Experimentally, the PBP-CMU RF-gun had been operated at the half cell/full cell field ratio (R) of 0.52 and 0.7. Particle distributions at the RF-gun exit obtained from PARMELA [7] at these two field ratios for various field gradients are shown in Fig. 2 and will be under further investigation for bunch compression efficiency.

Electrons are continuously emitted with thermal energies from the thermionic cathode and are extracted by RF-acceleration during an accelerating phase of the RF-fields at 2856 MHz, in the RF-gun. The first electron is accelerated rapidly and reaches the end of the half cell just before the RF-phase becomes decelerating. It is further accelerated through the full cell to reach a maximum kinetic energy of 2–3 MeV at the gun-exit depending on accelerating field gradients. Later electrons feel some decelerating fields before they exit the half cell and gain less and less overall energy. The bunch that exits the RF-gun is about 100 ps long having the highest energy electrons at the head of the bunch within 10–15 ps [8] forming the useful fraction of the electron bunch. Higher field ratios (half cell/full cell) for the same field in the full cell result in lower kinetic energy at the RF-gun exit.

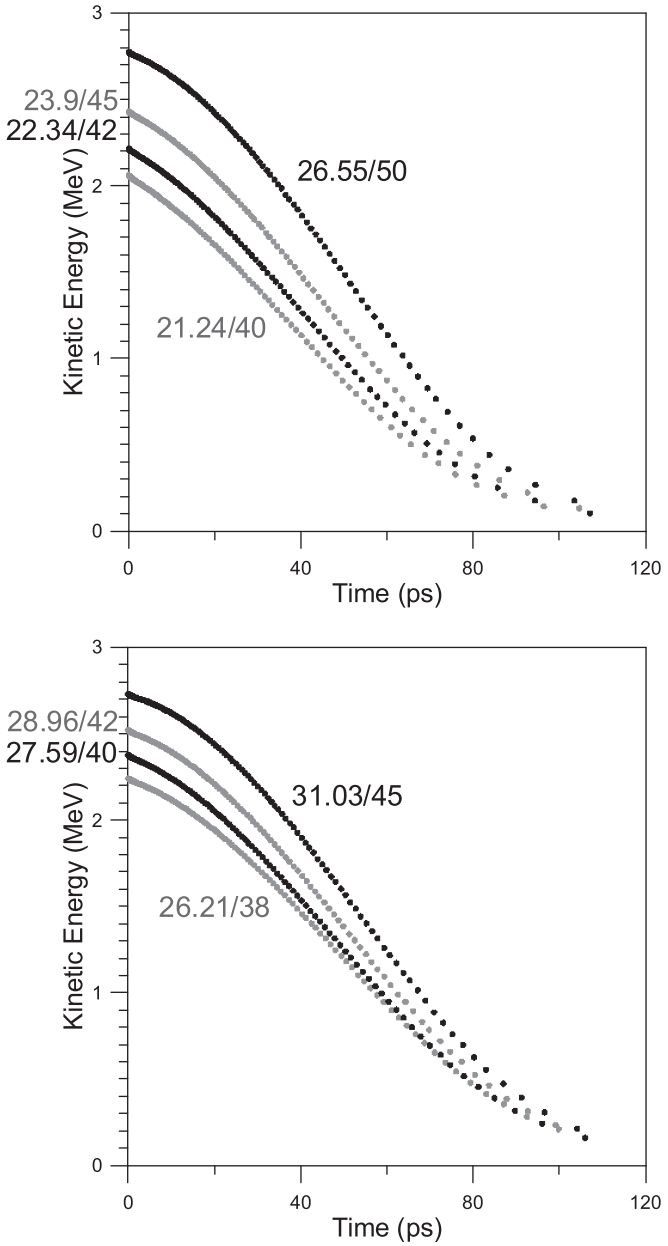

Fig. 2. Energy–time distribution of the electron bunch at the RF-gun exit for $R=0.52$ (top) and $R=0.7$ (bottom), half cell/full cell fields are shown in MV/m.

3. Bunch compression

Bunch compression is accomplished by guiding the 20–30 ps electron bunches from the RF-gun through an alpha-magnet [8]. The electrons enter the alpha-magnet at an angle of 49.29° with respect to the magnet axis. Particles entering at this angle follow a closed loop similar to the letter α and exit the magnet exactly at the entrance point independent of the particle momentum. The particle path length is, however, momentum dependent. The momentum dependent path length S scales with the magnetic field gradient g as $S \propto \sqrt{\beta\gamma/g}$ [2]. In the alpha-magnet, the particle path length, therefore, increases with energy. This allows the lower energy particles, emitted later in each bunch, to catch up with the front for effective bunch compression. Later on, the optimized and compressed part of the electron bunch will be filtered by energy slits located in the α-magnet vacuum chamber and then accelerated in a SLAC type linac and passing through a beam transport line to experimental stations. At the experimental station, the electron bunches reach a minimum bunch length of less than 1 ps.

To evaluate the bunch compression efficiency, particles are tracked numerically through all components from the RF-gun to

experimental stations. The traveling time within each component is calculated by the equations listed in Table 1 and the beam line parameters are listed in Table 2. The effect of traverse particle motion is not included in this calculation. The parameters l_d and l_q are drift length and effective quadrupole magnet length, respectively, g is the alpha-magnet field gradient (G/cm), and A is the linac acceleration gradient (MeV/m). The calculation starts by varying the alpha-magnet gradient while observing the particle bunch distribution. The optimum compression occurs when the bunch distribution (at least the head of the bunch) is close to a vertical line. The optimum compression at various RF-fields for the field ratio, $R=0.52$ and, $R=0.7$ are shown in Figs. 3 and 4, respectively.

As the RF field increases, a higher alpha-magnet field gradient will be required for optimum bunch compression. Optimum compression for higher field ratio R can be achieved at lower full cell RF-field. The bunch lengths evaluated from the simulation by a FWHM of the particle histogram are summarized in Tables 3 and 4 The calculations suggest an optimum compression for a field of 45 MV/m in the full cell for RF field ratio $R=0.52$, and 40 MV/m for the field ratio $R=0.7$.

Experimentally, bunch length measurements by an autocorrelation technique indicated an average bunch length of $\sigma_z \approx 170$ fs [4] for the field ratio $R=0.52$ and a bunch length of $\sigma_z \approx 350$ fs for the field ratio $R=0.7$. The operating full cell RF field is approximately 42–44 MV/m. Therefore, in case of the $R=0.7$, a lower RF-field than the current operating condition would allow generation of shorter electron bunches.

Table 1
Traveling time within beam line components.

Component	Traveling time
Drift space	$t_d = l_d/\beta c$
Quadrupole magnet	$t_q = l_q/\beta c$
Alpha-magnet	$t_a = (1.91655/\beta c)\sqrt{\beta\gamma/g}$
Linac	$t_L = \Delta(cp)/cA$

Table 2
Beam line parameters.

Component	Length (cm)	Gradient
Gun to alpha	67.9	–
Alpha-magnet	–	Varied
Alpha to linac	113.4	–
Linac	304.0	2.7 MeV/m
Linac to experimental station	119.9	–

4. Conclusion

Bunch compression efficiency depends greatly on the cavity RF-fields and the alpha-magnet gradient. Calculation of bunch

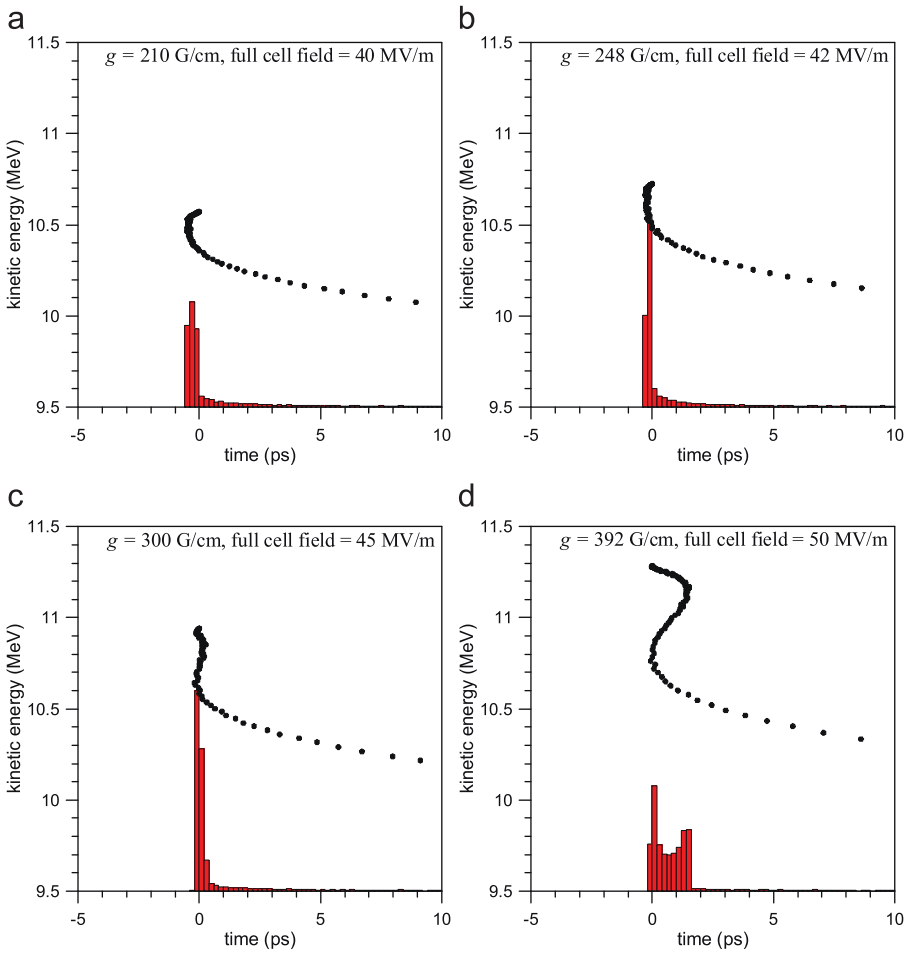

Fig. 3. Optimum electron distributions at the experimental station for $R=0.52$ when using 40, 42, 45, and 50 MV/m full cell RF-fields with alpha-magnet gradient, $g=210$, 248, 300, and 392 G/cm, respectively.

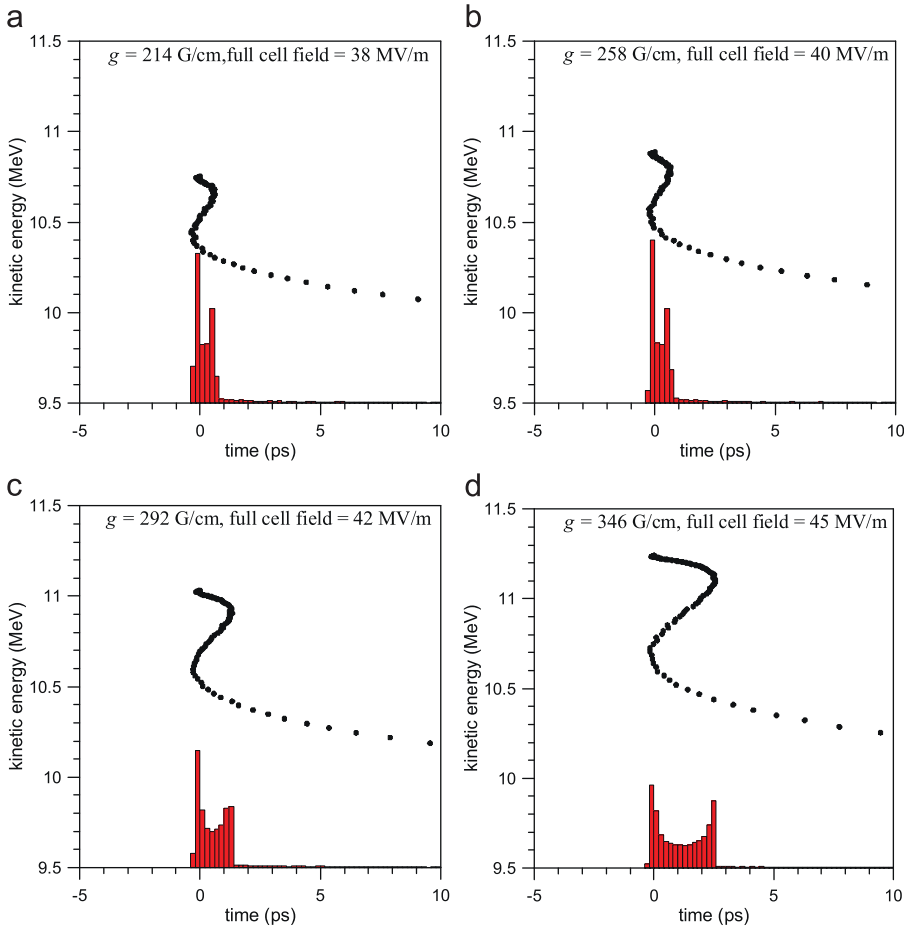

Fig. 4. Optimum electron distributions at the experiment station for $R=0.7$ when using 38, 40, 42, and 45 MV/m full cell RF-fields with alpha-magnet gradient, $g=214$, 258, 292, and 346 G/cm, respectively.

Table 3
Condition for optimum electron distributions at the experimental station for the field ratio, $R=0.52$.

Half cell field/full cell field (MV/m)	Optimum alpha-magnet gradient (G/cm)	Bunch length (ps)
21.24/40	210	0.5
22.34/42	248	0.3
23.9/45	300	0.4
26.55/50	392	1.7

Table 4
Conditions for optimum electron distributions at the experiment station for the field ratio, $R=0.7$.

Half cell field/full cell field (MV/m)	Optimum alpha-magnet gradient (G/cm)	Bunch length (ps)
26.21/38	214	1.0
27.59/40	258	0.9
28.96/42	292	1.5
31.03/45	346	3.0

compression efficiency can be done by tracking particle distribution numerically from the RF-gun exit through the alpha-magnet and beam transport. Experimental results of bunch length measurement agree with the calculation. The calculations suggest an optimum compression at 45 MV/m for half cell/full cell field ratio $R=0.52$ and at 40 MV/m for the field ratio $R=0.7$.

Acknowledgements

The authors are grateful to Helmut Wiedemann for his comments and suggestions. We would like to thank M.W. Rhodes, P. Wichaisirimongkol, and N. Kangrang for technical assistance. We acknowledge the support from Department of Physics and Materials Science, Faculty of Science and Graduate School of Chiang Mai University, National Research Council of Thailand, the Thailand Research Fund, the (Thailand) Commission on Higher Education, and the Thailand Center of Excellence in Physics.

Reference

[1] H. Wiedemann, Particle Accelertor Physics, 3rd edition, Springer-Verlag, Berlin Heidelberg New York, 2007.
[2] M. Borland, A high-brightness thermionic microwave electron gun, Ph.D. Thesis, Stanford University, Stanford, CA, 1991.
[3] H.A. Enge, Rev. Sci. Instrum. 34 (1963) 385.
[4] C. Thongbai, et al., Nucl. Instr. and Meth. 587 (2008) 130.
[5] J. Saisut et al., Nucl. Instr. and Meth., in press, doi:10.1016/j.nima.2010.02.032.
[6] S. Rimjeam, et al., Nucl. Instr. and Meth. 533 (2004) 258.
[7] L.M. Young, J.H. Billen, Los Alamos National Laboratory Technical Note, LA-UR-96-1834, Los Alamos, NM, 1999.
[8] P. Kung, et al., Phys. Rev. Lett. 73 (1994) 967.

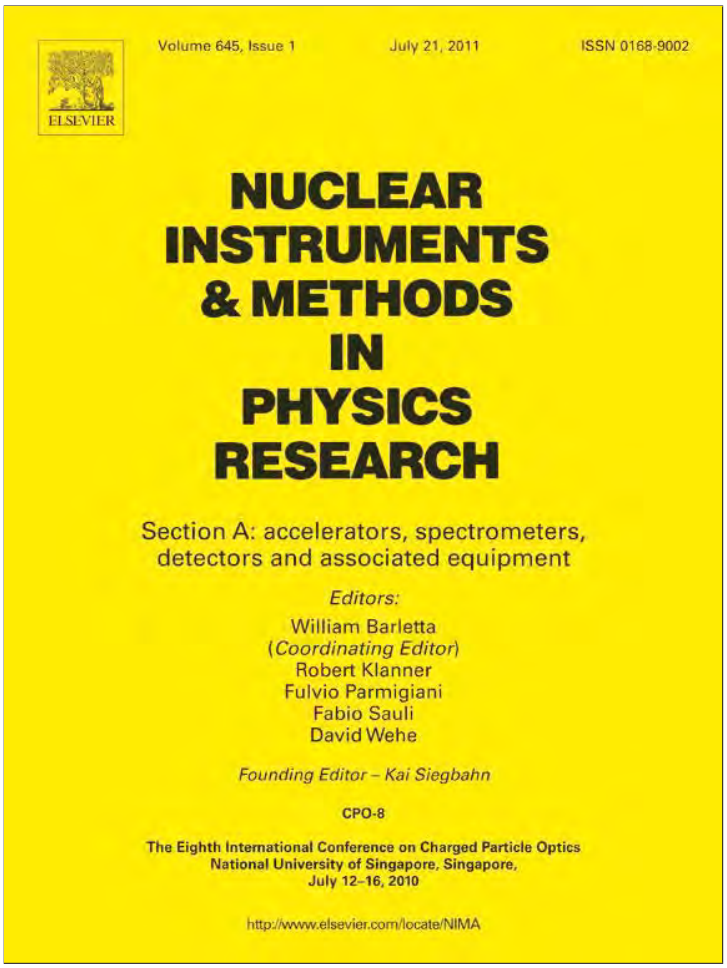

Nuclear Instruments and Methods in Physics Research A 645 (2011) 191–196

Contents lists available at ScienceDirect

Nuclear Instruments and Methods in Physics Research A

journal homepage: www.elsevier.com/locate/nima

Study of thermionic RF-gun phase-space dynamics and slice emittance under influence of external electromagnetic fields

K. Kusoljariyakul [a,b], C. Thongbai [a,b,*]

[a] Department of Physics and Materials Science, Faculty of Science, Chiang Mai University, Chiang Mai 50200, Thailand
[b] ThEP Center, Commission on Higher Education, Ministry of Education, Bangkok 10400, Thailand

ARTICLE INFO

Available online 16 December 2010

Keywords:
Bunch compression
Femtosecond electron bunch
RF-gun

ABSTRACT

A high brightness electron source of ultra-small emittance and high-average current is one of the most important components for future accelerators. In a RF-electron-gun, rapid acceleration can reduce emittance growth due to space charge effects. However, twisting or rotation of the transverse phase-space distribution as a function of time is observed in thermionic RF-electron-guns and may set a lower limit to the projected beam emittance. Such rotation being caused by the variation of the RF field with time may be compensated by fields from a specific cavity. In this work, we study RF-electron-gun phase-space dynamics and emittance under the influence of external fields to evaluate the compensation schemes.

1. Introduction

A high brightness electron source of ultra-small emittance and high-average current is one of the most importance components for future electron accelerators [1,2]. Such beams are used as sources of very high energy linear colliders, wake-field laser accelerator and X-ray free electron laser.

In order to achieve high brightness beams, it is necessary to master the production of such beams in special RF-guns, to develop diagnostic techniques that provide information of the six-dimensional phase-space distribution of electron bunches on sub-picosecond time scales, to control the six-dimensional distribution of the bunch in various ways and to be able to accelerate the electrons to higher energies without diluting the brightness.

Electron bunches produced from a thermionic cathode RF-gun is subjected to detrimental effects on the beam emittance, specifically to a twisting of the time-sliced phase-space. The transverse phase-space rotation can increase the projected emittance by several orders of magnitude. Thus, in order to obtain a high brightness beam, it is highly desirable to minimize this effect. This phenomenon may be compensated by passing the beam through a proper time dependent external electromagnetic field. In this study, we investigate schemes that reduce the projected emittance while preserving Louville's theorem of constancy of the beam emittance by lining up temporal slices of phase-space distribution.

2. Method

In this study, we focus on compensation of the particle distribution from the PBP-CMU RF-gun at the Plasma and Beam Physics facility (PBP), Chiang Mai University, Thailand. The PBP-CMU RF-gun consists of $1\frac{1}{2}$ S-band cavities and a thermionic cathode attached to one wall of the first half-cell as shown in Fig. 1. The full-cell and the half-cell are coupled through a side coupling cavity, which can be seen in the 3D drawing of the RF-gun in Fig. 1. The details of RF-gun optimization for the production of femtosecond electron bunches as well as beam dynamic studies have been described in Ref. [3]. In this study, the dynamics of particle motion in the RF-gun and in the external electromagnetic fields has been simulated with the code PARMELA [4]. Note that the average half-cell and full-cell fields used in the simulation are 23.9 and 45.5 MV/m as specified in Ref. [3].

2.1. Beam emittance

Beam emittance is the region in phase-space occupied by particles in a beam [5]. By definition, phase-space is represented by coordinates and their conjugate momenta. However, for constant energy particles it is more convenient to replace the conjugate momentum with the slope of the trajectory (x'), defined as

$$p_x = p_o \tan x' \approx p_o \tan x'. \quad (1)$$

In this paper, the term "beam emittance" is used for transverse apparent or projected emittance while "slice emittance" is used for emittance of a time-sliced beam. In either case, the emittance is

* Corresponding author at: Department of Physics and Materials Science, Faculty of Science, Chiang Mai University, Chiang Mai 50200, Thailand. Tel.: +66 53943379; fax: +66 53222776.
E-mail addresses: chlada@yahoo.com, chlada123@gmail.com (C. Thongbai).

0168-9002/$ - see front matter © 2010 Elsevier B.V. All rights reserved.
doi:10.1016/j.nima.2010.12.058

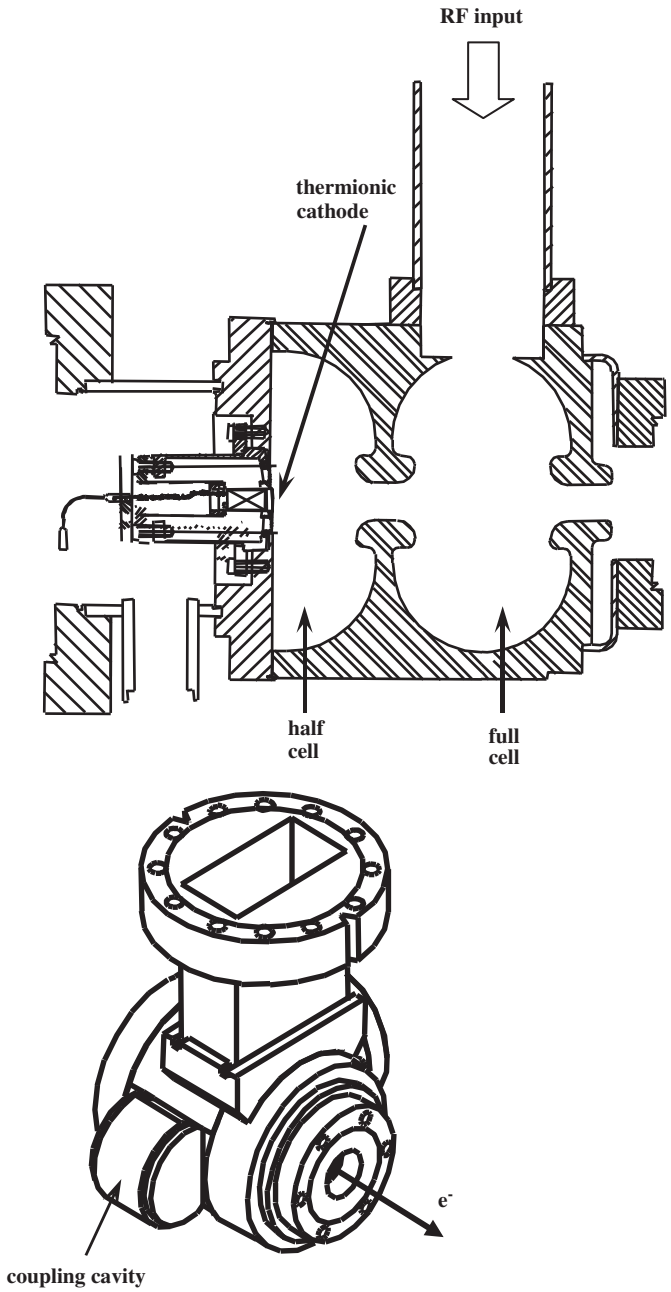

Fig. 1. PBP-CMU RF-gun at Plasma and Beam Physics facility (PBP), Chiang Mai University.

calculated as the r.m.s. emittance, defined by

$$\varepsilon_x = \sqrt{\langle x_i^2 \rangle \langle x'^2_i \rangle - \langle x_i x' \rangle^2} \quad (2)$$

where the average is taken over all particles i. Space charge forces and radial fields in RF-cavities can degrade the beam emittance significantly. The space-charge effect is inversely proportional to the square of the particle energy. Thus, rapid acceleration in a RF-gun reduces the space-charge effect. Moreover, space charge effect causes rotation of the transverse phase-space distribution due to its energy dependence. Eq. (2) indicates that if all particles lie on a line in phase space, in other words, $x = mx'$, the beam emittance will vanish. Since m is time dependent, this rotation cannot be ignored if a high brightness beam is to be achieved. There are several approaches suggested for emittance minimization, for example, using a solenoid magnet [5], using RF radial focusing [6], alternative cathode material [7] and special RF-gun designing.

2.2. Slice phase-space

Fig. 2 shows the transverse phase-space distribution at the PBP-CMU RF-gun exit every ps along the microbunch. The twisting or rotation of the time-sliced phase-space can obviously be seen. Closer inspection of the 1 ps phase-space distribution in terms of time correlation can be obtained by looking at x'/x and y'/y ratios. The ratio for each phase-space slice is obtained by fitting data with robust straight-line fit [8]. The x'/x and y'/y ratios as a function of time is shown in Fig. 3. This time response will give an estimation of compensation needed for each phase-space slice. The rotation of horizontal and vertical phase-space slice are very much alike. Fig. 4 shows the energy–time phase space of the electron bunch at the RF-gun exit with a histogram. The head of the bunch contains higher energy particles followed by lower energy ones and the particles are more concentrated at the head of the bunch. The energy–time phase-space information should be taken into account for beam dynamics studies.

2.3. Transverse magnetic fields

To compensate the observed phase-space rotation, different deflections should be applied to particles that are off-center. Increasing deflection should be applied for particles at increasing distance from the beam center. Transverse magnetic modes of a circular cylindrical cavity TM_{01p} with azimuthal magnetic fields increasing with radial positions seem to serve our purpose. The general expression for the TM_{01p} field components are [9]

$$E_z = E_o J_o(k_1 r)\cos\frac{p\pi z}{l} e^{i\omega t}$$
$$E_r = \frac{-p\pi}{l}\frac{a}{x_1} E_o J'_o(k_1 r)\sin\frac{p\pi z}{l} e^{i\omega t}$$
$$B_\phi = -j\omega\frac{a}{x_1 c^2} E_o J'_o(k_1 r)\cos\frac{p\pi z}{l} e^{i\omega t}. \quad (3)$$

3. Results and discussion

The TM_{010} mode and TM_{011} mode were investigated in this study. Since the rotations of horizontal and vertical phase-space slices are very much alike and the TM fields under the investigation are azimuthally symmetric, only the results for horizontal phase space will be presented. The field amplitudes are optimized by considering the compensation required in each phase-space slice. The required deflection can be calculated using the x'/x ratio normalized to the average energy of each beam slice. Analysis of the time response for the compensation suggested the $\sin(\omega t)$ field at S-band frequency. The dimensions of the S-band TM_{010} and TM_{011} cavities used in this study are listed in Table 1. Fig. 5 shows the phase-space distribution of the simulated beam after passing the TM_{010} cavity with the cavity length of the 1 S-band wavelength. Figs. 6 and 7 show the phase-space distribution of the simulated beam after passing the TM_{011} cavities with the cavity lengths of 1 S-band and 1/2 S-band wavelengths, respectively. The insets show the energy–time phase space of the electron bunch after passing each cavity. Fig. 8 shows the phase-space distribution for all slices (projected) of the beam at the RF-gun exit and after passing the TM_{010} and TM_{011} cavities. The compensation results in terms of projected emittance, calculated using Eq. (2), are listed in Table 2. The beams have gained some energy after passing through the TM_{011} cavities. Therefore, normalized projected emittance to the beam average energy will be used for comparison.

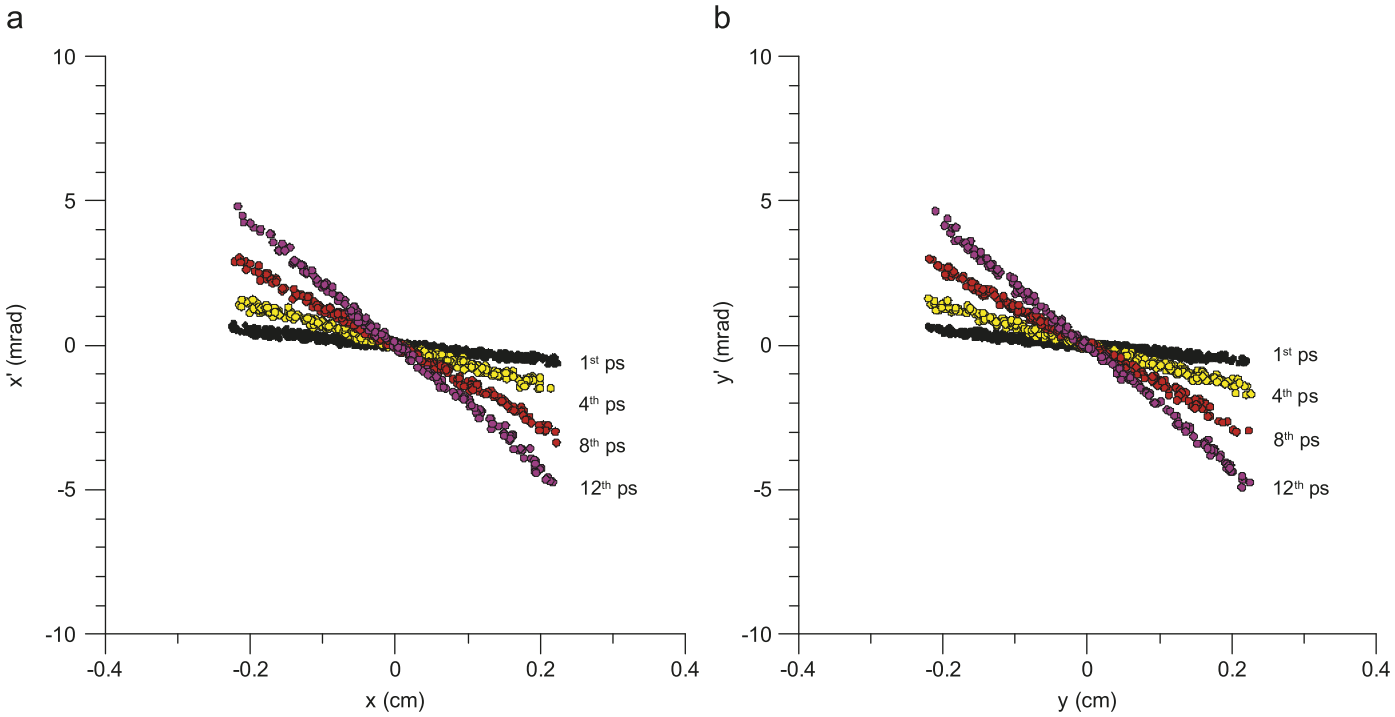

Fig. 2. Transverse phase-space distribution [(a) horizontal and (b) vertical] at PBP-CMU RF-gun exit every ps along microbunch.

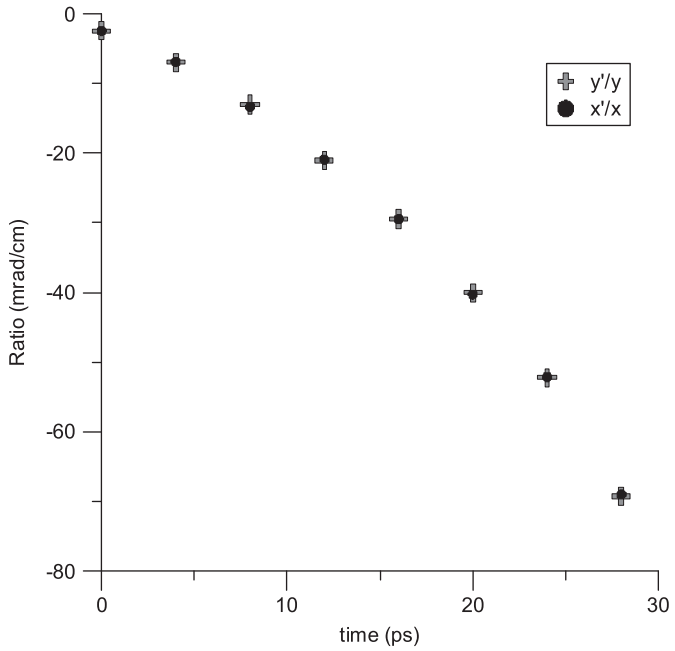

Fig. 3. x'/x and y'/y ratios at RF-gun exit as function of time.

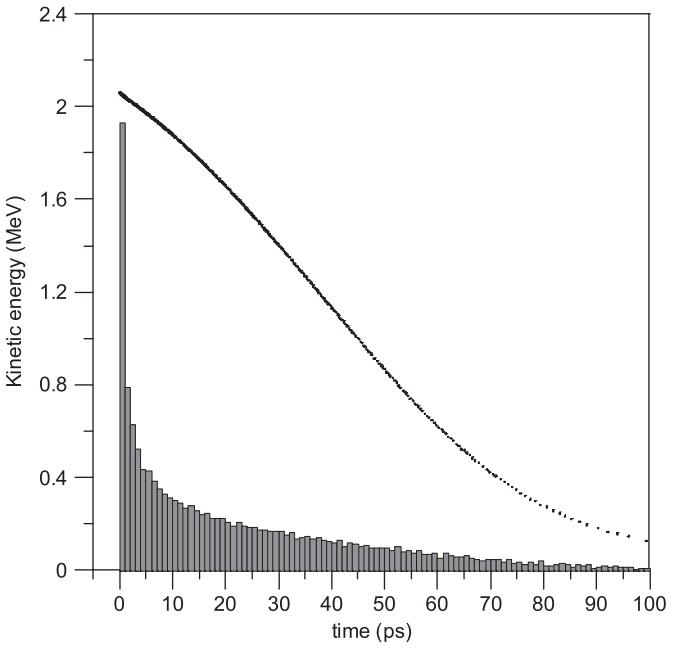

Fig. 4. Energy–time phase-space of electron bunch at RF-gun exit with histogram.

The normalized projected emittance and the beam energy increase after passing the 1-wavelength-long TM_{011} cavity. With the 1-wavelength-long TM_{010} cavity, the normalized projected emittance decreases by 10–20% while the beam energy and the energy–time phase-space remain the same. The 1/2-wavelength-long TM_{011} cavity offers the best compensation of around 30% reduction but the energy–time phase space becomes undesirable for bunch compression purposes. Moreover, the geometry of such a cavity is not practical.

Table 1
Cavity dimensions.

Cavity	Cavity length (cm)	Cavity radius (cm)
$1-\lambda_{S\text{-band}}$-TM010	10.497	4.018
$\frac{1}{2}-\lambda_{S\text{-band}}$-TM011	5.249	1140.00
$1-\lambda_{S\text{-band}}$-TM011	10.497	4.640

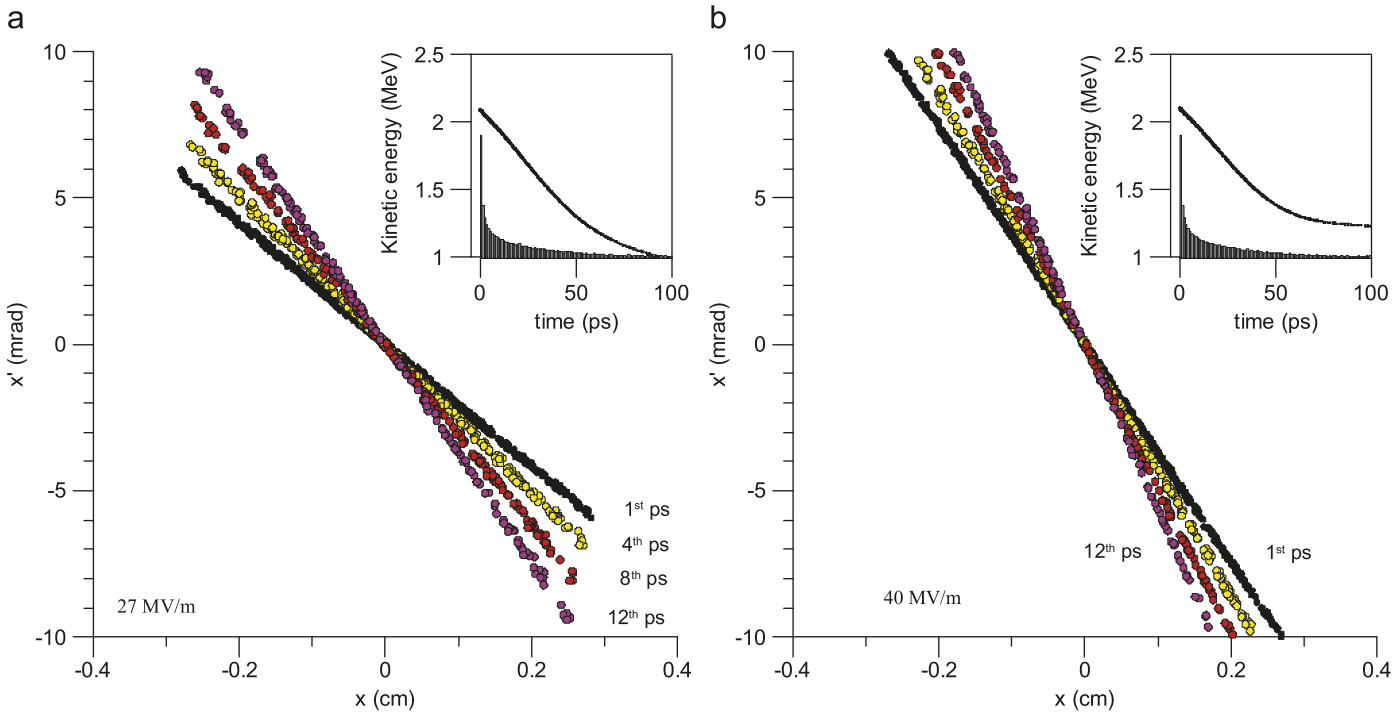

Fig. 5. Phase-space distribution of simulated beam after passing TM_{010} cavity with cavity length of 1 S-band wavelength.

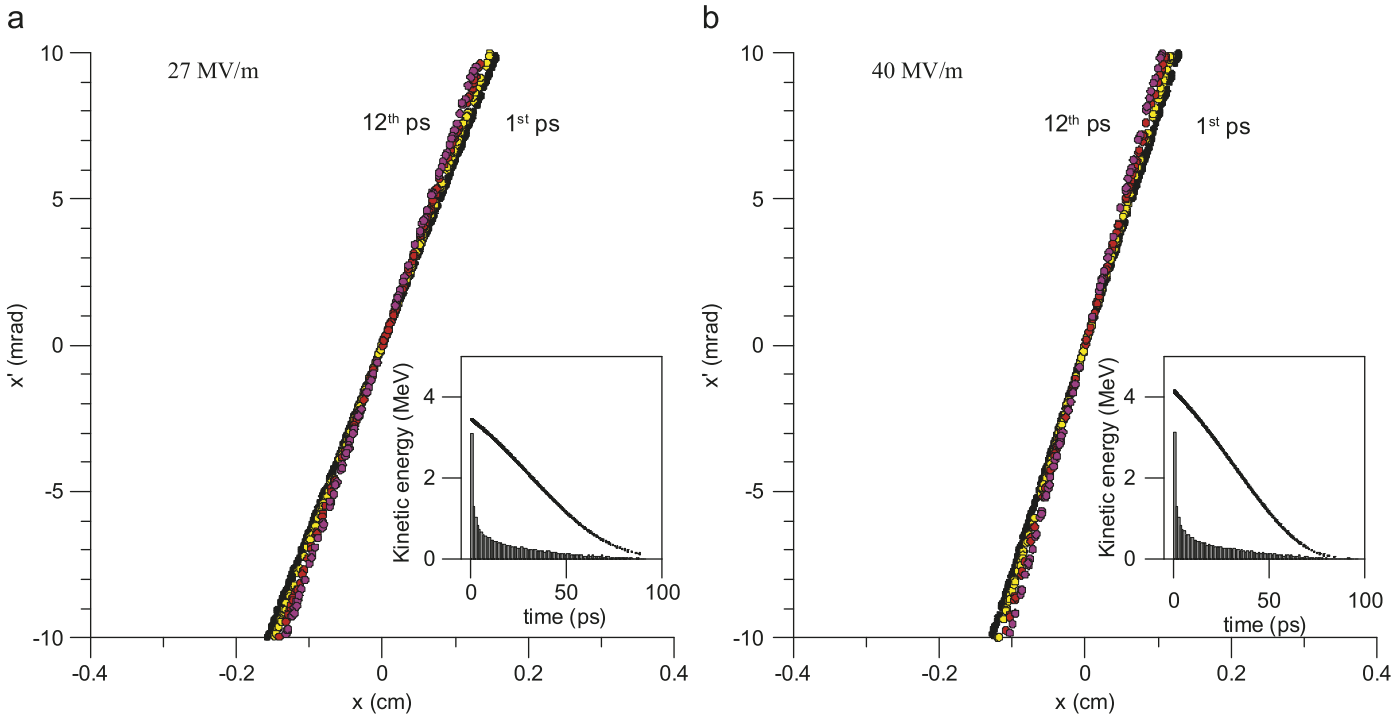

Fig. 6. Phase-space distribution of simulated beam after passing TM_{011} cavity with cavity lengths of 1 S-band wavelength.

4. Conclusion

The study of phase-space dynamics of the electron beam from the PBP-CMU thermionic cathode RF-gun through some compensation electromagnetic fields has been conducted. The preliminary simulation results show that the TM_{010} and TM_{011} cavities are capable of lining up the phase-space slice and reducing the projected emittance of the PBP-CMU beam. However, there are more parameters that should be included and optimized in the study. Further study to find more specific parameters of the cavities will be conducted. The final results may lead us to a new emittance compensation scheme.

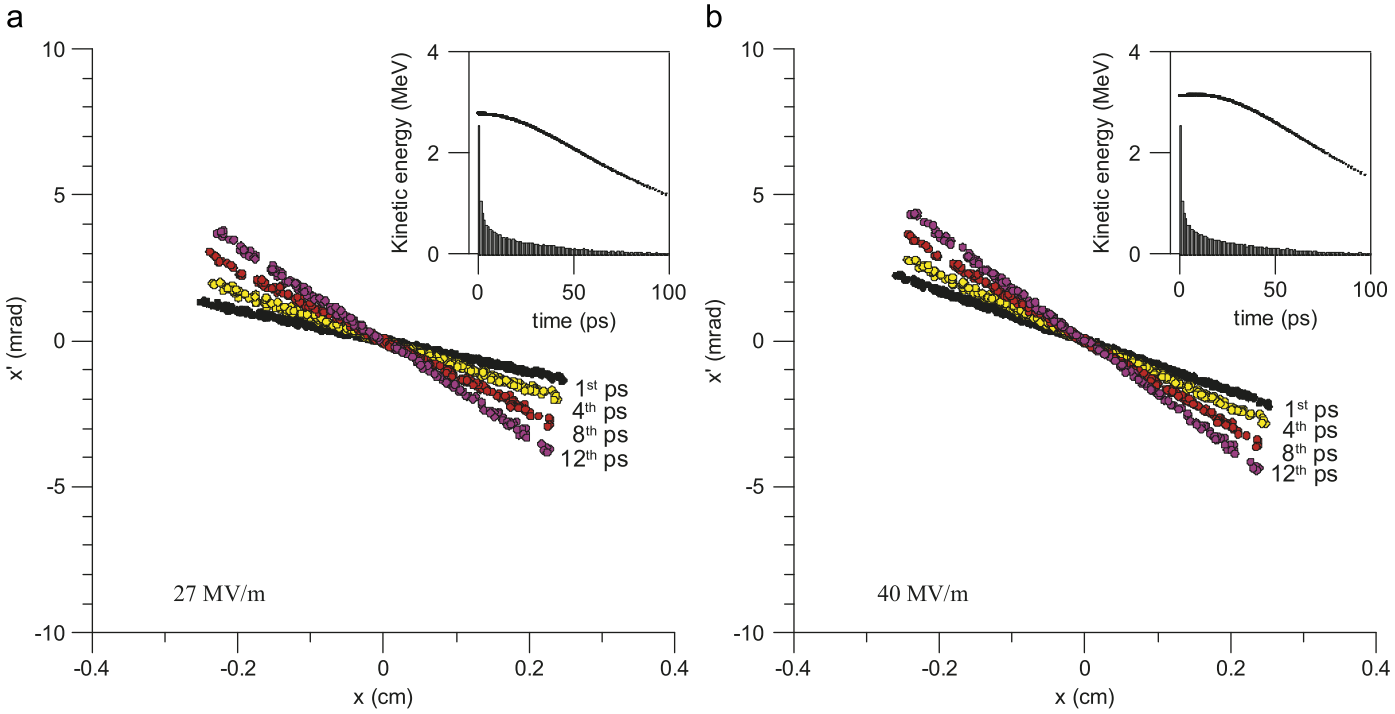

Fig. 7. Phase-space distribution of simulated beam after passing TM_{011} cavity with cavity lengths of 1/2 S-band wavelength.

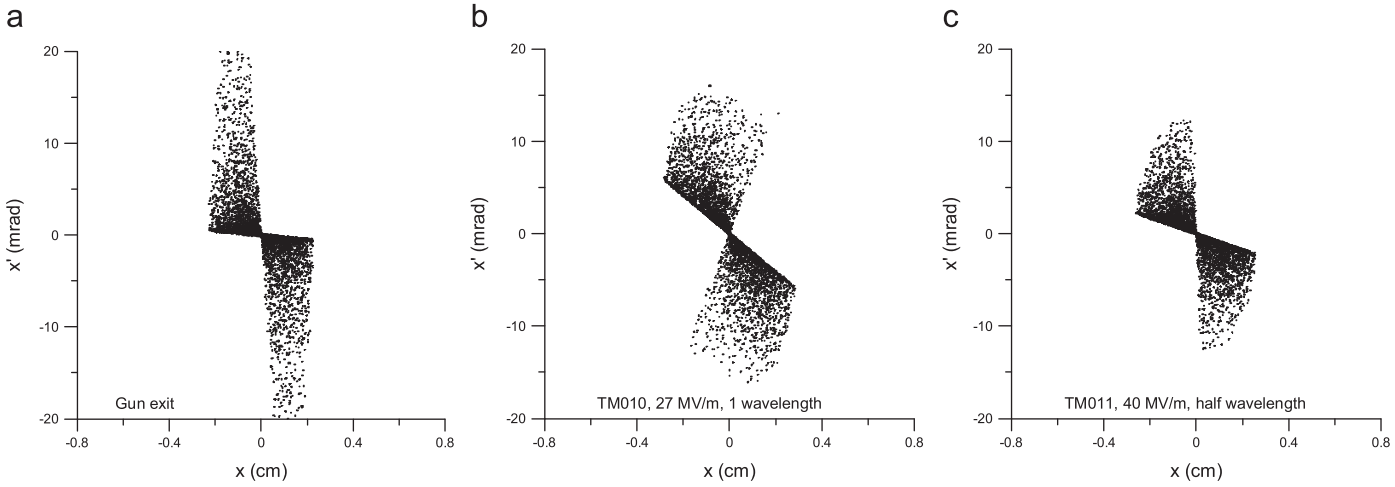

Fig. 8. Phase-space distribution (projected) of beam at RF-gun exit and after passing TM_{010} and TM_{011} cavities.

Table 2
Projected emittance obtained from simulation.

	Projected ε_{rms} (mm mrad)	Normalized ε_{rms} (mm mrad)	Maximum kinetic energy (MeV)
Gun exit			
(x)	6.406	27.673	2.06
(y)	6.423	27.749	
$1-\lambda_{S\text{-band}}$-TM010 27 MV/m	4.788	21.340	2.09
$1-\lambda_{S\text{-band}}$-TM010 40 MV/m	5.507	24.943	2.11
$\frac{1}{2}-\lambda_{S\text{-band}}$-TM011 27 MV/m	3.292	20.105	2.79
$\frac{1}{2}-\lambda_{S\text{-band}}$-TM011 40 MV/m	2.829	19.687	3.16
$1-\lambda_{S\text{-band}}$-TM011 27 MV/m	5.174	31.571	3.46
$1-\lambda_{S\text{-band}}$-TM011 40 MV/m	5.113	35.895	4.15

Acknowledgements

The authors are grateful to Helmut Wiedemann for his comments and suggestions. We would like to acknowledge the support from Department of Physics and Materials Science, Faculty of Science and Graduate School of Chiang Mai University, National Research Council of Thailand, the Thailand Research Fund, the (Thailand) Commission on Higher Education and the Thailand Center of Excellence in Physics.

References

[1] K.J. Kim, et al., Toward advanced electron beam brightness enhancement and conditioning, ANL/APS/LS-305, 2004.
[2] J.W. Lewellen, Overview of high-brightness electron guns, in: Proceedings of LINAC2004, 2004.
[3] S. Rimjeam, et al., Nucl. Instr. and Meth. A 533 (2004) 258.
[4] L.M. Young, PARMELA, LANL Technical Note, LA-UR-96-1835, 2002.
[5] B.E. Carlsten, Nucl. Instr. and Meth. A 285 (1989) 313.
[6] B.E. Carlsten, D.T. Palmer, Nucl. Instr. and Meth. A 425 (1999) 37.
[7] S.H. Kong, J. Appl. Phys. 77 (1995) 6031.
[8] William H. Press, et al., Numerical Recipes, 3rd edition, Cambridge University Press, 2007.
[9] Thomas Wangler, RF Linear Accelerator, John-Wiley & Sons, Inc., New York, 1998.

Journal of the Korean Physical Society, Vol. 59, No. 2, August 2011, pp. 534∼541

Accelerators and Related R & D Activities in Thailand

T. Vilaithong,* S. Singkarat, L. D. Yu, C. Thongbai and T. Kamwanna
Thailand Center of Excellence in Physics, Commission on Higher Education, 328 Si Ayutthaya Road, Bangkok 10400, Thailand and Plasma and Beam Physics Research Facility, Department of Physics and Materials Science, Faculty of Science, Chiang Mai University, Chiang Mai 50200, Thailand

P. Songsiriritthigul
Thailand Center of Excellence in Physics, Commission on Higher Education, 328 Si Ayutthaya Road, Bangkok 10400, Thailand and School of Physics, Suranaree University of Technology and Synchrotron Light Research Institute, 111 University Avenue, Nakhon Ratchasima 30000, Thailand

(Received 11 November 2010, in final form 17 April 2011)

The production and the utilization of four fundamental probes, namely, electron, ion, neutron and photon probes, have played a vital role in the research and development in modern science and technology. These probes are generated by various types of particle accelerators. In Thailand, beams of charged particles are accelerated to energies ranging from keV to GeV. Low-energy (<200 keV) heavy-ion implanters are applied to research in material surface modification, biology and nanotechnology whereas the MeV tandem accelerator is employed in material surface analysis and lithography. Relativistic femtosecond electron beams are used to produce transition radiation with wavelengths in the tera-Hertz (THz) region. Synchrotron radiation is generated from a 1.2-GeV electron synchrotron coupled to a storage ring. The details of present and future accelerator R & D activities are presented and discussed.

PACS numbers: 29.20.Ba, 29.20.dk, 29.20.Ej, 81.05.-t, 87.53.-j, 41.60.Dk, 07.85.Qe
Keywords: Accelerator, Ion implanter, Ion beam, Electron beam, Synchrotron, Material modification, Ion beam biotechnology, Transition radiation, Linac
DOI: 10.3938/jkps.59.534

I. INTRODUCTION

In Thailand, the first accelerator facility was established in Chiang Mai about four decades ago. A nanosecond pulsed neutron generator was constructed and installed at the Fast Neutron Research Facility on the main campus of Chiang Mai University (CMU) [1]. The high stability Cockcroft-Walton-type accelerator was modified to incorporate beam chopping and bunching devices. A 140-keV deuteron beam was used to produce neutrons from the $T(d,n)^4$ He reaction. Pulsed neutrons, 1.5 – 2 ns, were initially utilized in the measurement of double differential neutron emission cross sections with a 10-m flight path [2]. A few years later, a 150-kV heavy-ion implanter with 0° and 45° beam lines was designed and constructed [3]. Gaseous ions such nitrogen ions were generated and used to modify tribological properties of metals and alloys. Subsequent machines were installed for ion-bioengineering studies. A decade ago, femtosecond electron bunches from a thermionic RF-gun with a bunch compressing α-magnet were built at CMU for the SURIYA facility [4]. At the beginning of this century, a synchrotron radiation facility based on a 1-GeV electron beam coupled to a storage ring was commissioned at the Synchrotron Light Research Institute in Nakorn Ratchasima. In this paper, the development and the present status of accelerator technology and its utilizations are reviewed.

II. ION BEAM

Development of low- and medium-energy (keV – MeV) ion-beam accelerators and related technology and applications has been a main focus of the national research in accelerator physics. We have established an ion beam research center at CMU as a unique comprehensive ion beam and plasma research laboratory in the ASEAN (Association of Southeast Asian Nations) region. The laboratory, named Plasma and Beam Physics Research Facility, is now equipped with a 1.7-MV Tandetron tandem accelerator mainly for ion beam analysis (Fig. 1),

*E-mail: thirapat@fnrf.science.cmu.ac.th; Fax: +66-53-222774

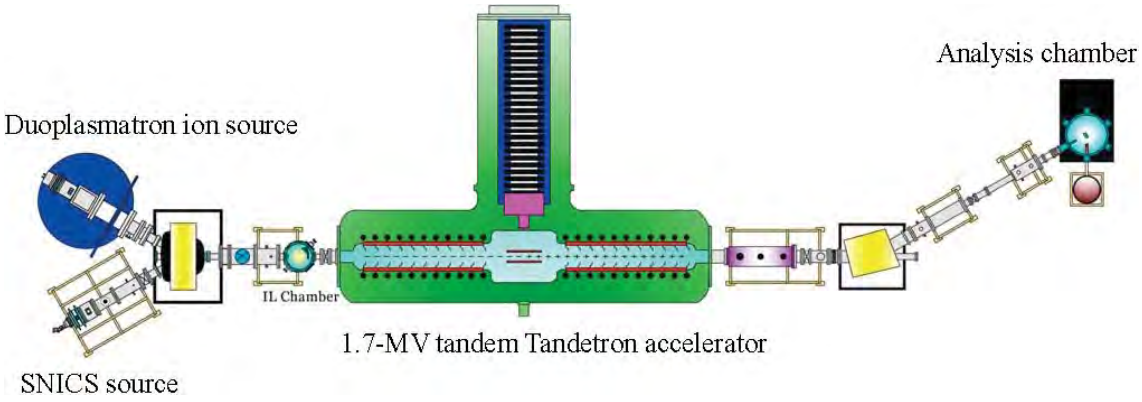

Fig. 1. Schematic diagram of the 1.7-MV tandem accelerator and ion beam line for ion beam analysis.

a 220-kV Varian versatile ion implanter for various ion implantations, a 30-kV bioengineering-specialized vertical ion beam line for biological applications, a 30-kV plasma immersion ion implantation facility for material surface modification, a 10-kV ion beam neutralizer for neutral beam implantation in non-conducting materials, and a number of plasma facilities. Historically, a 150-kV deuteron-accelerator-based 14-MeV fast neutron generator, a 150-kV heavy-ion implanter, a 150-kV high-current broad-beam ion implanter and a 300-kV ns-pulsed accelerator-based beam line with a chopper-buncher system [5] for time-of-flight (TOF) Rutherford backscattering spectrometry (RBS) analysis were also constructed, but have since been demolished. With applying all of these ion beam facilities, Thai scientists have been able to carry out very much research work on materials modification, surface analysis and biological applications and achieve significant attainments.

In Thailand, ion beams were first applied for modification of solid materials, such as local steels [6], alloys [7], cermets [8], ceramics [9,10], and semiconductors [11]. We achieved improvements in material surface hardness, wear resistance, friction coefficient, corrosion resistance, high-temperature oxidation resistance, optical properties and formation of nanostructures.

Based on the success in the conventional materials modification by ion beams, the application of ion beams was extended to biology. The ion beam biology (IBB) research has been an emphatic research program in the field of low-energy accelerator applications. It was launched in 1998 and since then has continued in Thailand. The research is generally aimed at utilizing ion beam and plasma technology for applications in biology, agriculture, horticulture, medical science and life science. This is a highly interdisciplinary field requiring highly international and inter-departmental collaborations. Our work involves equipment development, technology development and basic research. The research has led to establishment of ion beam biotechnology in the country and has succeeded in ion-beam-induced mutations of local rice (Fig. 2), flowers and vegetables and DNA transfer in bacteria and yeasts [12–14]. The basic research has been focused on investigations of the mechanisms involved in the ion-beam-induced mutation and DNA transfer, such as low-energy ion interactions with DNA and cell envelope materials [15–17].

Fig. 2. Photograph of Thai local rice mutants in either short straw (the two in the middle) or tall straw (left) induced by N-ion beam bombardment compared with the control (right).

Besides the applications in materials modification, ion beams have been applied for material analysis. Two accelerators, namely, the 1.7-MV Tandetron tandem accelerator and the 300-kV medium-energy ns-pulsed ion beam accelerator, have been employed for material analysis. The Tandetron accelerator employs two ion sources, a duoplasmatron ion source and a source of negative ions by cesium sputtering (SNICS), capable of producing analyzing ion beams of light species, such as hydrogen and helium, and heavy species. The beam line is currently capable of being used for ion beam analysis techniques such as Rutherford backscattering spectrometry (RBS), RBS/channeling, particle induced X-ray emission (PIXE), elastic (non-Rutherford) backscattering (EBS) and ionoluminescence (IL) with the assistance of commercial and self-developed softwares. The medium-energy ion accelerator is featured with ns-pulsed beam so that time-of-flight (ToF) RBS analysis using medium-energy ion beams is available for detailed anal-

Table 1. Operating and beam parameters of the electron beam accelerator at CMU.

Parameters	RF-gun	Linac
Beam energy [MeV]	2.2 – 3	6 – 10
Macropulse peak current [mA]	1000	50 – 150
RF-pulse length (FWHM) [μs]	2.8	8
Repetition rate [Hz]	10	10
Beam-pulse length [μs]	$\sim$2	$\sim$0.8
Number of microbunches/macropulse	5700	2300
Number of electrons/microbunches	1.4×10^9	$8 \times 10^7 - 6 \times 10^8$

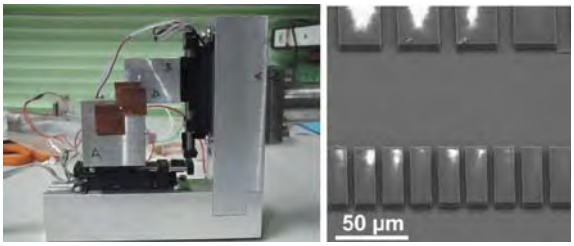

Fig. 3. The MeV ion beam lithography system and application. Left: photograph of the L-shape aperture system. The arrow points to the aperture. Right: SEM micrographs of patterns written in a 7.5-μm-thick PMMA layer by using the L-shape aperture system with a 3-MeV He beam.

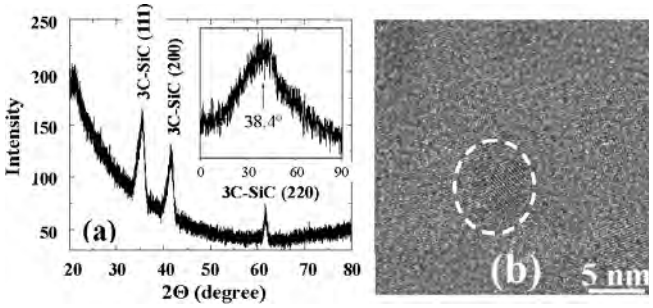

Fig. 4. SiC nanocrystallite formed by C-ion implantation in a Si wafer: ion beam energy: 40 keV, fluence: 6.5×10^{17} ions/cm^2, implantation temperature: 400 °C. (a) XRD spectrum from the sample. The measurement was done for the Θ-2Θ plane positioned at the angle of 38.4° from the (001) direction of the substrate. The inset shows the 3C-SiC (111) peak intensity as a function of the Θ-2Θ plane angle with respect to the substrate (001) orientation (for the 90° case, the plane is parallel to the wafer surface). The mean SiC grain size was calculated by using the Scherrer formula to be 8.4 nm. (b) TEM micrograph of the SiC nanograin; one of the examples, as indicated by the white circle, is seen to be about 6 – 8 nm in size, which is in good agreement with the result calculated from the XRD spectral peaks.

ysis of materials. Ion beam analysis experiments and applications have been vigorously used in analyses of elements, elemental depth distributions, radiation damage in crystals, thin or hierarchical films, and nanostructures of various materials, including metals, semiconductors, ceramics, gemstones, airborne dusts and biological organisms [18,19].

The MeV ion beam has been utilized in Thailand for ion beam lithography, which has been a useful technique for microfluidics applications. MeV-ion beam lithography is a direct writing technique capable of producing microfluidic patterns and lab-on-chip devices with straight walls in thick resist films. In this technique, a small beam spot of MeV ions is scanned over the resist surface to generate a latent image of the pattern. In our system, the size of the rectangular beam spot is programmably defined by two L-shaped tantalum blades with well-polished edges [20,21] (Fig. 3). The minimum beam spot size is now 1 μm. This allows rapid exposure of entire rectangular pattern elements up to 500 × 500 μm^2 in one step. If different dimensions of the defining aperture are combined with the sample movements relative to the beam spot, entire fluidic patterns with large reservoirs and narrow flow channels can be written over large areas in short time. Fluidic patterns were written on silicon (Si) and polymeric PMMA (polymethylmethacrylate) for preliminary studies (Fig. 3).

Accelerator-based ion beams have been working, together with plasma technology, for ion beam nanotechnology applications. Not only is the ion beam itself intrinsically a nanotechnology as it works in nanoscale materials when the ion energy is appropriately controlled, but also it can be applied to process a material surface in a way of either top-down or bottom-up for nanostructure formation. The ion beam nanotechnology research was initiated with carbon ion implantation in tungsten carbide cemented by cobalt (WC-Co) cermet to achieve a surface nanostructure, which resulted in ultralow friction coefficient [22]. This work has led to two US patents. Later on, the research topics were extended to include ion beam synthesis of nanocrystalline materials such as silicon carbide (SiC) [23,24] (Fig. 4), ion beam and plasma deposition of nanofilms such as diamond-like carbon (DLC) coatings [25], ion beam lithography of micro/nanopatterns, ion beam and plasma-induced surface nanostructures such as nanofibers and nanoislands, ion beam nanoanalysis, and ion beam nanobiotechnology.

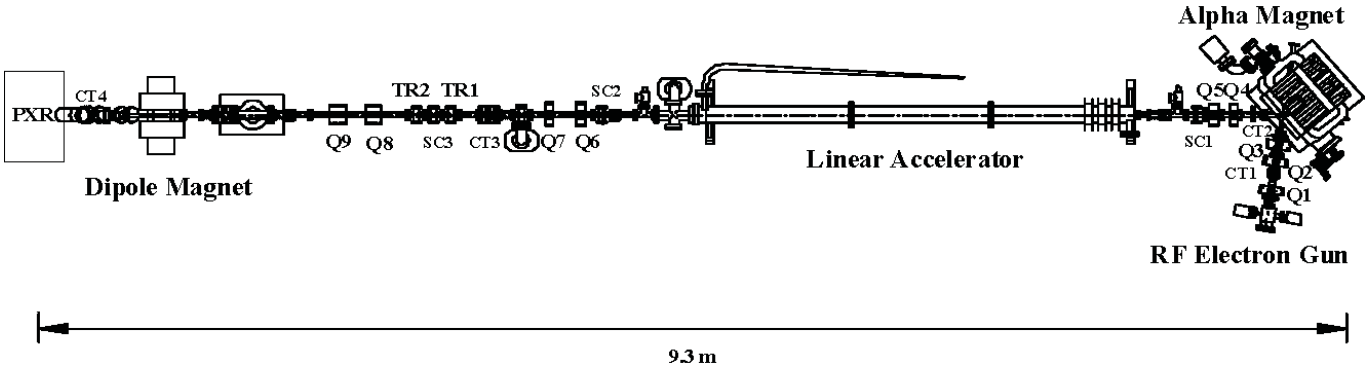

Fig. 5. Schematic layout of the accelerator system at Chiang Mai University for generation of short electron bunches. Q: quadrupole magnet, SC: screen, CT: current monitor, and TR and PXR: transition and parametric X- radiation experimental stations.

III. ELECTRON BEAM

The SURIYA electron beam facility to produce femtosecond electron bunches and THz radiation has been under development for a decade. Figure 5 shows a schematic diagram of the bunch generation and compression system [26] using a specially designed radiofrequency (RF) gun [27]. In the RF gun, electrons are continuously emitted with thermal energies from a thermionic cathode and are extracted and accelerated during an accelerating phase of the RF field with a frequency of 2856 MHz. At first, electrons are accelerated rapidly and reach the end of the half-cell just before the RF phase decelerates. They are further accelerated through the full-cell to reach the maximum kinetic energy of 2.0 –2.5 MeV at the gun exit depending on the accelerating field gradients. Later on, the electrons feel some decelerating fields and gain less and less overall energy, resulting in a well-defined correlation between energy and time. Electron bunches of 20 – 30 ps from the RF gun are then compressed in an α-magnet, where the particle path length increases with energy. This allows the lower energy particles, emitted later in each bunch, to catch up with the front for effective bunch compression. The optimized and compressed part of the electron bunch is then filtered by using energy slits located in the α-magnet vacuum chamber and is then transported through a SLAC-type linac and a beam transport line to experimental stations. At the experimental stations, the bunches are compressed to less than 1 ps [28]. The operating and beam parameters are shown in Table 1.

The femtosecond electron bunches are used to generate intense THz or far-infrared radiation in the form of coherent radiation. Such radiation is of great interest for THz spectroscopy and THz imaging applications [29,30]. After acceleration, the compressed electron bunches are used to generated coherent transition radiation (TR) by passing through a thin aluminum (Al) foil. The Al foil or radiator is tilted by 45° facing the electron beam direction. The backward transition radiation is emitted perpendicularly to the beam axis and is transmitted through a high-density polyethylene (HDPE). The radiation energy of 19 μJ per macropulse or a peak power of 24 W was measured by collecting over an acceptance angle of 160 mrad. The available THz radiation, measured using a Michelson interferometer with a room-temperature pyroelectric detector, covers wavenumbers from 5 cm^{-1} to around 80 cm^{-1} (0.15 THz – 2.4 THz). THz spectroscopy can be done easily by measuring the power transmission or the power reflection of a sample via a Michelson interferometer and the Fourier transformation, as well as with dispersive Fourier transform spectroscopy (DFTS). THz spectroscopy experiments, especially those on highly absorbing substances, using coherent THz transition radiation sources and DFTS techniques, have been reported [31]. Reflection and transmission THz imaging experiments have been conducted as examples of THz radiation applications using our radiation source [32]. It is possible to extend the spectral range further by using shorter electron bunches.

IV. SYNCHROTRON LIGHT

The Siam Photon Laboratory (SPL) is an accelerator complex of the Synchrotron Light Research Institute (SLRI), under the Ministry of Science and Technology of Thailand. The laboratory is in the technopolis of Suranaree University of Technology in Nakhon Ratchasima, 250 km from Bangkok to the northeast.

The Siam Photon Source (SPS) is the first synchrotron light source in Thailand [33]. It is a modified SORTEC ring, which was owned by the SORTEC Corporation in Tsukuba, Japan, but is now owned by SLRI, along with an injector linac and a booster synchrotron. The linac and the booster synchrotron are being used in the SPS almost without change. A layout of the SPS is illustrated in Fig. 6. The injector linac consists of an electron gun producing electrons, which are later accelerated to 40 MeV with a 6-MeV buncher and two 17-MeV ac-

Table 2. Major parameters of the storage ring of SPS (in addition to those given in the text.

Electron beam energy [GeV]	1.2
Maximum beam current [mA]	120
Horizontal emittance [nm·rad]	41
Coupling [%]	0.8
Betatron tunes ν_x, ν_y	4.75, 2.82
Synchrotron tune ν_s	2.33×10^{-3}
Natural chromaticities ξx, ξy	-9.40, -6.61
Momentum compaction	0.0170
RF frequency [MHz]	118
Harmonic number	32
RF voltage [kV]	120
RF power [kW]	14
Number of RF cavity	1
Energy loss per turn [keV]	65.94

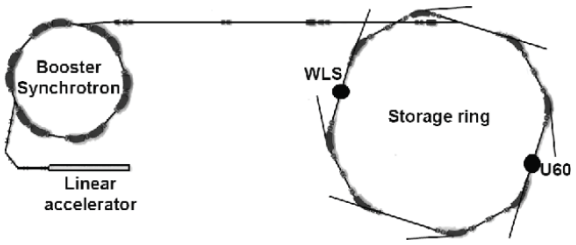

Fig. 6. Schematic diagram of the SPS at the SPL.

celeration tubes. The acceleration system is powered by a 35-MW klystron microwave power supply. The typical electron beam current is 60 – 80 mA. The electrons transported from the linac are further accelerated from 40 MeV to 1.0 GeV by the booster synchrotron. An inflector magnet and four bump magnets are used for beam injection. The yokes of the bending magnet and quadrupole magnets are made of laminated silicon steel plate of 0.5 mm in thickness. The reentrant-type RF acceleration cavity is driven by a 108-MHz RF power supply. The storage ring of the SPS was designed to store 1.0-GeV electrons with a beam emittance of 72π nm-rad. The circumference of the ring is expandable from 43 m to 81.3 m to provide 4 long straight sections for the installation of insertion devices. The lattice of the new ring is a double-bend achromat (DBA) lattice with four superperiods for a total of 8 bending magnets. The modification requires additional 12 quadrupole magnets, 8 sextupole magnets and 20 steering magnets. The first synchrotron light was produced in December 2001. After that, the light source has continuously been upgraded [34,35]. In 2005, the storage ring energy was upgraded from 1.0 GeV to 1.2 GeV by replacing the power supply of the bending magnets [31]. Operating the light source, thus, requires a ramp-up procedure after injection. The energy upgrade further reduces the emittance. The energy of the booster

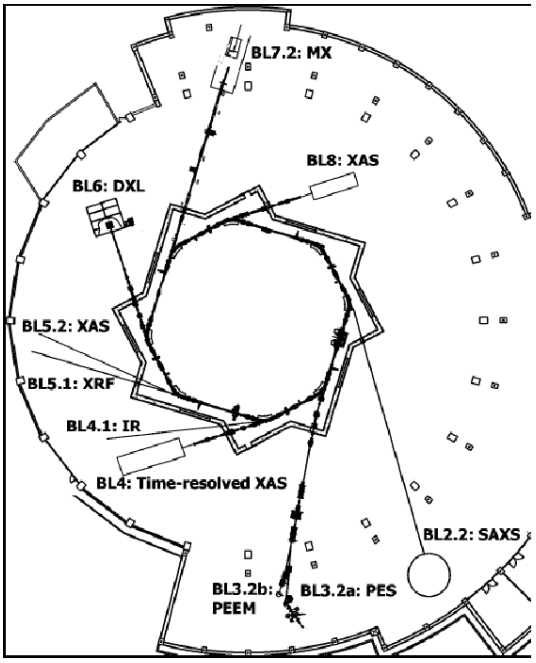

Fig. 7. Schematic diagram of the experimental floor plan of the SPL.

synchrotron is also planned to be upgraded to 1.2 GeV to allow full energy injection. With the improved water cooling system and many small sub-systems of the SPS, the beam lifetime at present is 23 hours at 100 mA. Since 2009, a planar undulator has been installed and is now being commissioned. To serve the X-ray community, a 6.4-T superconducting wavelength shifter (WLS) transferred from MAXLab (Lund, Sweden) is planned for producing hard X-rays from the 1.2 GeV ring. The parameters characterizing the current storage ring are given in Table 2.

The storage ring of the SPS has 8 beam ports. The layout of the experimental floor plan is shown in Fig. 7. Originally, the SPS was constructed, along with the first beamline, for photoemission experiments (BL4: PES) [36]. BL4 was later decommissioned in 2009 and was modified for use with the undulator light (BL3.2a: PES and BL3.2b: PEEM). Currently, three beamlines are open to the users. Those are for small-angle X-ray scattering experiments (BL2.2: SAXS), deep X-ray lithography (BL6: DXL) [37] and X-ray absorption spectroscopy (BL8: XAS) [38]. The number of projects using BL4: PES, BL6: DXL and BL8: XAS and the number of publications have been constantly increasing in recent years.

The beamlines to utilize radiation from the undulator for PES and PEEM (BL3.2a:PES and BL3.2b:PEEM) are now being commissioned. Four more beamlines are currently under construction. Those are for time-resolved XAS (BL4: XAS), infrared (IR) spectroscopy and imaging (BL4: IR), X-ray fluorescence (XRF) (BL5.1) and XAS (BL5.2). The latter two beamlines,

BL5.1 & 5.2, are being jointly constructed by a consortium of three institutes (Suranaree University of Technology, Nanotechnology Center and SLRI). In addition, a hard X-ray beamline has been constructed to utilize hard X-ray from the 6.4 T WLS for macromolecule crystallography (BL7.2: MX).

The SPL has dedicated tremendous service to research applications. Here are examples. Application of synchrotron light with the X-ray absorption technique was used to study cadmium accumulation in rice stems in an attempt to use bacteria to reduce the Cd that contaminates local rice. Rice stems grown with bacteria Cupriavidus taiwanensis S2500-3 were found to have 61% reduction of cadmium accumulation. With the help of the synchrotron-radiation-based X-ray absorption technique at the SPL, Thai scientists found that "Wan Mahakarn", a typical plant in tropical countries, was able to accumulate heavy metals by the so-called phytoremediation process. A quantum mechanical modeling for movement of water molecules around an ion in solution was done and was used to calculate the absorption of X-rays. The calculations were confirmed by results of X-ray absorption spectroscopy measurements at BL8 [39]. In an archeological study, researchers using X-ray absorption spectroscopy at BL8 studied the forms of copper inside 1300- to 2000-year-old beads found in four archeological sites in Thailand. They found that the structures and the chemical forms of copper in the beads were very similar to those in 600- to 700-year-old beads found in southern Italy. "This may indicate a long history of trade between the south of Thailand and the Mediteranian", the researchers commented [40].

V. FUTURE PLAN FOR AN INFRARED FREE ELECTRON LASER

At Chiang Mai University, we plan to establish a new research facility centered on the production and the utilization of femtosecond electron pulses and free electron lasers (FEL) optimized for mid- and far-infrared/THz radiation. The main goal of the extension to the THz facility would be the generation of infrared (IR) radiation covering the mid- and the far-infrared region to wavelengths up to the THz region. This broad interest is fueled by promises in support of basic and applied research, security, biology, chemistry, medicine, *etc.* Infrared and THz radiation can be used for security to replace or amplify, for example, metal detectors to detect non-metallic, but dangerous, articles. Furthermore, quality controls of food products would be possible through packing material by examining chemical composition, water content and freshness of food. In biology and chemistry, IR and THz radiation is used in spectroscopy to investigate vibrations of macro-molecules. Especially, high-intensity THz radiation has been used to study biological samples in watery environments rather than in dry condensed states. The structure and the integrity of semiconductor devices can be investigated through packaging while studying the circuit layers. All of these are planned applications.

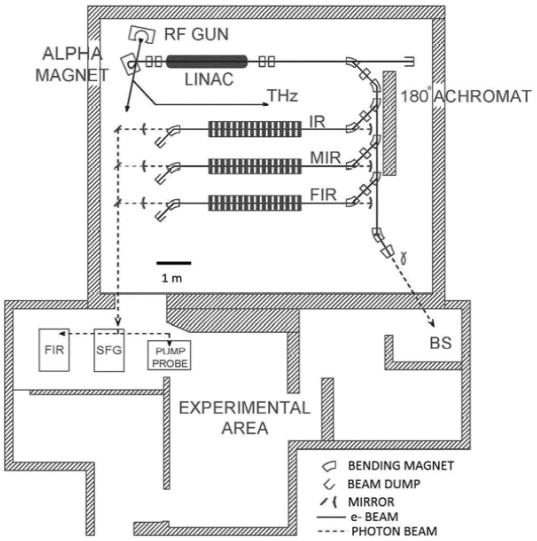

Fig. 8. Schematic diagram of the planned layout of the new facility for free electron lasers.

In order to realize the applications, we will rearrange and construct the facility area. Recently, a large well-shielded area became available through the decommissioning of a fast neutron facility, and it is planned to establish a new center there by first relocating SURIYA to this location. The size of the new location (12×13.5 m^2) will allow the installation of several FELs side by side. The beam from SURIYA will be turned around by several 180° achromatic deflections to let the electron beam pass through one of the $2 - 3$ FEL undulators that are required to optimally cover the desired radiation spectrum. The electron beam from the SURIYA facility is not optimal now, but by only a modest increase of the RF power to the RF gun, a beam condition can be generated that will be optimal for a FEL, but will no longer be optimal for bunch compression. The source of the electron beam being a 2.5-MeV RF gun ensures that the beam emittance is sufficiently small for all FELs. Similarly, the energy spread from the gun is less than 1%. A schematic outline of the facility is shown in Fig. 8. The free space available for each FEL with optical cavities is about 10 m. A photon beam line attached to each FEL will guide the photons to a well-shielded, radiation-free area ($\sim$150 m^2) and an associated experimental location. We expect to commission the first FEL within five years.

VI. CONCLUSION

In Thailand, accelerators have been vigorously being developed and related research activities have been

taken during the last 20 years. Two accelerator bases are the representatives, namely, the ion and electron beam laboratory at Chiang Mai University and the Synchrotron Light Research Institute near Bangkok. At present, in Thailand, there are nearly ten ion accelerators in operation and several are under construction. Ion beam technology has been broadly applied for materials modification, material analysis, biology, agriculture and nanotechnology. High-energy electron beam accelerator technology has been constantly developed for advanced applications, including THz radiation spectroscopy. The synchrotron light research has formed a nationally focused high-technology accelerator base to be used by various users. The construction, installation and applications of accelerators and related technology have significantly promoted scientific, technological and educational development for the country.

ACKNOWLEDGMENTS

The authors thank Helmut Widermann for his contribution to the planning of the free electron laser project and for reviewing part of the manuscript. The projects have been supported by the Thailand Research Fund, the National Research Council of Thailand, the Ministry of Science and Technology, Thailand, the National Metal and Materials Technology Center, Thailand, the National Nanotechnology Center, Thailand, the Thailand Center of Excellence in Physics, Chiang Mai University, Suranaree University of Technology, and the International Atomic Energy Agency. We wish to thank all of project participants for their various contributions.

REFERENCES

[1] T. Vilaithong, S. Singkarat, W. Pairsuwan, J. F. Kral, D. Boonyawan, D. Suwannakachorn, S. Konklong, P. Kanjanarat and J. J. Hoyes, in *Proceedings of the International Conference on Nuclear Data for Science and Technology*, edited by S. M. Qaim (Juerlich, Germany, 1991), p. 483.
[2] T. Vilaithong, D. Boonyawan, S. Konklong, W. Pairsuwan and S. Singkarat, Nucl. Instrum. Methods Phys. Res., Sect. A **332**, 561 (1993).
[3] D. Suwannakachorn, D. Boonyawan, J. P. Green, S. Aumkaew, C. Thongleurm, P. Vichaisirimongkol and T. Vilaithong, Nucl. Instrum. Methods Phys. Res., Sect. B **89**, 354 (1994).
[4] S. Rimjaem, R. Farius, C. Thongbai, T. Vilaithong and H. Wiedemann, Nucl. Instrum. Methods Phys. Res., Sect. A **533**, 258 (2004).
[5] T. G. Yang *et al.*, J. Korean Phys. Soc. **56**, 1960 (2010).
[6] L. D. Yu, T. Vilaithong, D. Suwannakachorn, S. Intarasiri and S. Thongtem, Nucl. Instrum. Methods Phys. Res., Sect. B **127**, 954 (1997).
[7] L. D. Yu, S. Thongtem, T. Vilaithong and M. J. McNallan, Surf. Coat. Technol. **128**, 410 (2000).
[8] L. D. Yu, G. W. Shuy and T. Vilaithong, Surf. Coat. Technol. **128**, 404 (2000).
[9] C. Chaiwong, L. D. Yu, K. Schinarakis and T. Vilaithong, Surf. Coat. Technol. **196**, 108 (2005).
[10] S. Intarasiri, D. Bootkul, L. D. Yu, T. Kamwanna, S. Singkarat and T. Vilaithong, Surf. Coat. Technol. **203**, 2788 (2009).
[11] S. Intarasiri, T. Kamwanna, A. Hallén, L. D. Yu, M. S. Janson, C. Thongleum, G. Possnert and S. Singkarat, Nucl. Instrum. Methods Phys. Res., Sect. B **249**, 851 (2006).
[12] B. Phanchaisri, R. Chandet, L. D. Yu, T. Vilaithong, S. Jamjod and S. Anuntalabhochai, Surf. Coat. Technol. **201**, 8024 (2007).
[13] A. Krasaechai, L. D. Yu, T. Sirisawad, T. Phornsawatchai, W. Bundithya, U. Taya, S. Anuntalabhochai and T. Vilaithong, Surf. Coat. Technol. **203**, 2525 (2009).
[14] S. Anuntalabhochai, R. Chandej, B. Phanchaisri, L. D. Yu, T. Vilaithong and I. G. Brown, Appl. Phys. Lett. **78**, 2393 (2001).
[15] R. Norarat, N. Semsang, S. Anuntalabhochai and L. D. Yu, Nucl. Instrum. Methods Phys. Res., Sect. B **267**, 1650 (2009).
[16] S. Sarapirom, K. Sangwijit, S. Anuntalabhochai and L. D. Yu, Surf. Coat. Technol. **204**, 2960 (2010).
[17] K. Prakrajang, P. Wanichapichart, S. Anuntalabhochai and L. D. Yu, Nucl. Instrum. Methods Phys. Res., Sect. B **267**, 1645 (2009).
[18] S. Intarasiri, T. Kamwanna, A. Hallén, L. D. Yu, M. S. Janson, C. Thongleum, G. Possnert and S. Singkarat, Nucl. Instrum. Methods Phys. Res., Sect. B **249**, 859 (2006).
[19] T. Kamwanna, N. Pasaja, L. D. Yu, T. Vilaithong, A. Anders and S. Singakarat, Nucl. Instrum. Methods Phys. Res., Sect. B **266**, 5175 (2008).
[20] S. Gorelick, N. Puttaraksa, T. Sajavaara, M. Laitinen, S. Singkarat and H. J. Whitlow, Nucl. Instrum. Methods Phys. Res., Sect. B **266**, 2461 (2008).
[21] N. Puttaraksa, S. Gorelick, T. Sajavaara, M. Laitinen, S. Singkarat and H. J. Whitlow, J. Vac. Sci. Technol., B **26**, 1732 (2008).
[22] L. D. Yu, G. W. Shuy and T. Vilaithong, J. Surf. Fini. Soc. Jpn. **54**, 749 (2003).
[23] H.-J. Woo, G.-D. Kim, H.-W. Choi and J.-K. Kim, J. Korean Phys. Soc. **56**, 2063 (2010).
[24] S. Intarasiri, A. Hallén, J. Lu, J. Jensen, L. D. Yu, K. Bertilsson, S. Singkarat and G. Possnert, Appl. Surf. Sci. **253**, 4836 (2007).
[25] L. D. Yu, S. Aukkaravittayapun, D. Boonyawan, S. Sarapirom and T. Vilaithong, Surf. Coat. Technol. **203**, 2771 (2009).
[26] J. Saisut, K. Kusoljariyakul, S. Rimjaem, N. Kangrang, P. Wichaisirimongkol, P. Thamboon, M. W. Rhodes and C. Thongbai, Nucl. Instrum. Methods Phys. Res., Sect. A **637**, S99 (2011).
[27] S. Rimjaem, R. Farias, C. Thongbai, T. Vilaithong and H. Wiedemann, Nucl. Instrum. Methods Phys. Res., Sect. A **533**, 258 (2004).
[28] X.-C. Zhang and J. Xu, *Introduction to THz Wave Photonics* (Springer, New York, 2010).
[29] Y. Kim, D. S. Yee, M. Yi and J. Ahn, J. Korean Phys. Soc. **56**, 255 (2010).

[30] C. Thongbai, K. Kusoljariyakul, S. Rimjaem, M. W. Rhodes, J. Saisut, P. Thamboon, P. Wichaisirimongkol and T. Vilaithong, Nucl. Instrum. Methods Phys. Res., Sect. A **587**, 130 (2008).
[31] K. N. Woods and H. Wiedemann, Chem. Phys. Lett. **393**, 159 (2004).
[32] P. Thamboon, P. Buaphad, C. Thongbai, J. Saisud, K. Kusoljariyakul, M. W. Rhodes and T. Vilaithong, Nucl. Instrum. Methods Phys. Res., Sect. A **637**, S161 (2011).
[33] P. Kengkan, W. Paisuwan, G. Isoyama, T. Yamakawa and T. Ishii, J. Synchrotron **5**, 348 (1998).
[34] S. Rugmai, G. G. Hoyes, S. Prawanta, A. Kwankasem, S. Siriwattanapitoon, N. Suradet, P. Pimol, N. Junthong, S. Boonsuya, P. Janpuang, P. Prawatsri, S. Rujirawat and P. Klysubun, AIP (American Institute of Physics) Proceedings **879**, 58 (2007).
[35] G. G. Hoyes, in *APAC2007 Proceedings* (2007), p. 461.
[36] P. Songsiriritthigul, W. Pairsuwan, T. Ishii and A. Kakizaki, Surf. Rev. Lett. **8**, 497 (2001).
[37] P. Klysubun, N. Chomnawang and P. Songsiriritthigul, AIP Proceedings **879**, 1490 (2007).
[38] W. Klysubun, P. Tarawarakarn, P. Sombunchoo, S. Klinkhieo and P. Songsiriritthigul, AIP Proceedings **879**, 860 (2007).
[39] A. Thongraar, J. T-Thienprasert, S. Rujirawat and S. Limpijumnong, Phys. Chem. Chem. Phys. **12**, 10876 (2010).
[40] W. Klysubun, Y. Thongkam, S. Pongkrapan, J. T-Tienprasert and P. Dararutana, Anal. Bioanal. Chem. **399**, 3033 (2011).

Applied Mechanics and Materials Vols. 110-116 (2012) pp 2301-2307

doi:10.4028/www.scientific.net/AMM.110-116.2301

Progress on Reflective Terahertz Imaging for Identification of Water in Flow Channels of PEM Fuel Cells

P. Buaphad [1,3*] , P. Thamboon [2,3] , C. Tengsirivattana [3] , J. Saisut [1,3] , K. Kusoljariyakul [1,3] ,M. W. Rhodes [2,3] , C. Thongbai [1,3]

[1]Department of Physics and Materials Science, Chiang Mai University, Chiang Mai 50200, Thailand.

[2] STRI, Chiang Mai University, Chiang Mai 50200, Thailand

[3]ThEP Center, Commission on Higher Education, Bangkok 10400, Thailand

* E-mail: Luck_phys@hotmail.com

Keywords: Terahertz; imaging; reflective; PEM fuel cells; water management

Abstract. This work reports an application of reflective terahertz (THz) imaging for identification of water distribution in the proton exchange membrane (PEM) fuel cell. The THz radiation generated from relativistic femtosecond electron bunches is employed as a high intensity source. The PEM fuel cell is designed specifically for the measurement allowing THz radiation to access the flow field region. The THz image is constructed from reflected radiation revealing absorptive area of water presence. The technique is proved to be a promising tool for studying water management in the PEM fuel cell. Detailed experimental setup and results will be described.

Introduction And Background

"Terahertz (THz) radiation" is the most common term used to refer to frequency 10^{12} Hz which lies between the microwave and infrared regions of electromagnetic spectrum [1]. THz radiation has attracted increasing interest in imaging and spectroscopy in a broad range of applications such as in medical diagnosis, security measures for airports and screening, radio astronomy, communication and sensing, and atmospheric studies [2]. This is because THz is non-ionizing and capable of penetrating a wide variety of non-conducting materials (e.g., clothes, papers, plastics and ceramics); but it is strongly absorbed by polar molecules such as water, and is reflected by metals [3].

The proton exchange membrane (PEM) fuel cell is a transducer that converts chemical energy into electrical. The basic single cell consists of a membrane electrode assembly (MEA) sandwiched between flow-field plates. In the flow channels, water is brought in with reactants in the form of humid fuels. Meanwhile, water is generated as a byproduct from electrochemical reaction and must be removed. Visualization of water formation and transport in an operating PEM fuel cell is a challenging phenomenon due to the opaque nature of traditional gas diffusion layer (GDL), flow fields and end-plate materials [4]. As water is one of the main constituents of fuel cell, it should be possible to use THz wave to detect water buildup and removal in the PEM fuel cell.

Our femtosecond electron source, developed at the Plasma and Beam Physics Research Facility, Chiang Mai University, Thailand, can generate coherent transition radiation in the THz regime ranging from 0.15 - 2.4 THz (5-80 cm^{-1}). In this paper, we demonstrate promising results for identification of water presence in the flow channels of a PEM fuel cell by reflective THz imaging.

THz Radiation Source

At the Plasma and Beam Physics (PBP) Research Facility, THz radiation is generated in the form of coherent transition radiation from femtosecond electron bunches [5]. The system to produce such short electron bunches consists of a thermionic cathode RF-gun, an alpha magnet, and a linear accelerator (Linac), shown in Fig. 1. At the THz radiation experimental station (Fig. 2), the short

electron bunches are used to generate coherent transition radiation by passing through a radiator made of a 25.4 μm-thick Al-foil. The radiator is tilted by 45° facing the electron beam direction. The backward transition radiation is emitted perpendicular to the beam axis and transmits through a high density polyethylene (HDPE) window of 1.25–mm-thick and 32-mm diameter. The coherent radiation, covering much THz spectral range up to 80 cm^{-1} (2.4 THz), yields high intensity radiation which can be detected with a room temperature detector. The beam profile after 6-cm focal-length lens shown in Fig. 3 indicates the focused beam width at FWHM to be approximately 2 mm.

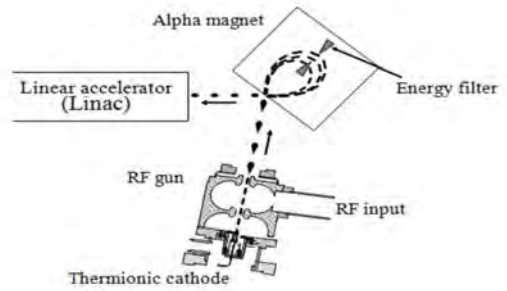

Figure 1. Schematic diagram of the system to generate femtosecond electron bunches.

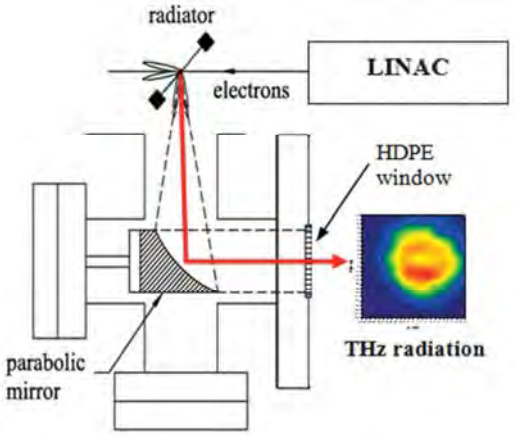

Figure 2. Schematic diagram of the THz radiation system

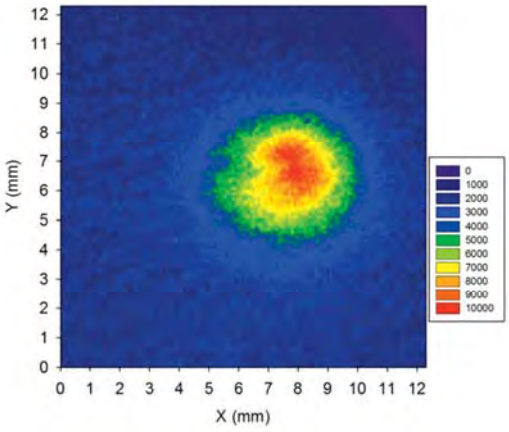

Figure 3. THz beam profile after 6 -cm focal -length lens

Experimental Technique & Results

The PEM fuel cell for THz imaging must allow THz radiation to probe the flow channels. From outer to inner layers (see Fig. 4), our PEM fuel cell consists of end plates, flow fields and a membrane electrode assembly (MEA). The end plates provide structure rigidity. The flow fields with serpentine channels guide water and reactant gases to flow in to and out of the cell. The MEA

is where the electrochemical reaction occurs. On the THz probing side, we insert a THz window and cut a circular opening on the end plate. The flow field made of brass is machined through its channels with 2 mm in width and 2 mm in depth. Silicon is selected to be a window of our fuel cell. It is often used as a window material for THz spectroscopy of liquid samples due to its high reflectivity in this spectral regime [6]. The Nafion® membrane and the carbon cloth including Pt 5 mg/cm^2 were used for the MEA. This PEM fuel cell must operate in conditions as close as possible to those prevailing in practice (especially in term of current density, gas hydration and stoichiometry).

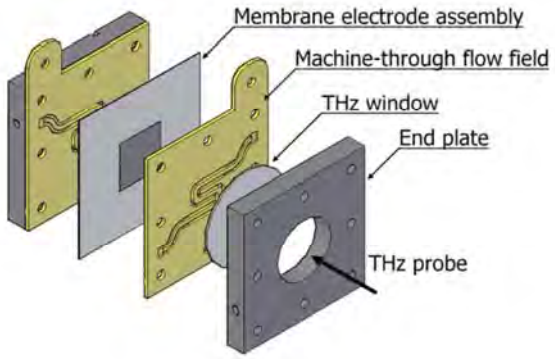

Figure 4. PEM fuel cell components designed with machine through flow field channels made of brass enclosed with a THz window.

Figure 5. Distribution of droplets in the flow channels after 180 minutes from the start of operation with active dimension of 50x100 mm^2 and current drawn at 10 A.

Visible image.

Fig. 5 shows water buildup in the flow channels of cathode side operating at 30%RH and constant current 10 A. The water droplets diffused from a membrane electrode assembly (MEA) merged with the condensed droplets on the flow channel wall forming water columns. At some part of the flow channel, the surface of the MEA and inner surface of the transparent window were covered with a water film. Along an arc of the flow channel, more water gathered and clogged the gas flow. Therefore, gas and water transportation along the flow channels is crucial for PEM fuel cell performances.

THz Response of Fuel Cell Structures.

For multilayer normal incidence, the overall reflection coefficient Γ is given by the relation between the reflected beam and the incident beam. It can be derived through the elementary reflection ($\rho_j = \frac{n_j - n_{j+1}}{n_j + n_{j+1}}$), the phase thickness ($k_j l_j = \frac{2\pi(n_j l_j)}{\lambda}$) of the j^{th} layer and assuming no backward waves in the most right medium ((M + 1)th layer) [7], resulting in Equation (1):

$$\Gamma_j = \frac{\rho_j + \Gamma_{j+1} e^{-2ik_j l_j}}{1 + \rho_j \Gamma_{j+1} e^{-2ik_j l_j}} \quad j = M, M\text{-}1, \ldots, 1 \qquad (1)$$

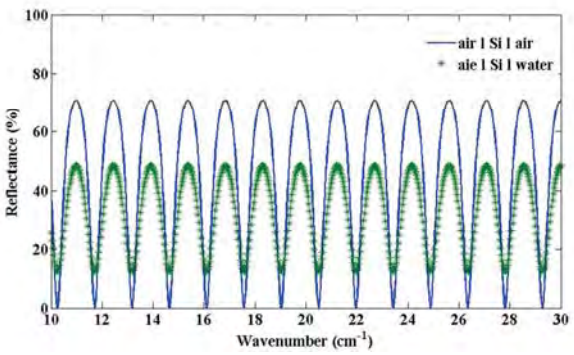

Figure 6. Caculation of spectral reflectance of the mulilayer structures.

The radiation spectral reflection from two interfaces of the sample has specific frequency dependence depending on the refractive indices of the layers. The refractive index of air, silicon and water in THz region is 1.000, 3.416 and 2.098 respectively. Calculations of reflected signal respect to wavenumber from multilayer structures of air|Si|air and air|Si|water are shown in Fig. 6.

Reflectance of air|Si|air is noticeably higher than that of air|Si|water. The calculation results suggest that we should be able to distinguish the flow channels from those without water.

Reflective THz Imaging Setup.

Preliminary measurements on non-invasive diagnostics for multilayered fuel cell structures have been conducted utilizing a reflective imaging setup. A parallel THz beam is reflected off a gold-coated mirror to a THz lens of 6-cm focal-length. The beam is then focused onto a sample at approximately 30° incident angle. The focused beam-size at the sample is approximately 2 mm. The reflected signal from the fuel cell is collected by another THz lens of 3-cm focal-length and continued to a pyroelectric detector. The model fuel cell under investigation is placed on top of the X–Y translational stages and scanned using computerized motion controllers with 0.5 -mm travel range on both axes (see Fig. 7).

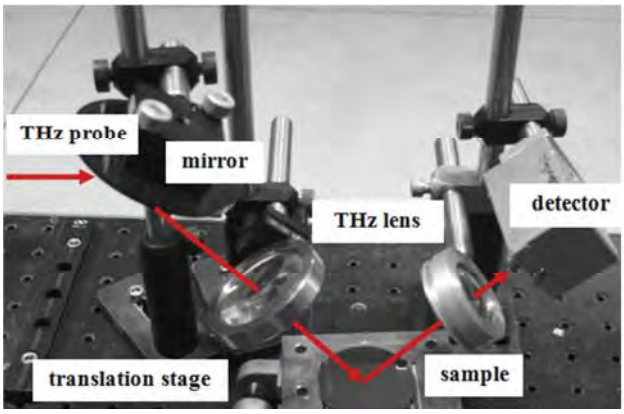

Figure 7. A photograph of the reflective THz imaging setup

Reflective THz Image.

Visible images of the flow field before and after covering with Si window are shown in Fig. 8(a) and 8(b) respectively. As can be seen in Fig. 8(c) representing two channels in the flow field, a reflective THz image of the flow field taken through Si window provides sufficient contrast. Because the reflection of brass was high and that of flow channel was low, the shape of flow channels is recognizable.

Identification of Water Presence in the Channel.

Because hydrated substances are highly absorptive in the THz region, water exhibits strong contrast to surrounding materials in a THz image. We filled water into the flow channel covered with Si window for water identification experiment. The THz image in Fig. 9 compares a water-filled channel with an unfilled channel indicated as air-filled in the figure. The darker area reveals

absorptive region within the flow channels, with the darkest region lies in water-filled channel. In order to clearly distinguish the water-filled and the air-filled region, we perform a line-scan plot (along the dash-line shown in Fig. 10). It is evident that we are able to identify water presence in the flow field with THz imaging.

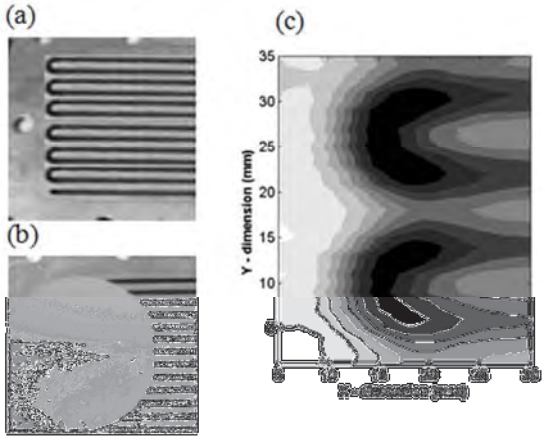

Figure 8. Visible images of a flow field channel (a) before and (b) after covering with Si window; (c) THz image of (b).

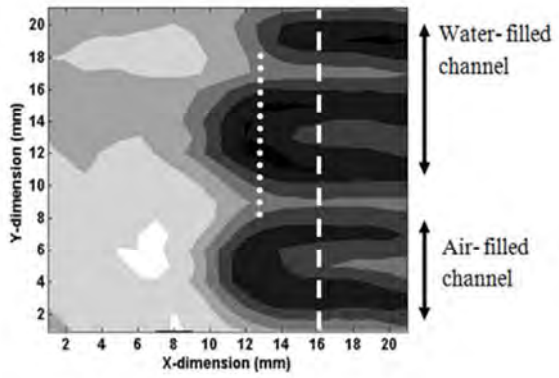

Figure 9. THz image of machine-through-brass flow field channel with silicon window.

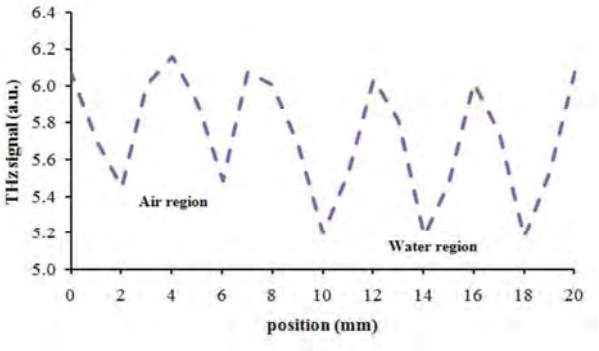

Figure 10. THz -signal line -scan along the dashed line in Fig. 9.

Improve Resolution of THz Image with Mesh Filter.

The resolution is generally the key to determine the quality of the images. In this section, we discuss the spatial resolution in the context of the geometrical configuration of the reflective THz imaging system. We investigated the spatial resolution of our reflective THz imaging by one--

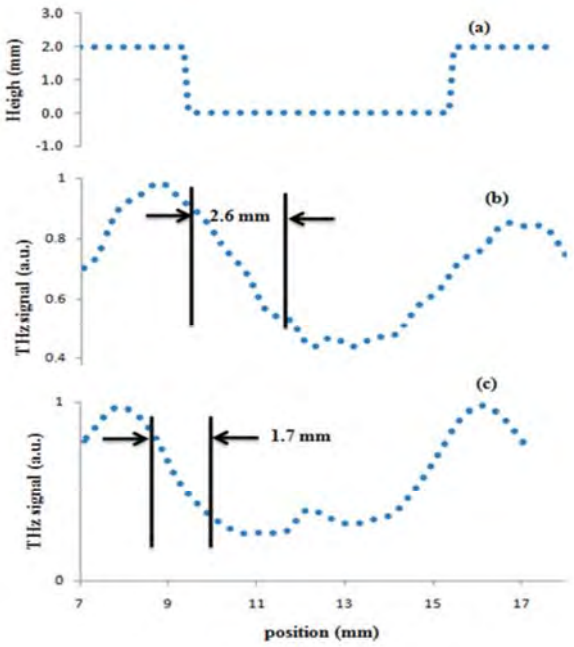

Figure 11. Line scans along the dotted line in Fig. 9 illustrate (a) real profile of the flow field channel groove at the arc of the cell compared to THz signal with (b) resolution of 2.6 mm without mesh and (c) resolution of 1.7 mm with mesh.

dimension THz intensity across an arc of the flow field channel (the dotted line in Fig. 9). Fig. 11(a) illustrates the real profile of an arc of the flow channel having a width of 6 mm. An abrupt decrease of the THz signal is observed when the detector moves from a position over a rib of the flow channel to the trench etched into the flow channel, as shown in Fig. 11(b). From THz data, we achieve a 10% to 90% resolution of about 2.6 mm. Spatial resolution can be improved using a THz band-pass filter. Reflective THz image of the flow channel was taken with a 180x180 μm copper mesh as a THz filter which has a transmission band between 20–40 cm^{-1}. The resolution was analyzed as described previously and the intensity across the dotted line is shown in Fig. 11(c). The spatial resolution with the mesh filter yields 1.7 mm.

Conclusions

In conclusion, we demonstrated an application of reflective technique for THz imaging. In this investigation, a reflective THz imaging system is successfully established and employed for identifying water presence in flow channels of a PEM fuel cell. A spatial resolution of image may fall to 1.7 mm when using 180x180 μm thin copper mesh. The image results are convincing evidences for further employing THz radiation from the femtosecond electron source at the PBP Research facility, Chiang Mai, Thailand as a visualizing tool to study water transport dynamic in PEM fuel cells.

Acknowledgment

Authors would like to thank Mr. N. Kangrang, Mr. P. Wichaisirimongkol and Mr. V. Jinamoon for technical supports. Authors would like to acknowledge the support from the National Research Council of Thailand (NRCT), the Thailand Research Fund (TRF), the (Thailand) Commission on Higher Education (CHE), the Thailand Center of Excellence in Physics (ThEP), and the Graduate School Chiang Mai University.

References

[1] L. Yun-Shik, "T-Ray Imaging," in Principles of Terahertz Science and Technology, Springer, 2009, pp. 259 – 294.

[2] M. Tonomouchi, "Review Articles: Cutting–edge terahertz technology", Nature photonic, vol. 1, February 2007.

[3] H. Zhang, A. Redo-Sanchez, and X. Zhang, "Identification and classification of chemicals using terahertz reflective spectroscopic focal-plane imaging system", Optics Express 9130, vol. 14, No. 20, October 2006.

[4] A. Bazylak, "Liquid water visualization in PEM fuel cells: A review", J. Hydrogen Energy, vol. 34, pp. 3845 – 3857, April 2009.

[5] C. Thongbai *et al.*, "Femtosecond electron bunches, source and characterization" Nucl. Instr. and Meth. A, vol. 587, pp. 130-135, 2008.

[6] P. Thanboon *et al.*, "Investigation of water distribution in proton exchange membrane fuel cells via Terahertz imaging" Nucl. Instr. and Meth. A, 2010, doi:10.1016/j.nima.2010.02.047.

[7] S. Orfanidis, "Multilayer structures," in Electromagnetic Wave and Antennas, Rutgers University, 2008, www.ece.Rutgers.edu/~orfanidi /ewa.

Available online at www.sciencedirect.com

SciVerse ScienceDirect

Energy Procedia 00 (2013) 000–000

Energy Procedia

www.elsevier.com/locate/procedia

10th Eco-Energy and Materials Science and Engineering

(EMSES2012)

Simulations and Measurements of Dipole and Quadrupole Magnets for PBP-CMU Linac System

P. Boonpornprasert[a,b,*], S. Rimjaem [a,b], J. Saisut [a,b], and C. Thongbai [a,b]

[a]*Department of Physics and Materials Science, Faculty of Science, Chiang Mai University, Chiangmai 50200, Thailand*
[b]*ThEP Center, Commission on Higher Education, Bangkok 10400, Thailand*

Abstract

The PBP-CMU Linac system has been established to generate femtosecond electron bunches and to study their applications, especially for generation of coherent terahertz (THz) radiations. The dipole magnet and the prototype quadrupole magnet for the system have been designed and fabricated in house. Both the simulated and the measured results were used for evaluating the magnet performance and will be used as a guideline for design and fabrication of magnet devices in the future.

Selection and/or peer-review under responsibility of COE of Sustainalble Energy System, Rajamangala University of Technology Thanyaburi(RMUTT)
Keywords: dipole magnet; quadrupole magnet; magnetic field measurement; Radia code

1. Main text

The femtosecond electron and photon pulses research laboratory under the Thailand Center of Excellent in Physics (ThEP Center) has been established at the Plasma and Beam Physics Research Facility (PBP), Chiang Mai University (CMU). The laboratory aims are to develop a relativistic electron source with femtosecond (10^{-15}) bunch length and to study its applications, especially generation of coherent terahertz (THz) radiations via transition radiation (TR). The radiation in THz frequency range is widely used, for example, for non-ionizing spectroscopy, chemical and biological imaging, medical imaging and airport security scanning [1,2].

A layout of the PBP-CMU Linac system is shown in Figure 1(a). The main components are an RF-gun with a thermionic cathode, an alpha magnet, a linear accelerator (Linac), experimental stations, a dipole spectrometer magnet and a Faraday cup. Furthermore, along the beamline, there are quadrupole and

* Corresponding author. Tel.: +66-5394379; fax: +66-53222376.
E-mail address: ppugpug@gmail.com.

steering magnets for beam focusing and guiding; and beam diagnostics instruments for probing the beam properties. Detail of the current PBP-CMU Linac system was reported in [3].

The PBP-CMU Linac system demands some dipole magnets and quadrupole magnets to support an expansion of the system to an infrared free electron laser (FEL) facility as the layout shown in Figure 1(b). We have planned to construct the magnet iron cores by using Thai local low carbon steel. Generally, low carbon steel is classified by percent by weight of carbon (%C) in the steel. Each type of carbon steel has different B-H saturation curve. For this reason, magnet simulations with various type iron core materials are needed to evaluate the efficiency of the magnet. The result comparisons will be used for the iron core material choosing.

This paper presents and compares the magnetic field simulation results and the magnetic fields measurement results for a dipole magnet and a quadrupole magnet. Both the dipole magnet and the prototype quadrupole magnet have been designed [4] and fabricated in house at our facility.

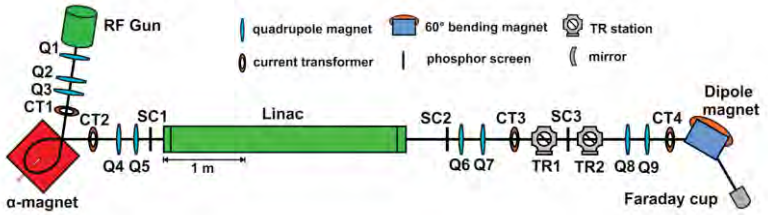

(a) Current system

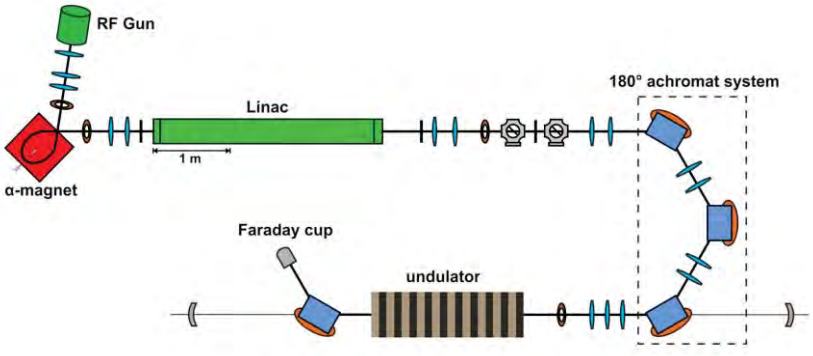

(b) Future expansion for an IR-FEL facility.

Fig. 1. Layout of the PBP-CMU Linac system.

2. Dipole Magnet

Dipole magnet is a magnetic deflection device. In our system the dipole magnet serves as an electron beam dump and a beam energy analyzer. Figure 2 illustrates a C-shape dipole magnet with a gap of *h*. The magnet is excited by electric currents in the coils which are mounted around the two poles. The magnetic field (*B*) produce by the dipole magnet is

$$B = \frac{\mu_0 NI}{h}, \tag{1}$$

where I is the excitation current, N is the number of turns in a coil and h is the air gap. Note that, the equation (1) is only an approximation since it neglects fringe fields and iron saturation [5]. The radius of curvature (ρ) of an electron trajectory in dipole fields is often expressed in terms of the dipole field (B) and the electron momentum (p) as

$$\frac{1}{\rho}[\mathrm{m}^{-1}] = 0.2998 \frac{B\ [\mathrm{T}]}{p\ [\mathrm{GeV/c}]}\,. \tag{2}$$

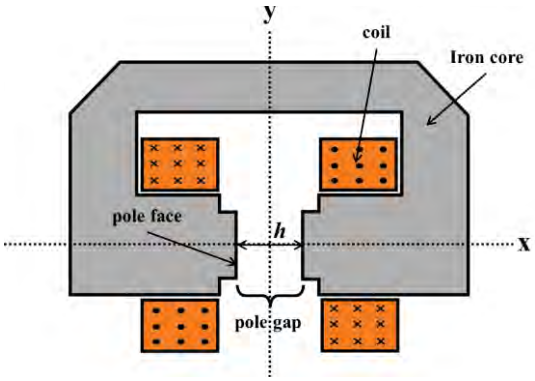

Fig. 2. C-shape dipole magnet layout

The dipole magnet of the PBP-CMU Linac system, as shown in Figure 3, was placed around the end of the beamline (Figure 1(a)). The magnet is a C-shape magnet which has been designed to deflect a 15 MeV electron beam by 60° into a Faraday cup. The magnet has 125×125 mm square pole faces with the gap of 40 mm. The magnet coils were made from water cooled copper wire.

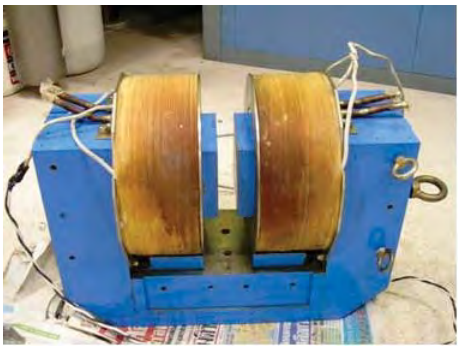

Fig. 3. Dipole magnet of the PBP-CMU Linac system

3. Quadrupole Magnet

With a finite emittance, the transverse beam size will increase as the beam move through a drift space. Some quadrupole magnets are therefore needed for focusing the beam transverse sizes. Figure 4 shows a quadrupole magnet layout with a bore radius of R. The magnet consists of 4 pole pieces, 4 coils and a circular yoke. The red arrow lines in Figure 4 are the magnetic field lines which point from the north

poles (N) to the south poles (S). A quadrupole magnet focus electron beam on one transverse axis while defocus on the other. Therefore beam focusing for both transverse axes demands at least 2 quadrupole magnets, called a quadrupole doublet.

The magnetic fields of a quadrupole magnet are zero at the center of transverse positions and linearly increase with the transverse positions as

$$B_x = gy\,,\ B_y = gx\,, \tag{3}$$

where B_x and B_y are the magnetic field components, x and y are the positions in the transverse axes and g is the magnetic gradient. The magnetic gradient depends on the excitation current (I) as

$$g = \frac{2\mu_0 NI}{R^2}\,, \tag{4}$$

where N is the number of turns per coil. Focusing properties of a quadrupole magnet is described by the focusing strength k, whose value depends on the magnetic gradients.

$$k\ [\mathrm{m}^{-2}] = 0.2998\frac{g\ [\mathrm{T/m}]}{\beta E\ [\mathrm{GeV}]}, \tag{5}$$

where β is the particle relativistic factor [6].

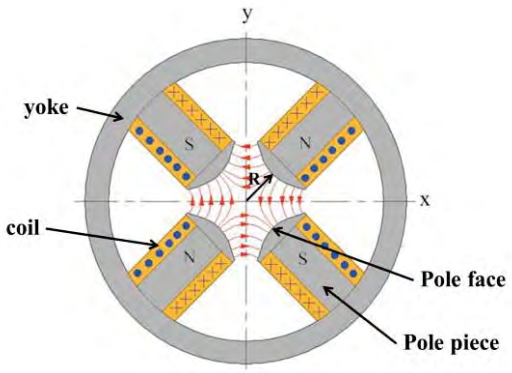

Fig. 4. Quadrupole magnet layout showing components and field lines

The quadrupole magnet which is presented in this work is the prototype quadrupole magnet of the PBP-CMU Linac system as shown in Figure 5. Some of the magnet parameters are shown in Table 1.

Table 1. Quadrupole magnet parameters

Parameter	Value	Unit
Thickness (ℓ)	60	mm
Bore radius (R)	20	mm
Number of turns in a coil (N)	110	turn
Coil (15 AWG) Diameter	1.450	mm

Fig. 5. Prototype qaudrupole magnet of the PBP-CMU Linac system

4. Magnet Simulations

In this work, we use the RADIA code for magnet simulation. RADIA code [7], running as an add-on application to Mathematica [8], is developed by insertion devices laboratory of the European Synchrotron Radiation Facility, France. The code is used for calculating the 3D magnetostatic fields of magnetic devices, especially the devices in charged particle accelerators.

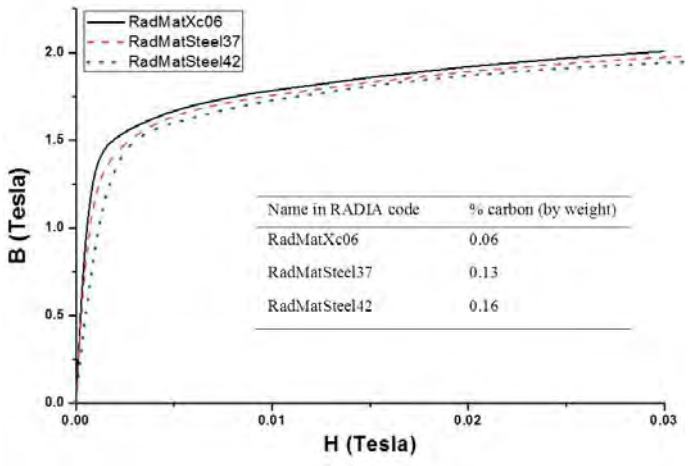

Fig. 6. B-H saturation curves of RADIA carbon steel materials

There are 3 types of carbon steel materials available in RADIA. Their B-H saturation curves and carbon percentages are shown in Figure 6. The RADIA simulations of the dipole magnet and the quadrupole magnet were evaluated with various iron core materials listed in Table 2. Figure 7(a) and

Figure 7(b) show the RADIA simulation model of the dipole magnet and the quadrupole magnet, respectively.

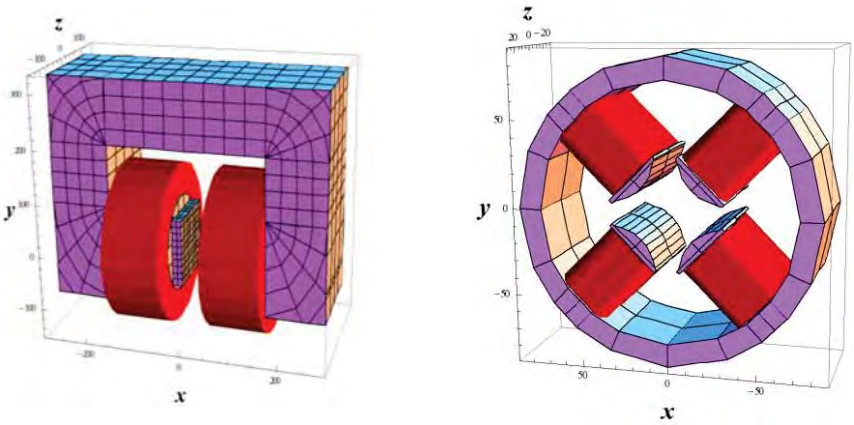

(a) Dipole magnet (b) Quadrupole magnet

Fig. 7. Model of the magnets for RADIA simulation.

5. Magnet Measurements

The magnetic field measurement device is a Hall probe of a size $1.0\times1.3\times0.2$ cm^3 (GMW Group 3 Digital Hall Effect Teslameter). Figure 8 shows measurement setup for the dipole magnet. The hall probe was attached to a holder which can be moved along y- and z-axes. For the quadrupole magnet, the measurement setup is shown in Figure 9. The magnet was placed on the measurement stand where probe could be moved within the quadrupole field region. The Hall probe was placed on x- and z- axes translation stages equipped with linear actuators and can be moved precisely through computer interface. The magnet is excited by a current regulated DC power supply and a 0.01Ω shunt resistor was used to determine the supplied current.

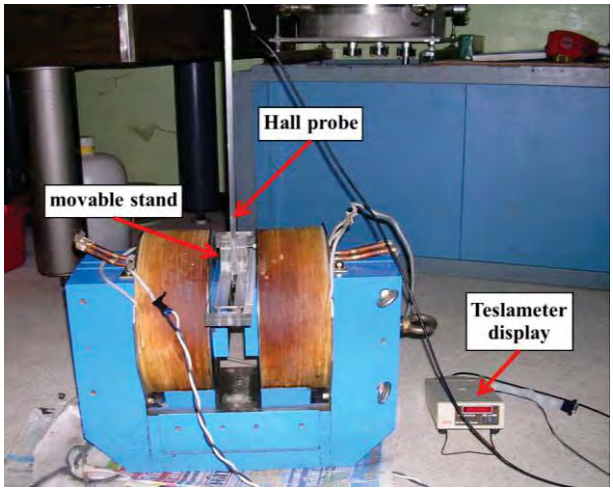

Fig. 8. Dipole magnet measurement setup

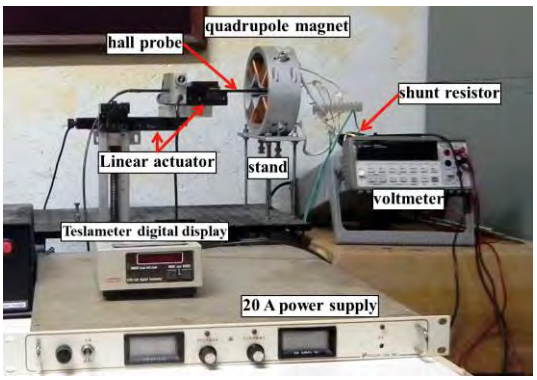

Fig. 9. Quadrupole magnet measurement setup

6. Simulation and Measurement Results

6.1. Dipole Magnet

The dipole magnet excitation curve was measured by measuring the magnetic fields B_y at the pole center while increasing currents from 0 to 18 A with 0.5 A step. The measurement results and RADIA simulations results are shown together in Figure 10. The equation from fitting of measurement data is

$$B = 0.0459I + 0.0244 . \quad (9)$$

This equation will be used for evaluate the magnetic field values from given excitation currents. The simulation and the measurement results show that, at the same excitation current, carbon percentage in the magnet core affects to the magnetic field intensity. The magnet core with lower carbon percentage can generate higher magnetic field.

The magnetic fields in yz-plane were measured and the results are shown Figure 11. The field distribution benefits for the electron deflection angle and energy calculation.

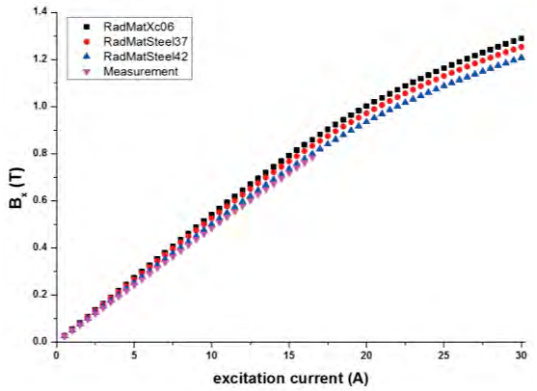

Fig. 10. Dipole magnet excitation curves

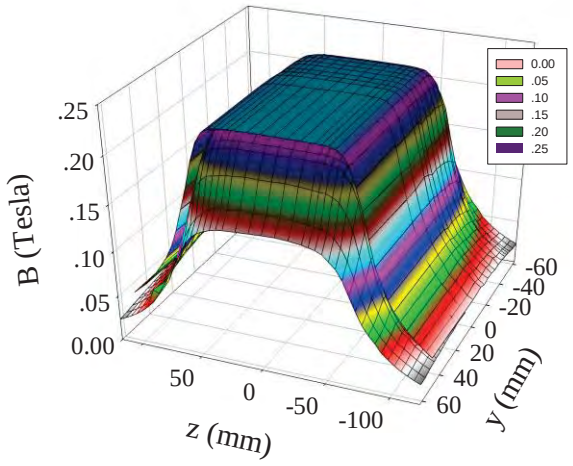

Fig. 11. Measured magnetic field distribution of the Dipole magnet (I = 5A).

6.2. Quadrupole Magnet

The quadrupole magnet excitation curve was measured by measuring the fields at (x,y,z) = (20,0,0) mm position, while increasing current from 0 - 18 A with 0.5A step. The results in Figure 12 show that the saturation effect starts to occur around 10.5 A for the measurement and at higher current for the simulations. Polynomial fit of the curves in unsaturated region (0-10.5A) and saturated region (10.5-18.0A) are

$$g = 5.62I + 1.57, \tag{9}$$

$$g = -0.11\,I^2 + 7.63I - 8.33, \tag{10}$$

respectively. These equations will be used in the magnet control and operation of the accelerator system. The comparisons between the simulation and the measurement results are corresponding to the dipole magnet as the magnet core with lower carbon percentage generate higher magnetic field gradient.

For transverse gradient measurement, The B_y field along the x-axis were recorded at (x,y,z) = (0 to 40,0,0) mm with a 1 mm step and the field gradients were then calculated. The results are shown in Figure 13 along with RADIA simulation results. The average gradient, within the bore radius range (0-20 mm), from the measurement (for 5 A) is 29 $\times 10^{-4}$ T/mm and the average gradients from simulation results are 30.1, 32.2 and 33.5 $\times 10^{-4}$ T/mm for RadMatSteel42, RadMatSteel37 and RadMatXc06, respectively.

The effective length of a quadrupole magnet is the length which is derived from the longitudinal field profiles of the magnet as [5,6]

$$\ell_{\text{eff}} = \frac{\int g \cdot dz}{g_0}, \tag{11}$$

where g_0 is the gradient at the center of the magnet along z. For the effective length measurement, we measured the magnetic field B_y along z-axis at the position x = 10 mm and y = 0 mm. The measurement

result and the simulation results are shown in Figure 14. The effective lengths can then be calculated by using (11) with the integral term, $\int g \cdot ds$, equals to the area under a graph in Figure 14 and g_0 equal to the gradient value at z = 0 mm. The measured effective length is 76.6 mm and the effective lengths from simulation are 76.9, 77.0 and 77.0 mm for RadMatSteel42, RadMatSteel37 and RadMatXc06, respectively.

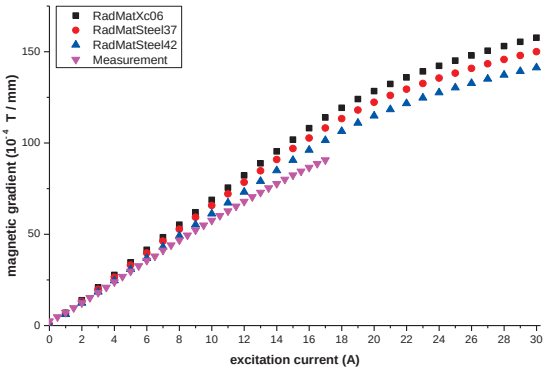

Fig. 12. Quadrupole magnet excitation curves.

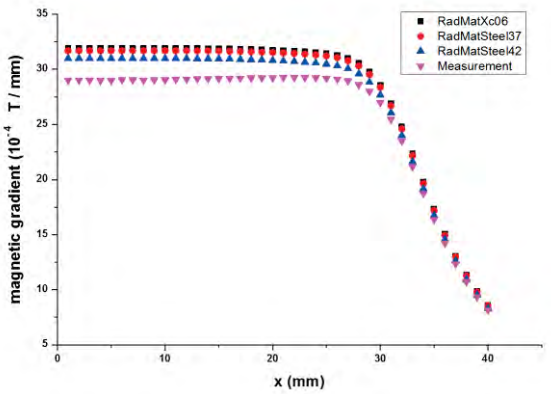

Fig. 13. Quadrupole magnet gradients along x-axis (I = 5A).

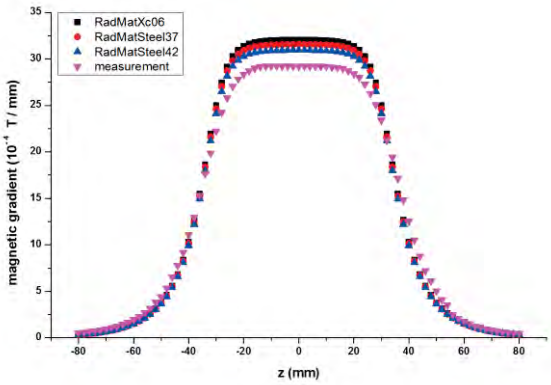

Fig. 14. Quadrupole magnet gradient along z-axis (I = 5A).

7. Conclusion

The simulations by using RADIA code and the measurements of the dipole magnet and the prototype quadrupole magnet were conducted and their results were analyzed. The simulations can evaluate well the magnet properties; including, the excitation curves and the field distributions for the dipole magnet; the excitation curves, the transverse gradient and the effective length for the quadrupole magnet. at the same excitation current, carbon percentage in the magnet core affects to the magnetic field intensity. The magnet core with lower carbon percentage generates higher magnetic field intensity. The excitation curves and field distributions from the measurements will be used in the magnet control and operation of the accelerator system. Both the simulated and the measured results will be used as a guideline for design and fabrication of magnets for the 180 degree achromat system in the future expansion for an IR-FEL facility.

Acknowledgements

Authors would like to thank Mr. M. Rhodes, Mr. P. Wichaisirimongkol, Mr. K. Kusoljariyakul, Mr. N. Kangrang and Miss S. Chunjareon for technical supports. Authors would like to acknowledge the support from the National Research Council of Thailand (NRCT), the Thailand Research Fund (TRF), the (Thailand) Commission on Higher Education (CHE), the Thailand Center of Excellence in Physics (ThEP), and the department of Physics and Materials Science, Chiang Mai University.

References

[1] Siegel PH. Terahertz Technology. *IEEE Transactions on Microwave Theory and Techniques*, 2002;**50**:910-928.

[2] Tonouchi M. Cutting-edge terahertz technology. *Nature photonic*, 2007;**1**:97-105.

[3] Thongbai C, et al. Femtosecond Electron Bunches, Source and Characterization. *NIM A*, 2008;**587**:130-135.

[4] Russenschuck R. Electromagnetic design of accelerator magnets. *CERN Accelerator School: Intermediate Course on Accelerator Physics*, Zeuthen, Germany, 25–26 september 2003. pp 411-440.

[5] Tanabe JT. *Iron dominated Electromagnets.* Singapore: World Scientific Publishing; 2005.

[6] Wiedemann H. *Particle Accelerator Physic*. 3rd ed. New York: Springer; 2007.

[7] Retrieved August 25, 2012 from: http://www.esrf.eu/Accelerators/Groups/InsertionDevices/Software/Radia

[8] Mathematica is a registered trademark of Wolfram Research, Inc.

[9] Umezawa M, et al. Magnetic Field Measurement of the Air Slot Dipole Magnet. In *Proceeding of PAC1999*. New York, USA: 1999, p. 3366-3368

[10] Takeuchi T, et al. Magnetic Field Measurement of Quadrupole Magnets for S-LSR. In *Proceeding of EPAC2004*. Lucerne, Switzerland: 2004, p. 1693-1695

Available online at www.sciencedirect.com

SciVerse ScienceDirect

Energy Procedia 00 (2013) 000–000

Energy Procedia

www.elsevier.com/locate/procedia

10th Eco-Energy and Materials Science and Engineering

(EMSES2012)

Optimization of longitudinal electron beam properties for linac-based infrared free-electron laser at Chiang Mai University

S. Suphakul[a,b], S. Chunjarean[b], C. Thongbai[a,b], S. Rimjaem[a,b]*

[a]*Department of Physics and Materials Science, Faculty of Science, Chiang Mai University, Chiang Mai 50200, Thailand*

[b]*Thailand Center of Excellence in Physics, CHE, Bangkok 10400, Thailand*

Abstract

A study to upgrade the linear accelerator system at the Plasma and Beam Physics (PBP) Research Facility at Chiang Mai University (CMU) to be an injector system for an infrared free-electron laser (IR FEL) is underway. The current PBP linac system consists of an S-band thermionic cathode RF-gun, a bunch compressor in a form of alpha-magnet and a SLAC-type linear accelerating structure. Since characteristics of the emitted FEL light strongly depend on electron beam properties, a dedicated work to develop and optimize the injector system to drive the FEL is particularly important. In this paper, the results of numerical study to optimize the longitudinal electron beam properties as well as some preliminary results of FEL simulations are presented and discussed.

Selection and/or peer-review under responsibility of COE of Sustainalble Energy System, Rajamangala University of Technology Thanyaburi(RMUTT)

Keywords: beam dynamics; infrared free-electron laser; FEL injector; linac-based FEL

1. Introduction

At the Plasma and Beam Physics (PBP) Research Facility, Chiang Mai University, Thailand, the project to produce THz transition radiation based on femtosecond electron bunches has been establised for many years [1]. The accelerator system consists of an S-band (2.856 GHz) thermionic RF electron gun [2], a magnetic bunch compressor in a form of an alpha-magnet [3], an S-band travelling wave linear accelerator (linac), and various beam diagnostic components. Electron beams with a bunch charge of about 16-96 pC and an rms bunch length as short as 70 fs were experimentally measured. When the electron bunches with the mentioned bunch length pass through an undulator, the radiation with a

* Corresponding author. Tel.: +66-53-943-379; fax: +66-53-222-376.
E-mail address: sakhorn.rimjaem@cmu.ac.th.

frequency of about 0.3 to 3 THz is emitted in phase resulting in an intense coherent radiation. However, the intensity of the coherent radiation falls off at the frequency higher than 3 THz or at the wavelength shorter than 100 μm. When the radiation wavelength is shorter than the electron bunch length, the incoherent radiation part dominates the coherent radiation part. To increase the radiation intensity, an external electric field can be used to stimulate the electrons to emit more coherent radiation via a microbunching process. The external field must have a frequency and phase such that the electrons loss their energies into the radiation. This mechanism is a basic principle in production of free-electron lasers, which can be achieved either using a long undulator, or an external seed laser, or a reclying spontaneous undulator radiation. The later principle is commonly used in a compact, low energy, and long radiation wavelength free-electron laser.

A possibility to develop an infrared free-electron laser (IR FEL) facility is studied at Chiang Mai University. The project focuses on the production and utilization of the mid-infrared (MIR) and far-infrared (FIR) or THz radiation based on a linac injector and free-electron laser technology [4]. The goal of the project is to produce the intense coherent radiation with tunable wavelengths covering from 2.5-20 μm (MIR) to 20-200 μm (THz).

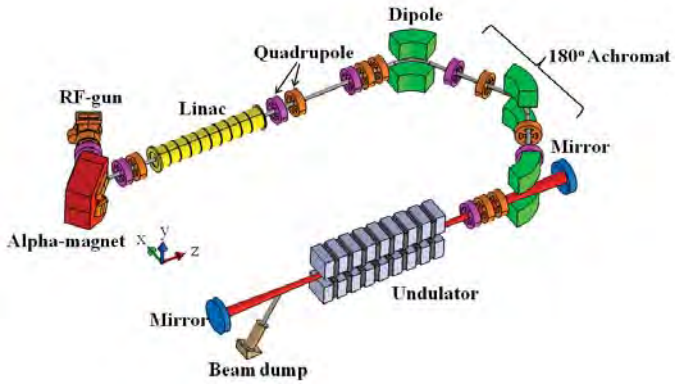

Fig. 1. Schematic layout and components of the possible IR FEL system at Chiang Mai University, Thailand

A plan to upgrade the existing PBP linac system to be the injector for both coherent THz transition radiation and free-electron lasers is proposed. The foreseen FEL facility will consist of a thermionic cathode RF-gun, an alpha-magnet, an S-band SLAC-type linac, a 180^o achromat section, a planar type undulator, and an optical resonator (Figure 1). Details of the components in the current PBP linac system were already reported in [1]. The 180^o achromat section, the undulator magnet, and the optical cavity are new components, which are under detailed consideration. The undulator magnet is chosen to be a planar type with 22 periods and a total length of 1.67 m. The optical cavity composes of two symmetric spherical mirrors with a coupling hole on one of the mirrors. To design and optimize the 180^o achromat section, we adopt the magnet lattice of the Kyoto University Free-Electron Lasers (KU-FEL) for initial study. The achromat section consists of three 60^o bending magnets and two sets of doublet quadrupole magnets. Details of the KU-FEL achromatic system have been described in [5]. Schematic layout of the proposed IR FEL at Chiang Mai University is shown in Figure 1.

For benchmark, we have investigated the injector parameters of the MARK-III FEL of Duke University, USA [6] and the FEL–SUT of Tokyo University, Japan [7]. Both facilities use the same type of the electron source, the magnetic bunch compressor and the accelerating section as the current PBP linac system. The beam dynamics study and optimization of the proposed injector system starting from the parameters of both accelerators [6, 7] are performed to achieve the proper electron beam properties for

driving the IR FEL. The computer code PARMELA (Phase And Radial Motion in Electron Linear Accelerator) [8] has been used to investigate multi-particle beam dynamics from the RF-gun to the exit of the 180^o achromat section and to optimize the electron beam lattice parameters. For the FEL radiation due to the interaction between the electron beam and the undulator magnetic field, the study has been studied using the numerical code GENESIS 1.3 [9]. Some preliminary results of the FEL simulation are presented and discussed in the last section of the paper.

2. Electron Beam Optimization

The FEL performance depends greatly on electron beam characteristics. Generally, the injector system for the FEL facility should produce electron beams with high peak current, small transverse emittance, and low energy spread in order to generate intense coherent FEL light in an undulator. In this study, we focus on optimization of longitudinal electron beam properties by adjusting the parameters of three main components; the RF-gun, the linac, and the 180^o achromatic section.

PARMELA simulations were performed to study electron beam dynamics in all components, except the alpha magnet. Since the goal of the optimization aims to produce electron beams with a very low energy spread (<1%), the electrons with high energy level have been optimized to form a quasi-monogenetic beam at the head of the bunch. Therefore, the compression in the alpha-magnet for this useful part of the bunch can be neglected. In this case, the alpha-magnet will serve only as the energy filter element. Some small energy spread will be induced during the post acceleration of the electron beam through the linac leading to the electron distribution suitable for the bunch compression downstream the linac. In our case, the 180^o achromat is used as both turn around section and as the magnetic bunch compressor. For the simulation of multi-particle beam dynamics, we assume that the cathode emits a uniform stream of 30,000 (macro) particles per 2.856 GHz with a current of 2.9 A. Thus, a single particle represents a charge of 33.85 fC, which equivalents to 2.12×10^5 electrons.

2.1. Beam dynamics simulation of the RF-gun

The RF-gun at the PBP facility is a one and a half-cell S-band resonant cavity with a thermionic cathode and a side coupling cavity. To simulate the RF field distribution inside the RF-gun, the code SUPERFISH is used [10]. Then, the particle-in-cell code PARMELA is utilized to track multi-particles through the fields obtained from the SUPERFISH simulation.

The accelerating field gradients of both half- and full-cell cavities were adjusted to produce an electron bunch with low energy spread, especially at the head of the bunch. These concentrated electrons at the head of the bunch will be the main contribution in the FEL lasing. The field ratio of the RF-gun is defined as a ratio of the accelerating field amplitudes at the cathode plane and at the center of the full-cell. For the field ratio of 1:2 with the accelerating field gradients of 35 and 70 MV/m, the RF-gun provides an electron beam with low energy spread at the head of the bunch. The three dimensional electron beam distributions at the RF-gun exit are shown in Figure 2. The distributions for transverse and logitudinal phase spaces are shown in Figures 3 and 4, respectively.

The electron bunch that actually exits the RF-gun is about 100 ps long (Figure 4). The high energy electrons with small energy spread are accumulated at the head of the bunch of about 10-15 ps, which is the most useful fraction of the bunch. Then, the electron bunches are filtered by the energy slits inside the vacuum chamber of the alpha-magnet to remove low energy electrons. For the RF-gun condition noted above, we set the energy filter level at 3.81 MeV. This leads to the output electron beams with the maximum electron energy of 3.91 MeV and the rms energy spread of 0.82%. Parameters of the electron beam after energy filtering using the alpha-magnet energy slits are listed in Table 1.

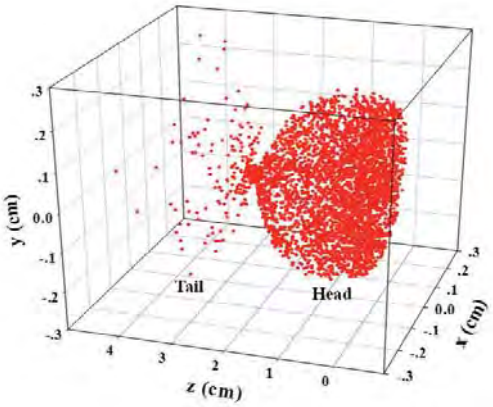

Fig. 2. Three dimensional particle distributions at the RF-gun exit for the field ratio of 1:2 and the accelerating field amplitudes of 35 and 70 MV/m

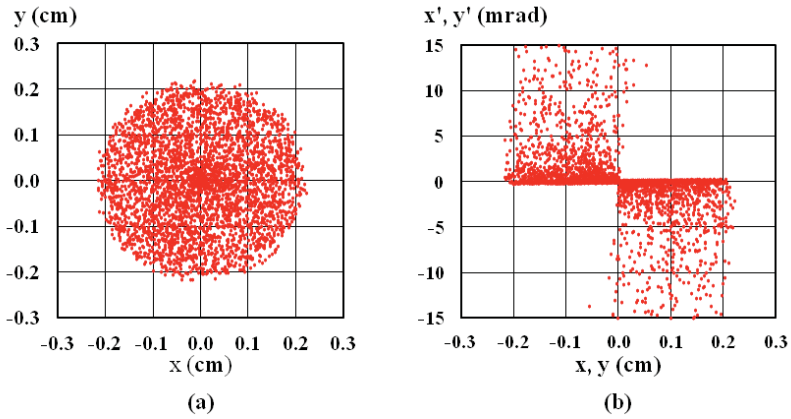

Fig. 3. (a) Particle distributions in x-y plane and (b) Transverse phase space distribution (x-x′ and y-y′) at the RF-gun exit

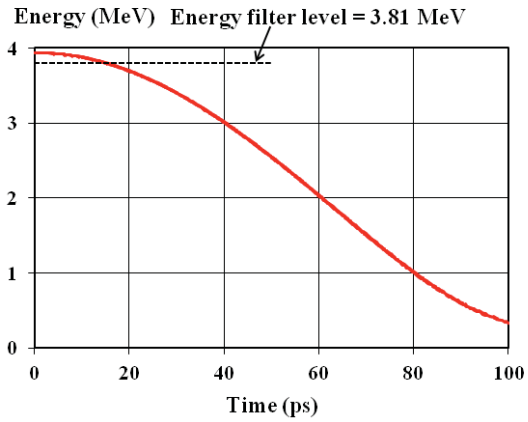

Fig. 4. Particle distributions in longitudinal phase space (energy-time) at the RF-gun exit

Table 1. Parameters of RF-gun and its output electron beam

Parameter	Value
Field ratio	1 : 2
Accelerating field	Half-cell: 35 MV/m Full-cell: 70 MV/m
Beam output energy	
- Average	3.91 MeV
- Maximum	3.94 MeV
- Minimum	3.81 MeV
Energy spread	0.82 %
Energy filter level	3.81 MeV
Bunch length (FWHM)	15 ps
Bunch charge	33 pC

2.2. Beam dynamics simulation of the Linac

The linac at the PBP facility is an S-band SLAC-type travelling wave linear accelerator. In this study, we consider that the electron beam is accelerated through the linac to reach an average energy of about 15 MeV. In order to achieve an electron bunch with low energy spread, the linac initial phase is varied between 0^o and -90^o relative to the reference particle phase at the entrance of the linac. Then, the number of particles is counted within the desired energy bin (1% in this study). Figure 5 shows the number of particles within 1% energy spread ($N_{1\%}$) normalized to the total number of the particles entering the linac (N_{total}) for different linac phases.

The energy gain from the linac can be adjusted by optimizing the product of the accelerating field (E_0) and the transit-time factor (T), which is linearly proportional to the electron energy at the linac exit. The product of the accelerating field and transit time factor (E_0T) has been optimized to achieve the electron beam with low energy spread and short bunch length at the exit of the 180^o achromat section. The optimized value of E_0T is 4 MV/m, which provides the final maximum and average electron energies of 15.6 and 15.4 MeV, respectively. The longitudinal phase space distributions of the particles at the exit of the RF-gun and at the exit of the linac for the linac initial phase of -53.7^o are illustrated in Figure 5. Parameters of the electron bunch after exiting the linac are shown in Table 2.

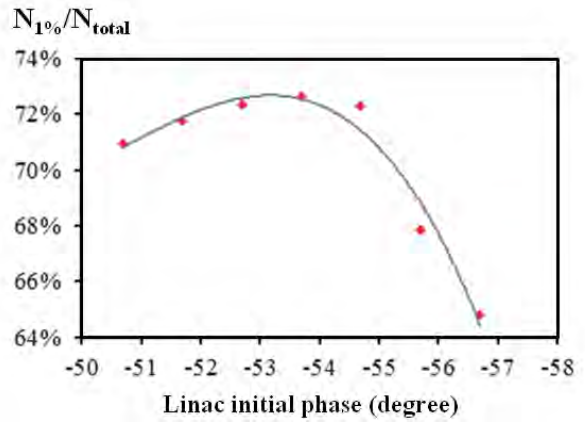

Fig. 5. Number of particles within 1% energy spread normalized to the total number of the particles entering the linac as a function of the linac initial phase respect to the reference particle phase entering the linac

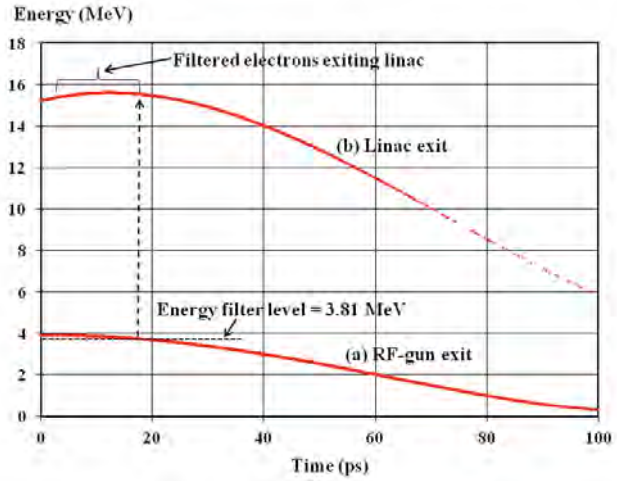

Fig. 6. Particle distributions in longitudinal phase space of all particles at (a) the RF-gun exit for the field ratio of 1:2 and the accelerating field amplitudes of 35/70 MV/m and (b) the linac exit with the linac accelerating initial phase of -53.7^{o} and the product between the accelerating field gradient and the transit time factor (E0T) of 4 MV/m

Table 2. Parameters of the linac and the electron beam exiting the linac

Parameter	Value
Accelerating length	3 m
Initial phase	-53.7^{o} w.r.t. reference particle entering linac
Beam output energy	
- Average	15.4 MeV
- Maximum	15.6 MeV
- Minimum	15.2 MeV
Energy spread	0.78 %
Energy filter level	3.81 MeV
Bunch length (FWHM)	10.1 ps
Bunch charge	33 pC

2.3. Beam dynamics simulation of the 180° achromat and the bunch compressor

In this study, we consider the 180° achromat as a turn-around element and a magnetic bunch compressor. It is a triple bend type consisting of three dipole magnets and two sets of quadrupole magnet, which are placed at the straight section between the dipoles (see Figure 1). The goal of the optimization of this section is to establish the parameters of the dipole and the quadrupole magnets as well as the drift lengths for transporting the electron beam through and exit the section with a shorter bunch length and no change of energy spread.

The dipole magnets have the deflecting angle of 60^{o} and the effective length of 35 cm. The electron bunch length can be adjusted by changing the gradient of the doublet quadrupoles to have the minimum bunch compression condition. At the electron beam energy of 15.4 MeV, the simulated shortest electron bunch length of 0.85 ps is achieved with the doublet quadrupoles' strengths of 56.4 m^{-2} and -44.6 m^{-2}, respectively. The particle distributions and energy spectrum of the electron bunch at the exit of the 180^{o} achromat section with the optimized condition are shown in Figure 7. Optimized specifications of the

components in the 180° acromat and the electron beam parameters at the exit of the acromat section are listed in Table 3.

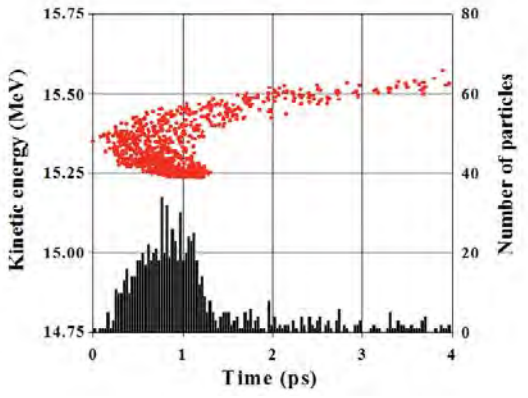

Fig. 7. Particle distributions in longitudinal phase space at the 180° achromat exit

Table 3. Specifications of the components in the 180° achromat and the electron beam parameters at the achromat exit

Parameter	Value
Bending magnet	
- Defection angle	60°
- Effective length	35 cm
- Curvature	2.99 m^{-1}
Quadrupole	
- Focusing strength	56.4 m^{-2}
- Defocusing strength	- 44.6 m^{-2}
Beam output energy	
- Average	15.4 MeV
- Maximum	15.6 MeV
- Minimum	15.2 MeV
Energy spread	0.74 %
Bunch length (FWHM)	0.85 ps
Bunch charge	33 pC
Peak current	38.8 A

3. FEL Simulations

The code GENESIS 1.3 is used to simulate the FEL radiation due to the interaction between optical fields and an electron beam inside the undulator. At this early stage, the simulations have been performed in the time-independent mode. The undulator considered for the IR FEL at CMU is a planar type with specifications listed in Table 4. The undulator gab is adjustable to vary the deflection parameter (K) between 0.4 and 2.6 in order to provide the radiation wavelengths of 50-200 μm. As an example, the electron beam with an average energy of 15 MeV and an rms bunch length of 1 ps is used in the initial

simulations. Some preliminary required beam parameters used in the simulations are given in Table 4. The optical cavity length is set to be 5 m with the diffraction and out coupling losses in the cavity of 5%.

Figure 7 shows the time evolution of the simulated FEL radiation peak power at radiation wavelengths of 200, 100, 75 and 50 μm for the electron beam with an average energy of 15 MeV, an rms energy spread of 0.5%, and a peak current of 30A. It can be seen that the longer FEL radiation wavelength reaches the power saturation faster than the shorter one. The numbers of round trips needed to accumulate the radiation amplification until reaching the saturation condition are within 60 turns for the radiation wavelengths of 200, 100 and 75 μm, while it needs 120 turns for the case of 50 μm. It seems that GENESIS simulation in the time-independent mode has a limit of the simulation for the case of electron bunch length shorter than the radiation wavelength. Further study using the code GENESIS in time-dependent mode together with the Optical Propagation Code (OPC) [11] will be performed.

Table 4. Undulator and electron beam parameters used in FEL simulations

Parameter	Value
Undulator type	Planar
Undulator period length	7.7 cm
Number of undulator period	22
Undulator deflecting parameter	0.036 - 3.39
Beam energy	15 MeV
Energy spread	0.5%
Bunch length (RMS)	1 ps
Peak current	30 A
Normalized emittance (ε_x, ε_y)	3 mm-mrad
Beam transverse size (σ_x, σ_y)	0.42 mm
Twiss parameters (β_o, α_o)	0.72, 0

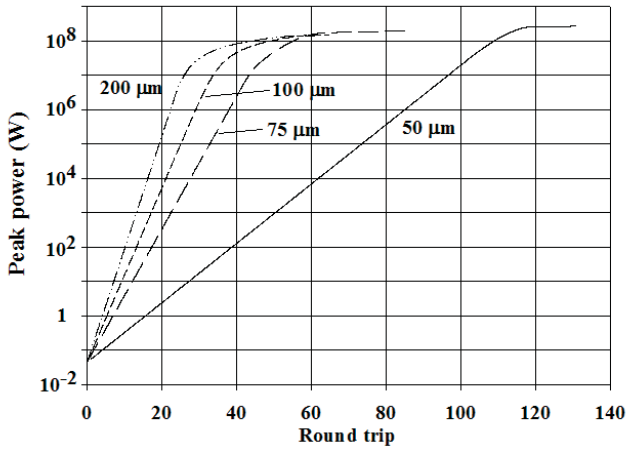

Fig. 8. Calculated time evolution of the peak power at the radiation wavelengths of 200, 100, 75 and 50 μm for the electron beam with an average energy of 15 MeV, an energy spread of 0.5 %, and a peak current of 30 A

4. Conclusion

The longitudinal beam dynamics of the injector system for an IR FEL at Chiang Mai University has been studied using numerical simulations. The results have achieved the parameters suitable for the IR FEL lasing requirements. By properly adjusting the machine parameters, the electron bunches exiting the 180° achromat section have an average energy of 15.4 MeV, an rms energy spread of 0.74%, a bunch length of 0.85 ps, and a bunch charge of 33 pC. Further studies and optimization will be proceeded to investigate both transverse and longitudinal electron beam dynamics. The initial study of the FEL radiation with wavelengths of 50 to 200 μm has been performed for the electron beam energy of 15 MeV and the bunch length of 1 ps without considering the slippage influence. The total FEL peak power in the optical cavity of about 10^8 W can be achieved. However, the time-dependent simulation including optical cavity parameters will be conducted to investigate the realistic loss in the cavity and the slippage effect.

Acknowledgements

Authors would like to acknowledge the support of the Department of Physics and Materials Science, Chiang Mai University, the Thailand center of Excellence in Physics (ThEP-center), the (Thailand) Commission on Higher Education (CHE), and the Thailand Research Fund (TRF). We would like to express our gratitude to Prof. H. Ohgaki from Kyoto University for the very useful discussion and suggestion in the beam dynamic simulations.

References

[1] Thongbai C, et al. Femtosecond Electron Bunches, Source and Characterization. *Nuclear Instruments and Method A*, 2008; **587**: 130-135.

[2] Rimjaem S. Generation of Far Infra-red Radiation from Relativistic Electron Beam. *Ph.D Thesis, Chiang Mai University*, 2006.

[3] Saisut J, et al. Construction and Performance of the Magnetic Compressor for the THz Facility at Chiang Mai University. *Nuclear Instruments and Method A*, 2010; **637**: S99-S106.

[4] Vilaithong T, Singkarat S, Yu L.D, Kamwannaa T, Thongbai C, Songsiriritthigul P. The Accelerators and Related R & D Activities in Thailand. *Journal of the Korean Physical Society*, 2011; **59**: 534-541.

[5] Zen H, et al. Numerical study on the optimum cavity voltage of RF gun and bunch compression experiment in KU-FEL. In *Proceeding of the 2007 Free-Electron Laser Conference*. Novosibirsk, Russia: 2007.

[6] Retrieved October 1, 2012 from the World Wide Web: http://www.fel.duke.edu/lightsources/mk3.html.

[7] Retrieved October 1, 2012 from the World Wide Web: http://www.rs.noda.tus.ac.jp/fel-tus/.

[8] Young L.M, Billen J.H. PARMELA. *Technical Note No. LA-UR-96-1835 Los Alamos National Laboratory*, 2002.

[9] Reiche S. GENESIS 1.3: a fully 3D time-dependent FEL simulation code. *Nuclear Instruments and Method A*, 1999; **429**: 243-248.

[10] Young L.M., Billen J.H. POISSON/ SUPERFISH. *Technical Note No. LA-UR-96-1834 Los Alamos National Laboratory*, 1999.

[11] Retrieved October 1, 2012 from the World Wide Web: http://lf.tnw.utwente.nl/opc.html.

THAI JOURNAL OF PHYSICS, SERIES 6, (2010)

RF-gun Phase-space Dynamics and Slice Emittance under Influence of External Electromagnetic Fields

K. Kusoljariyakul[1,2,*] and C. Thongbai[1,2]

[1]*Department of Physics and Materials Science, Faculty of Science, Chiang Mai University, Chiang Mai 50200, Thailand.*
[2]*ThEP Center, Commission on Higher Education, Bangkok 10400, Thailand.*

A high brightness electron source of ultra-small emittance and high average current is one of the most important components for the future accelerators. Rapid acceleration in an RF-electron-gun can reduce emittance growth due to space charge, however twisting of slice emittances from an RF-electron-gun may be its limitation. Such rotation may be compensated by an external electromagnetic field. In this work, RF-electron-gun phase-space dynamics and slice emittance in some electromagnetic field distribution are studied.

Keywords: Beam Emittance, High Brightness Beam, Emittance Compensation.

1. INTRODUCTION

A high brightness electron source of ultra-small emittance and high-average current is one of the most importance components for the future electron accelerators [1-2]. Such beams are used as sources of very high energy linear collider, wake-field laser accelerator and X-ray Free Electron Laser.

In order to achieve high brightness beams, it is necessary to master the production of such beams in special RF-guns, to develop diagnostic techniques that provide information of the 6-D distribution of electron bunches on sub-picosecond time scales; to control the 6-D distribution of the bunch in various ways; and to be able to accelerate the electrons to high energies without diluting the brightness.

The electron bunches produced from an RF-gun are subjected to detrimental effects on the beam emittance, specifically twisting of the time-sliced emittance or slice emittance. This effect can increase apparent emittance by several orders of magnitude. Thus, in order to obtain high brightness beam, one has to consider this effect crucially. This phenomenon may be compensated by dispatch the beam through a proper external electromagnetic field, for example, a magnetic field of a solenoid magnet.

2. THEORETICAL BACKGROUND

Beam emittance

Beam emittance is a certain region in phase space occupied by particles in a beam [3]. By definition, phase space is represented by coordinate and its conjugate momentum. However, it is more convenience to replace the conjugate momentum with slope of the trajectory, x', defined as:

$$p_x = p_0 \tan x' \approx p_0 x' . \qquad (1)$$

In this paper, the term "beam emittance" is used for transverse apparent or projected emittance while "slice emittance" is used for emittance of time-slice beam. In either case, the emittance is calculated as r.m.s. emittance, defined by

$$\varepsilon_x = \sqrt{\langle x^2 \rangle \langle x'^2 \rangle - \langle xx' \rangle^2} \qquad (2)$$

Emittance compensation

Space charge forces and radial fields in RF-cavities can degrade beam emittance significantly. The space charge effect is inverse proportional to square of particle energy. Thus, rapid acceleration in an RF-gun can reduce space charge effect. Moreover, space charge effect causes rotation of phase-space distribution due to its energy dependence. Equation (2) indicates that if all particles lie on a line in phase-space, in other words, $x = mx'$ where m is a slope, the beam emittance will vanish [4]. Thus, this rotation cannot be ignored if high brightness beam is to be achieved. Some space charge effects can be compensated, as suggested by E. Carlson [?] using solenoid magnet focusing. Apart from using a solenoid magnet, there are several approaches suggested for emittance minimization, for example, using RF radial focusing [4], alternative cathode material [5] and special RF gun designing. Only effect of solenoid magnet will be discussed further.

Transfer matrix of a solenoid magnet

There are several approaches to obtain positions of particles in phase-space. One of the best options is numerical integrator. Another option is matrix formalism of linear beam dynamics. The matrix approach is easier to use and understand but provide less accuracy and flexibility.

A first-order transfer matrix of a solenoid magnet can be written as [6]

Corresponding author. *E-mail*: zartpart@gmail.com

$$M_{sol}(0 \mid L_s) =$$

$$\begin{pmatrix} \cos^2\Phi & \frac{1}{K}\sin\Phi\cos\Phi & \sin\Phi\cos\Phi & \frac{1}{K}\sin^2\Phi \\ -K\sin\Phi\cos\Phi & \cos^2\Phi & -K\sin^2\Phi & \sin\Phi\cos\Phi \\ -\sin\Phi\cos\Phi & -\frac{1}{K}\sin^2\Phi & \cos^2\Phi & \frac{1}{K}\sin\Phi\cos\Phi \\ K\sin^2\Phi & -\sin\Phi\cos\Phi & -K\sin\Phi\cos\Phi & \cos^2\Phi \end{pmatrix}$$

where $K = \dfrac{eB_s}{2p}$ is a solenoid strength and $\Phi = KL_s$.

3. CALCULATION RESULTS AND DISCUSSIONS

The input phase space data for this calculation is PARMELA [ ] output of SURIYA RF-gun [7] and SUNSHINE RF-gun [8]. The $x - x'$ distribution of SURIYA electron beam is shown in figure 1.

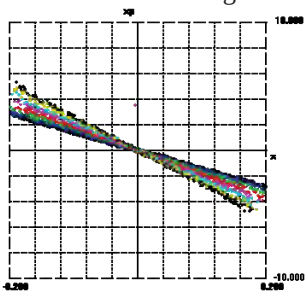

FIGURE 1. Phase space distribution of 1-ps-slices at SURIYA RF-electron-gun exit.

A solenoid magnet with 3 cm effective length is positioned at the RF-gun exit. The phase-space distributions of SURIYA RF-gun after the solenoid magnet and a 10-cm-drift-space are shown in figure 2. The apparent emittance of the beam at the same location is shown in Figure 3 for various solenoid field strengths. The minimum…. occurs when using…

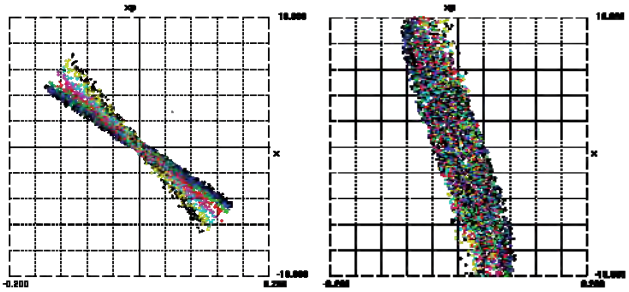

FIGURE 2. SURIYA RF-gun phase space distribution of 1ps slices at 10 cm after the solenoid magnet. Left: 1000 gauss solenoid field. Right: 2000 gauss.

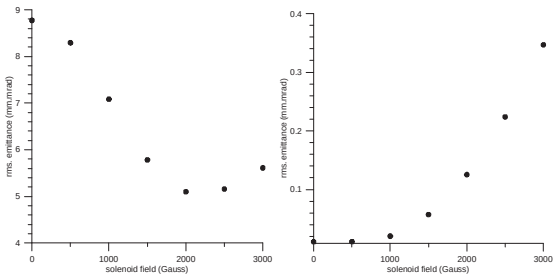

FIGURE 3. Apparent emittance of electron beam from SURIYA RF-gun., Left: Apparent emittance as a function of solenoid magnet field and Right: Slice emittance of the first slice (0-1 ps).

The $x - x'$ distribution of SUNSHINE electron beam is shown in figure 4. By placing a solenoid and a drift-space as the previous case, the phase-space distributions for SUNSHINE RF-gun are shown in figure 5. The apparent emittance of the beam is shown in figure 6 (Left) and the slice emittance of the first slice (0-1 ps) is shown in figure 6 (Right).

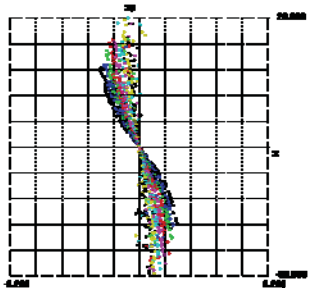

FIGURE 4. Phase space distribution of 1ps slices at SUNSHINE RF-electron-gun exit.

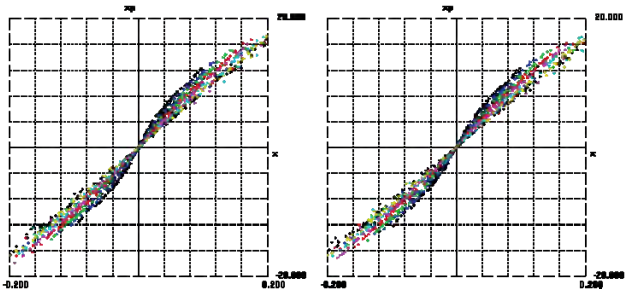

FIGURE 5. SUNSHINE RF-gun phase space distribution of 1ps slices at 10 cm after the solenoid magnet. Left: 1000 gauss solenoid field. Right: 2000 gauss.

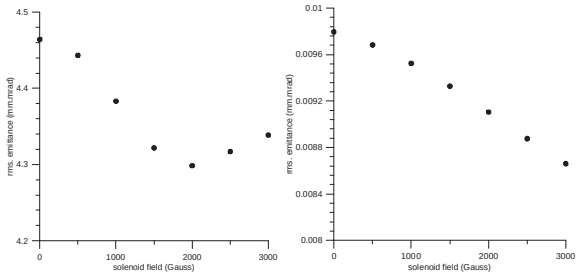

FIGURE 6. Emittance of electron beam from SUNSHINE RF-gun, Left: Apparent emittance as a function of solenoid magnet field and Right: Slice emittance of the first slice (0-1 ps).

The results show that apparent emittance changes with solenoid field strength. The emittance can be reduced using 3 cm solenoid magnet and 10 cm drift space up to about 40% for SURIYA RF-gun. However, only about 4% emittance reduction for SUNSHINE RF-gun was observed from a similar setup. Noting that, the beam from SUNSHINE RF-gun is already focused within the RF-gun cavities while the beam from SURIYA RF-gun is parallel beam. Thus, the two systems may require different parameters.

4. CONCLUSION

Study of…. Matrix….The preliminary results show that solenoid magnet is capable of reducing apparent emittance of SURIYA beam. However, there are many parameters which are not included in this study. Further study of other devices that may be able to reduce apparent emittance, for example, cylindrical RF cavity will be conducted. The final results may lead us to a new emittance compensation scheme.

ACKNOWLEDGMENTS

Authors would like to acknowledge the support from the National Research Council of Thailand (NRCT), the Thailand Research Fund (TRF), the (Thailand) Commission on Higher Education (CHE), the Thailand Center of Excellence in Physics (ThEP), and the department of Physics and Materials Science, Chiang Mai University.

1. K.J. Kim, et. Al., "Toward Advanced Electron Beam Brightness Enhancement and Conditioning", ANL/APS/LS-305, 2004.
2. J. W. Lewellen, "Overview of High-Brightness Electron Guns", in Proceeding of LINAC2004, 2004.
3. H. Wiedemann, "Particle Accelerator Physics", 3rd edition, Springer-Verlag, 2007.
4. B. E. Carlsten, D. T. Palmer, "Enhanced emittance compensation in a high-frequency RF photoinjector using RF radial focusing", NIM A, 425 (1999) 37-50.
5. S. H. Kong, "Cesium Telluride Photocathodes", Jounal of Applied Phsics 77 (1995) 6031-6038.
6. K. L. Brown, et. al., "TRANSPORT: A COUMPTER PROGRAM FOR DESIGNING CHARGED PARTICLE BEAM TRANSPORT SYSTEMS", Revision 3, SLAC, 1983.
7. S. Rimjeam, et. al., "Femtosecond electron bunches from an RF-gun", NIM A, 533 (2004) 258-269.
8. P. Kung, "Generation and Characterization of Sub-picosecond Electron Bunches", Ph.D. thesis, Stanford University, 1996.

Investigation of Water Distribution in Proton Exchange Membrane Fuel Cells via Terahertz Imaging

P. Buaphad [a,c], P. Thamboon [b,c,*], K. Kusoljariyakul [a,c], M.W. Rhodes [b,c], J. Saisut [a,c], T. Vilaithong [c] and C. Thongbai [a,c]

Abstract— *Terahertz (THz) radiation in the form of coherent transition radiation generated from femtosecond electron bunches is explored for its potential use in imaging applications. Due to water sensitivity, the THz imaging experiment is performed on a Proton Exchange Membrane Fuel Cell (PEMFC) to assess the ability to quantify water in the flow field of the cell. In this investigation, the PEMFC design and the experimental setup for the THz imaging will be described. Results of terahertz images in the flow field will also be discussed.*

***Keywords*—transition radiation, terahertz, imaging, PEM fuel cells**

1. INTRODUCTION

Proton Exchange Membrane Fuel Cell (PEMFC) is an electrochemical device being widely developed as one of alternative sources for clean energy. The basic single cell consists of a membrane electrode assembly sandwiched between flow fields. In the flow fields, water in the form of humidifier to reactants is brought in, and water generated as a byproduct from electrochemical reaction is transported out. Imbalanced of water formation and removal can cause state of drying-flooding in different areas within the cell, resulting in poor cell performance [1]. In order to overcome water management problem and advance the PEMFC for practical usage, it is vital to be able to visualize and study dynamic of water distribution in the PEMFC. Tools such as digital camera, neutron imaging, and magnetic resonance imaging have been exploited so far for *in situ* measurements of water in different parts of PEMFCs [2]. As example, water transport problem in the flow field is given here in Figure 1. A snapshot from a video camera of one of the flow field channels in PEMFC when the channel is empty is compared with when the channel is water-clogged.

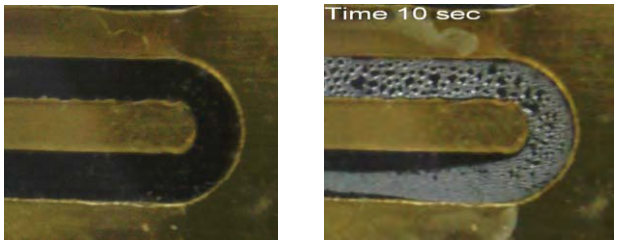

(a) **(b)**

Fig. 1. Photographs of (a) empty flow field, and (b) water-clogged flow field after 10 seconds into operation time.

THz radiation, lies between deep infrared and microwave, has been known to be water sensitive. Strong attenuation by water content has earned THz beam as a preferable tool for non-destructive inspection such as in food industry and in medical applications [3-4]. Our femtosecond electron source – developed at Plasma and Beam Physics Research Facility, Chiang Mai University, Thailand – can generate a coherent transition radiation in the THz regime ranging from 0.15 - 2.4 THz (5-80 cm^{-1}) [5]. Therefore, we aim to investigate a potential use of THz imaging to water distribution in PEMFCs. The present paper focuses on water presence in the flow field of PEMFC via reflective THz imaging. Our preliminary results reported here indicate promising application of THz imaging to water management problems in PEMFCs.

2. THz RADIATION SOURCE

At the Plasma and Beam Physics (PBP) Research Facility, Chiang Mai University, Thailand, THz radiation is generated in the form of coherent transition radiation from femtosecond electron bunches [5]. The system to produce such short electron bunches consists of a thermionic cathode RF-gun, an alpha magnet, and a linear accelerator (Linac), shown in Figure 2(a). At the THz radiation experimental station (Figure 2(b)), the short electron bunches are used to generated coherent transition radiation by passing through a radiator made of a 25.4-μm-thick Al-foil. The radiator is tilted by 45^{o} facing the electron beam direction. The backward transition radiation is emitted perpendicular to the beam axis and transmits through a high density polyethylene (HDPE) window of 1.25-mm-thick and 32-mm diameter. The coherent radiation spectrum covering much of the far-infrared or THz spectral range and high intensity radiation from mm-waves up to 80 cm^{-1} (2.4 THz) can be detected with a room temperature detector.

* Corresponding author. Tel: +66 53 943379; Fax: +66 53 222776; E-mail: thamboon@yahoo.com
[a] Department of Physics and Materials Science, Chiang Mai University, Chiang Mai 50200, Thailand.
[b] STRI, Chiang Mai University, Chiang Mai 50200, Thailand.
[c] ThEP Center, Commission on Higher Education, Bangkok 10400, Thailand.

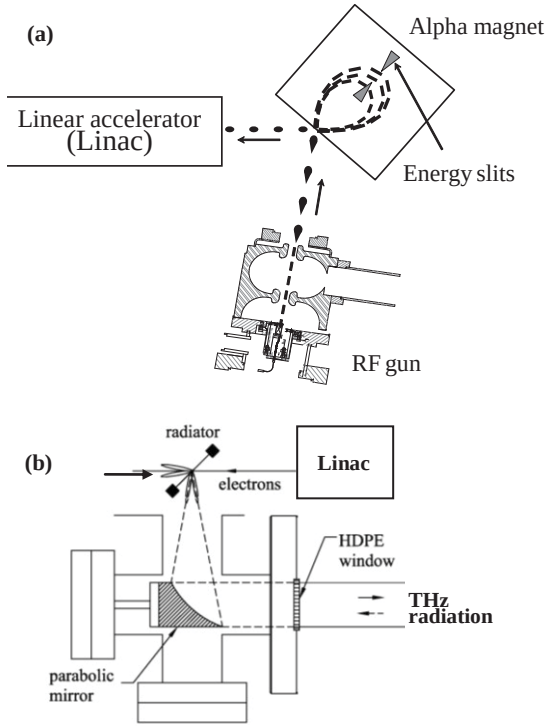

Fig.2. (a) Schematic diagram of the system to generate femtosecond electron bunches and (b) THz radiation.

3. PEMFC DESIGN FOR THz IMAGING

The flow field of PEMFC is typically made of graphite, which is machined into channel pattern that allows water and reactants to flow in and out. For a single cell, only one surface of the graphite is machined (called dead-end flow field). Unfortunately, the dead-end flow field made of graphite is not transparent to THz. In order to image the water in the flow field, we will need to machine through the channels and enclosed with an appropriate window for THz probing. Our PEMFC design for THz imaging is shown in Figure 3.

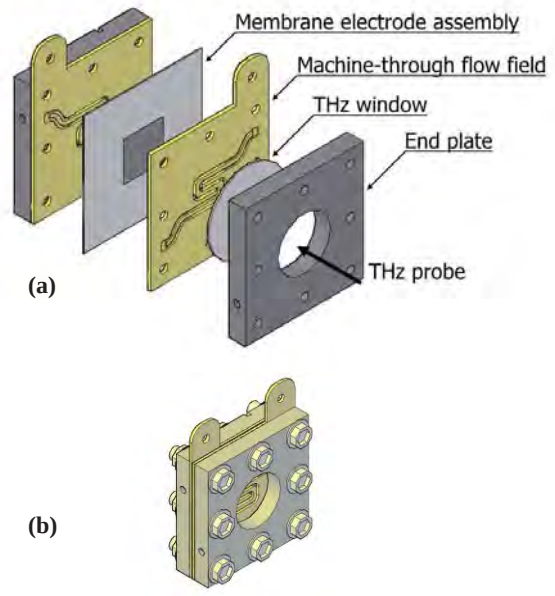

Fig.3. (a) PEMFC components designed with machine-through flow field made of brass enclosed with THz window. (b) A drawing of finished cell.

As graphite is too brittle for machining through, we instead chose brass for our machine-through flow field. For the THz window, we have two candidates: one is a plexiglass window and the other is a silicon window. Both window materials are transparent to a certain degree in THz region. Silicon in particular has been reported to be used as a window in reflective far infrared fourier transform spectroscopy of water [6]. In this work, we compare THz images obtained from the two materials in order to determine a more suitable THz window prior to constructing the finished cell.

4. REFLECTIVE THz IMAGING SETUP

Schematic diagram of our reflective THz imaging setup is shown in Figure 4. A parallel THz beam is reflected off a gold-coated mirror to a THz lens (L1) with f = 6 cm. The beam is then focused onto a sample at approximately 30° incident angle. The reflected signal from the sample is then collected by another THz lens (L2) with f = 3 cm and continued to a pyroelectric detector. The sample is placed on X-Y stages with computerized motion controllers. The focused beam size at the sample (at the focal point of L1) is determined by an array pyroelectric detector (Pyrocam III beam profiler). The focused beam profile shown in Figure 5 indicates the width at FWHM to be approximately 2 mm.

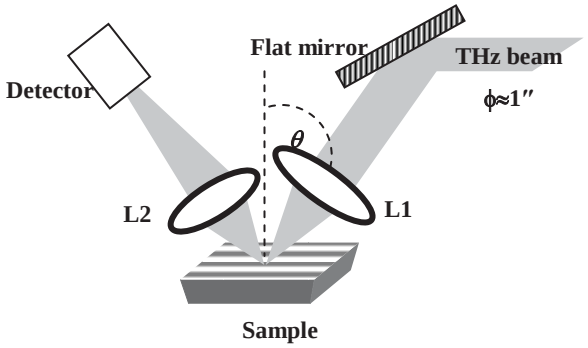

Fig. 4. Schematic diagram for reflective THz imaging, where L1: focusing lens (f = 6 cm); L2: collective lens (f=3 cm); and θ: 30°.

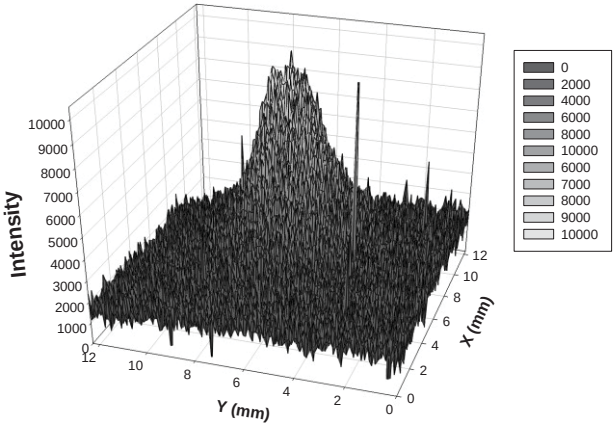

Fig. 5. THz beam profile, taken via Pyrocam III, at a focal point of the 6 cm-focal length lens.

To determine which window material yields a better THz image of water distribution in the flow filed, we prepared a sample in the following. First, we machined brass into 2 mm-width channels, and we sealed the bottom of the brass tightly with cloth tape. As illustrated in Figure 6, the channel that is filled with water will be indicated as a water-filled channel, while the one that is left unfilled will be indicated as an air-filled channel. Then, we physically taped down the window material on top of the brass. The plexiglass window that we used has a thickness of 1 mm. The silicon window is a silicon wafer of p-type doping with a thickness of 0.5 mm. Once the sample is securely placed on X-Y stages, the THz scanning is started from top-right corner of the sample along x-direction (horizontal) followed by y-direction (vertical) with a step of 1 mm through out the experiment.

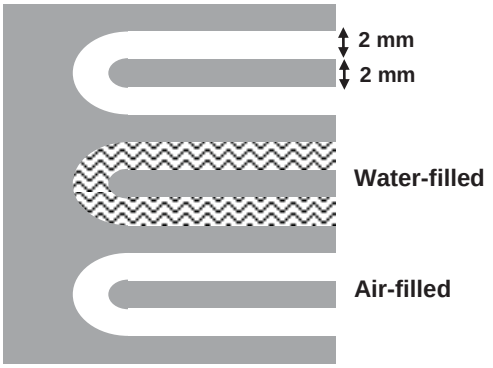

Fig. 6. Preparation of a machine-through brass with water filling for THz imaging.

5. RESULTS AND DISCUSSION

The THz image of machine-through-brass flow field with plexiglass window is shown in Figure 7. The scanning area of 20x20 mm^2 sufficiently covers two channels: the top channel is water-filled and the bottom is air-filled. The shape of channel – even though, it seems rough around the u-bend due to a course scanning step – is still recognizable. In gray-scale, the lighter area indicates a more reflective region of brass. The darker area reveals absorptive region within the channels, with the darkest region lies in water-filled channel. Clearly, we can identify the water-filled and the air-filled channels from the image. A small deeply dark area in the air-filled channel can be spotted, however, which could be attributed to the fact that our window is not tightly placed and thus there is a chance of water leakage into the air-filled channel to which THz radiation is very sensitive.

Similarly, the THz image of machine-through-brass flow field with silicon window in Figure 8 reveals deep absorptive region in the water-filled channel. Small deeply dark area in the air-filled channel can be implied as water leakage explained earlier. However, the overall reflected signals from the silicon window are greater than that from the plexiglass. This is because silicon is more reflective and is believed to have smaller or minimal THz absorption than plexiglass. As a result, the gray scale in Figure 8 can be divided into 7 levels while only 5 levels are available for Figure 7. Hence, the THz image using the silicon window should provide more resolved image than that using the plexiglass window.

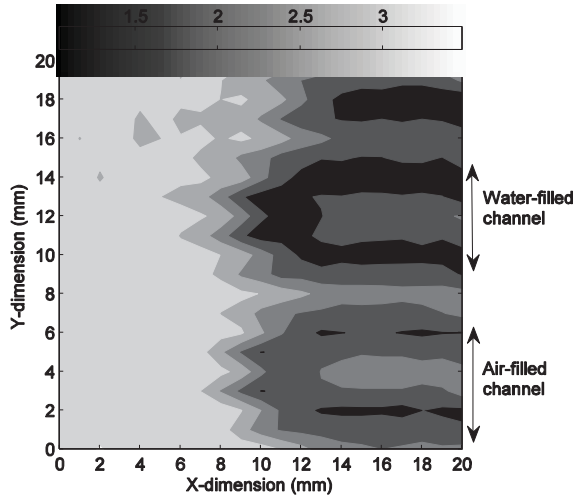

Fig. 7. THz image of machine-through-brass flow field with plexiglass window.

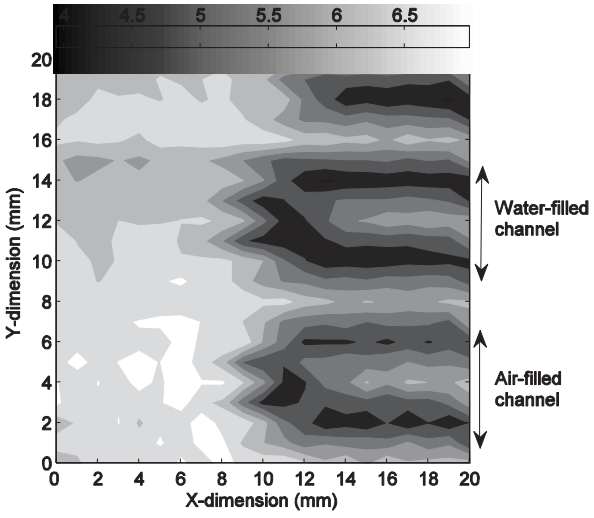

Fig. 8. THz image of machine-through-brass flow field with silicon window.

6. CONCLUSION

In this investigation, the reflective THz imaging system is successfully established for identifying water presence in the flow field of PEMFC. The PEMFC is redesigned to have a machine-through brass and a THz window for THz probing in the flow field region. In search of THz window materials for the PEMFC, we found that THz images from both plexiglass and silicon windows clearly distinguish water-filled region in the machine-through-brass flow field. However, the silicon window provides greater reflected signals, yielding more depth into details of the image than the plexiglass window. The image results are convincing evidence for further employing THz radiation from the femtoelectron source at the PBP Research facility, Chiang Mai, Thailand as a visualizing tool to study water transport dynamic in PEMFCs.

ACKNOWLEDGEMENT

Authors would like to thank Mr. N. Kangrang, Mr. P. Wichaisirimongkol and Mr. V. Jinamoon for technical supports. Authors would like to acknowledge the support from the National Research Council of Thailand (NRCT), the Thailand Research Fund (TRF), and the (Thailand) Commission on Higher Education (CHE).

REFERENCES

[1] Li, H. *et al*. 2008. A review of water flooding issues in the proton exchange membrane fuel cell. *J. Power Source* 178:103-11.

[2] Ito, K. in: S. Basu (Ed.). 2007. *Recent Trends in Fuel Cell science and Technology*. Anamaya Publishing. New Delhi. pp. 129-136.

[3] Woodward, R. M. *et al.* 2002. Terahertz pulse imaging in reflection geometry of human skin cancer and skin tissue. *Phys. in Med. and Biol.* 47**:**3853-3863.

[4] Morita, Y. *et al.* 2005. Terahertz technique for detection of microleaks in the seal of flexible plastic packages. *Opt. Eng.* 44: 019001.

[5] Thongbai, C. *et al.* 2008. Femtosecond electron bunches, source and characterization. *Nucl. Instr.and Meth. A* 587:130-135.

[6] Woods, K. N., and Wiedemann, H. 2004. The relationship between dynamics and structure in the far infrared absorption spectrum of liquid water. *Chem. Phys. Lett.* 393: 159-165.

Femtosecond Electron Bunches and Terahertz Radiation Source at Chiang Mai University

J. Saisut [a,c] , K. Kusoljariyakul [a,c] , S. Rimjaem [d] , N. Kangrang [a,c], P. Wichaisirimongkol [a,c], P. Thamboon [b,c], M.W. Rhodes [b,c] and C. Thongbai [a,c,*]

Abstract— *A system to produce femtosecond electron bunches and THz radiation has been developed at the Plasma and Beam Physics Research Facility, Chiang Mai University, Thailand. The system consists of a thermionic cathode RF-gun, an alpha magnet as a magnetic bunch compressor, and a linear accelerator as a post acceleration section. High intensity THz radiation in the form of coherent transition radiation is produced when short electron bunches traverse a vacuum-metal interface. The radiation is of great interest as a potential high intensity THz or far-infrared radiation source. Overview of the system, the generation of femtosecond electron bunches, the generation of coherent THz transition radiation and the recent experimental results on THz spectroscopy and THz imaging will be presented and discussed.*

***Keywords*— electron bunch, far-infrared, femtosecond, THz**

1. INTRODUCTION

Femtosecond electron and photon pulses have become interesting tools for basic and applied application [1-3]. Such short electron bunches can be used directly [1] or to generate intense THz radiation [4], ultra short X-ray pulses [5], and free electron lasers (FELs) [6].

Short electron bunches can be produced in a small accelerator facility from a thermionic cathode RF-gun and a magnetic bunch compression system in form of an α-magnet. At the Stanford SUNSHINE facility, it has been possible to produce electron pulse as short as 120 fs rms and a bunch intensity of 100 pCb [7]. A similar system was established at the Plasma and Beam Physics Research Facility, Department of Physics and Materials Science, Faculty of Science, Chiang Mai University. Figure 1 shows a schematic layout of the system set-up and area. The main components of the system are a thermionic cathode RF-gun, an α-magnet, a SLAC-type linear accelerator (linac), beam steering and focusing elements, beam diagnostic instruments, RF system, and control units. The femtosecond electron bunches will be used to generate intense THz or far-infrared radiation in the form of coherent radiation. Such radiation is of great interest for THz spectroscopy and THz imaging applications.

2. GENERATION OF FEMTOSECOND ELECTRON BUNCHES

Figure 2 shows the schematic diagram of the bunch generation and compression system using the specially-design RF-gun, which was studied and reported in [8]. In the RF-gun, electrons are continuously emitting with thermal energies from the thermionic cathode and are extracted and accelerated during an accelerating phase of the RF-fields at 2856 MHz. The first electron is accelerated rapidly and reach the end of the half-cell just before the RF-phase becomes decelerating. It is further accelerated through the full-cell to reach maximum kinetic energy of 2.0-2.5 MeV at the gun-exit depending on accelerating field gradients. Later electrons feel some

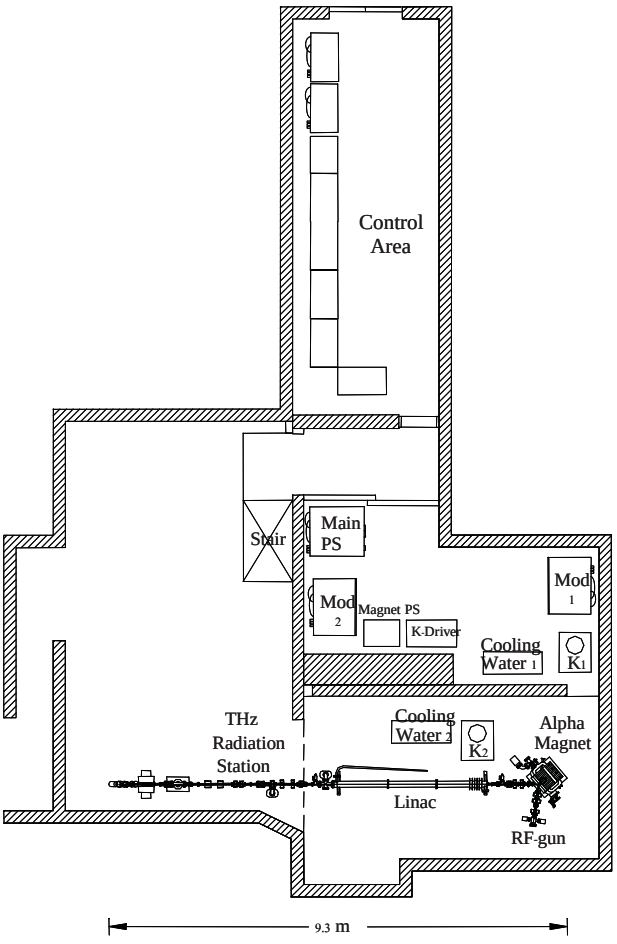

Fig.1. Schematic layout of the system at Chiang Mai University for generation of short electron bunches and terahertz radiation

* Corresponding author. Tel: +66 53 943379; Fax: +66 53 222776; E-mail: chlada@chiangmai.ac.th
[a] Department of Physics and Materials Science, Chiang Mai University, Chiang Mai 50200, Thailand.
[b] STIR, Chiang Mai University, Chiang Mai 50200, Thailand.
[c] ThEP Center, Commission on Higher Education, Bangkok 10400, Thailand.
[d] DESY Zeuthen, Platanenallee 6, Zeuthen 15738, Germany.

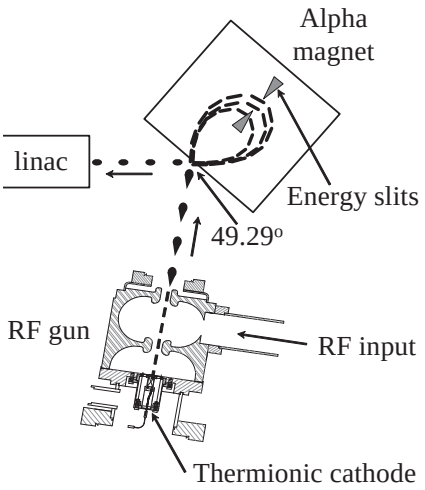

Fig.2. Schematic diagram of the electron bunch generation and compression system.

decelerating fields and gain less and less overall energy resulting in a well-defined correlation between energy and time.

Electron bunches of 20-30 ps from the RF-gun are then compressed in an α-magnet, where the particle path length increases with energy. This allows the lower energy particles, emitted later in each bunch, to catch up with the front for effective bunch compression. The optimized and compressed part of the electron bunch is then filtered by energy slits located in the α-magnet vacuum chamber and then transported through a SLAC type linac and a beam transport line to experimental stations. At the experimental station, the bunches are compressed to less than 1 ps [9]. Operating and beam parameters are shown in Table1.

TABLE 1. Operating and beam parameters.

Parameters	RF-gun	Linac
Beam energy [MeV]	2.2-3	6-10
Macropulse peak current [mA]	1000	50-150
RF-pulse length (FWHM) [μs]	2.8	8
Repetition rate [Hz]	10	10
Beam-pulse length [μs]	~2	~0.8
Number of microbunch/macropulse	5700	2300
Number of electrons /microbunch	1.4×10^{9}	8×10^{7} - 6×10^{8}

3. GENERATION OF THz RADIATION

The electron beam after acceleration was used to generate intense THz radiation in the form of coherent transition radiation (TR) utilizing a 25.4-μm-thick Al-foil of 24 mm diameter as a radiator. The radiator is tilted by 45° facing the electron beam direction. The backward transition radiation is emitted perpendicular to the beam axis and transmits through a high density polyethylene (HDPE) window of 1.25-mm-thick and 32-mm diameter. A copper light cone is used to collect the radiation into a room-temperature pyroelectric detector. A cross-sectional diagram of the experimental setup to generate the THz transition radiation is shown in Figure 3.

The radiation energy of 19 μJ per macropulse or a peak power of 24 W was measured by collecting over an

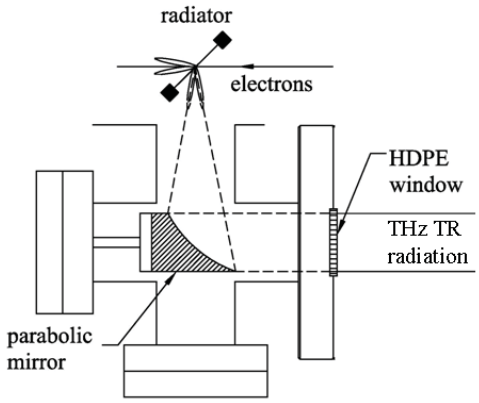

Fig.3. Setup to generate THz Transition radiation.

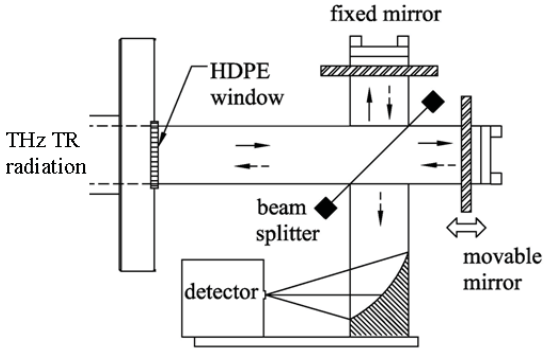

Fig.4. Schematic diagram of the THz Michelson interferometer.

acceptance angle of 160 mrad. The Radiation Spectrum was measured using a Michelson interferometer, whose schematic diagram is shown in Figure 4. Backward coherent transition radiation exits through a HDPE window and enters a Michelson interferometer. The interferometer consists of a beam splitter, a fixed and a movable first surface mirror, arranged as shown in the figure. The radiation field entering the Michelson interferometer is split into two parts by the beam splitter, both travelling in different directions to be reflected back by mirrors. After reflection, parts of the two radiation pulses are combined again and absorbed by a detector to determine the intensity. By scanning the movable mirror position, an autocorrelation of the radiation pulses can be obtained. The radiation power spectrum as displayed in Figure 5 can then be derived via the Fourier Transformation of the autocorrelation pattern. The available THz radiation covers from 5 cm^{-1} to around 80 cm^{-1} wavenumber (0.15 THz – 2.4 THz). At low frequency (< 5 cm^{-1}), the spectrum was suppressed by effects of the beam splitter, by mirror diffractions and by shielding inside the small metallic vacuum chamber [10, 11]. The spectrum seem to extend to above 80 cm^{-1} (2.4 THz) where noise becomes dominate. These can be further minimized with better detection and amplification system.

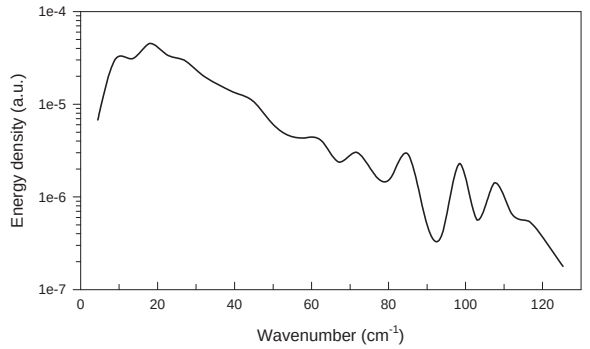

Fig.5. THz Radiation power spectrum.

4. THz SPECTROSCOPY

The THz spectroscopy can be done easily by measuring power transmission or power absorption of a sample via a Michelson interferometer and the Fourier Transformation. Although phase information has been lost in the measurement, optical constants of the sample can be obtained by some modeling or Kramers-Kronig calculation [12]. Dispersive Fourier Transform Spectroscopy (DFTS) [13] may also be used for direct determination of optical constants of a sample. In a DFTS setup, a sample is inserted in one arm of the interferometer, causing attenuation and dispersion of the radiation pulse. The attenuated and dispersed pulse can be recorded and its attenuation factor and phase shift can then be recovered. The attenuation and dispersion can be related to optical constants of the sample depending on the optical configuration of the measurements. With the DFTS technique, the phase information can be recovered in measurements using a Michelson interferometer.

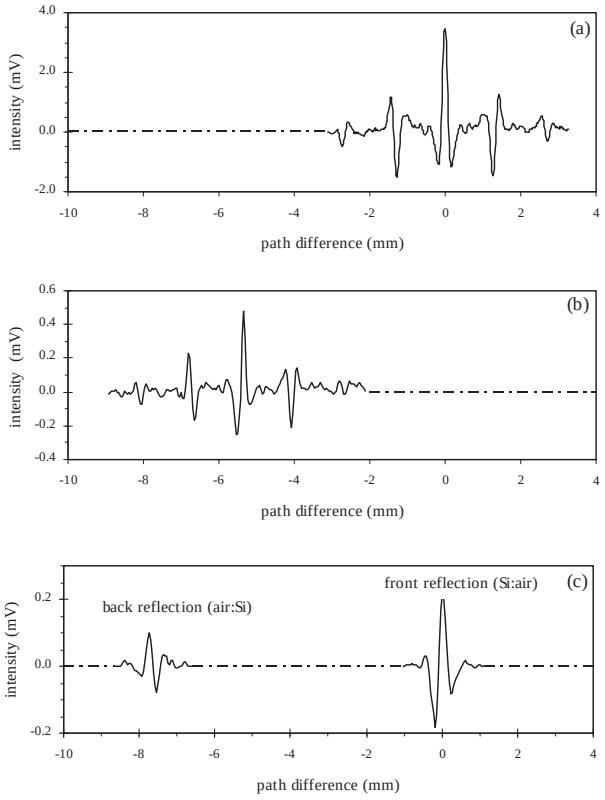

Fig.6. (a) radiation interferogram, (b) double-pass transmission iterferogram, and (c) reflection interfeogram.

Mesurements of silicon refractive index from transmission and reflection experiment had been conducted to demonstrate THz spectroscopy using our coherent THz transition radiation. Figure 6 shows interferograms obtained from the experiments. Figure 7 shows the measurement results compare to the results from [14, 15]. The measurements confirm that silicon has an almost constant real refractive index of about 3.42. THz spectroscopy experiments, especially that of highly absorbing substances using coherent THz transition radiation source, had been reported in [16].

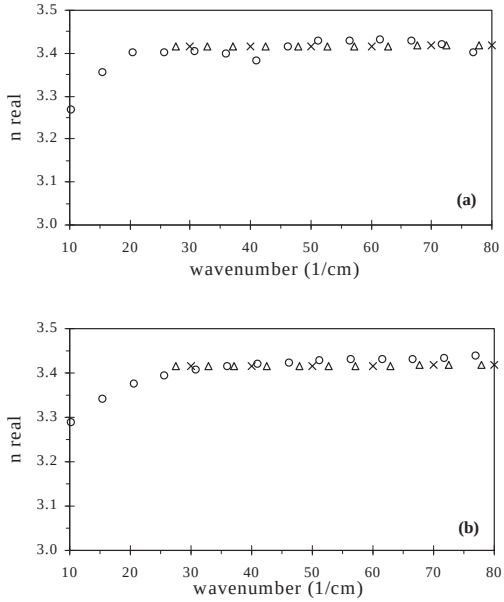

Fig.7. Experimental results for real refractive index of silicon (o : our measurement, Δ : from [14], x : from [15])

5. THz IMAGING EXPERIMENTS

The Schematic diagram of THz imaging system is shown in Figure 8. THz radiation from the source is focused on a sample and the sample is then scanned using an xy-translation stage controlled by a computer. The transmitted radiation is detected by a room-temperature pyroelectric detector. Computer program is employed to calculate and analyze THz intensity at difference points on the sample for THz images construction. Figure 9 shows an example of THz imaging obtained from the opening pattern on Al-foil concealed in an envelope.

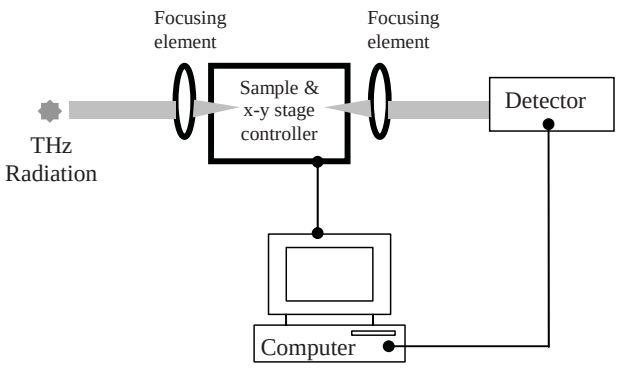

Fig 8. Schematic diagram of THz imaging system

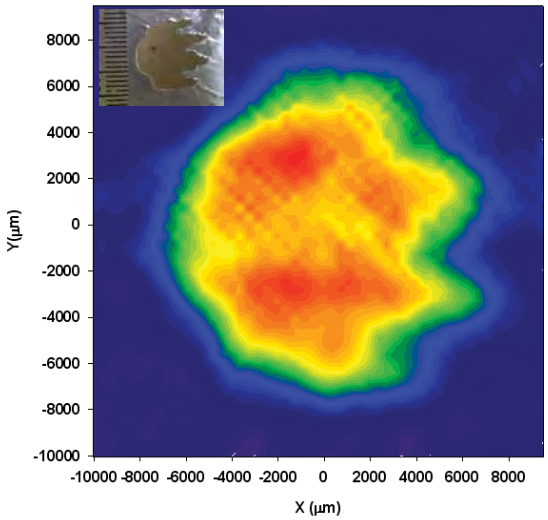

Fig 9. THz imaging of the opening pattern (shown in the inset) on Al-foil concealed in an envelope.

6. CONCLUSION

A system to produce femtosecond electron bunches and THz radiation has been developed at the Plasma and Beam Physics Research Facility, Chiang Mai University, Thailand. The system consists of an RF-gun with a thermionic cathode, an alpha magnet as a magnetic bunch compressor, and a linear accelerator as a post acceleration section. After acceleration, the compressed electron bunches are used to generated coherent transition radiation by passing through a thin Al-foil. The radiation spectrum covers much of the far-infrared or THz spectral range and high intensity radiation from mm-waves up to 80 cm^{-1} (2.4 THz) can be detected with a room temperature detector. Reflection and transmission spectroscopy as well as THz imaging experiments were conducted as an examples of THz applications using our radiation source. It is possible to extend the spectral range further by using shorter electron bunches.

ACKNOWLEDGMENT

Authors are grateful to Prof. Helmut Wiedemann for his comment and suggestion. We would like to acknowledge the support from the National Research Council of Thailand (NRCT), the Thailand Research Fund (TRF), the (Thailand) Commission on Higher Education (CHE) and the graduate school of Chiang Mai University.

REFERENCES

[1] Ihee, H. *et al.* (2001) Direct Imaging of Transient Molecular Structures with Ultrafast Diffraction. *Science* 291 : 458-462.

[2] Bauer, M. *et al.* (2001) Direct Observation of Surface Chemistry Using Ultrafast Soft-X-Ray Pulses. *Phy. ReV. Lett.* 87 : 025501.

[3] Reis, D. A. e*t al.* (2001) Probing Impulsive Strain Propagation with X-Ray Pulses. *Phy. ReV. Lett.* 86 : 3072.

[4] Thongbai, C. S. and Vilaithong, T. (2007) Coherent transition radiation from short electron bunches. *Nucl. Instr. and Meth.* 581(3): 874-881.

[5] Endo, I. e*t al.* (1995) Parametric x radiation from thick crystals. *Phy. Rev. E*. 51: 6305.

[6] Bonifacio, R.: Pellegrini, C.; and Narducci, L. M. (1984) Collective instabilities and high-gain regime in a free electron laser, *Opt. Commun.* 50 313.

[7] Lihn , H. C.; Kung, P.; Settakorn, C.; Bocek, D.; and Wiedemann, H. (1996) Measurement of subpicosecond electron pulses. *Phy. Rev. E*. 53: 6413.

[8] Rimjaem, S.; Farias, R.; Thongbai, C.; Vilaithong, T.; and Wiedemann, H. (2004) Femtosecond electron bunches from an RF-gun. *Nucl. Instr. and Meth.* 533: 258-269.

[9] Thongbai, C. *et al.* (2008) Femtosecond electron bunches, source and characterization. *Nucl. Instr.and Meth*. A 587:130-135.

[10] Nodvick, J. S. and Saxon, D. S. (1954) Suppression of coherent radiation by electrons in a synchrotron. *Phys. Rev.* 96: 180-184

[11] Settakorn, C. T. 2009. *Coherent THz Transition Radiation; Generation, Characterization, and Applications.* VDM Verlag & Co. KG.

[12] Bell, R. J. 1972. *Introductory Fourier Transform Spectroscopy*. London: Academic Press.

[13] Birch, J.R. and Parker, T.J. Dispersive fourier transform spectroscopy. In *Infrared and Millimeter Waves V.2: Instrumentation*, Button, K.J. Ed. NewYork: Academics Press.

[14] Randall, C, and Rawcliffe, R. (1967) Refractive indices of germanium, silicon, and fused quartz in the far-infrared. *Appl. Opt.* 6(11): 1889-1895.

[15] Smith, D. ; Loewenstein, E.; and Morgan, R. (1973) Optical constants of far-infrared materials. *Appl. Opt.* 12(2): 398-406.

[16] Woods, K. N., and Wiedemann, H. (2004) The relationship between dynamics and structure in the far infrared absorption spectrum of liquid water. *Chem. Phys. Lett.* 393: 159-165.

RECENT UPGRADE OF THE PITZ FACILITY*

J. W. Bähr[1], H. Al-Juboori, A. Donat, U. Gensch, H.-J. Grabosch, L. Hakobyan, M. Hänel, R. Heller, Y. Ivanisenko, L. Jachmann, M. A. Khojoyan, G. Klemz, W. Köhler, G. Koss, M. Krasilnikov, A. Kretzschmann, H. Leich, M. Mahgoub, J. Meißner, D. Melkumyan, M. Otevrel, M. Penno, B. Petrosyan, M. Pohl, S. Rimjaem, C. Rüger, M. Sachwitz, B. Schöneich, J. Schultze, A. Shapovalov, F. Stephan, M. Tanha, G. Trowitzsch, G. Vashchenko, L. V. Vu, T. Walther, †

A. Brinkmann, K. Flöttmann, W.Gerdau, S. Lederer, L.Lilje, F. Obier, D. Reschke, S. Schreiber, DESY, Hamburg, Germany,

J. Saisut, C. Thongbai, Chiang Mai University and Thailand Center of Excellence in Physics, Thailand

J.Knobloch, D. Richter, Helmholtz-Zentrum Berlin für Materialien und Energie GmbH; Berlin, Germany

P. Michelato, L. Monaco, C. Pagani, D. Sertore, INFN / LASA, Segrate MI, Italy

G. Asova, I. Bonev, L.Staykov, I. Tsakov, INRNE Sofia, Bulgaria

W. Sandner, I. Will, MBI Berlin, Germany

A.Naboka, V. Paramonov, RAS / INR Moscow, Russia

B. L. Militsyn, B. Muratori, STFC / DL / ASTeC, Daresbury, United Kingdom

M.Korostelev, The Cockroft Institute, Daresbury Laboratory,Warrington,United Kingdom

T. Vilaithong, Thailand Center of Excellence in Physics, Thailand

W. Ackermann, W. F. O. Müller, S. Schnepp,
T. Weiland, TEMF, TU Darmstadt, Darmstadt, Germany

I. Ullmann,Universitaet Erlangen, Erlangen, Germany

J. Rönsch-Schulenburg, J. Rossbach, Universität Hamburg, Hamburg, Germany

* Supported by : EU contract: IASFS RII-CT-2004-506008

[1] Corresponding author:J.Baehr: juergen.baehr@desy.de

Abstract

The Photo Injector Test facility at DESY, Zeuthen site (PITZ), is dedicated to develop and optimize high brightness electron sources for short wavelength Free-Electron Lasers (FELs) like FLASH and the European XFEL, both in Hamburg (Germany). Since October 2009 a major upgrade is ongoing with the goal to improve the accelerating components, the photocathode drive laser system and the beam diagnostics as well. The essential new feature in the running will be an in-vacuum 10 MW RF directional coupler to be used for the RF monitoring and control. In this context a significant improvement of the RF stability is expected. RF pulses of 800 microseconds with 10 Hz repetition rate will be used. The most important upgrade of the diagnostics system will be the implementation of a phase space tomography module (PST) consisting of three FODO cells each surrounded by two screen stations. The goal is an improved measurement of the transverse phase space at different charge levels. The upgraded facility will be described.

INTRODUCTION

High brightness electron sources for short wavelength Free Electron Lasers (FEL) are being developed and optimized at the Photo Injector Test facility at DESY, Zeuthen site [1]. In the recent running break major components are being replaced or newly installed. The major items of this upgrade are the exchange of the electron gun, the exchange of the booster cavity and the installation of a phase space tomography module. The schematic of the upgraded facility is shown in Fig.1. A gun of the same type as the previous one is installed now in PITZ. The conditioning has started and the gun will be characterized in 2010. Currently, a peak RF power of 2.7 MW was reached during gun conditioning.

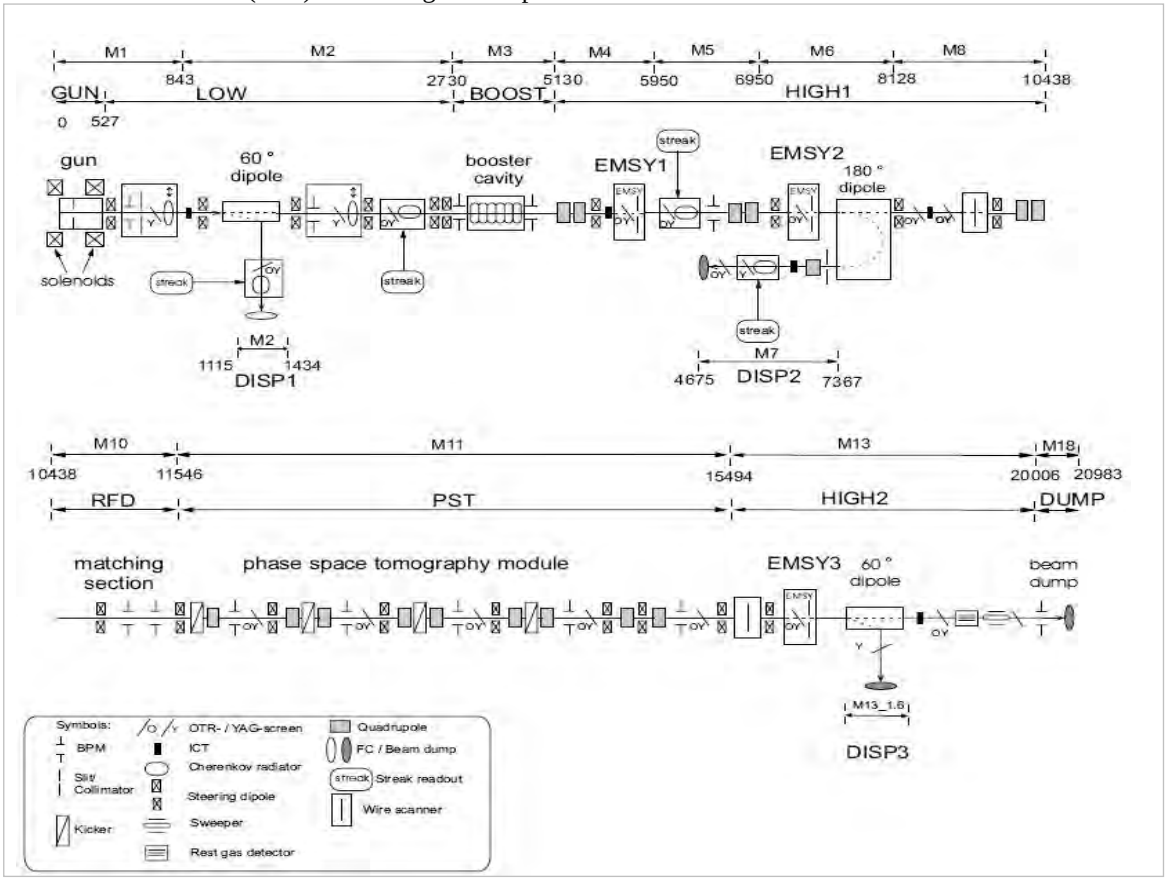

Fig.1 Schematic of the upgraded PITZ facility

NEW 10 MW IN-VACUUM RF COUPLER

In the previous PITZ setup [2] signals from 2 directional couplers (5 MW each) have been used to control the RF power in the gun cavity. This setup implies ceramic vacuum windows after each coupler and a T-combiner to mix both waves and feed them into the gun cavity. A possible cross-talk of both directional couplers and uncertainty in the gun cavity response complicated significantly the operation of the LLRF system. The feed-back loop became extremely complex, non-reliable and could not be used for the beam measurements. This resulted in large gun phase fluctuations since only the RF feed-forward has been applied [3].

To improve the control on the RF in the new PITZ gun (gun prototype 4.1) a newly developed 10-MW in-vacuum directional coupler has been installed [4] after the T-combiner. The main advantage of its usage compared to the previous RF feeding scheme is a direct control on the combined forward wave and on the wave reflected from the gun cavity. First signals from antennas of the 10-MW in-vacuum directional coupler are shown in Fig.2, where the amplitude (power) and the phase of gun forward and reflected pulses are presented. After the upgrade of the RF system, the optimization of the phase shifter position located in one of two arms of the 10-MW klystron became more straightforward. It is reduced to the maximization of the gun forward power amplitude while the gun is being kept close to the resonance temperature. Preliminary studies on the possibility of feedback loop implementation have been done at a power level of ~0.3 MW and different gun resonance temperatures. The feed-back applied at these conditions resulted in an improvement of the gun phase stability by a factor of about 3. Preliminary measurements of the RF phase jitter of the vector sum with a closed feed back loop yielded the RMS value of ~0.2 deg. More detailed studies on LLRF

regulation are foreseen when the nominal RF power in the gun cavity (~7 MW) will be achieved.

THE NEW BOOSTER CAVITY

A new booster cavity based on a Cut Disk Structure (CDS) was developed and will be mounted at PITZ in spring 2010 [5]. The booster cavity will have an improved cooling system. It will be able to accelerate electrons above 20 MeV/c and will be suitable for long bunch trains. The booster cavity is under preparation to be inserted in the beam line of PITZ.

The photo injector arrangement is a full metal system and operates in the ultra high vacuum range. The residual gas should be free of hydrocarbons and the contribution to the total pressure of oxygen or oxygen containing gases should be negligible. Otherwise, one would get an oxidation or

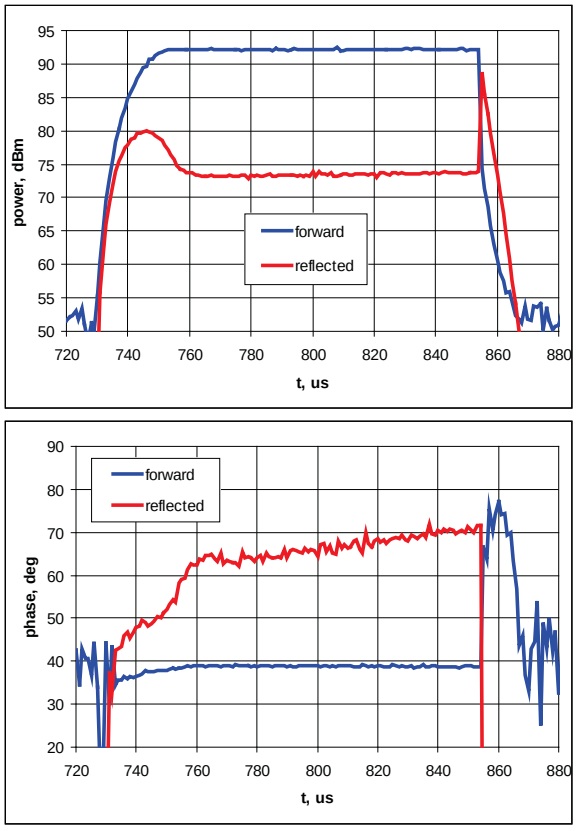

Fig.2. Signals from 10-MW in-vacuum coupler - forward and reflected RF pulses. RF power in dBm (upper Fig.) and the phase along the RF pulse (below) have been measured at the power level of ~1.6 MW for the pulse length of 100 µs. No feed-back has been used for this measurement.

poisoning of the photo cathode and consequently reducing its life time. Presently, a vacuum conditioning of the booster is running to reduce the out-gassing rate. It is done by baking at a separated test arrangement. After that, the booster will be installed at PITZ whereby the pumping will start using turbo molecular pumps. Later an ion getter pump arrangement supplemented by titanium sublimation pumps will allow stable RF conditions.

THE PHASE SPACE TOMOGRAPHY MODULE

The module consists of three FODO cells, whereby pairs are separated by a screen station. The number of screens, namely four, has been chosen in order to obey the requirement for as much as possible projections used for the reconstruction. The tomography theory proposes equidistant angular steps between each two projections, wherefrom the phase advance between two adjacent screens is 45 degrees. It has been shown in [5] that such a phase advance delivers the smallest emittance measurement discrepancy using a multi-screen method with four screens. An upstream cell with identical geometry can be used as well to increase the number of projections.

The desired systematic uncertainty of the measured emittance is below 10 %. This corresponds to a relative deviation of the measured spot size on a screen of 10 %. As the geometry of the module is rather compact with short but strong focusing quadrupole magnets, the 10 % deviation of the spot size sets tight requirements on the mechanical alignment of the components. Those are given in the table 1 below:

Table 1: Components mounting tolerances in rms values.

Misalignment	Value	Units
Longitudinal quadrupole off-set	0.1	µm
Quadrupole roll angle	10	mrad
Quadrupole pitch angle	20	mrad
Quadrupole yaw angle	20	mrad
Longitudinal screen off-set	0.1	µm
Screen rotation around x- and y- axes	10	mrad

The positioning of the screen stations and quadrupoles is done by means of a laser tracker and a hexapod, see Fig.3: Five of those screen stations and eleven quadrupoles have to be installed in the module.

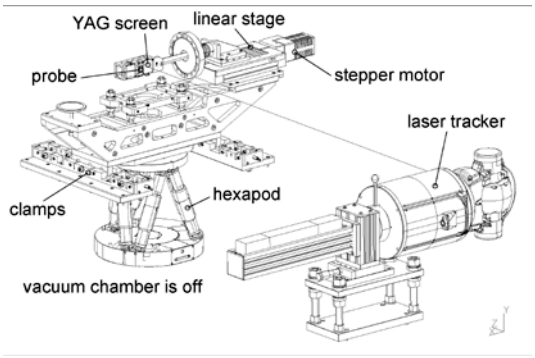

Fig. 3: The alignment of a screen station of the tomography section by means of a laser tracker and a hexapod.

IONIZATION PROFILE MONITOR

An Ionization Profile Monitor (IPM) [7] will be inserted in the rear part of the beam line, in the first step only for one projection of the beam profile. One of the advantages of such a device is the possibility to work at high bunch charge and long bunch trains.

The IPM consists of an electrode, called the "Repeller plate", and a high spatial resolution detector (MCP). Both components have a definite potential. Additional electrodes are installed to provide an uniform electrical field between the Repeller plate and the MCP, see Fig 4. The residual gas inside the beam tube is ionized by the electron beam. The produced ions are accelerated in a homogeneous electrical field toward the MCP. After amplification inside the MCP, electrons hit a phosphor screen. A CCD camera records the phosphorescence to a computer for further evaluation.

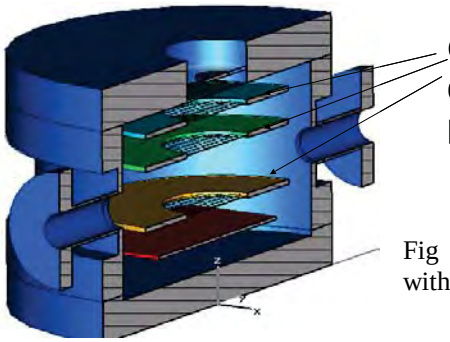

Fig 4: IPM set up with grids

LASER SYSTEM

For generation of flat-top pulses an Yb:YAG laser system is used. This laser generates long pulse trains that contain up to 800 individual "micropulses" in the train. A flat-top shape of the individual pulses of the train is accomplished by means of a multicrystal birefringent filter [8]. In this filter, the flat-top pulse shape is obtained by stacking several replicas of the input pulse, where the number of replicas is by one larger than the number of crystals used. The temperature of the individual crystals is precisely controlled in such a manner that the light field of the neighbouring replicas of the input pulse interfere constructively. High-quality flat-top pulses with rising and falling edges of approx. 2 ps duration are generated this way. In contrast to other arrangements [9,10], the produced pulses exhibit a precisely linear polarisation, which allows to further amplify them in a diode-pumped Yb:YAG amplifier chain and convert them to the fourth harmonics (λ = 257.5 nm) while maintaining the flat-top shape.

The duration of the pulses emerging from the bi-refringent filter depends on the effective number of crystals in it. Changing the pulse shape is accomplished by appropriately rotating the birefringent crystals in the shaper. Figure 5 shows the flat-top pulses of approximately 23.4 ps duration (FWHM) generated by using thirteen 2.7 mm thick YVO_4 crystals in the shaper following further amplification in Yb:YAG amplifier stages and after conversion to the fourth harmonics. An innovation of the laser beam line is the integration of a gated intensified CCD camera. A fraction of the UV laser beam propagating from the laser to the photo injector is split off and directed onto a fast intensified CCD camera.

The shape of the UV pulse was measured by cross-correlating it with a second femtosecond infrared pulse.

Alike the photocathode, this camera is also located at an image position of the aperture that is used for generating the spatial flat-top profile. By selecting an exposure time of approximately 500 ns as well as an appropriate trigger it is possible to measure the spatial intensity distribution for each laser bunch within the pulse train. These images will be used to extract position, size and intensity of the UV laser beam as well as their variations within the pulse train. A first example of such a measurement is shown in Fig. 6.

The air conditioning in the laser room was improved with the goal to minimize oscillations of the temperature. The maximum temperature oscillation is now +/- 0.1 degree as specified.

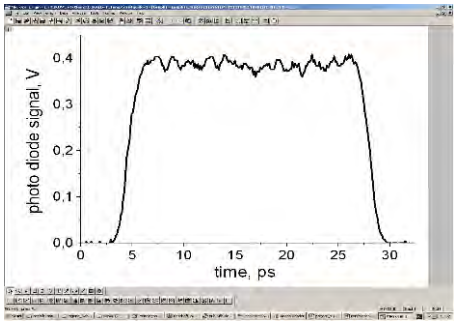

Fig. 5: Flat-top UV pulse of 23 ps duration produced by the photo injector drive laser at PITZ.

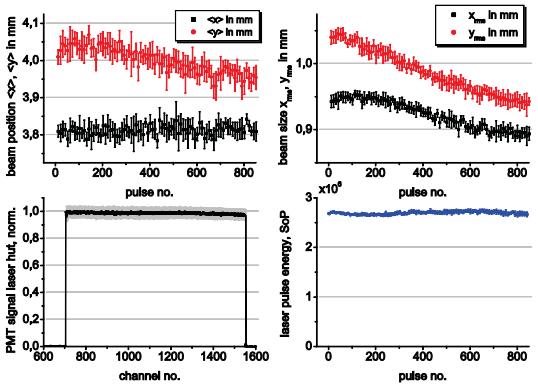

Fig. 6: Variation of beam position (upper left), beam size (upper right) and laser pulse energy (lower right) during a train of 850 laser bunches derived from the signal of the gated, intensified CCD camera. For comparison, the UV pulse energy as observed using a photomultiplier (PMT) on the laser table is also depicted (lower left).

THE BEAM INHIBIT SYSTEM (BIS)

The BIS is an independent hardware, which protects parts of the system from destruction due to false operation. The logic is processed by a Siemens SPS S7-300 [10[.
The communication with the control system is realized via Ethernet UDP protocol. The BIS detects the state of magnets, vacuum valves, screens, cathode, shutters, Emittance Measurement Systems (EMSYs) and Faraday cups to define maximum pulse length for the klystron, charge and numbers of laser pulse. The operating modes can be predefined or are self-detected from the state of the facility.

TV SYSTEM – CAMERA TESTS

The following cameras were tested in the lab:

- JAI (CCD): TM-2040, BM-141 [12].
- Prosilica (CCD): GC-13050, GC-1380, GE-1380 [13]
- PhotonFocus (CMOS): D1312-80, D1312-40 [14]

All cameras have a GigE interface. The Prosilica GC-1350 was measured each time as a reference camera. The main criteria the comparison are sensitivity of the camera, shutter speed, signal to noise ratio and radiation hardness.
The camera measurements procedure can be divided in two parts:

- taking frames for different gain levels with closed cap, so called dark frame
- taking frames for different gain levels from the object which was illuminated by a lamp.

The first measurement gives a noise distribution in the camera itself.
Also some other important features like gain range, possibility to adjust the black level, shutter control were studied. All cameras except PhotonFocus series have a possibility to control the gain at range approximately up to 24 dB. All cameras except PhotonFocus series and JAI TM-2040 have good noise distribution, mean and rms values. Unfortunately all Prosilica series have automatic black level control and look up tables made in such a way that they cut in a part of the signal. All the cameras have a good controllable shutter speed with a minimum shutter time of about 10 us. A radiation hardness test is foreseen in the near future. The summary plots are shown in the figures 7 and 8. To summarize we can say that the JAI BM-141 is the best choice for our measurements.

CONCLUSION

A major upgrade of the PITZ facility is ongoing. The electron gun is exchanged and under commissioning. A new accelerating booster cavity is under preparation to Be installed in the beam line. The upgrade of the beam diagnostics is ongoing mainly by installation of the phase space tomography module. The complete restart is assumed in summer 2010.

REFERENCES

[1] F.Stephan et al., Photo Injector Test Facility and Construction at DESY, FEL 2000, Durham.
[2] F.Stephan et al., Detailed characterization of electron sources at PITZ, yielding first demonstration of European X-ray Free-Electron Laser beam quality, Phys.Rev. Special Topics-Acc. And beams, 13, 020704, (2010)
[3] F.Stephan, M.Krasilnikov, "High Brightness Beam Measurements at PITZ", talk at Workshop on the physics and applications of high brightness electron beams, Maui, Hawaii,16-19.11.2009, http: //pbpl.physics.ucla.edu /HBEB/.
[4] MEGA Industries, H28 Sanford Drive, Gorham, ME 04038
[5] V.V. Paramonov et al., Design Parameters of the Normal Conducting Booster cavity for the PITZ-2 Test Stand.
[6] G. Asova et al., Phase space tomography diagnostics at the PITZ facility, Proceedings ICAP 2006, Chamonix, France

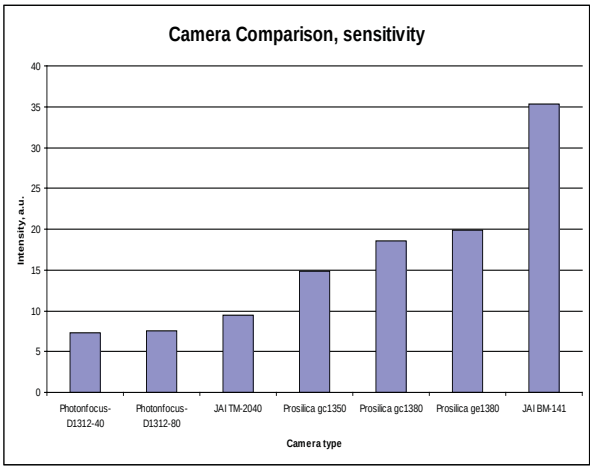

Fig. 7: CCD camera comparison: Sensitivity in arbitrary units

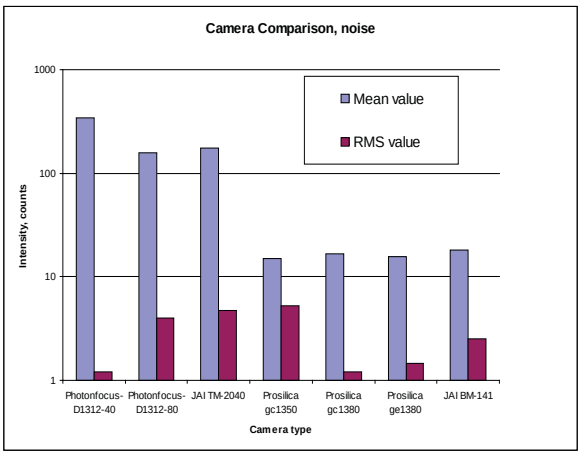

Fig. 8: CCD camera comparison: noise in counts

[7] A. Hofmann et. al., EPAC2008, Genoa
[8] I.Will, G.Klemz, Generation of flat-top picosecond pulses by coherent pulse stacking in a multicrystal birefringent filter, Opt. Express 16, 14922 (2008).
[9] S. Zhou, et al., Efficient temporal shaping of ultrashort pulses with birefringent crystals, Appl. Opt. 46, 8488-8492 (2007).
[10] I. Bazarov et al., Efficient temporal shaping of electron distributions for high-brightness photoemission electron guns, Physical Review ST – Accel. Beams 11, 040702 (2008).
[10] http://www.automation.sicmens.com
[12] http://www.jai.com/
[13] http://www.prosilica.com/
[14] http://www.photonfocus.com/

LOW-CHARGE SIMULATIONS FOR PHASE SPACE TOMOGRAPHY DIAGNOSTICS AT THE PITZ FACILITY

J. Saisut*†, G. Asova‡, M. Krasilnikov, S. Rimjaem, F. Stephan, DESY, 15738 Zeuthen, Germany
C. Thongbai, CMU, Chiang Mai 50200, and ThEP Center, Bangkok 10400,Thailand

Abstract

The Photo Injector Test Facility at DESY, Zeuthen site (PITZ) aims to optimize high brightness electron sources for linac-based FELs. Since the performance of an FEL strongly depends on the transverse electron beam emittance, the electron source is studied in details at PITZ by measuring the emittance with the help of the Emittance Measurement SYstems (EMSY). The EMSY employs the slit scan technique which is optimized for 1 nC bunch charge and, therefore, it might not be an optimal choice for low charge bunches. To extend the ability of the facility for transverse phase space measurements, a module for phase-space tomography diagnostics and its matching section are installed in 2010. The basic components of the module are four screens separated by FODO cells. It is designed for operation with high charge and low energy beams. This work studies the performance of the tomography module when it is operated with low charge beams. The influence of different beam parameters is evaluated according to the requirement to match the envelope to the optics of the FODO lattice. Simulation results and phase space reconstructions are presented.

INTRODUCTION

PTTZ aims to optimize high brightness electron sources for linac-based FELs like FLASH and the future European XFEL. Since the performance of an FEL strongly depends on the transverse electron beam emittance, the last is a major point for the photo-injector optimization process done at PITZ. In the last run period only the single slit scan technique using an Emittance Measurement System - EMSY, has been used [1, 2]. EMSY consists of horizontal and vertical actuators with 10 and 50 μm slits masks and a YAG/OTR screen for beam size measurement. A new module for phase space tomographic diagnostics and its matching section, both undergoing commissioning at the moment, extends the ability of the facility to characterize the transverse phase space. At the same time the old TESLA booster cavity was replaced by a CDS booster which is expected to deliver beam momentum up to 30 MeV/c. Figure 1 shows the new schematics of the PITZ beamline - PITZ 1.8. The tomography module, situated in the second part of the beamline, consists of three FODO cells and four diagnostic screens as shown in Fig. 1.

* jatuporn.saisut@desy.de
† On leave CMU, Chiang Mai, Thailand
‡ On leave INRNE, Sofia, Bulgaria

More details about the design of tomography module can be found in [3, 4]. The phase advance between the FODO cells is 45° which is expected to deliver the smallest emittance measurement error using the four screen method as shown in [4]. The FODO cells are only 0.76 m and therefore the design Twiss parameters for a periodic solution to be achieved are rather stringent - $\beta_{x,y} = 0.999\,\mathrm{m}$ and $\alpha_{x,y} = \pm 1.125$. In order to deliver the expected Twiss parameters up to nine quadrupole magnets upstream the tomography module can be used. In this paper simulations with 100 pC bunch charge for tomography diagnostics are presented. In the first part the emittance optimization at EMSY1, which is normally used for emittance measurements, using ASTRA [5] is presented and then matching solutions are shown. Finally, phase space reconstructions for some of the matching cases are demonstrated.

EMITTANCE OPTIMIZATION

To study the performance of the tomography module when it is operated with low charge bunches, simulations are performed using ASTRA. The beam evolution is simulated from the cathode to the EMSY1 station. The initial conditions for the simulations are shown in Table 1. The laser spot size is chosen as a compromise between small emittance at EMSY1 and bigger spot size considered as suffering less from space-charge effects. The criteria for the simulations is to optimize the emittance at the EMSY1 station for a momentum range from 15 MeV/c to 32 MeV/c. The focusing solenoid magnetic field and gun phase are optimized. Simulation results predict that the maximum emittance at EMSY1 for this momentum range is 0.185 mm mrad.

Table 1: The Initial Parameters of the Simulations

	parameter	value	units
Laser	pulse length	20	ps
	rise/fall time	2	ps
	kinetic energy	0.55	eV
	rms laser spot size	0.150	mm
	bunch charge	100	pC
RF-gun	gradient at the cathode	60	MV/m
Booster	phase	on-crest	
Tracking particles	macro particles	200000	particles

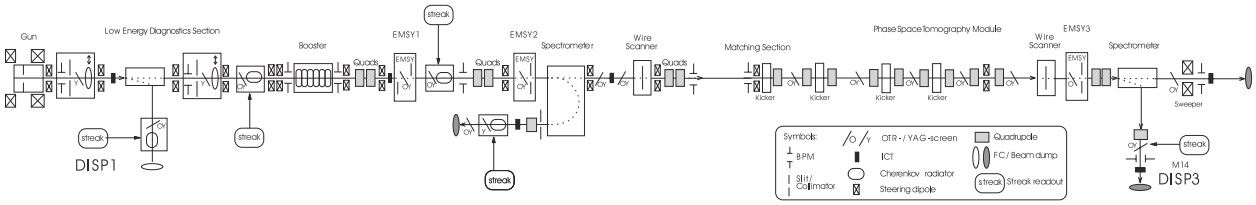

Figure 1: The new layout of PITZ beamline (PITZ 1.8).

Figure 2 shows the evolution of the normalized emittance and rms beam size along the beamline until 10 m for a beam momentum of 20.6 MeV/c. The normalized projected emittance and rms beam size on EMSY1 are correspondingly 0.183 mm mrad and 0.172 mm. Figure 3 shows the obtained slice emittance and slice β-function, at the same location. Both show alignment of the longitudinal slices and expected easier matching.

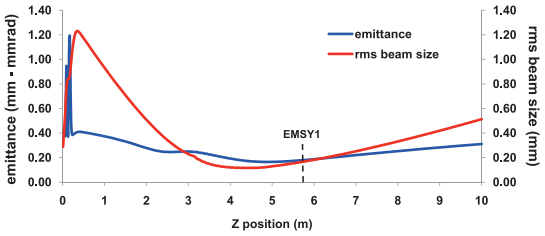

Figure 2: Simulated rms beam size and normalized emittance evaluated along the beam line for 100 pC bunch charge and 20.6 MeV/c beam momentum. The position of EMSY 1 is shown at 5.74 m downstream the cathode.

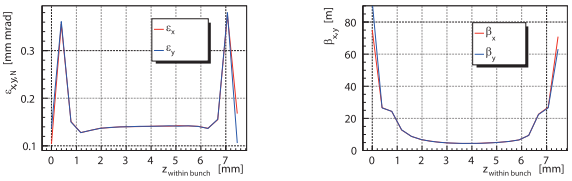

Figure 3: Slice emittance (left) and slice beta function (right) for a beam momentum of 20.6 MeV/c at EMSY1.

MATCHING SOLUTION

At the beginning of the next run period the new booster cavity will accelerate the beam momentum only up to 24 MeV/c, therefore the matching solutions were achieved for momenta from 15 to 25 MeV/c. Matching into the tomography section has been performed using the V-code [6]. The V-code is a beam dynamics simulation tool which is able to calculate the statistical moments of a bunch distribution as an input and calculate trajectories of those moments through electro-magnetic fields. The matching starts from EMSY1 to the first screen of the tomography module and uses seven quadrupoles. In practice it is desirable to use as few magnets as possible but according to simulations the four Twiss parameters cannot be matched simultaneously having a limited range of quadrupole gradients. In the simulations, the gradients of the last two quadrupoles in the matching section are kept constant and have values close to the magnets inside the module in order to make the first periodic cross in front of the first screen. This is needed because those two magnets have stronger influence on the Twiss α parameters which are harder to adjust in the presence of space charge and short quadrupoles. The other five quadrupoles are varied to match and minimize the deviation of the Twiss parameters on the first screen. The solutions from the V-code are plugged into ASTRA and tracked from EMSY1 until the end of the module. In this tracking 3D space charge and the measured quadrupole fields are included. The solutions which deliver β-mismatch $\Delta\beta$[1], both for the horizontal and vertical planes, less than 50% are evaluated. At the moment the best solution is the one that can achieve a β-mismatch of 24% in the horizontal and 17% in the vertical plane for a beam momentum of 20.6 MeV/c. The β-functions for the best solution from EMSY1 until the end of the tomography module is shown in Fig. 4(a).

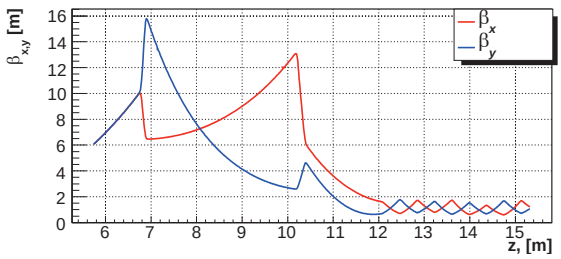

(a) β-functions from EMSY1 up to the end of the tomography module.

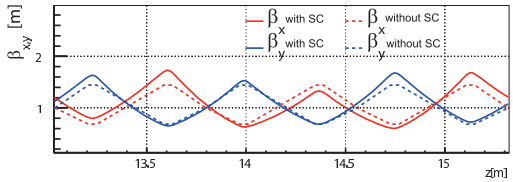

(b) Comparison of the β-functions with- and without space charge SC effect inside the tomography module.

Figure 4: Twiss β -functions for beam momentum of 20.6 MeV/c.

[1] $\Delta\beta\,[\%] = 100 \cdot \frac{\beta_{design} - \beta_{measured}}{\beta_{design}}$

Figure 4(b) shows a comparison of the β-functions along the FODO lattice for the case with- and without space charge effects. The matching is not as easy as expected for 100 pC bunch charge because these simulations for optimized emittance are in a space charge dominated regime as shown in Fig. 5. The space charge over emittance ratio

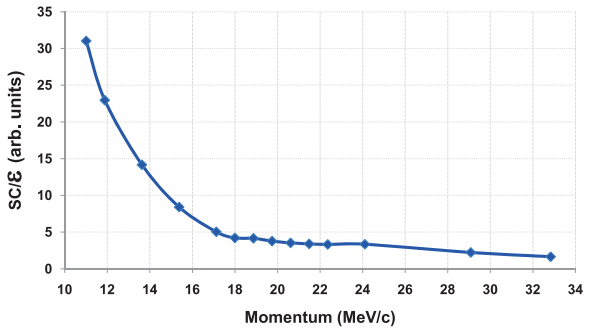

Figure 5: Space charge over emittance ratio as a function of beam momentum.

as defined in [7] and shown in Eq. (1) is higher than 1 for the whole range of momenta which corresponds to space charge dominated regime.

$$\rho = \frac{I\sigma^3}{2\beta\gamma I_0 \varepsilon_N^2}, \qquad (1)$$

where I is beam peak current, I_0 = 17 kA is the Alfven current, σ - the rms beam size, and ε_N is the normalized emittance.

PHASE SPACE RECONSTRUCTION

The transverse phase space of the electron beam on the first screen can be reconstructed from projections of the (x, y) distributions on the four screens of the tomography section using the **M**aximum **ENT**ropy-MENT [8] algorithm. More details about the phase space reconstruction can be found in [4]. Figure 6 shows results of the $(\mathrm{y}, \mathrm{y}')$ reconstruction using a perfectly matched solution for the case without space charge forces.

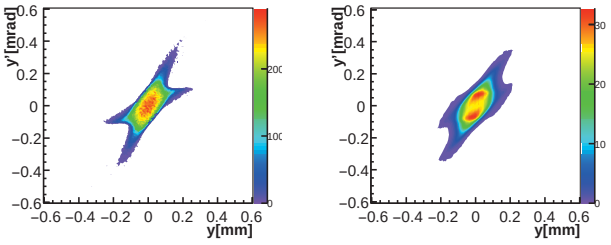

(a) Original distribution. (b) Reconstruction result.

Figure 6: Original and reconstructed vertical phase space of a perfectly matched case for a beam momentum of 20.6 MeV/c.

Figure 7 shows the result from a solution which has a β-mismatch of 17% in the vertical plane. Visually it can be concluded that in the second case the spot size is bigger and the reconstruction delivers higher density in the tails then there is. Table 2 summarises parameters of the original and reconstructed phase spaces for both cases.

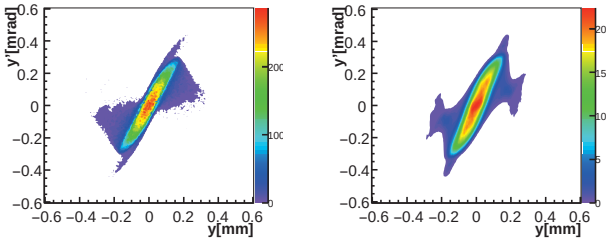

(a) Original distribution. (b) Reconstruction result.

Figure 7: Original and reconstructed vertical phase space for beam momentum of 20.6 MeV/c with 17% mismatch.

Table 2: Summarized Parameters of the Original and Reconstructed Phase Spaces (subscripts case 1, 2 referred to a perfectly matched and 17% mismatched case accordingly).

Parameters	Original	Reconstruction	Δ[%]
$\sigma_{y,1}$	0.068	0.069	0.67
$\sigma_{yy',1}$	0.051	0.052	1.00
$\varepsilon_{y,N,1}$	0.182	0.181	0.89
$\sigma_{y,2}$	0.092	0.080	4.97
$\sigma_{yy',2}$	0.0102	0.010	1.45
$\varepsilon_{y,N,2}$	0.296	0.355	20.0

CONCLUSIONS

The simulation results show that it is not easy to match a 100 pC bunch charge optimized for minimum emittance since the beam is still in the space charge dominated regime. It is possible to achieve good solutions but it is cumbersome to do fine quadrupole gradient adjustments. Higher energy is another possibility to overcome this problem. The work continues to find a good matching with this setup. To decrease the space charge effects others parameters will be adjusted - for example laser spot size and the case which emittance is not fully optimize will be matched. Simulations with even lower charges are considered.

ACKNOWLEDGMENTS

Authors would like to acknowledge the support from the (Thailand) Commission on Higher Education and the Thailand Research Fund.

REFERENCES

[1] L. Staykov, “Characterization of the transverse phase space at the Photo-Injector Test Facility DESY, Zeuthen cite”, PhD thesis. Universität Hamburg, 2008.

[2] F. Stephan, C. H. Boulware, M. Krasilnikov, J. Bähr et al., “Detailed characterization of electron source at PITZ yielding first demonstration of European X-ray Free-Electron Laser beam quality”, PRST-AB 13, 020704(2010).

[3] D.J. Holder et al.,“A phase space tomography diagnostic for PITZ”, proceedings of EPAC 2006, Edinburgh, UK.

[4] G. Asova et al.,“Phase space tomography diagnostics at the PITZ facility”, proceedings of ICAP 2006, Chamonix, France.

[5] K. Flöttmann, ASTRA, http://www.desy.de/˜mpyflo/

[6] S. Franke et al., V-code, Institut für Theorie Elektromagnetischer Felder, TU Darmstadt, Germany.

[7] M. Ferrario et al., “Recent advances and novel ideas for high brightness electron beam production based on photo-injectors”, INFN Rep. LNF-03/06 (P), May 2003.

[8] J.J. Scheins, “Tomographic reconstruction of transverse and longitudinal phase space distribution using maximum entropy algorithm”, TESLA Report 2004-08.

THz Radiation Based on Femtosecond Electron Bunches and THz Imaging

J. Saisut [a,c] , K. Kusoljariyakul [a,c] , N. Kangrang [c], P. Wichaisirimongkol [b,c],
C. Tengsirivattana [c] , P. Thamboon [b,c], M.W. Rhodes [b,c] and C. Thongbai [a,c]
[a] Department of Physics and Materials Science, Chiang Mai University, Chiang Mai 50200, Thailand
[b] STRI, Chiang Mai University, Chiang Mai 50200, Thailand
[c] ThEP Center, Commission on Higher Education, Bangkok 10400, Thailand

Abstract—**The THz radiation from femtosecond electron bunches is focused on a sample which will be scanned using an xy-translation stage. The transmission intensity at different points of the sample are detected to construct a THz image. THz images of some samples were demonstrated using the THz imaging system.**

I. Introduction and Background

THz radiation is electromagnetic wave having wavelengths of 1000μm to 100 μm (300 GHz - 3 THz) and lies in a gap between Microwave and Infrared. Over the past 20 years, this gap has been an unexplored region but nowadays sources and applications of THz radiation have rapidly developed [1-4]. One of its major applications is THz imaging, especially for noninvasive or nondestructive inspection. Applications of THz imaging which are widely developed are, for example, detections of weapons, explosives and drugs in packaging materials [5-8] as well as noninvasive inspection of defect in integrated circuits (IC) [9]. THz imaging has been investigated for cancer diagnostic because the radiation is highly sensitive to water content [10] and, for the same reason, it can be applied for quality control of agricultural products [11]. These examples show that THz imaging can becomes a powerful tool for defense, science, industry, agriculture, medical, and pharmaceutical applications.

Intense THz radiation can be generated in form of coherent transition radiation by using short electron bunches which are available at the Plasma and Beam Physics Research Facility (PBP), Department of Physics and Materials Science, Faculty of Science, Chiang Mai University. This THz radiation is used as a source of the THz imaging system

II. Generation of THz Radiation

A THz facility based on femtosecond electron bunches has been established at the Plasma and Beam Physics Research Facility (PBP), Chiang Mai University. Femtosecond electron bunches are generated from a system consisting of an RF-gun with a thermionic cathode, an alpha-magnet as a magnetic bunch compressor and a linear accelerator as a post acceleration section. These short electron pulses can be used to produce high intensity THz radiation in the form of coherent transition radiation by placing an aluminum foil (Al-foil) in the electron path, representing a transition between vacuum and conductor [12]. The available THz radiation covers from 5 cm^{-1} to around 80 cm^{-1} wavenumber which corresponded to frequency range from 0.3 THz to 2.4 THz.

III. THz Imaging System

Schematic diagram of a THz imaging system (transmission measurement) at the Plasma and Beam Physics Research Facility (PBP), Chiang Mai University is illustrated in Fig. 1 for transmission measurement. THz radiation is focused on a sample which will be scanned using an xy- translation stage controlled by a computer. The transmission intensity (I_T) will be detected by a room-temperature pyroelectric detector. Computer program will be employed to calculate and analyze intensity at difference points on the sample for THz image construction.

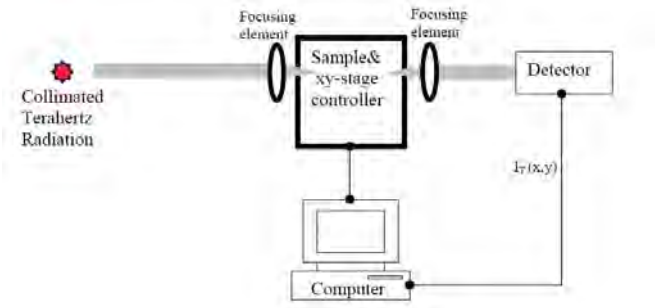

Fig. 1 Schematic diagram of the THz imaging system at Chiang Mai University

IV. Results

THz radiation can penetrate into non-polar dielectric materials such as paper, plastic and textile. The radiation is blocked by metal and is absorbed by water content.

By using a copper cone as a focusing element, the THz image of holes on Al-foil [Fig. 2(a)] placed in an envelope is shown in Fig. 2(b). Positions and spot sizes of the patterns from the THz image correspond well to those of the Al-foil sample. Using a Tsurupica THz lens [13] as a focusing element, Fig. 3 (a) and (b) show a water drop sample and its THz image. Low intensity area on the THz image displays feature of the drop which absorb THz radiation. The resolution of THz images can be improved by using a copper mesh [14] shown in Fig. 4(a) as a high pass THz filter. The copper mesh filter is placed in front of the first focusing element in the imaging system. A THz image of a cut pattern on Al-foil [Fig. 4(b)] obtained with filter is shown in Fig. 4(d) which resolves finer structure the pattern.

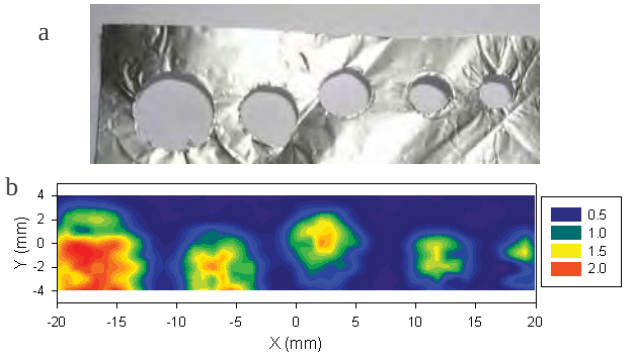

Fig. 2 (a) Holes on Al-foil and (b) THz image of holes.

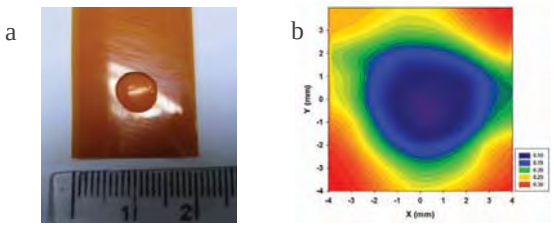

Fig. 3 (a) Water drop sample and (b) its THz image.

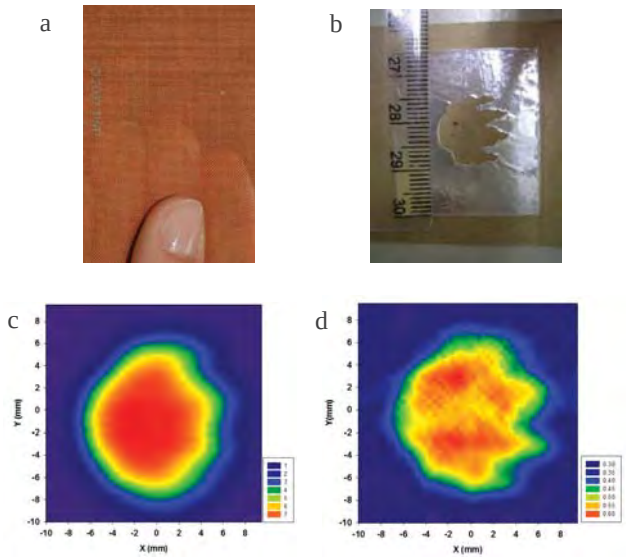

Fig. 4 (a) Copper mesh filter (b) Cut pattern on Al-foil and THz image (c) without and (d) with copper mesh filter.

V. Conclusions

A THz imaging system based on femtosecond electron bunches was successfully setup and tested at the Plasma and Beam Physics Research Facility (PBP), Chiang Mai University. The system can construct THz images of Al-foil patterns concealed in an envelope and water content samples. The image resolution can be improved by using a copper mesh as THz filters. Image processing techniques can be applied to further improve image resolution.

Acknowledgments

Authors would like to acknowledge the support from the National Research Council of Thailand, the Thailand Research Fund, the (Thailand) Commission on Higher Education, the Thailand Center of Excellence in Physics and Chiang Mai University.

References

[1] P. H. Siegel, "Terahertz Technology", *IEEE Trans. Microwave. Theory & Tech*., vol.55, pp. 910-928 ,2002.

[2] B. Ferguson and X.C. Zhang, "Materials for terahertz science and technology", *Nature materials*, vol 1, pp. 26-33, 2002.

[3] G.P. Gallerano *et al*., "Overview of terahertz radiation sources", *in the 2004 FEL conference*, 2002, pp. 216-221.

[4] M. Tonouchi, "Cutting-edge terahertz technology", *Nature photonics*, vol. 1, pp 97-105, 2007.

[5] J. F. Federici *et al*., "THz imaging and sensing for security applications—explosives, weapons and drugs," *Semicond. Sci. Technol.*, vol. 20, pp. S266-S280, 2005.

[6] K. Kawase *et al*., "Non-destructive terahertz imaging of illicit drugs using spectral finger prints," *Opt. Express*, vol.11, pp. 2549-2554 ,2003.

[7] M. Lu *et al*., "Detection and Identification of illicit drug using terahertz imaging," J. Appl. Phys., vol. 100, pp. 103104-103106, 2006.

[8] Y. C. Shen *et al*.,"Detection and identification of explosives using terahertz pulsed spectroscopic imaging," *Appl. Phys. Lett.*, vol. 86, issue 24, pp. 241116, 2005.

[9] M. Yamashita, K. Kawase, and C. Otani, "Imaging of Large-scale integrated circuits using laser terahertz emission microscopy," Opt. Express, vol. 13, issue 1, pp. 115-120, 2005.

[10] R. M. Woodward *et al*., "Terahertz pulse imaging in reflection geometry of human skin cancer and skin tissue," *Phys. Med. Biol*., vol. 47**,** issue 21, pp. 3853-3863, 2002.

[11] Y. Morita Y *et al*, "Terahertz technique for detection of microleaks in the seal of flexible plastic packages," *Opt. Eng.*, vol. 44, issue 1, pp 019001-019006, 2005.

[12] C. Thongbai *et. al*., "Femtosecond Electron Bunches: Source and Characterization", *Nucl. Instr. Meth. Phys. Res.* A, No.587 pp. 130–135, 2008

[13] http://www.bblaser.com/bbl_item/bbli003_thz_lens.html

[14] http://www.twpinc.com/twpinc/control/category/~category_id=TWPCAT_3

The Accelerators and Related R&D Activities at Chiang Mai University

C. Thongbai [a,b*], S. Singkarat [a,b], L.D. Yu [b], and T. Vilaithong [b]

Abstract— The production and utilization of four fundamental probes, namely, electron, ion, neutron and photon, have played vital role in the research and development of modern science and technology. These probes are generated by various types of particle accelerators. At the Plasma and Beam Research Facility (PBP), Chiang Mai University, Thailand, beams of charged particles are accelerated to energies ranging from the keV to the MeV region. Low energy (< 200 keV) heavy ion implanters are applied to research in material surface modification, biology and nanotechnology whereas the MeV tandem accelerator is employed in material surface analysis and lithography. Relativistic femtosecond electron beam is used to produce transition radiation with wavelength in the THz region. Details of the present and future accelerator R & D activities are presented and discussed.

***Keywords*— accelerator, ion beam, electron beam, material modification, ion beam biotechnology, linac, THz radiation, FEL**

1. INTRODUCTION

In Thailand, the first accelerator facility was established in Chiang Mai about four decades ago. A nanosecond pulsed neutron generator was constructed and installed at the Fast Neutron Research Facility on the main campus of Chiang Mai University (CMU) [1]. The high stability Cockcroft-Walton type accelerator was modified to incorporate beam chopping and bunching devices. The 140 keV deuteron beam was used to produce neutrons from the $T(d,n)^4He$ reaction. The 1.5 – 2 ns pulsed neutrons were initially utilized in the measurement of double differential neutron emission cross sections with a 10-m flight path [2]. A few years later, a 150 kV heavy ion implanter was designed and constructed [3]. Gaseous ions such nitrogen ions were generated and used to modify tribological properties of metals and alloys. Subsequent machines were installed for ion-bioengineering studies. A decade ago, femtosecond electron bunches from a thermionic RF-gun with a bunch compressing α-magnet were built at CMU [4]. In this paper, the development and present status of the accelerator technology and its utilizations are reviewed.

2. ION BEAMS

Development of low and medium energy (keV – MeV) ion beam accelerators and related technology and applications has been a main focus of the national research in accelerator physics. We have established an ion beam research center at CMU as a unique comprehensive ion beam and plasma research laboratory. The Plasma and Beam Physics Research Facility (PBP), formerly named the Fast Neutron Research Facility (FNRF), is now equipped with a 1.7-MV Tandetron tandem accelerator mainly for ion beam analysis (Fig. 1), a 220-kV Varian versatile ion implanter for various ion implantations, a 30-kV bioengineering-specialized vertical ion beam line for biological applications, a 30-kV plasma immersion ion implantation facility for material surface modification, a 10-kV ion beam neutralizer for neutral beam implantation in non-conducting materials, and a number of plasma facilities. Historically, a 150-kV deuteron accelerator based 14-MeV fast neutron generator, a 150-kV heavy ion implanter, a 150-kV high-current broad-beam ion implanter and a 300-kV ns-pulsed accelerator-based beam line with a chopper-buncher system for time-of-flight (TOF) Rutherford backscattering spectrometry (RBS) analysis were also constructed but now demolished. With applying all of these ion beam facilities Thai scientists have been able to carry out so much research work on materials modification, surface analysis and biological applications and achieve significant attainments.

The ion beam has been applied for modification of solid materials such as local steels [5], alloys [6], cermet [7], ceramics [8,9] and semiconductors [10]. We achieved improvements in material surface hardness, wear resistance, friction coefficient, corrosion resistance, high-temperature oxidation resistance, optical properties and formation of nanostructures. Based on the success in the conventional materials modification by ion beams, the application of ion beam was extended to biology. The ion beam biology (IBB) research has been an emphatic research program in the field of low-energy accelerator applications since 1998. The research is generally aimed at utilizing ion beam and plasma technology for applications in biology, agriculture, horticulture, medical science and life science. The research has led to establishment of the ion beam biotechnology in the country and succeeded in ion-beam-induced mutations of local rice, flowers and vegetables and DNA transfer in bacteria and yeasts [11-13]. The on-going basic research is focused on investigations of mechanisms involved in the ion-beam-induced mutation and DNA [14-16].

Besides the applications in materials modification, ion beam has been applied for material analysis. Two accelerators, namely, the 1.7-MV Tandetron tandem

* Corresponding author. Tel: +66 53 943369; Fax: +66 53 943445; E-mail: chlada@yahoo.com

[a] Department of Physics and Material Science, Chiang Mai University, Chiang Mai, Thailand.

[b] Thailand Center of Excellence in Physics, Commission on Higher Education, Bangkok, 10400, Thailand.

accelerator and the 300-kV medium-energy ns-pulsed ion beam accelerator, have been employed for the purpose. The Tandetron accelerator employs two ion sources, a duoplasmatron ion source and a cesium (Cs) sputter ion source, capable of producing analyzing ion beams of light species such as hydrogen and helium and heavy species. The beam line is currently able to perform ion beam analysis techniques such as Rutherford Backscattering Spectrometry (RBS), RBS/channeling, Particle Induced X-ray Emission (PIXE), Elastic (non-Rutherford) BackScattering (EBS) and Ionoluminescence (IL) with assistance of commercial and self-developed softwares. The medium-energy ion accelerator is featured with ns-pulsed beam so that Time-of-Flight (ToF) RBS analysis using medium-energy ion beams can be available for detailed analysis of materials. Ion beam analysis experiments and applications have been vigorously developed in analyses of elements, elemental depth distribution, radiation damage in crystals, thin or hierarchical films, and nanostructures of various materials including metals, semiconductors, ceramics, gemstones, airborne dust and biological organisms [17,18]. Furthermore, the MeV ion beam has been utilized for ion beam lithography which has been a useful technique for microfluidics application. MeV ion beam lithography is a direct writing technique capable of producing microfluidic patterns and lab-on-chip devices with straight walls in thick resist films [19,20].

Accelerator-based ion beams have been working together with plasma technology for ion beam nanotechnology applications. The ion beam nano technology research was initiated with carbon ion implantation in tungsten carbide cemented by cobalt (WC-Co) cermet to achieve surface nanostructure which resulted in ultra-low friction coefficient [21]. Later on, the research topics have been extended to include ion beam synthesis of nanocrystalline materials such as silicon carbide (SiC) [22], ion beam and plasma deposition of nanofilms such as diamond-like carbon (DLC) coatings [23], ion beam lithography of micro/nanopatterns, ion beam and plasma induced surface nanostructures such as nanofibers and nanoislands, ion beam nanoanalysis, and ion beam nanobiotechnology.

3. ELECTRON BEAM

The SURIYA electron beam facility to produce femtosecond electron bunches and THz radiation has been developed for a decade. Fig. 2 shows the schematic diagram of the bunch generation and compression system using a specially designed radiofrequency (RF)-gun [24,25]. In the RF-gun, electrons are continuously emitted with thermal energies from a thermionic cathode and are extracted and accelerated during an

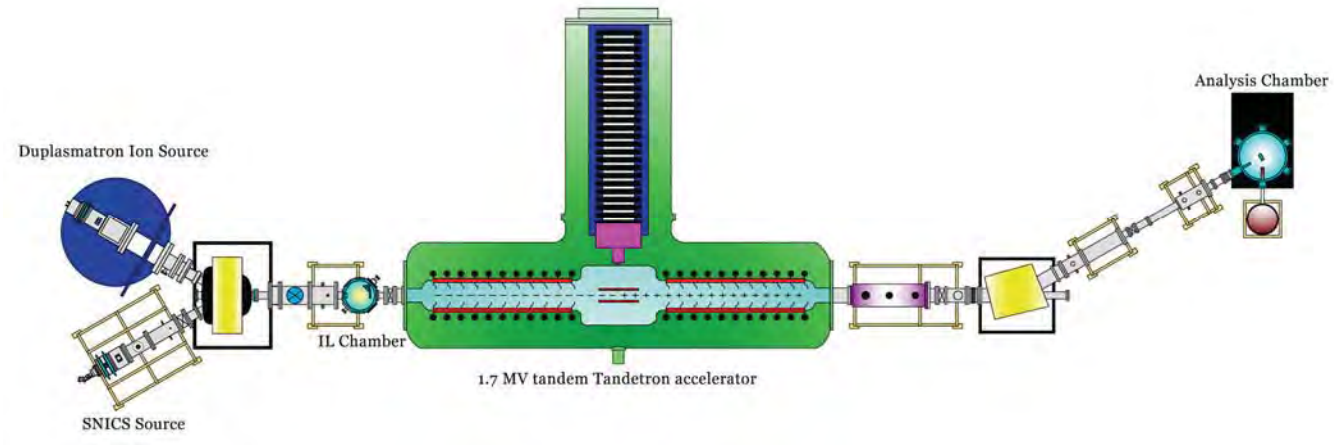

Fig. 1. Schematic diagram of the 1.7-MV tandem accelerator and ion beam line for ion beam analysis.

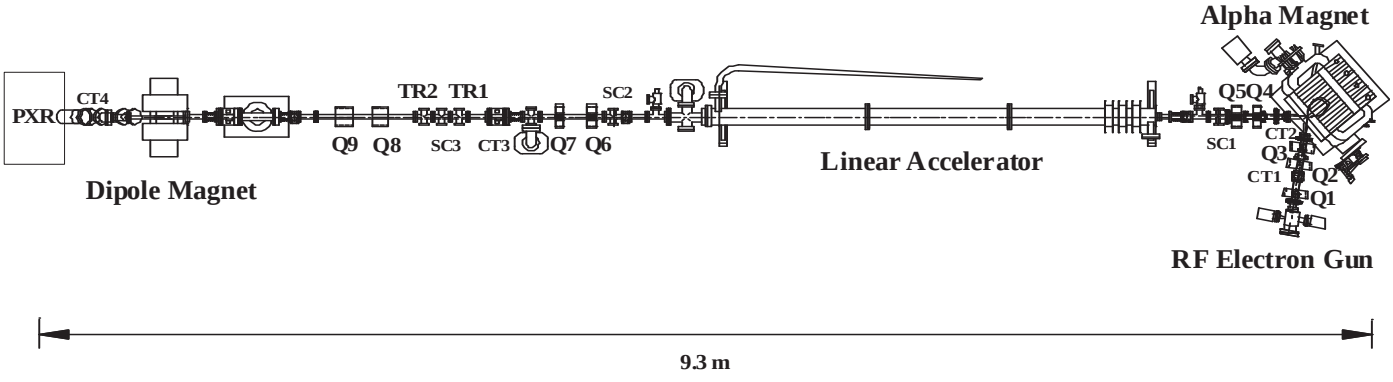

Fig. 2. Schematic layout of the accelerator system at Chiang Mai University for generation of short electron bunches. Q: quadrupole magnet, SC: screen, CT: current monitor, TR and PXR: transition and parametric X- radiation experimental stations.

accelerating phase of the RF-fields at 2856 MHz. At first electrons are accelerated rapidly and reach the end of the half-cell just before the RF-phase becomes decelerating. They are further accelerated through the full-cell to reach the maximum kinetic energy of 2.0-2.5 MeV at the gun-exit depending on the accelerating field gradients. Later on the electrons feel some decelerating fields and gain less and less overall energy resulting in a well-defined correlation between energy and time. Electron bunches of 20-30 ps from the RF-gun are then compressed in an α-magnet, where the particle path length increases with energy. This allows the lower energy particles, emitted later in each bunch, to catch up with the front for effective bunch compression. The optimized and compressed part of the electron bunch is then filtered by energy slits located in the α-magnet vacuum chamber and then transported through a SLAC type linac and a beam transport line to experimental stations. At the experimental stations, the bunches are compressed to less than 1 ps [26]. Operating and beam parameters are shown in Table 1.

Table 1. Operating and beam parameters of the electron beam accelerator at CMU.

Parameters	**RF-gun**	**Linac**
Beam energy [MeV]	2.2-3	6-10
Macropulse peak current [mA]	1000	50-150
RF-pulse length (FWHM) [μs]	2.8	8
Repetition rate [Hz]	10	10
Beam-pulse length [μs]	~2	~0.8
Number of microbunch/macropulse	5700	2300
Number of electrons /microbunch	1.4×10^{9}	8×10^{7} - 6×10^{8}

The femtosecond electron bunches are used to generate intense THz or far-infrared radiation in the form of coherent radiation. Such radiation is of great interest for THz spectroscopy and THz imaging applications [27-28]. After acceleration, the compressed electron bunches are used to generated coherent transition radiation (TR) by passing through a thin aluminum (Al)-foil. The Al-foil or radiator is tilted by 45^{o} facing the electron beam direction. The backward transition radiation is emitted perpendicularly to the beam axis and transmits through a high density polyethylene (HDPE). The radiation energy of 19 μJ per macropulse or a peak power of 24 W was measured by collecting over an acceptance angle of 160 mrad. The available THz radiation, measured using a Michelson interferometer with a room-temperature pyroelectric detector, covers from 5 cm^{-1} to around 80 cm^{-1} wavenumber (0.15 THz – 2.4 THz). THz spectroscopy can be done easily by measuring power transmission or power reflection of a sample via a Michelson interferometer and the Fourier Transformation as well as with Dispersive Fourier Transform Spectroscopy (DFTS) technique. THz spectroscopy experiments, especially that of highly absorbing substances using coherent THz transition radiation source and DFTS technique, have been reported [29]. Reflection and transmission THz imaging experiments were conducted as examples of THz radiation applications using our radiation source [30]. It is possible to extend the spectral range further by using shorter electron bunches.

4. FUTURE PLAN FOR IR-THz FEL

At Chiang Mai University, we plan to establish a new research facility centered on the production and utilization of femto-second electron pulses and Free Electron Lasers (FEL) optimized for mid and far infrared/THz radiation. The main goal of the extension into the THz facility would be the generation of infra-red (IR) radiation covering the mid and far-infrared regime to wavelengths up to the THz regime. The broad interest is fueled by the promises in support of basic and applied research, security, biology, chemistry, medicine etc. Infrared and THz radiation could be used for security to replace or amplify, for example, metal detectors to detect non-metallic but dangerous articles. Furthermore, quality controls of food products would be possible through packing material by examining chemical composition, water content and freshness of food. In biology and chemistry IR and THz radiation is used in spectroscopy to investigate vibrations of macro-molecules. Especially, high intensity THz radiation has been used to study biological samples in watery environment rather that in dry condensed states. The structure and integrity of semiconductor devices can be investigated through packaging while studying the circuit layers. All of these are our planned applications.

In order to realize the applications, we will rearrange and construct the facility area. Recently, a large well shielded area became available through the decommissioning of a fast neutron facility, and it is planned to establish the new center there by first relocating SURIYA to this location. The size of the new location (12 x 13.5 m^2) allows the installation of several FELs side by side. The beam from SURIYA will be turned around by several 180^{o} achromatic deflections to let the electron beam pass through one of 2 - 3 FEL undulators which are required to optimally cover the desired radiation spectrum. The electron beam from the SURIYA facility is not optimal now, but by only a modest increase of the RF-power to the RF-gun a beam condition can be generated which is optimal for a FEL although not anymore for bunch compression. The source of the electron beam being a 2.5 MeV RF-gun ensures that the beam emittance is sufficiently small for all FELs. Similarly, the energy spread from the gun is less than 1 %. A schematic outline of the facility is shown in Fig. 3. The free space available for each FEL with optical cavities is about 10 m. A photon beam line attached to each FEL will guide the photons to a well shielded, radiation free area (~ 150 m^2) and associated experimental location.

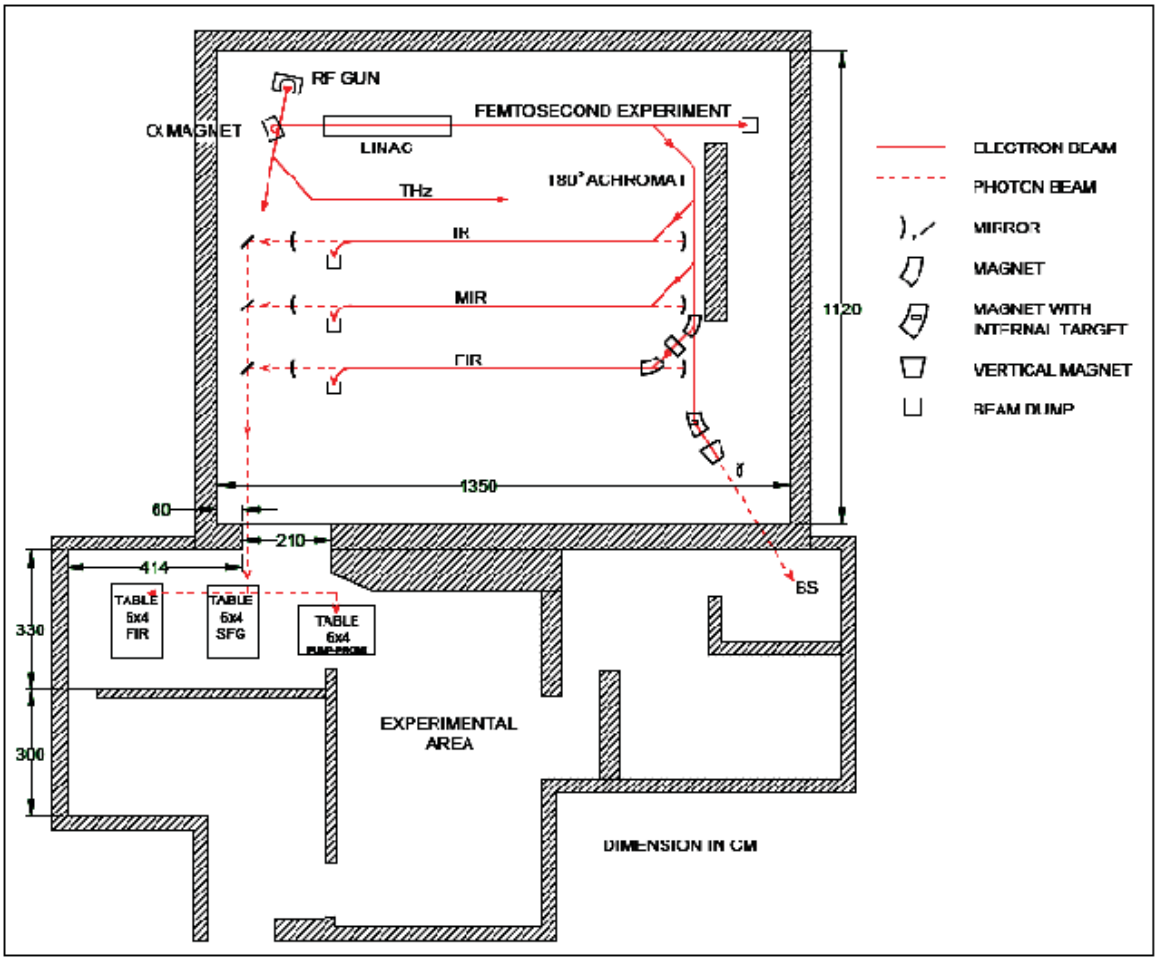

Fig. 3. Schematic diagram of the planned layout of the new facility for free electron lasers.

5. CONCLUSION

At Chiang Mai University, accelerators and the accelerator-based research activities have been vigorously being developed in recent 20 years. Two accelerator bases are representatives, namely the ion and electron beam. Ion beam technology has been broadly applied for materials modification, material analysis, biology, agriculture and nanotechnology. Electron beam accelerator technology has been constantly developed for advanced applications including THz radiation spectroscopy. The construction, installation and applications of the accelerators and related technology have significantly promoted the scientific, technological and educational developments.

ACKNOWLEDGMENT

The authors thank Helmut Widermann for his contribution to the planning of the free electron laser project and for reviewing part of the manuscript. The projects have been supported by the Thailand Research Fund, Commission on Higher Education, National Research Council of Thailand, Ministry of Science and Technology, National Metal and Materials Technology Center, National Nanotechnology Center, Thailand Center of Excellence in Physics, Chiang Mai University, and International Atomic Energy Agency. We wish to thank all of project participants for their various contributions.

REFERENCES

[1] T. Vilaithong, et al., *Proc Int. Conf. on Nuclear Data for Science and Technology*, Juerlich, Germany, S.M. Qaim (Ed.) (Springer Verlag. May 1991) pp. 483-486.

[2] T. Vilaithong, D. Boonyawan, S. Konklong, W. Pairsuwan and S. Singkarat, Nucl. Instr. Meth. A **332**, 561 (1993).

[3] D. Suwannakachorn, et al., Nucl. Instr. Meth. B **89**, 354 (1994).

[4] S. Rimjaem, R. Farius, C. Thongbai, T. Vilaithong and H. Wiedemann, Nucl. Instr. Meth. A **533**, 258 (2004).

[5] L.D. Yu, T. Vilaithong, D. Suwannakachorn, S. Intarasiri and S. Thongtem, Nucl. Instr. Meth. B **127-128**, 954 (1997).

[6] L.D. Yu, S. Thongtem, T. Vilaithong and M.J. McNallan, Surf. Coat. Technol. **128-129**, 410 (2000).

[7] L.D. Yu, G.W. Shuy and T. Vilaithong, Surf. Coat. Technol. **128-129**, 404 (2000).

[8] C. Chaiwong, L.D. Yu, K. Schinarakis, T. Vilaithong, Surf. Coat. Technol. **196**, 108 (2005).

[9] S. Intarasiri, D. Bootkul, L.D. Yu, T. Kamwanna1, S. Singkarat and T. Vilaithong. Surf. Coat. Technol.

203, 2788 (2009).
[10] S. Intarasiri, et al., Nucl. Instr. Meth. B **249**, 851 (2006).
[11] B. Phanchaisri, R. Chandet, L.D. Yu, T. Vilaithong, S. Jamjod, and S. Anuntalabhochai, Surf. Coat. Technol. **201**, 8024 (2007).
[12] A. Krasaechai, et al., Surf. Coat. Technol. **203**, 2525 (2009).
[13] S. Anuntalabhochai, R. Chandej, B. Phanchaisri, L.D. Yu, T. Vilaithong, and I.G. Brown, Appl. Phys. Lett. **78**, 2393 (2001).
[14] R. Norarat, N. Semsang, S. Anuntalabhochai, and L.D. Yu, Nucl. Instr. Meth. B **267**, 1650 (2009).
[15] S. Sarapirom, K. Sangwijit, S. Anuntalabhochai, and L.D. Yu, Surf. Coat. Technol. **204**, 2960 (2010).
[16] K. Prakrajang, P. Wanichapichart, S. Anuntalabhochai and L.D. Yu, Nucl. Instr. Meth. B **267**, 1645 (2009).
[17] S. Intarasiri, et al., Nucl. Instr. Meth. B **249**, 859 (2006).
[18] T. Kamwanna, N. Pasaja, L.D. Yu, T. Vilaithong, A. Anders, and S. Singakarat, Nucl. Instr. Meth. B **266**, 5175 (2008).
[19] S. Gorelick, N. Puttaraksa, T. Sajavaara, M. Laitinen, S. Singkarat, and H.J. Whitlow, Nucl. Instr. Meth. B **266**, 2461 (2008).
[20] N. Puttaraksa, S. Gorelick, T. Sajavaara, M. Laitinen, S. Singkarat, and H. J. Whitlow, J. Vac. Sci. Tech. B **26**, 1732 (2008).
[21] L.D. Yu, G.W. Shuy, and T. Vilaithong, J. The Surface Finishing Society of Japan **54**, 749 (2003).
[22] S. Intarasiri, et al., Appl. Surf. Sci. **253**, 4836 (2007).
[23] L.D. Yu, S. Aukkaravittayapun, D. Boonyawan, S. Sarapirom, T. Vilaithong, Surf. Coat. Technol. **203**, 2771 (2009).
[24] J. Saisut, et al., Nucl. Instr. Meth. A (2010), doi:10.1016/j.nima.2010.02.032.
[25] S. Rimjaem, R. Farias, C. Thongbai, T. Vilaithong, and H. Wiedemann, Nucl. Instr. Meth. A 533, 258 (2004).
[26] C. Thongbai, et al., Nucl. Instr. Meth. A **587**, 130 (2008).
[27] X.-C. Zhang and Jingzhou Xu, *Introduction to THz Wave Photonics*, Springer, New York, 2010.
[28] Y. Kim, et al., J. Korean Physical Society **56,** 255 (2010).
[29] K.N. Woods and H. Wiedemann, Chem. Phys. Lett. **393**, 159-165 (2004).
[30] P. Thamboon, et al., Nucl. Instr. and Meth. A (2010), doi:10.1016/j.nima.2010.02.047

Accelerator-based THz Radiation source at Chiang Mai University

J. Saisut [a,c,*] , K. Kusoljariyakul [a,c] , P. Wichaisirimongkol [a,c], P. Thamboon [b,c], M.W. Rhodes [b,c] and C. Thongbai [a,c]

Abstract— *A THz radiation source based on femtosecond electron bunches has been constructed at the Plasma and Beam Physics (PBP) research facility, Chiang Mai University. The accelerator system consists of an RF-gun with a thermionic cathode, an alpha-magnet as a magnetic bunch compressor, and a linear accelerator as a post acceleration section. Coherent transition radiation emitted from short electron bunches was used as the THz radiation source. This THz radiation can be used as a source of the THz imaging system and THz or far-infrared spectroscopy. The generation and characterization of the THz will be presented. Recent experimental results on THz spectroscopy and THz imaging will be presented and discussed.*

***Keywords*— femtosecond electron bunches, Coherent transition radiation, THz radiation**

1. INTRODUCTION

A THz facility based on femtosecond electron bunches has been established at the Plasma and Beam Physics Research Facility (PBP), Chiang Mai University. Femtosecond electron bunches are generated from a system consisting of an RF-gun with a thermionic cathode, an alpha-magnet as a magnetic bunch compressor and a linear accelerator as a post acceleration section as shown in Fig.1. In the RF-gun, electrons are continuously emitting with thermal energies from the thermionic cathode and are extracted and accelerated during an accelerating phase of the RF-fields at 2856 MHz. The first electron is accelerated rapidly and reach the end of the half-cell just before the RF-phase becomes decelerating. It is further accelerated through the full-cell to reach maximum kinetic energy of 2.0-2.5 MeV at the gun-exit depending on accelerating field gradients. Later electrons feel some decelerating fields and gain less and less overall energy resulting in a well-defined correlation between energy and time. Electron bunches of 20-30 ps from the RF-gun are then compressed in an α-magnet, where the particle path length increases with energy. This allows the lower energy particles, emitted later in each bunch, to catch up with the front for effective bunch compression. The optimized and compressed part of the electron bunch is then filtered by energy slits located in the α-magnet vacuum chamber and then transported through a SLAC type linac and a beam transport line to experimental stations. At the experimental station, the bunches are compressed to less than 1 ps. These short electron pulses can be used to produce high intensity THz radiation in the form of coherent transition radiation. Typical operating parameters and electron beam characteristics at SURIYA facility are complied in Table 1.

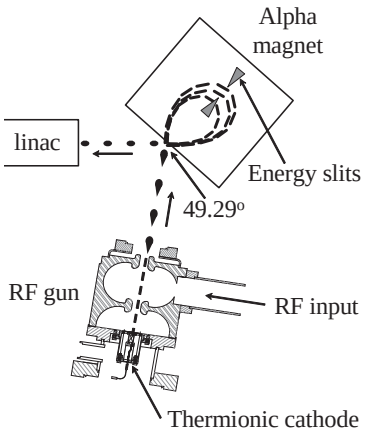

Fig.2. Schematic diagram of the electron bunch generation and compression system.

TABLE 1. Operating and beam parameters.

Parameters	RF-gun	Linac
Beam energy [MeV]	2.2-3	6-10
Macropulse peak current [mA]	1000	50-150
RF-pulse length (FWHM) [μs]	2.8	8
Repetition rate [Hz]	10	10
Beam-pulse length [μs]	~2	~0.8
Number of microbunch/macropulse	5700	2300
Number of electrons /microbunch	1.4×10^{9}	8×10^{7} - 6×10^{8}

2. GENERATION OF THz RADIATION

At PBP facility, the THz radiation is generated in the form of transition radiation by placing an aluminium foil (Al-foil) in the electron path, representing a transition between vacuum and Al-foil. When electron passes through an interface between two media of different dielectric constants, it emits electromagnetic fields. In the case of a normal incidence, the radiation energy *W* per

* Corresponding author. Tel: +66 53 943379; Fax: +66 53 222776;
E-mail: jsaisut@chiangmai.ac.th
[a] Department of Physics and Materials Science, Chiang Mai University, Chiang Mai 50200, Thailand.
[b] STIR, Chiang Mai University, Chiang Mai 50200, Thailand.
[c] ThEP Center, Commission on Higher Education, Bangkok 10400, Thailand.

unit angular frequency $d\omega$ per unit solid angle $d\Omega$ for the backward transition radiation from vacuum-conductor interfaces is given by [7]

$$\frac{dW}{d\omega d\Omega} = \frac{e^2\beta^2 \sin^2\theta}{\pi^2 c(1-\beta^2\cos^2\theta)^2}, \qquad (1)$$

where θ is the angle between the emitted radiation direction and the inverse direction of electron trajectory (-z axis). For relativistic electrons ($\gamma >> 1$ and $\beta \to 1$), the maximum intensity can be obtained at $\theta \approx \pm 1/\gamma$. In case of a 45° incidence, the backward radiation emitted at 90° with respect to the beam axis with its spectral-angular distribution given by the contribution of parallel and perpendicular polarization radiation.

$$\frac{dW^{II}}{d\Omega d\omega} = \frac{e^2\beta^2}{2\pi^2 c}\left[\frac{2\sin\theta - \sqrt{2}\beta\cos\phi}{(\sqrt{2}-\beta\sin\theta\cos\phi)^2 - \beta^2\cos^2\theta}\right]^2 \qquad (2)$$

and

$$\frac{dW^{\perp}}{d\Omega d\omega} = \frac{e^2\beta^2}{2\pi^2 c}\left[\frac{\sqrt{2}\beta\cos\theta\sin\phi}{(\sqrt{2}-\beta\sin\theta\cos\phi)^2 - \beta^2\cos^2\theta}\right]^2, \qquad (3)$$

where y is the emission angle between the direction of emitted radiation and the -z axis, while ϕ is the azimuthal angle defined in the xy-plane with respect to the -x axis.

The radiation from an electron bunch becomes coherent and highly intense at wavelength about or longer than the bunch length. The intensity of coherent radiation is proportional to the number of radiating electrons squared and thus exceeds greatly that of incoherent radiation at the same wavelength. Total electromagnetic radiation emitted from a bunch of *N* electrons at radiation frequency ω is $I(\omega) = NI_e(\omega)[1+(N-1)f(\omega)]$, where $I_e(\omega)$ is the radiation intensity from a single electron and the bunch *form factor* $f(\omega)$ is the Fourier transform of the longitudinal bunch distribution square. Since the radiation spectrum is proportional to the Fourier transform of the bunch distribution, the short bunch is therefore desired for production of broadband radiation spectrum. The radiation brightness in Fig.3 shows that electron bunches of 100 fs can provide broadband radiation in far-infrared regime with the wavenumber cover from 5 cm^{-1} to 200 cm^{-1}. This intense coherent transition radiation greatly exceeds that of a black body as well as that of synchrotron radiation.

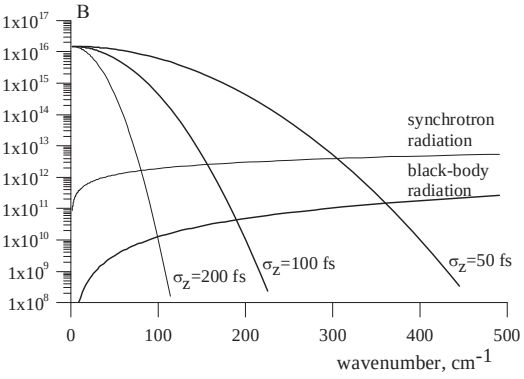

Fig.2. Radiation brightness B (ph/s/mm^2/100%BW) for coherent transition radiation from electron bunches of σ_z = 50, 100, and 200 fs compared to black body radiation and synchrotron radiation.

3. CHARACTERIZATION OF THz RADIATION

The electron beams after acceleration was used to generate coherent transition radiation utilizing a 25.4-μm-thick Al-foil of 24 mm diameter as a radiator. The radiator is tilted by 45° facing the electron beam direction. The backward transition radiation is emitted perpendicular to the beam axis. The radiation is collimated by a 1-inch 90° parabolic mirror and transmits through a high density polyethylene (HDPE) window of 1.25-mm-thick and 32-mm diameter. A copper light cone is used to collect the radiation into a room-temperature pyroelectric detector. A cross-sectional diagram of the experimental set up for measuring the transition radiation is shown in Fig.4.

3.1. THz RADIATION INTENSITY

The detector signal of THz radiation was clearly observed. The radiation energy of 9 μJ per macropulse or a peak power of 12.5 W was measured by collecting over an acceptance angle of 160 mrad.

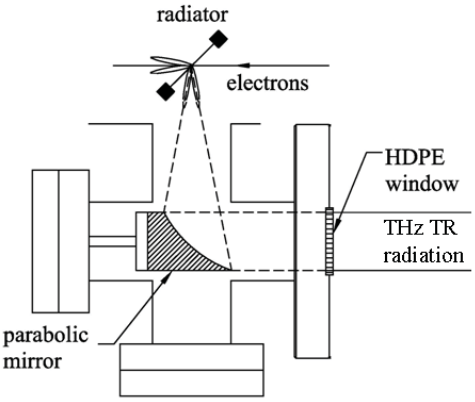

Fig.3. Setup to generate THz Transition radiation.

3.2. THz RADIATION PROFILE

The THz radiation profile or the spatial distribution is obtained from the setup as shown in Fig.4. The system consists of Tsurupica lens [8], a translation stage and Pyrocam III camera [9]. The collimated THz radiation is focused by the lens to Pyrocam III which attached on the translation stage. The recorded profiles are shown in Fig.5.

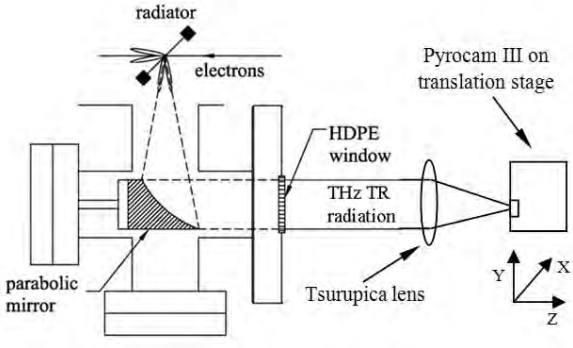

Fig.4. THz radiation profile measurement setup.

The radiation beam size is estimated from the projection of the profile both X and Y plane. By applying Gaussian distribution to the projections, the FWHM of the projection can be obtained. It is then able to scale back to

the radiation beam size in front of the lens by recording the profiles along Z axis. According to the fitting results, the radiation beam diameter is equal to 2.42 cm. The result agrees well with the radiation beam diameter limited by the size of the parabolic mirror (2.54 cm diameter). The maximum intensity is located at angle of 70 mrad with respect to the center of the radiation cone. Theoritically for a 7 MeV beam, which is the mean energy of the beam in the measurement, the maximum intensity is located at 68 mrad with respect to the center of the radiation cone. Figure 6 shows comparision of THz profile betaween calculation for beam energy of 7 MeV and experiment at Z = 0.6 cm. The experimental results is slightly difference from the simplify of the theoretical even the electron beam have a large energy spread ranging from 5 to 10 MeV. Possible reason for this small discrepancy is that the in coming radiation is not perfectly parallel but it has small divergence due to the parabolic mirror focusing. The radiation might not be radiated at the focal point of parabolic mirror.

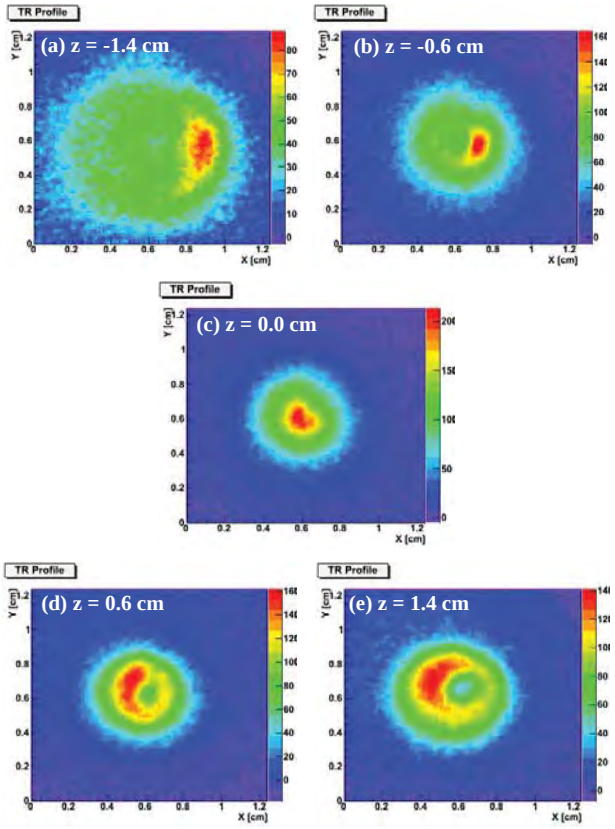

Fig.5. THz radiation profile along Z axis; (a) Z = - 1.4 cm, (b) Z = - 0.6 cm, (c) Z = 0.0 cm, (d) Z = 0.6 cm, (e) Z = 1.4 cm.

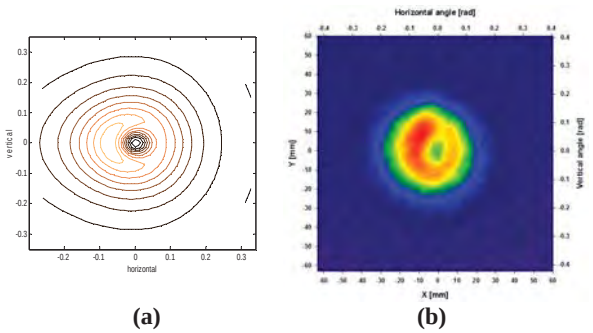

(a) **(b)**

Fig.6. THz radiation profile from; (a) theoretical calculation for beam energy of 7 MeV and (b) experiment at Z = 0.6 cm.

3.3. THz RADIATION POWER SPECTRUM

The radiation power spectrum can be derived via Fourier Transformation of the autocorrelation pattern or interferogram which obtain from Michelson interferometer as shown in Fig.7 coherent transition radiation exits through a HDPE window and enters a Michelson interferometer. The interferometer consists of a beam splitter, a fixed and a movable first surface mirror, arranged as shown in the figure. The radiation field entering the Michelson interferometer is split into two parts by the beam splitter, both travelling in different directions to be reflected back by mirrors. After reflection, parts of the two radiation pulses are combined again and absorbed by a detector to determine the intensity.

At an optical path difference δ between both spectrometer arms, the combined radiation pulses are the radiation from the fixed arm, $E_1(t) = TRE(t)$, and the radiation from the movable arm delayed in time by δ / c, $E_2(t) = RTE(t + \delta / c)$. Here $R = R(\omega)$ and $T = T(\omega)$ are the reflection and transmission coefficients of the beam splitter. The intensity measured at the detector is then

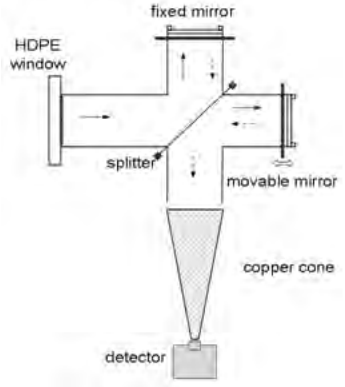

Fig.7. Schematic diagram of the THz Michelson interferometer.

$$I_d(\delta) \propto \int \left| TRE(t) + RTE(t + \delta / c) \right|^2 dt \propto I_{d0} + 2\int |RT|^2 E(t) E^*(t + \delta / c)\, dt \,, \quad (5)$$

where $I_{d0} \propto 2\int |RTE(t)|^2 dt$ is independent of the path difference δ and represents the baseline. The autocorrelation pattern obtained from the measurement is shown in Fig. 8. By scanning movable mirror, we can construct "an interferogram' which is the variation intensity above the base line as a function of path difference. An interferogram just represent the radiation autocorrelation.

$$I(\delta) = 2\,\mathrm{Re}\int |RT|^2 E(t) E^*(t + \delta / c) dt \,. \quad (6)$$

The expression of interferogram in frequency domain using a Fourier transformation is then

$$I(\delta) = 2\,\mathrm{Re}\int_{-\infty}^{+\infty} \left| R(\omega) T(\omega) \tilde{E}(\omega) \right|^2 e^{i\omega\delta/c} d\omega \,. \quad (7)$$

The radiation power spectrum is the Fourier transform of the interferogram from eq.(7)

$$\left| R(\omega) T(\omega) \tilde{E}(\omega) \right|^2 \propto \int I(\delta) e^{i\omega\delta/c} d\delta = FT\{I(\delta)\} \,. \quad (8)$$

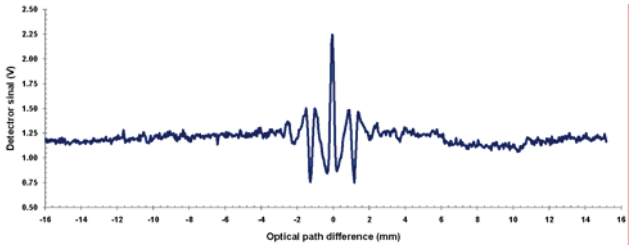

Fig.8. Autocorrelation pattern or interferogram

The radiation power spectrum displayed in Fig.9 can be derived via Fourier Transformation of the interferogram. The available THz radiation covers from 5 cm^{-1} to around 55 cm^{-1} wavenumber which correspondeding to a frequency range from 0.3 THz to 1.8 THz.

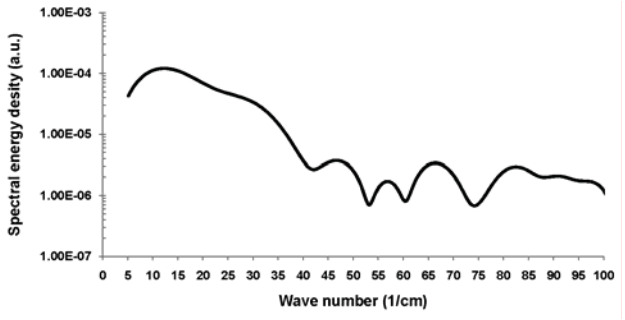

Fig.9. THz Radiation power spectrum.

5. APPLICATIONS

5.1 THz SPECTROSCOPY

The THz spectroscopy can be done easily by measuring power transmission or power absorption of a sample via a Michelson interferometer and the Fourier Transformation. Although phase information has been lost in the measurement, optical constants of the sample can be obtained by some modeling or Kramers-Kronig calculation [10]. Dispersive Fourier Transform Spectroscopy (DFTS) [11] may also be used for direct determination of optical constants of a sample. In a DFTS setup, a sample is inserted in one arm of the interferometer, causing attenuation and dispersion of the radiation pulse. The attenuated and dispersed pulse can be recorded and its attenuation factor and phase shift can then be recovered. The attenuation and dispersion can be related to optical constants of the sample depending on the optical configuration of the measurements. With the DFTS technique, the phase information can be recovered in measurements using a Michelson interferometer.

5.2 THz IMAGING

A schematic diagram of a THz imaging system (transmission measurement) at the Plasma and Beam Physics Research Facility (PBP), Chiang Mai University is illustrated in Fig. 9 for transmission measurement. THz radiation is focused on a sample which will be scanned using an xy- translation stage controlled by a computer. The transmission intensity (I_T) will be detected by a room-temperature pyroelectric detector. Computer program will be employed to calculate and analyze intensity at difference points on the sample for THz image construction. Figure 11 shows an example of THz imaging obtained from the leaf concealed in an envelope.

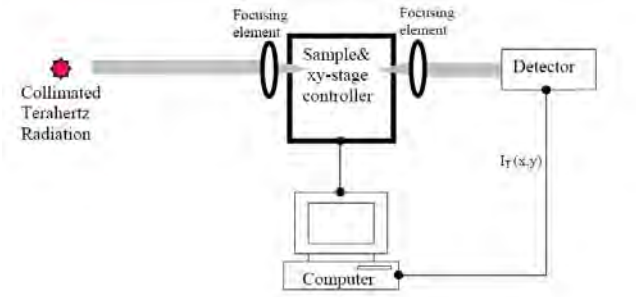

Fig. 9 Schematic diagram of the THz imaging system at Chiang Mai University.

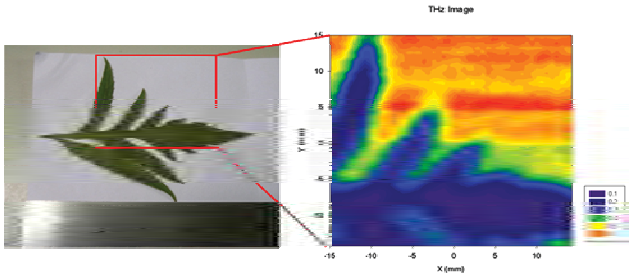

(a) **(b)**

Fig.11. (a) Leaf and (b) its THz image.

4. CONCLUSION

Intense THz radiation can be generated in form of coherent transition radiation by using short electron bunches which are available at the Plasma and Beam Physics Research Facility (PBP), Department of Physics and Materials Science, Faculty of Science, Chiang Mai University. The radiation energy is 9 μJ per macropulse or 12.5 W peak power collecting over an acceptance angle of 160 mrad. The available THz radiation covers from 5 cm^{-1} to around 55 cm^{-1} wavenumber. This THz radiation can be used as a source of the THz imaging system and far-infrared or THz spectroscopy. In additional, sub-pico second feature of the radiation pulse will open up opportunities for time-resolved studies of ultrafast processes using THz radiation.

ACKNOWLEDGMENT

Authors are grateful to Prof. Helmut Wiedemann for his comment and suggestion. We would like to thank Mr. N. Kangrang and Mr. V. Jinamoon for their technical support. We would like to acknowledge the support from the National Research Council of Thailand (NRCT), the Thailand Research Fund (TRF), the Thailand center of Excellence in Physics (ThEP Center), the (Thailand) Commission on Higher Education (CHE) and the graduate school of Chiang Mai University.

REFERENCES

[1] Ihee, H. *et al.* (2001) Direct Imaging of Transient Molecular Structures with Ultrafast Diffraction. *Science* 291 : 458-462.

[2] Bauer, M. *et al.* (2001) Direct Observation of Surface Chemistry Using Ultrafast Soft-X-Ray Pulses. *Phy. ReV. Lett.* 87 : 025501.

[3] Reis, D. A. e*t al.* (2001) Probing Impulsive Strain Propagation with X-Ray Pulses. *Phy. ReV. Lett.* 86 : 3072.
[4] Thongbai, C. S. and Vilaithong, T. (2007) Coherent transition radiation from short electron bunches. *Nucl. Instr. and Meth.* 581(3): 874-881.
[5] Endo, I. e*t al.* (1995) Parametric x radiation from thick crystals. *Phy. Rev. E*. 51: 6305.
[6] Bonifacio, R.: Pellegrini, C.; and Narducci, L. M. (1984) Collective instabilities and high-gain regime in a free electron laser, *Opt. Commun.* 50 313.
[7] Settakorn, C. T. 2009. *Coherent THz Transition Radiation; Generation, Characterization, and Applications.* VDM Verlag & Co. KG.
[8] http://www.bblaser.com/bbl_item/bbli003_thz_lens.html
[9] http://www.ophiropt.com/laser-measurement-instruments/beam-profilers/products/industrial-applications/the-cameras/pyrocam
[10] Bell, R. J. 1972. *Introductory Fourier Transform Spectroscopy*. London: Academic Press.
[11] Birch, J.R. and Parker, T.J. Dispersive fourier transform spectroscopy. In *Infrared and Millimeter Waves V.2: Instrumentation*, Button, K.J. Ed. NewYork: Academics Press.

INJECTOR SYSTEM FOR LINAC-BASED INFRARED FREE-ELECTRON LASER IN THAILAND

S. Rimjaem*, P. Boonpornprasert, J. Saisut, S. Suphakul, C. Thongbai, Department of Physics and Materials Science, Faculty of Science, Chiang Mai University, Chiang Mai, 50200, Thailand
S. Chunjarean, Thailand Center of Excellence in Physics, CHE, Bangkok 10400, Thailand

Abstract

A possibility to develop a compact linac-based Infrared free-electron laser (IR FEL) facility has been studied at Chiang Mai University (CMU) in Thailand. Characteristics of the emitted FEL light and reliability in operation of the FEL system are determined by the properties of the electron injector, the undulator, and the optical cavity. The proposed injector system for the future IR FEL is based on the electron linear accelerator system at the Plasma and Beam Physics Research Facility at CMU (PBP-CMU). Numerical and experimental studies to adjust the existing system to be able to drive the IR FEL have been performed. The results of preliminary studies and the proposed parameters for the injector and the FEL system are concluded in this contribution.

INTRODUCTION

Linac-based free-electron lasers (FELs) have recently gain interest worldwide in the accelerator and particle beam community as the new generation light source, which can be utilized in numerous applications. Characteristics of the output FEL radiation are determined by the properties of the electron beam and the undulator, where the light is emitted. Since the FEL light sources require electron beams of high quality, the development and optimization of the injector system are important.

Electromagnetic radiation in the infrared wavelength regime, especially the far-infrared (FIR) or THz radiation, is of a great interest source for applications in various fields [1-4]. A possibility to develop an infrared free-electron laser (IR FEL) is studied at the Plasma and Beam Physics Research Facility, Chiang Mai University (PBP-CMU). At this initial stage, we concentrate on the development of an FEL covering the THz radiation wavelength around 50-200 μm. Study of the FEL radiation in the mid-infrared (MIR) and near-infrared (NIR) regime will be considered in the future.

In order to develop the FEL system, optimization of both injector and FEL system is ongoing. In this paper, we concentrate on an overview of the project and preliminary optimization of a thermionic based electron radiofrequency (RF) injector to produce electron beams with properties yielding the requirements for an IR FEL.

PROPOSED IR FEL FACILITY

Generally, an IR FEL facility consists of an injector system for generating and accelerating electron beam, an undulator magnet for FEL lasing and an optical cavity for amplifying the FEL radiation output power. For the considered injector system of the proposed IR FEL at CMU, we plan to make use of the existing linac system as much as possible while maintaining its functionality as the femtosecond electron and photon pulse facility.

The proposed IR FEL system shown in Fig. 1 consists of an injector system, an accelerating structure, a 180° achromat section, an undulator magnet and an optical cavity. The injector system combines a thermionic cathode RF-gun and an alpha magnet as a magnetic bunch compressor. The accelerating structure is an S-band travelling wave SLAC-type linac, which can be used to accelerate an electron beam to reach a maximum energy of about 30 MeV. The injector system, the linac structure, beam steering and focusing elements as well as beam diagnostic instruments upstream the achromat section will be modified from the existing PBP-CMU linac system [5]. The undulator magnet is a planar type with a length of 1.67 m. The optical cavity composes of two symmetric spherical mirrors with a coupling hole on one of the mirrors. Some parameters of the undulator and the optical cavity used in preliminary FEL optimization are listed in Table 1.

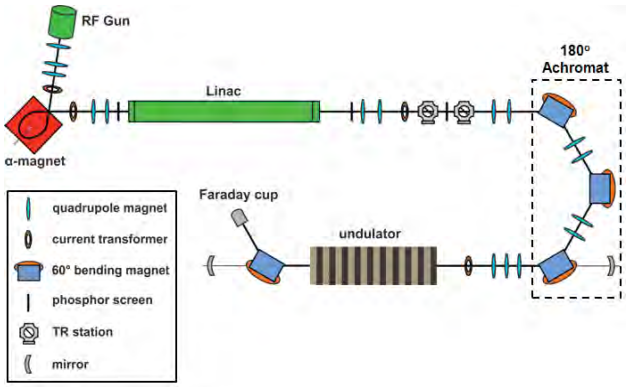

Figure 1: Schematic layout of the possible IR/THz FEL system at Chiang Mai University, Thailand.

In electron beam and FEL optimizations, we consider two scenarios. The first one is studying the FEL radiation in the case of the electron beam whose bunch length is longer than the radiation wavelength. The other one is for the case of the electron beam whose bunch length is shorter than the radiation wavelength.

*sakhorn.rimjaem@cmu.ac.th

ISBN 978-3-95450-123-6

Table 1: Parameters of Undulator and Optical Cavity Used in FEL Calculations

Parameter	Value
Undulator type	Planar
Undulator length	1.67 m
Number of period	22
Period length	7.7 cm
K-parameter	0.4 -1.52
Optical cavity length	5 m
Infrared reflectivity of optical cavity	95%

The FEL radiation due to the interaction between optical fields and an electron beam with a bunch length longer than the radiation wavelength has been studied using the numerical code GENESIS 1.3 [6]. As an example, the electron beam with an rms bunch length of a few ps has been considered. Preliminary required beam parameters used in the simulations for the radiated wavelength of 100 μm are shown in Table 2. With the aforementioned parameters, the expected FEL power is on the order of tens of megawatt as shown in Fig. 2. The numbers of round trips needed to accumulate the radiation amplification until reaching the saturation condition are about 60 and 80 turns for the cases of no loss and with 5% loss in the optical cavity, respectively. The undulator parameter (K) of 1.52 has been used in the simulation. With the optical cavity length of 5 m, the electron macropulse length of about 3 μs is required. Due to the back-bombardment effect, the available macropulse length of electron beam exiting the thermionic RF-gun at the PBP linac system is about 1-2 μs. Therefore, the modification of the RF power system may be required.

Table 2: Beam Parameters Use in GENESIS Simulations

Parameter	Value
Beam energy	15 MeV
Relative energy spread (rms)	0.5%
Longitudinal rms bunch length (σ_z)	2 ps
Bunch charge (Q_b)	30 pC
Peak current (I_p)	30 A
Normalized beam emittance (ε_x,ε_y)	3π mm-mrad
Beam size (σ_x,σ_y)	0.3 mm
Twiss parameters (β_o,α_o)	0.7, 0.3

For this conventional FEL scenario, the alpha magnet will serve only as the energy filter element. From the optimization of the electron distribution at the RF-gun exit, the electrons at the head of the bunch with high energy level form a quasi-monogenetic beam. Therefore, compression in the alpha magnet for this useful part the bunch can be neglected. Some small energy spread will be induced during the post acceleration of the electron beam in the linac leading to the electron distribution suitable for the bunch compressor downstream the linac. The 180° achromat is used as both turn around section and as the magnetic bunch compressor. Electron beam optimizations for this case are presented in another contribution [7].

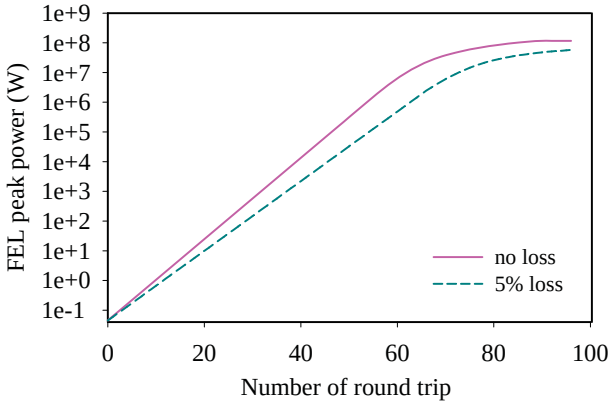

Figure 2: Simulated radiation power evaluation at the radiation wavelength of 100 μm for the electron rms bunch length of 2 ps without and with 5% power loss in the optical cavity.

The FEL mechanism in case of electron beams with bunch length shorter than the radiation wavelength has been studied and reported in [8]. This scenario is known as the pre-bunched FEL. The study results show that the saturation mechanism in the pre-bunched FEL seems to be different from the conventional FEL. The saturated peak power in this case is much higher than that for the long electron bunches. It has been proposed that to generate the THz light with the pre-bunch FEL, the electron beam with the bunch length less than 100 fs is required [8, 9].

We have previously shown that it is possible to generate electron bunches with an rms bunch length of less than 100 fs [10]. With this short bunches, the intense THz radiation from coherent Transition Radiation (TR) is expected to cover the wave number ranging from 5 cm^{-1} to 400 cm^{-1}. For this scenario, the alpha magnet will be used as a magnetic bunch compressor prior to the post acceleration by the linac. It will also be used as an energy filter utilizing its energy scrapers. The 180° achromat system for this case will be a turn-around section to save the space of the accelerator tunnel. Therefore, we can choose the position of the current experimental station to be the entrance of the 180° achromat. Then, the achromat section can be an isochronous magnetic system, which the beam characteristics before entering and after exiting the achromat system remain unchanged.

Since the FEL mechanism of the pre-bunched FEL cannot be simulated by using the well-known numerical

ISBN 978-3-95450-123-6

codes e.g. GENESIS, a further methodical study is required. The interaction between the electron beam and the optical fields in this case will be investigated and reported in the future.

ELECTRON BEAM OPTIMIZATIONS FOR PRE-BUNCHED FEL

Longitudinal Beam Dynamic Simulations

The FEL performance depends on both the longitudinal and transverse properties of the electron beam. Beam dynamics simulations using the code PARMELA [11] and BCompress [12] were performed to study the optimal longitudinal electron beam parameters suitable for driving the FEL. The transverse properties have been studied using the beam envelope optics code Particle Beam 2003 [13].

PARMELA simulations were performed to investigate electron beam dynamics inside the RF-gun including effects of the space-charge force. Results of optimization of the thermionic RF-gun for producing the femtosecond electron bunches for the linac-based FIR (THz) radiation source have been reported in [10]. The revised study for the injector system of the IR FEL has been performed based on some available information from the previous study. In PARMELA simulations, we assume that the cathode emits the uniform electron beam with 100,000 macro-particles at an emitted current of 2.9 A per 2856 MHz RF cycle. Therefore, each macro-particle represents a charge of 10.15 fC. Starting from these specifications, we assume that the entrance of the isochronous achromat system begins at the current TR station. Electron bunches will travel through the achromat section and reach the entrance of the undulator with unchanged longitudinal properties. The particle distribution in the energy-time phase spread of a single bunch with the kinetic energy of about 15 MeV is shown in Fig. 3.

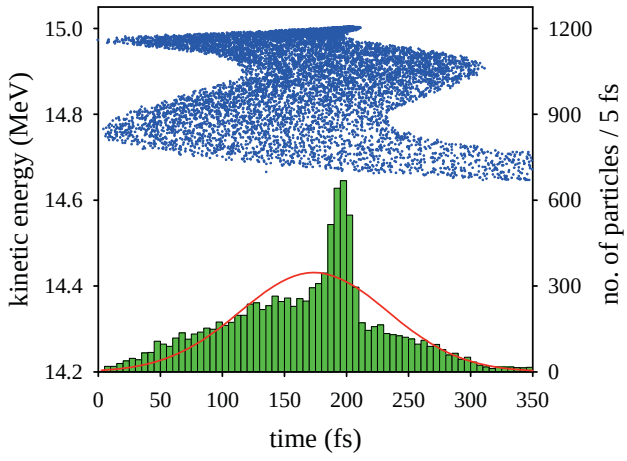

Figure 3: Simulated particle distribution in energy-time phase space of a single bunch at the entrance of the 180° acromat with histogram fitted by a Gaussian distribution with σ_z of 50 fs.

The relation between the relative rms energy spread of electrons and the bunch charge has been studied by selecting a fraction of the electron bunch using energy slits inside the alpha magnet vacuum chamber. A portion of electrons with different relative energy spreads are compressed differently inside the alpha magnet. By adjusting the alpha magnet gradient in the simulation, we can obtain the relationship between the energy spread and the bunch charge, which the results are shown in Fig. 4 for the case of an electron bunch length of 50 fs and 100 fs.

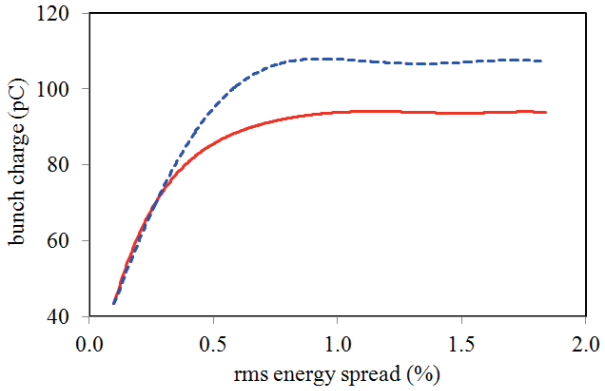

Figure 4: Simulated bunch charge as a function of relative rms energy spread for the electron bunch length of 50 fs (dash line) and 100 fs (solid line).

Results of the bunch compression study using the alpha magnet show that with a relative energy spread of below 0.7%, the bunch charge increase proportionally to the energy spread. Then, it stays constant with the bunch change of about 93 pC and 107 pC for the rms bunch length of 100 fs and 50 fs, respectively. This can be explained that with the rms energy spread larger than 0.7% the selected bunch contains some electrons with lower energies, which are not properly compressed inside the alpha magnet. Only the high energy electrons are compressed and form the condense distribution at the head of the bunch. Preliminary study results show that it is possible to produce the electron beam with the bunch length about or shorter than the suggested requirement for the pre-bunched FEL [8].

Optimization of Beam Transport Line

The beam envelope along the beam transport line from the RF-gun exit to the entrance of the achromat has been studied and optimized. Initial transverse beam parameters are estimated from the PARMELA distribution at the RF-gun exit with the rms beam size of 2.5 mm and the normalized beam emittance of 3.8 π mm-mrad. By carefully optimizing the parameters of each component along the beamline, we achieved the final beam at the entrance of the 180° achromat with the properties suitable for the FEL system. The proposed beam optics of the injector system is illustrated in Fig. 5. Some optimized

ISBN 978-3-95450-123-6

beam transverse parameters are shown together with longitudinal properties in Table 3.

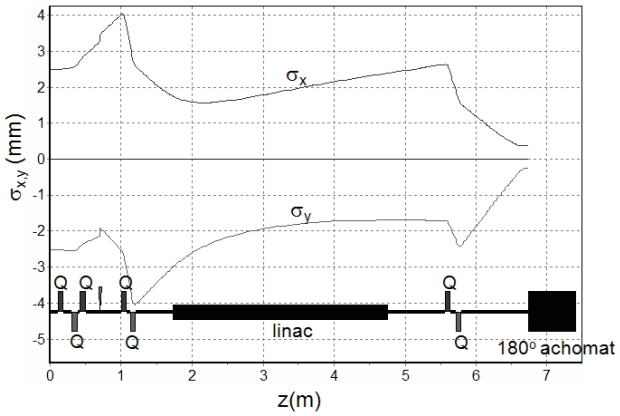

Figure 5: Simulated beam envelops from the exit of the RF-gun to the entrance of 180° achromat.

Table 3: Typical Parameters at the PBP Linac System and Optimized Electron Beam Parameters Using Beam Optics and Beam Dynamics Simulations

Parameter	**Value**
Microbunch repetition rate	2856 MHz
Macropulse repetition rate	1 -10 Hz
Current macropulse width	1-2 μs
Beam energy	15 MeV
Energy spread (rms)	0.7%
Minimum longitudinal rms bunch length (σ_z)	50 fs
Bunch charge (Q_b)	107 pC
Peak current (I_p)	844 A
Normalized rms emittance (ε_x, ε_y)	3.8 π mm-mrad
Horizontal beam size (σ_x)	0.394 mm
Vertical beam size (σ_y)	0.321 mm

CONCLUSION

The specifications of the injector system for the proposed IR FEL facility at Chiang Mai University in Thailand have been studied. Simulation and numerically studies showed that it is possible to use the existing linac system to produce electron beams with the specifications suitable for the IR FEL lasing requirements. The electron beam with a few ps bunch length can be used for the conventional IR FEL oscillator, while the electron beam with the bunch length less than 100 fs is considered for the pre-bunched FEL. By properly adjusting machine parameters, the 15 MeV electron beam with the minimum rms bunch length of 50 fs, a bunch charge of 107 pC and a peak current of 844 A can be produced. Further study will be performed to accumulate the useful information for technically modifying the current linac setup at Chiang Mai University to serve as the injector system for the future IR FEL.

ACKNOWLEDGMENTS

The authors would like to acknowledge the support by the Department of Physics and Materials Science at Chiang Mai University, the Thailand Center of Excellence in Physics, and the Thailand Research Fund.

REFERENCES

[1] G.P. Gallerano et al., in Proceedings of the 2004 Free Electron Lasers Conference, Trieste, Italy, FRBIS02.
[2] G.P. Gallerano et al., J. Infrared. Milli. Terhz Waves 30 (2009) 1351.
[3] V.P. Wallance et al., Brit. J. Derm. 151 (2004) 151, P.C. Ashworth et al., Opt. Express 17 (2009) 12444.
[4] A.J. Fitzgeld et al., Radiology 239 (2006) 533.
[5] C. Thongbai et al., Nucl. Instr. and Meth. A 587 (2008) 130.
[6] S. Reiche, Nucl. Instr. and Meth. A 429 (1999) 243.
[7] S. Supakul et al., "Beam Dynamics Simulation and Optimization of Electron Beam Properties for IR-FEL at Chiang Mai University," WEPD34, these proceedings.
[8] H. Hama et al., Nucl. Instr. and Meth. A 637 (2011) S57-S61.
[9] T. Muto et al., in Proceedings of the 2007 Free Electron Lasers Conference, Novosibirsk, Russia, WEPPH054.
[10] S. Rimjaem et al., Nucl. Instr. and Meth. A 533 (2004) 258.
[11] L.M. Young and J.H. Billen, Los Alamos National Laboratory Technical Note LA-UR-96-1835, 2002.
[12] H. Wiedemann, BCompress beam dynamics code, 2002.
[13] H. Wiedemann, Particle Beam 2003: Optics and Design Program, 2003.

ISBN 978-3-95450-123-6

THz RADIATION SOURCES BASED ON RF-LINAC AT CHIANG MAI UNIVERSITY

C. Thongbai#, P. Boonpornprasert, S. Chunjarean, K. kusoljariyakul,
S. Rimjaem, J. Saisut, S. Supakul
Chiang Mai University, Chiangmai, 50200, Thailand
Thailand Center of Excellence in Physics, Bangkok 10400, Thailand

Abstract

A THz radiation source in a form of coherent radiation from short electron bunches has been constructed at the Plasma and Beam Physics (PBP) research facility, Chiang Mai University. The accelerator system consists of an RF-gun with a thermionic cathode, an alpha-magnet as a magnetic bunch compressor, and a SLAC-type linear accelerator. Coherent transition radiation emitted from short electron bunches passing through an Al-vacuum interface was used as the THz radiation source. This THz radiation can be used as a source of the THz imaging system and THz spectroscopy. Details of the accelerator system and THz radiation production will be presented. A plan for extension to accommodate Free Electron Lasers (FEL) optimized for mid-infrared and far-infrared/THz radiation will also be discussed.

INTRODUCTION

THz radiation is electromagnetic radiation spectrum which has wavelength of 1000μm to 100 μm (300 GHz - 3 THz) and lies in gap between Microwave and Infrared. In the past, this gap is unexplored region but nowadays technologiesand applications of THz radiation were developed rapidly and were reviewed in [1-4]. A THz facility based on femtosecond electron bunches has been established at the Plasma and Beam Physics research facility (PBP), formerly the Fast Neutron Research Facility (FNRF), Chiang Mai University. Figure 1 shows a schematic layout of the system.The main components of the system are a thermionic cathode RF-gun, an alpha-magnet as a magnetic bunch compressor, a SLAC-type linear accelerator (linac), beam steering and focusing elements, and beam diagnostic instruments.

The 1-1/2 cell S-band RF-gun was designed and optimized [5] for bunch compression such that the first electron is accelerated and reaches the end of the half-cell just before the field becomes decelerating. It is then further accelerated through the full-cell to reach maximum kinetic energy of 2.0-2.5 MeV at the gun-exit depending on accelerating field gradients. Later electrons feel some decelerating fields and gain less and less overall energyresulting in a well-defined correlation between energy and time for bunch compression. Electron bunches of 20-30 ps from the RF-gun are then compressed in an α-magnet, where the particle path length increases with energy. This allows the lower energy particles, emitted later in each bunch, to catch up with the front for effective bunch compression. The optimized and compressed part of the electron bunch is filtered by energy slits located in the alpha-magnet vacuum chamber and then transported through the linac and the beam transport line to experimental stations. At the experimental station, the bunches are compressed to less than 1 ps [6]. These short electron pulses can be used to produce high intensity THz radiation in the form of coherent transition radiation. Typical operating parameters and electron beam characteristics are shown in Table 1.

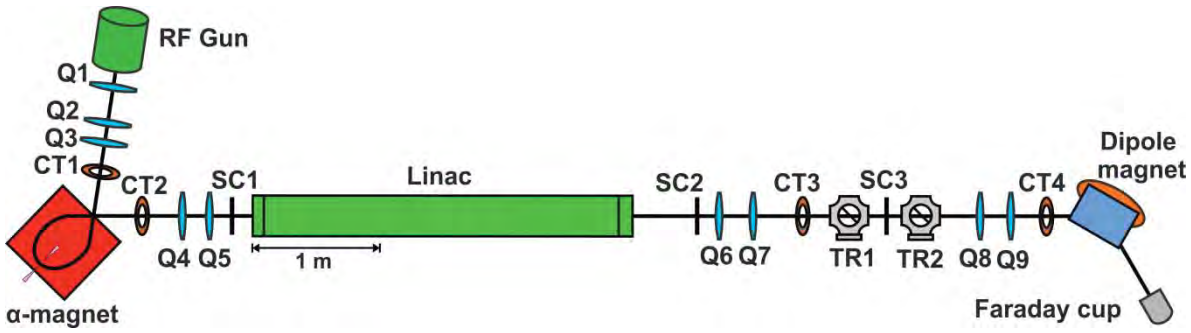

Figure 1: Schematic diagram of the accelerator system at Chiang Mai University for generation of short electron bunches and THz radiation [Q:quadrupole magnet, CT:current monitor, SC:screen, TR: transition radiation].

#chlada@yahoo.com

ISBN 978-3-95450-123-6

Table 1: Operating and Beam Parameters

Parameters	RF-gun	Linac
Max. beam energy [MeV]	2.5 - 3	10-15
Macropulse peak current [mA]	1000	150
Beam pulse length [μs]	~2	~0.8
Macropulserepetation rate [Hz]	10	10
Number of microbunch/macropulse	5700	2300
Number of electrons/macropulse	1.4×10^{9}	6×10^{8}

GENERATION OF THzRADIATION

Total electromagnetic radiation emitted from a bunch of *N* electrons at radiation frequency ω is

$$I(\omega) = NI_e(\omega)[1+(N-1)f(\omega)],$$

where $I_e(\omega)$ is the radiation intensity from a single electron and the bunch *form factor f(ω)* is the Fourier transformation of the longitudinal bunch distribution squared. As a consequence, the short bunch is suitable and desired for production of broadband radiation spectrum. At a wavelength about or longer than the bunch length, the radiation from an electron bunch becomes coherent and the intensity of coherent radiation, proportional to the number of radiating electrons squared, exceeds greatly that of incoherent radiation at the same wavelength. Electron bunches of around 100 fs can provide broadband radiation in THz regime covering up to 3 THz [7].

The electron beam after acceleration is used to generate THz radiation is in the form of coherent transition radiation (TR). At the experimental station, transition radiationis produced by placing an aluminium foil (Al-foil) in the electron path, representing a transition between vacuum and Al-foil. The Al-foil radiator is 25.4 μm thick and 24 mmin diameter. The radiator is tilted by 45° facing the electron beam direction. The backward transition radiation is emitted perpendicular to the beam axis and transmits through a high density polyethylene (HDPE) window of 1.25-mm-thick and 32-mm diameter.

A copper light cone or a THz lens are used to collect the THz radiation into a room-temperature pyroelectric detector. The radiation energy of 19 μJ per macropulse or a peak power of 24 W was measured by collecting over an acceptance angle of 160 mrad. Experimentally, the transition radiation spatial distribution as well as horizontal and vertical polarizations of radiation were observed using a PYROCAM and a wire-grid polarizer from Graseby-Spec (Model IGP223). The results are shown in Fig. 2. An asymmetry shown up in horizontally polarized beam should very well be a result of the Al-foil orientation which is tilted 45° horizontally as predicted theoretically.

The radiation spectrum measured using a Michelson interferometer is shown in Fig. 3 (dot-line). The available THz radiation covers from 5 cm^{-1} to around 80 cm^{-1} wavenumber (0.15 THz – 2.4 THz). At low frequency (< 5 cm^{-1}), the spectrum was suppressed by effects of the beam splitter and the periodic response is the effect of the pyroelectric detector [8]. The spectrum seem to extend to above 80 cm^{-1} (2.4 THz) where noise becomes dominate. These can be further minimized with better detection and amplification system.

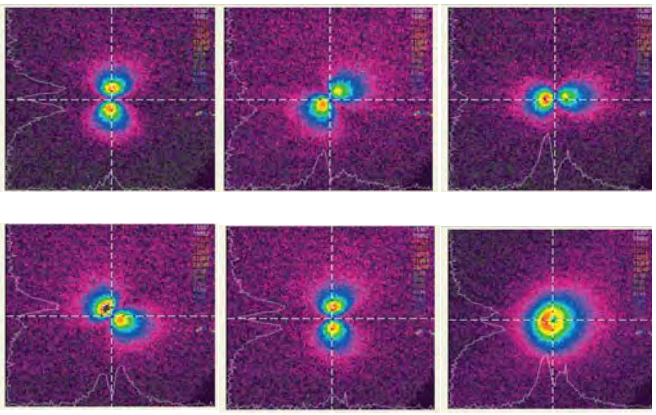

Figure 2: THz transition radiation profiles taken with a polarizer rotated 0, 45, 90, 135, 180 degree respectively. The last profile is taken without any polarizer.

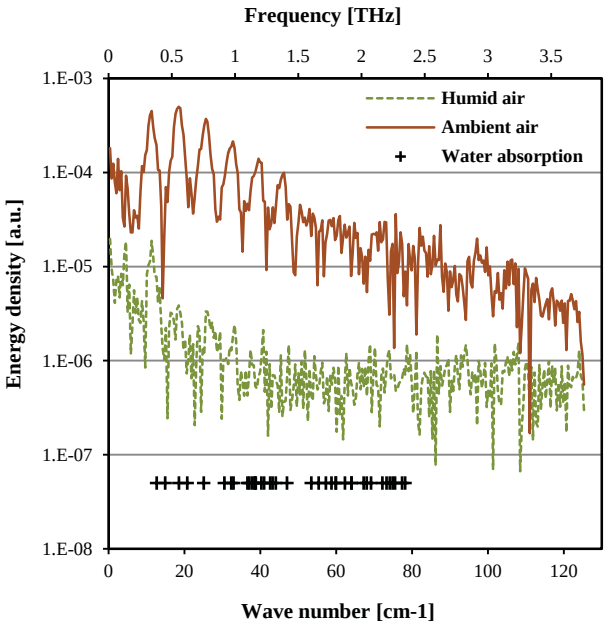

Figure 3: The radiation power spectra taken in humid air (solid) and in ambient air (dot-line).

THz SPECTROSCOPY AND IMAGING

THz spectroscopy can be done easily by measuring power transmission or power absorption of a sample via a Michelson interferometer and the Fourier Transformation. As shown in Fig. 3 (solid), the radiation spectrum taken in humid-air reveals several water absorption lines. Although phase information has been lost in the

ISBN 978-3-95450-123-6

measurement, optical constants of the sample can be obtained by some modeling or Kramers-Kronig calculation [9]. Dispersive Fourier Transform Spectroscopy (DFTS) [11] may also be used for direct determination of optical constants of a sample. In a DFTS setup, a sample is inserted in one arm of the interferometer, causing attenuation and dispersion of the radiation pulse. The attenuated and dispersed pulse can be recorded and its attenuation factor and phase shift can then be recovered. The attenuation and dispersion can be related to optical constants of the sample depending on the optical configuration of the measurements. With the DFTS technique, the phase information can be recovered in measurements using a Michelson interferometer. A THz imaging system has been setup and tested at PBP. For transmission measurement, THz radiation is focused on a sample which is scanned using an xy- translation stage controlled by a computer. The transmission intensity will be detected by a room-temperature pyroelectric detector. Computer program will be employed to calculate and analyze intensity at difference points on the sample for THz image construction. Figure 4 shows an example of THz imaging obtained from the leaf concealed in an envelope.

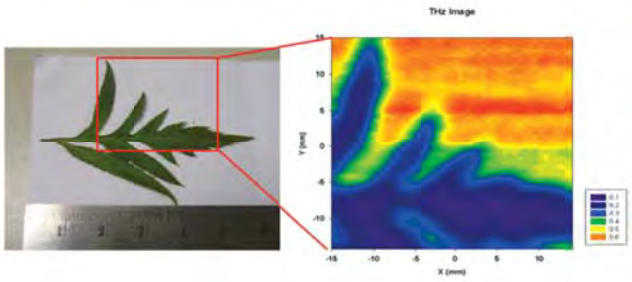

Figure 4: Leaf and its THz image.

FUTURE EXPANSION

As a plan to become a research facility centered on the production and utilization of femtosecond electron pulses and accelerator-based light sources covering the mid and far-infrared regime to wavelengths up to the THz regime. Preliminary designs of the extension have been studied as the diagrams shown in Fig. 5. A planar undulator can be added to the beamline to produce coherent undulator radiation from short electron bunches. The existing beamline can be extended and turned around by a 180° achromatic system to let the electron beam pass through an undulators and an optical cavity as an IR-THz FEL. Figure 6 shows results of a preliminary study of the radiation output from some electron bunch lengths and an undulator (22 periods of 0.077 m period length) with and without FEL optical cavity. The radiation outputs cover well beyond 6 THz spectral range. Details of the study to accommodate the extension are reported in [11-13].

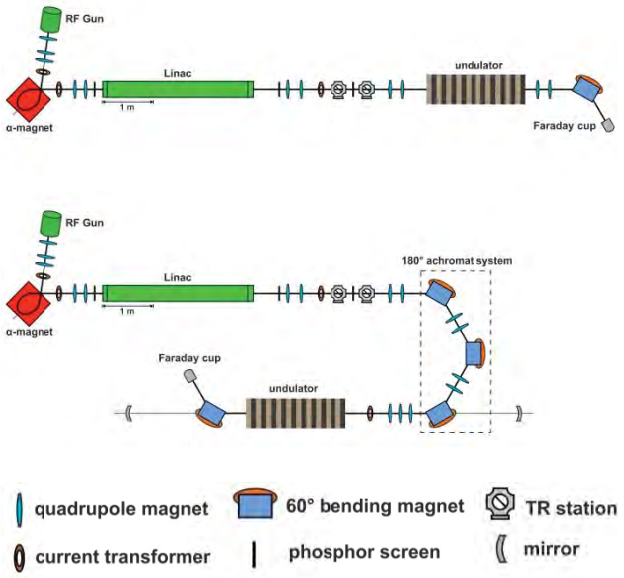

Figure 5: Diagrams for future expansion of the accelerator system with (bottom) and without (top) an FEL cavity.

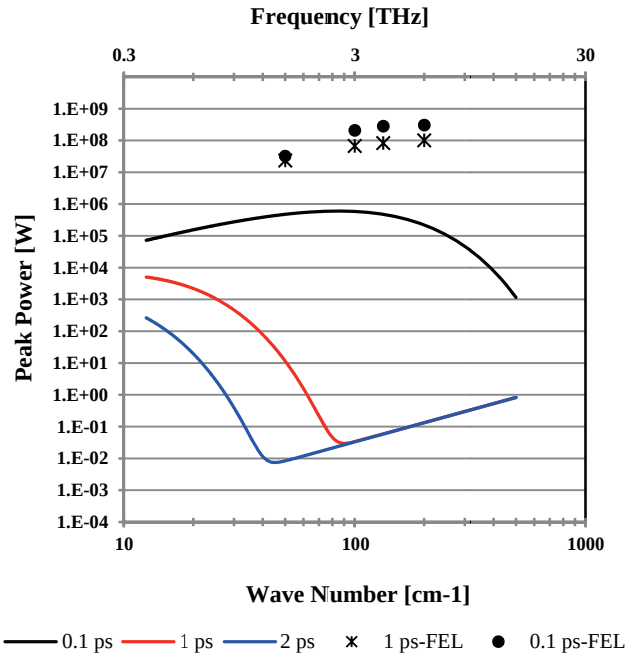

Figure 6: Radiation output from some electron bunch lengths and an undulator (22 periods of 0.077 m period length) with and without FEL optical cavity.

CONCLUSION

Intense THz radiation can be generated in form of coherent transition radiation by using short electron bunches which are available at the Plasma and Beam Physics Research Facility (PBP), Department of Physics and Materials Science, Chiang Mai University. The available THz radiation covers from 5 cm^{-1} to 80 cm^{-1} wavenumber. This THz radiation can be used as a source of the THz imaging system and far-infrared or THz

ISBN 978-3-95450-123-6

spectroscopy. Plan for future expansion with a planar undulator will allow more coverage of the IR-THz spectrum regime.

ACKNOWLEDGMENT

We would like to thank Mr. M. Rhodes, Mr. N. Kangrang and Mr. V. Jinamoon for their technical support. We would like to acknowledge the support from the National Research Council of Thailand (NRCT), the Thailand Research Fund (TRF), the Thailand center of Excellence in Physics (ThEP-Center), the (Thailand) Commission on Higher Education (CHE) and Chiang Mai University.

REFERENCES

[1] P. H. Siegel, "Terahertz Technology", *IEEETrans. Microwave. Theory & Tech*. 55 (2002) 910-928.
[2] B. Ferguson and X.C. Zhang, "Materials for terahertz science and technology", *Nature materials* 1 (2002) 26-33.
[3] G.P. Galleranoet al., "Overview of terahertz radiation sources", *in the 2004 FEL conference*, 2002, pp. 216-221.
[4] M. Tonouchi, "Cutting-edge terahertz technology", *Nature photonics*, 1 (2007) 97-105.
[5] S. Rimjeam et al., "Femtosecond electron bunches from an RF-gun" Nucl. Instr. and Meth. A 533 (2004) 258-269.
[6] C. Thongbai et al., "Femtosecond electron bunches, source and characterization" Nucl. Instr. and Meth. A 587 (2008) 130-135.
[7] C.S. Thongbai and T. Vilaithong, "Coherent transition radiation from short electron bunches", Nucl. Instr. and Meth. A 581 (2007) 874-881.
[8] C. Thongbai and H. Wiedemann, "Reviewand analysis of autocorrelation electron bunch length measurements", Nucl. Instr. and Meth. A. **568** (2006) 923 -932.
[9] Bell, R. J., *Introductory Fourier Transform Spectroscopy*, (London: Academic Press, 1972).
[10] Birch, J.R. and Parker, T.J., Dispersive fourier transform spectroscopy. In *Infrared and Millimeter Waves V.2: Instrumentation*, Button, K.J. Ed. (NewYork: Academics Press,1979).
[11] S. Rimjaem et al., "Injector System for Linac-based Infrared Free-electron Laser in Thailand" WEPD32, these proceedings.
[12] S. Chunjarean et al., "Simulation and Optimization Studies of an IR Free-electron Laser based on RF-Linac" WEPD35, these proceedings.
[13] S. Supakul et al., "Beam Dynamics Simulation and Optimization of Electron Beam Properties for IR-FELs at Chiang Mai University" WEPD34, these proceedings.

ISBN 978-3-95450-123-6

LINAC-BASED THZ IMAGING AT CHIANG MAI UNIVERSITY

J. Saisut#, P. Boonpornprasert, K. Kusoljariyakul, S. Rimjaem, C. Thongbai, Department of Physics and Materials Science, Chiang Mai University, Chiang Mai 50200, Thailand
M.W. Rhodes , P. Tamboon, STRI, Chiang Mai University, Chiangmai 50200, Thailand

Abstract

At the Plasma and Beam Physics Research Facility (PBP), Chiang Mai University, intense THz radiation is generated in a form of coherent transition radiation from femtosecond electron bunches. The THz radiation is used as a source of THz imaging system which was successfully setup and tested. The radiation is focused onto a sample which will be scanned using an xy-translation stage. The transmission or reflection at different points of the sample are recorded to construct a THz image. Details of the setup and the experimental results from the system will be presented. The THz imaging to accommodate a future IR-THz Free Electron Laser (FEL) will also be discussed.

INTRODUCTION

A THz facility based on femtosecond electron bunches has been established at the Plasma and Beam Physics Research Facility (PBP), Chiang Mai University. Femtosecond electron bunches are generated from a system consisting of an RF-gun with a thermionic cathode, an alpha-magnet as a magnetic bunch compressor and a linear accelerator as a post acceleration section. At the experimental station, the bunches are compressed to less than 1 ps. The experimental results reported in [1] show that electron bunches as short as σ_z =200 fs can be generated from the system. Typical operating parameters and electron beam characteristics of the facility are complied in Table 1.

The femtosecond electron bunches can be used to produce high intensity THz radiation in the form of coherent transition radiation by placing an aluminium foil (Al-foil) 45° in the electron path, representing a transition between vacuum and conductor [2]. The backward transition radiation is emitted perpendicular to the beam axis as shown in Fig. 1. The radiation is collimated by a 1-inch 90° parabolic mirror and transmits through a high density polyethylene (HDPE) window of 1.25-mm-thick and 32-mm diameter. The available THz radiation covers wavenumbers from 5 cm^{-1} to around 80 cm^{-1} which corresponding to a frequency range from 0.3 THz to 2.4 THz. This THz radiation is used as a source of the THz imaging system.

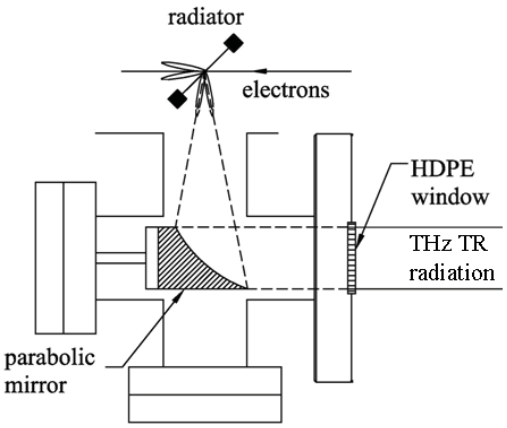

Figure 1: Setup to generate THz Transition radiation.

THZ IMAGING SYSTEM

A schematic diagram of the THz imaging system (transmission measurement) at the Plasma and Beam Physics Research Facility (PBP), Chiang Mai University is illustrated in Fig. 2 for transmission or reflection measurement. THz radiation is focused on a sample which will be scanned using an xy- translation stage

Table 1: Operating and beam parameters

Parameters	RF-gun	Linac
Maximum beam energy (MeV)	2.0-2.5	6 - 12
Macropulse peak current (mA)	700-1000	5-150
RF-pulse length (μs)	2.8	8
Repetition rate (Hz)	10	10
Beam-pulse length (μs)	2	0.8
Number of microbunches per macropulse	5700	2300
Number of electrons per microbunch	1.4×10^9	1.4×10^8

#jatuporn.saisut@cmu.ac.th

ISBN 978-3-95450-123-6

controlled by a computer. The transmission or reflection intensity will be detected by a room-temperature pyroelectric detector. Computer program will be employed to calculate and analyze intensity at difference points on the sample for THz image construction.

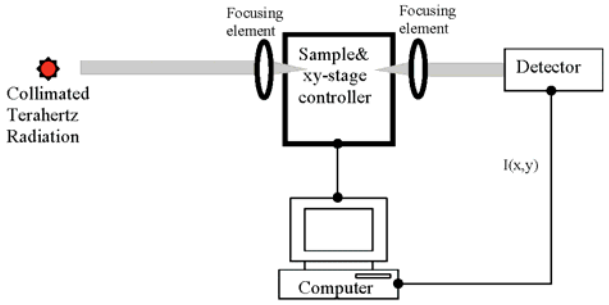

Figure 2: Schematic diagram of the THz imaging system at Chiang Mai University.

The Transmission Mode THz Imaging

The transmission mode THz imaging is suitable for materials which are transparent to THz radiation, e.g. non metallic and non polar materials. It is possible to construct contrast images from totally transmitted signals of various materials. Figure 3 shows the THz imaging system setup beside the electron beamline at the experimental station and this setup use Tsurupica lens as a focusing element.

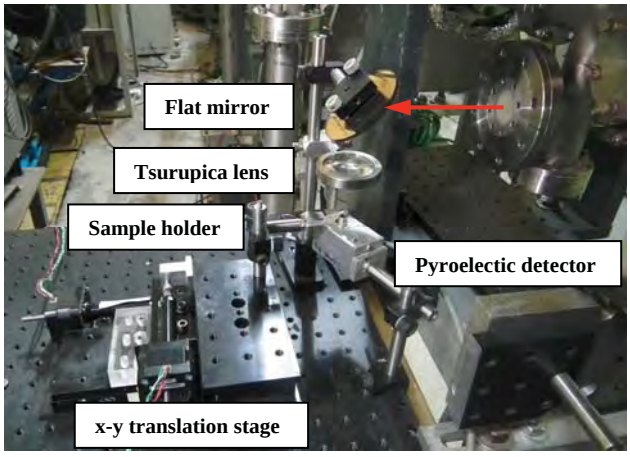

Figure 3: The THz imaging system setup at the experimental station.

By using a copper cone as a focusing element, the first THz image circular cuts of various sizes in an Al-foil [Fig. 4(a)] placed in an envelope is shown in Fig. 4(b). The holes diameter varies from 4 – 9 mm. Positions and spot sizes of the patterns from the THz image correspond well to those of the Al-foil sample.

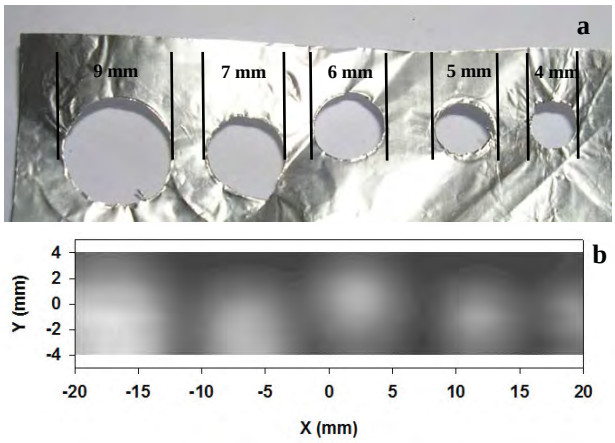

Figure 4: (a) Optical and (b) THz images of circular cuts of various sizes inan Al-foil.

Figure 5(a) is an Al-pattern and Fig. 5(b) is its THz image scanned using the Tsurupica lens as a focusing element. The THz image can demonstrate the rough feature of the sample but not its details especially at the big slot of the sample. Since our THz radiation source is board band, the focusing spot size of the THz radiation beam is about 3-4 mm. By using a copper mesh as a high pass THz filter [3, 4], the focusing spot size can be reduced to about 2 mm [4]. The copper mesh filter is placed in front of the focusing element in the imaging system. The image quality can be improved when the sample is scanned using mesh filter. Visually, more details of the sample can be seen as shown in Fig. 5(c).

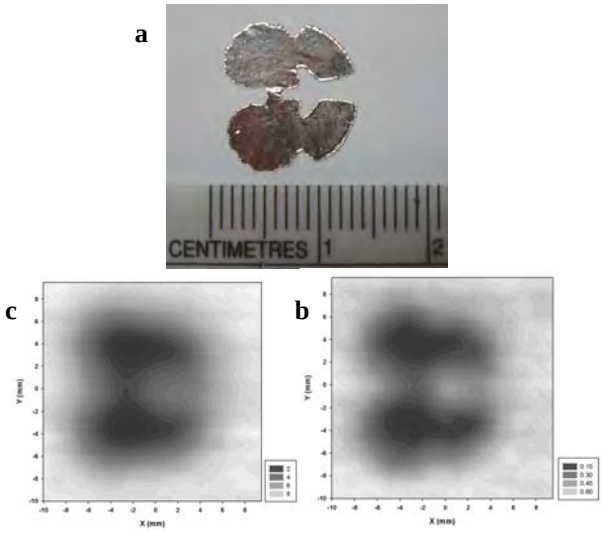

Figure 5: Cut pattern from Al-foil and its THz images; (a) Optical image of the sample, (b) its THz images achieved without mesh filter and (c) its THz image achieved with the mesh filter.

By using a transmission mode THz imaging, the THz image of a fresh leaf which contains water contents inside is successfully demonstrated. The THz image of a leaf sample [Fig. 6(a), (c)] placed in an envelope is shown in Fig. 6(b), (d). The low intensity area of THz image is

ISBN 978-3-95450-123-6

corresponding to the leaf. Obviously, it shows the shape of the leaf which corresponds to its optical image.

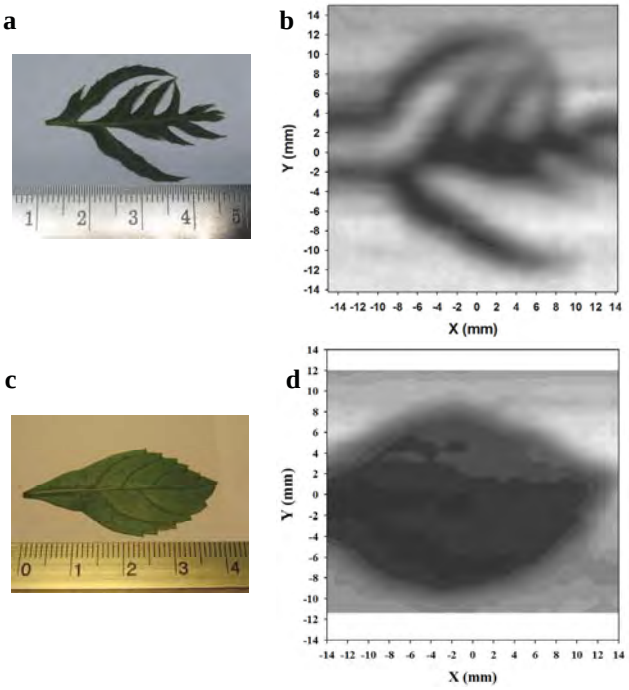

Figure 6: Leaf samples and its THz images; (a), (c) Optical images of the leaf which clearly shows the leaf structure and (b), (d) its THz images achieved with the mesh filter.

The Reflection Mode THz Imaging

The reflection mode THz imaging is suitable for materials which reflect THz radiation, e.g. metallic samples. The reflection mode THz imaging setup at PBP is shown in Fig. 7. A collimated THz beam is reflected off a gold-coated mirror to a THz lens of 6-cm focal-length. The beam is then focused onto a sample at approximately 30° incident angle. The reflected signal from the fuel cell is collected by another THz lens of 3-cm focal-length and continued to a pyroelectric detector. The sample under investigation is placed on top of the X–Y translational stages and scanned using computerized motion controllers.

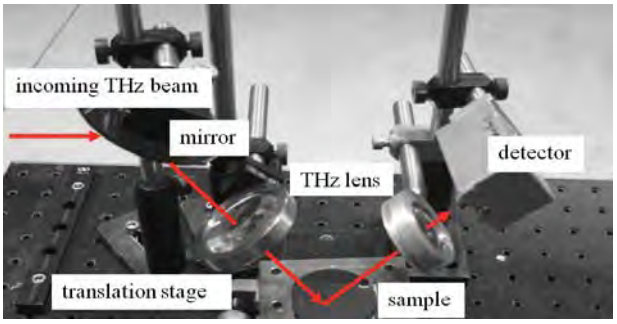

Figure 7: the reflection mode THz imaging setup.

Identification of Water in Flow Channels of PEM Fuel Cells using THz imaging [5] has been studied. A model cell of a PEM fuel cell shown in Fig.8(a) is machine-through-brass flow channel plate which sealed the bottom side of the plate tightly with a cloth tape. Then some channels were filled with water and the cell was covered by a Si window (see Fig. 8(b)) that allows THz access. The THz image in Fig. 8(c) shows a water filled channel and an unfilled channel indicated as air-filled in the figure. The darker area reveals absorptive region within the flow channels, with the darkest region lies in water-filled channel. In order to clearly distinguish the water-filled and the air-filled region, we perform a line-scan plot (along the dash-line shown in Fig. 9). It is evident that we are able to identify water presence in the flow field with THz imaging.

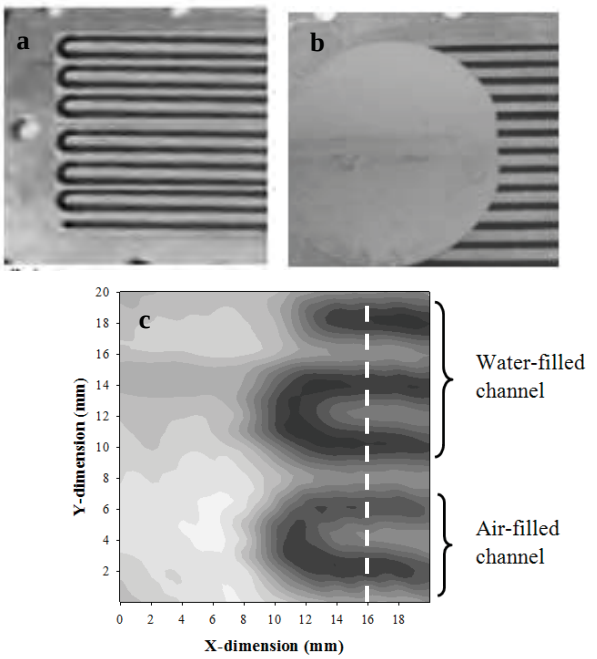

Figure 8: Photographs of a machine-through-brass flow channel plate (a) before and (b) after covering with Si window; (c) THz image of (b).

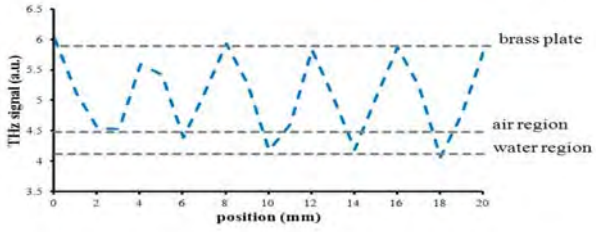

Figure 9: THz-signal line-scan along the dashed line in THz image.

CONCLUSION

At PBP, Chiang Mai University, the transmission mode and reflection mode THz imaging systems were successfully setup and tested. We successfully

ISBN 978-3-95450-123-6

demonstrate THz images of Al-foil patterns which reflect the THz radiation, THz images of water content samples which absorb the radiation and THz images of the model cell of a PEM fuel cell. The image resolution is limited by focusing spot size and it can be improved by scanning samples with mesh filter. To extend the ability of the imaging system based on the transition radiation source, the simple scanning system can be combined with the Michelson Interferometer to allow "Interferometric Imaging" [6]. This system is able to provide both information; typical THz imaging and the radiation power spectrum. The power spectrum, the Fourier Transform of the interferogram, from various positions on the sample will provide THz images of different frequencies. Both the transmission mode and reflection mode THz imaging experiments will be performed using a future IR-THz Free Electron Laser (FEL) which have wavelengths of 200μm to 50 μm as a source of the systems.

ACKNOWLEDGMENT

We would like to thank Mr. N. Kangrang and Mr. V. Jinamoon for their technical support. We would like to acknowledge the supports from the National Research Council of Thailand, the Thailand Research Fund, the (Thailand) Commission on Higher Education, the Thailand Center of Excellence in Physics and Chiang Mai University.

REFERENCES

[1] J. Saisut et al. Nucl. Instrum. Methods Phys. Res. A, 637(1) Supplement 1(2011) S99-S106.
[2] C. Thongbai, et al., Nucl. Instr. and Meth. A 587 (2008) 130
[3] R. Ulrich, Infrared Phys. **7**, 33 (1967)
[4] J. Saisut, Ph.D. thesis, Chiang Mai University, 2011.
[5] P. Buaphad, M.S. thesis, Chiang Mai University, 2012.
[6] W.L. Chan, J. Deibel and D.M. Mittleman, Rep. Prog. Phys. **70,** 1325(2007)

ISBN 978-3-95450-123-6

Simulations and Measurements of Dipole and Quadrupole Magnets for PBP-CMU Linac System

P. Boonpornprasert[1,2*], S. Rimjaem[1,2], J. Saisut[1,2], and C. Thongbai[1,2]
[1]Department of Physics and Materials Science, Faculty of Science,
Chiang Mai University, Chiangmai 50200, Thailand
[2]ThEP Center, Commission on Higher Education, Bangkok 10400, Thailand

***Abstract*—** *The PBP-CMU Linac system has been established to generate femtosecond electron bunches and to study their applications, especially for generation of coherent terahertz (THz) radiations. The dipole magnet and the prototype quadrupole magnet for the system have been designed and fabricated in house. Both the simulated and the measured results were used for evaluating the magnet performance and will be used as a guideline for design and fabrication of magnet devices in the future.*

***Keywords*— dipole magnet, quadrupole magnet, magnetic field measurement, Radia code.**

1. INTRODUCTION

The femtosecond electron and photon pulses research laboratory under the Thailand Center of Excellent in Physics (ThEP Center) has been established at the Plasma and Beam Physics Research Facility (PBP), Chiang Mai University (CMU). The laboratory aims are to develop a relativistic electron source with femtosecond (10^{-15}) bunch length and to study its applications, especially generation of coherent terahertz (THz) radiations via transition radiation (TR). The radiation in THz frequency range is widely used, for example, for non-ionizing spectroscopy, chemical and biological imaging, medical imaging and airport security scanning [1,2].

A layout of the PBP-CMU Linac system is shown in Figure 1(a). The main components are an RF-gun with a thermionic cathode, an alpha magnet, a linear accelerator (Linac), experimental stations, a dipole spectrometer magnet and a Faraday cup. Furthermore, along the beamline, there are quadrupole and steering magnets for beam focusing and guiding; and beam diagnostics instruments for probing the beam properties. Detail of the current PBP-CMU Linac system was reported in [3].

The PBP-CMU Linac system demands some dipole magnets and quadrupole magnets to support an expansion of the system to an infrared free electron laser (FEL) facility as the layout shown in Figure 1(b). We have planned to construct the magnet iron cores by using Thai local low carbon steel. Generally, low carbon steel is classified by percent by weight of carbon (%C) in the steel. Each type of carbon steel has different B-H saturation curve. For this reason, magnet simulations with various type iron core materials are needed to evaluate the efficiency of the magnet. The result comparisons will be used for the iron core material choosing.

This paper presents and compares the magnetic field simulation results and the magnetic fields measurement results for a dipole magnet and a quadrupole magnet. Both

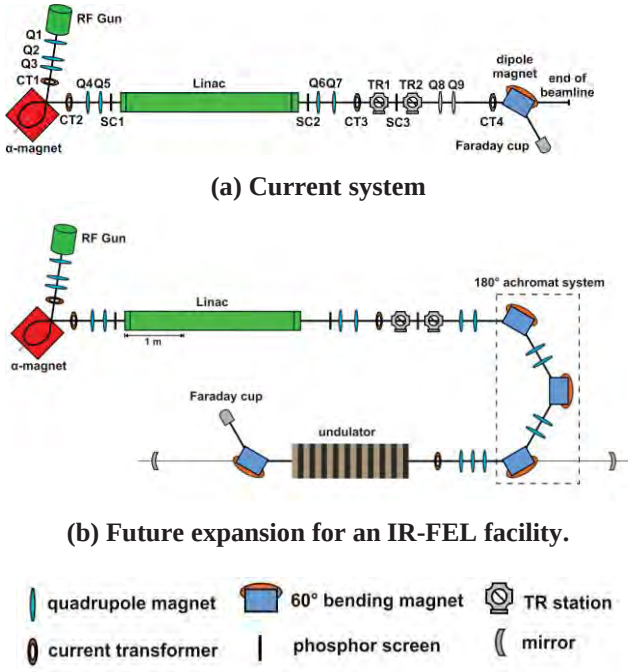

Fig. 1. Layout of the PBP-CMU Linac system.

the dipole magnet and the prototype quadrupole magnet have been designed [4] and fabricated in house at our facility.

2. DIPOLE MAGNET

Dipole magnet is a magnetic deflection device. In our system the dipole magnet serves as an electron beam dump and a beam energy analyzer. Figure 2 illustrates a C-shape dipole magnet with a gap of *h*. The magnet is excited by electric currents in the coils which are mounted around the two poles. The magnetic field (*B*) produce by the dipole magnet is

$$B = \frac{\mu_0 NI}{h}, \qquad (1)$$

*Corresponding author
Email : ppugpug@gmail.com

where I is the excitation current, N is the number of turns in a coil and h is the air gap. Note that, the equation (1) is only an approximation since it neglects fringe fields and iron saturation [5]. The radius of curvature (ρ) of an electron trajectory in dipole fields is often expressed in terms of the dipole field (B) and the electron momentum (p) as

$$\frac{1}{\rho}[\mathrm{m}^{-1}] = 0.2998\frac{B\ [\mathrm{T}]}{p\ [\mathrm{GeV/c}]}. \qquad (2)$$

The dipole magnet of the PBP-CMU Linac system, as shown in Figure 3, was placed around the end of the beamline (Figure 1(a)). The magnet is a C-shape magnet which has been designed to deflect a 15 MeV electron beam by 60° into a Faraday cup. The magnet has 125×125 mm square pole faces with the gap of 40 mm. The magnet coils were made from water cooled copper wire.

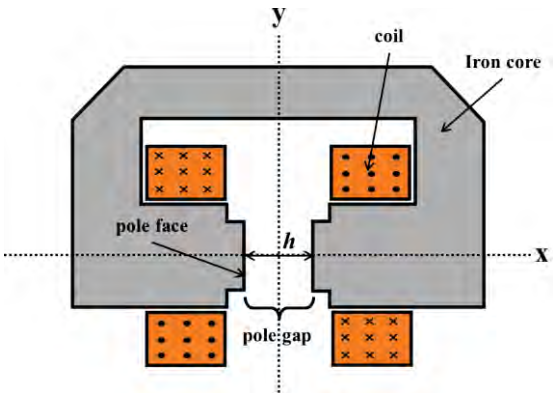

Fig. 2. C-shape dipole magnet layout

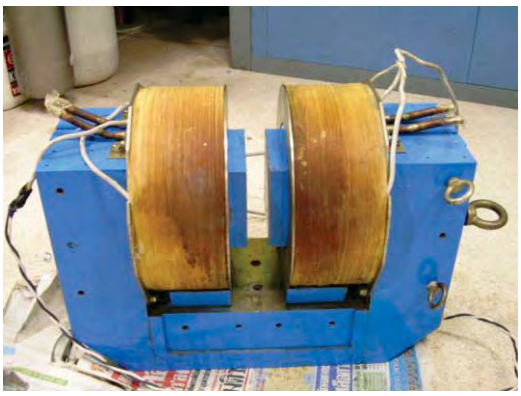

Fig. 3. Dipole magnet of the PBP-CMU Linac system

3. QUADRUPOLE MAGNET

With a finite emittance, the transverse beam size will increase as the beam move through a drift space. Some quadrupole magnets are therefore needed for focusing the beam transverse sizes. Figure 4 shows a quadrupole magnet layout with a bore radius of R. The magnet consists of 4 pole pieces, 4 coils and a circular yoke. The red arrow lines in Figure 3 are the magnetic field lines which point from the north poles (N) to the south poles (S). A quadrupole magnet focus electron beam on one transverse axis while defocus on the other. Therefore beam focusing for both transverse axes demands at least 2 quadrupole magnets, called a quadrupole doublet.

The magnetic fields of a quadrupole magnet are zero at the center of transverse positions and linearly increase with the transverse positions as

$$B_x = gy, \qquad B_y = gx, \qquad (3)$$

where B_x and B_y are the magnetic field components, x and y are the positions in the transverse axes and g is the magnetic gradient. The magnetic gradient depends on the excitation current (I) as

$$g = \frac{2\mu_0 NI}{R^2}, \qquad (4)$$

where N is the number of turns per coil. Focusing properties of a quadrupole magnet is described by the focusing strength k, whose value depends on the magnetic gradients.

$$k\ [\mathrm{m}^{-2}] = 0.2998\frac{g\ [\mathrm{T/m}]}{\beta E\ [\mathrm{GeV}]}, \qquad (5)$$

where β is the particle relativistic factor [6].

The quadrupole magnet which is presented in this work is the prototype quadrupole magnet of the PBP-CMU Linac system as shown in Figure 5. Some of the magnet parameters are shown in Table 1.

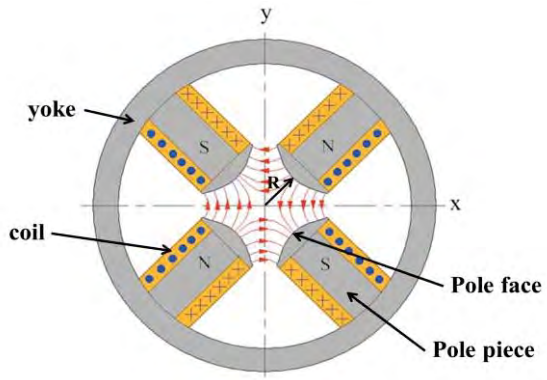

Fig. 4. Quadrupole magnet layout showing components and field lines

Fig. 5. Prototype qaudrupole magnet of the PBP-CMU Linac system

Table 1. Quadrupole magnet parameters

Parameter	Value
Thickness (ℓ)	60 mm
Bore radius (R)	20 mm
Number of turns in a coil (N)	110 turns
Coil (15 AWG) Diameter	1.450 mm

4. MAGNET SIMULATIONS

In this work, we use the RADIA code for magnet simulation. RADIA code [7], running as an add-on application to Mathematica [8], is developed by insertion devices laboratory of the European Synchrotron Radiation Facility, France. The code is used for calculating the 3D magnetostatic fields of magnetic devices, especially the devices in charged particle accelerators.

There are 3 types of carbon steel materials available in RADIA and their details are shown in Table 2. The B-H saturation curves are show in Figure 6. The RADIA simulations of the dipole magnet and the quadrupole magnet were evaluated with various iron core materials listed in Table 2. Figure 7(a) and Figure 7(b) show the RADIA simulation model of the dipole magnet and the quadrupole magnet, respectively.

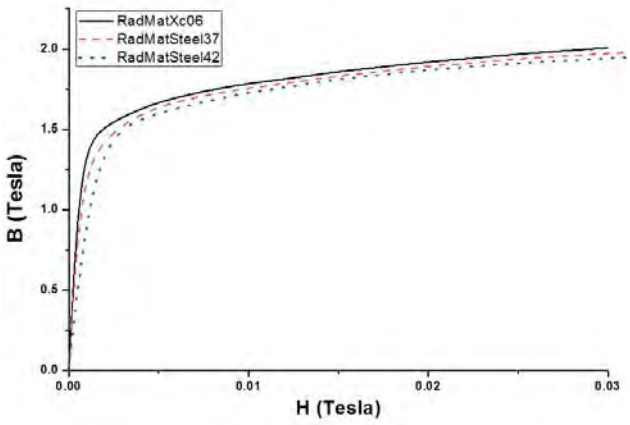

Fig. 6. B-H saturation curves of RADIA carbon steel materials

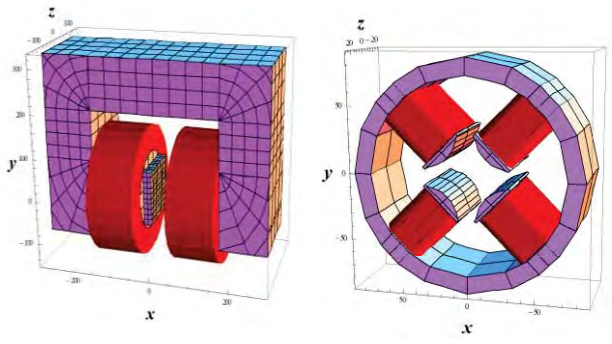

(a) Dipole magnet **(b) Quadrupole magnet**

Fig. 7. Model of the magnets for RADIA simulation

Table 2. Carbon percentage for low carbon steels available in RADIA

Name in RADIA code	% carbon (by weight)
RadMatXc06	0.06
RadMatSteel37	0.13
RadMatSteel42	0.16

5. MAGNET MEASUREMENTS [9,10]

The magnetic field measurement device is a Hall probe of a size $1.0\times1.3\times0.2$ cm^3 (GMW Group 3 Digital Hall Effect Teslameter). Figure 8 shows measurement setup for the dipole magnet. The hall probe was attatched to a holder which can be moved along y- and z-axes. For the quadrupole magnet, the measurement setup is shown in Figure 9. The magnet was placed on the measurement stand where probe could be moved within the quadrupole field region. The Hall probe was placed on x- and z- axes translation stages equipped with linear actuators and can be moved precisely through computer interface. The magnet is excited by a current regulated DC power supply and a 0.01Ω shunt resistor was used to determine the supplied current.

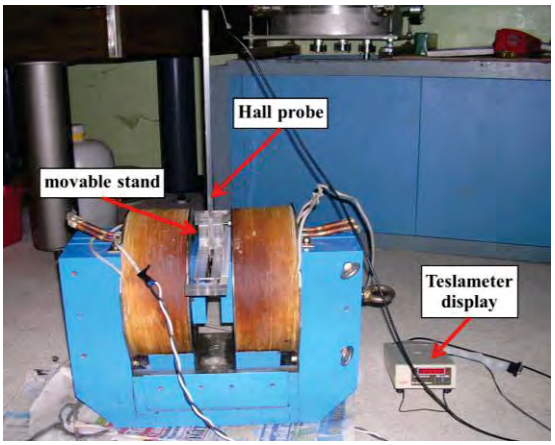

Fig. 8. Dipole magnet measurement setup

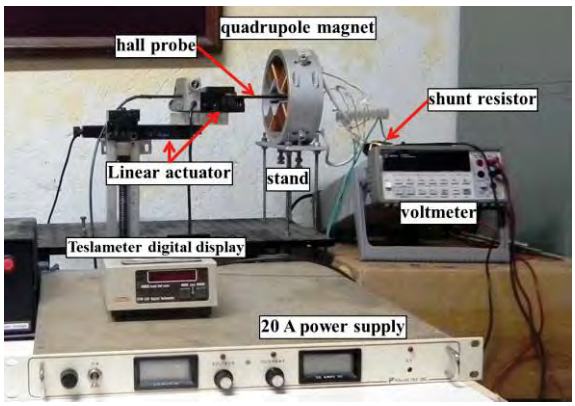

Fig. 9. Quadrupole magnet measurement setup

6. SIMULATION & MEASUREMENT RESULTS

Dipole Magnet

The dipole magnet excitation curve was measured by measuring the magnetic fields B_y at the pole center while increasing currents from 0 to 18 A with 0.5 A step. The measurement results and RADIA simulations results are shown together in Figure 10. The equation from fitting of measurement data is

$$B = 0.0459I + 0.0244 . \quad (9)$$

This equation will be used for evaluate the magnetic field values from the excitation currents. The simulation and the measurement results show that, at the same excitation current, carbon percentage in the magnet core affects to the magnetic field intensity. The magnet core with lower carbon percentage can generate higher magnetic field.

The magnetic fields in yz-plane were measured and the results are shown Figure 11. The field distribution benefits for the electron deflection angle and energy calculation.

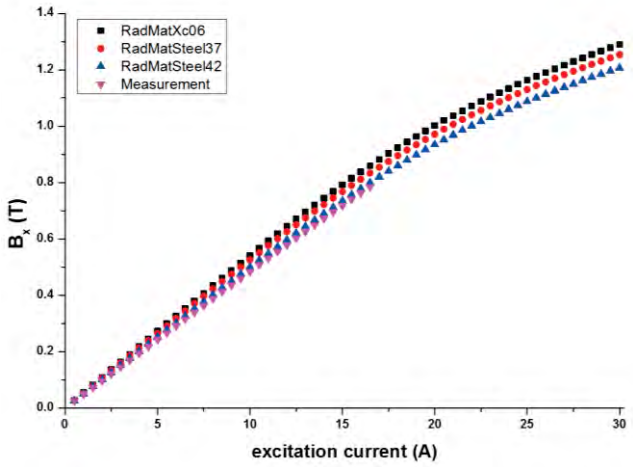

Fig. 10. Dipole magnet excitation curves

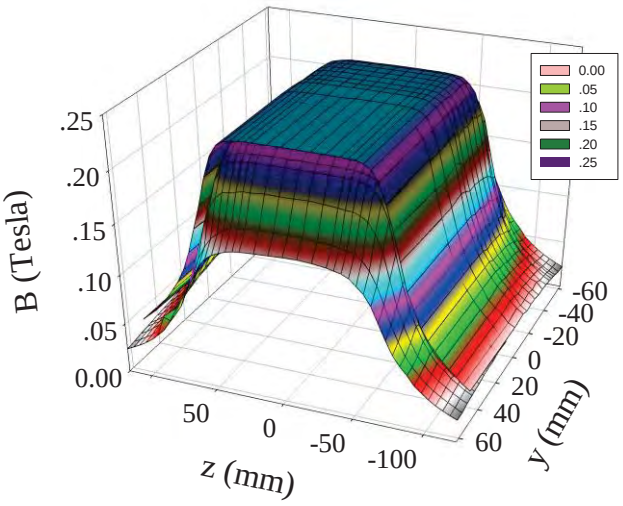

Fig. 11. Measured magnetic field distribution of the Dipole magnet (I = 5A).

Quadrupole Magnet

The quadrupole magnet excitation curve was measured by measuring the fields at (x,y,z) = (20,0,0) mm position, while increasing current from 0 - 18 A with 0.5A step. The results in Figure 12 show that the saturation effect starts to occur around 10.5 A for the measurement and at higher current for the simulations. Polynomial fit of the curves in unsaturated region (0-10.5A) and saturated region (10.5-18.0A) are

$$g = 5.62I + 1.57 , \quad (9)$$

$$g = -0.11 I^2 + 7.63I - 8.33 , \quad (10)$$

respectively. These equations will be used in the magnet control and operation of the accelerator system. The comparisons between the simulation and the measurement results are corresponding to the dipole magnet as the magnet core with lower carbon percentage generate higher magnetic field gradient.

For transverse gradient measurement, The B_y field along the x-axis were recorded at (x,y,z) = (0 to 40,0,0) mm with a 1 mm step and the field gradients were then calculated. The results are shown in Figure 13 along with RADIA simulation results. The average gradient, within the bore radius range (0-20 mm), from the measurement (for 5 A) is 29 $\times 10^{-4}$ T/mm and the average gradients from simulation results are 30.1, 32.2 and 33.5 $\times 10^{-4}$ T/mm for RadMatSteel42, RadMatSteel37 and RadMatXc06, respectively.

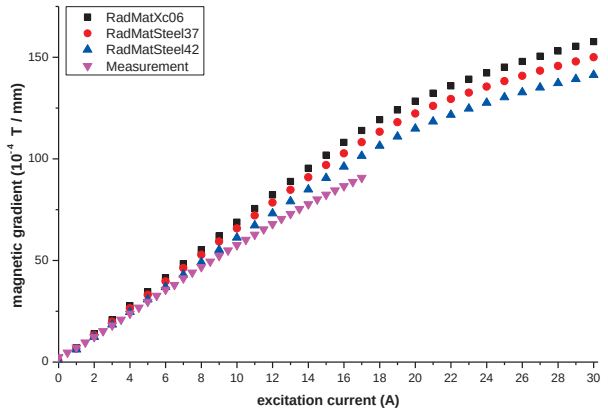

Fig. 12. Quadrupole magnet excitation curves.

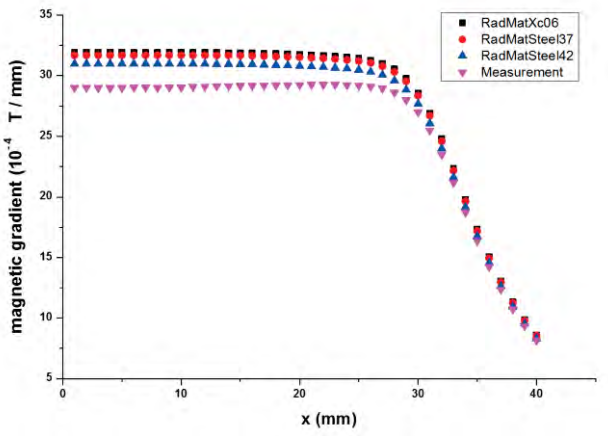

Fig. 13. Quadrupole magnet gradients along x-axis (I = 5A).

The effective length of a quadrupole magnet is the length which is derived from the longitudinal field profiles of the magnet as [5,6]

$$\ell_{\text{eff}} = \frac{\int g \cdot dz}{g_0}, \qquad (11)$$

where g_0 is the gradient at the center of the magnet along z. For the effective length measurement, we measured the magnetic field B_y along z-axis at the position x = 10 mm and y = 0 mm. The measurement result and the simulation results are shown in Figure 14. The effective lengths can then be calculated by using (11) with the integral term, $\int g \cdot ds$, equals to the area under a graph in Figure 14 and g_0 equal to the gradient value at z = 0 mm. The measured effective length is 76.6 mm and the effective lengths from simulation are 76.9, 77.0 and 77.0 mm for RadMatSteel42, RadMatSteel37 and RadMatXc06, respectively.

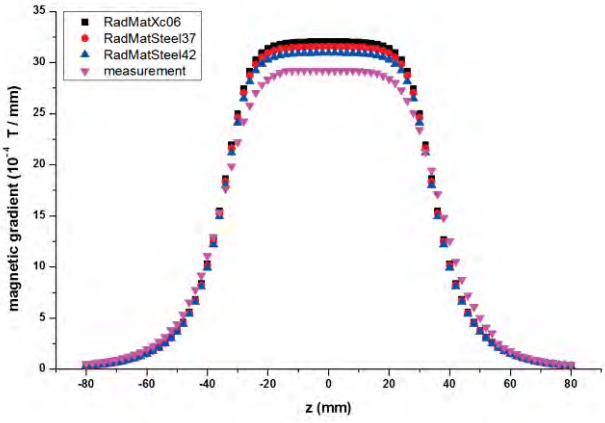

Fig. 14. Quadrupole magnet gradient along z-axis (I = 5A).

7. CONCLUSION

The simulations by using RADIA code and the measurements of the dipole magnet and the prototype quadrupole magnet were conducted and their results were analyzed. The simulations can evaluate well the magnet properties; including, the excitation curves and the field distributions for the dipole magnet; the excitation curves, the transverse gradient and the effective length for the quadrupole magnet. at the same excitation current, carbon percentage in the magnet core affects to the magnetic field intensity. The magnet core with lower carbon percentage generates higher magnetic field intensity. The excitation curves and field distributions from the measurements will be used in the magnet control and operation of the accelerator system. Both the simulated and the measured results will be used as a guideline for design and fabrication of magnets for the 180 degree achromat system in the future expansion for an IR-FEL facility.

ACKNOWLEDGEMENT

Authors would like to thank Mr. P. Wichaisirimongkol, Mr. K. Kusoljariyakul, Mr. N. Kangrang and Miss S. Chunjareon for technical supports. Authors would like to acknowledge the support from the National Research Council of Thailand (NRCT), the Thailand Research Fund (TRF), the (Thailand) Commission on Higher Education (CHE), the Thailand Center of Excellence in Physics (ThEP), and the department of Physics and Materials Science, Chiang Mai University.

REFERENCES

[1] Siegel, P.H. 2001. Terahertz Technology, *IEEETrans. Microwave. Theory & Tech*. 55: 910-928.

[2] Tonouchi, M. 2007 Cutting-edge terahertz technology, *Nature photonics*, 1: 97-105.

[3] Thongbai, C.; et al. 2008. Femtosecond Electron Bunches, Source and Characterization. *Nuclear Instruments and Method A* 587: 130-135.

[4] Russenschuck, R. 2003. Electromagnetic design of accelerator magnets. In *CERN Accelerator School: Intermediate Course on Accelerator Physics*. Zeuthen, Germany, 25–26 september. pp 411-440.

[5] Tanabe, J.T. (2005). Iron dominated Electromagnets. Singapore: World Scientific Publishing.

[6] Wiedemann, H. 2007. Particle Accelerator Physic, 3 ed. New York: Springer.

[7] Retrieved August 25, 2012 from the World Wide Web: http://www.esrf.eu/Accelerators/Groups/ InsertionDevices/Software/Radia

[8] Mathematica is a registered trademark of Wolfram Research, Inc.

[9] Umezawa, M. et al. 1999. Magnetic Field Measurement of the Air Slot Dipole Magnet. In *Proceeding of PAC1999*. New York, USA, 29 March – 2 April. pp 3366-3368.

[10] Takeuchi, T., et al. 2004. Magnetic Field Measurement of Quadrupole Magnets for S-LSR. In *Proceeding of EPAC2004*. Lucerne, Switzerland. 5-9 July .pp 1693-1695

Optimization of Longitudinal Electron Beam Properties for Linac-based Infrared Free-electron Laser at Chiang Mai University

S. Suphakul[1, 2], S. Chunjarean[2], C. Thongbai[1, 2], and S. Rimjaem*[1, 2]
[1]Department of Physics and Materials Science, Faculty of Science,
Chiang Mai University, Chiang Mai 50200, Thailand
[2]Thailand Center of Excellence in Physics, CHE, Bangkok 10400, Thailand

***Abstract*—** *A study to upgrade the linear accelerator (linac) system at the Plasma and Beam Physics (PBP) Research Facility at Chiang Mai University (CMU) to be an injector system for an infrared (IR) free-electron laser (FEL) is underway. The current PBP linac system consists of an S-band thermionic cathode RF-gun, a bunch compressor in a form of alpha-magnet and a SLAC-type accelerating structure. Since characteristics of the emitted FEL light strongly depend on electron beam properties, a dedicated work to develop and optimize the injector system to drive the FEL is particularly important. In this contribution, the results of numerical study to optimize the longitudinal electron beam properties as well as some preliminary results of FEL simulations are presented and discussed.*

***Keywords*— beam dynamics, infrared free-electron laser, FEL injector, linac-based FEL**

1. INTRODUCTION

At the Plasma and Beam Physics (PBP) Research Facility, Chiang Mai University, the project to produce THz transition radiation based on femtosecond electron bunches has been estabilised for many years [1]. The accelerator system consists of an S-band (2.856 GHz) thermionic RF electron gun [2], a magnetic bunch compressor in a form of an alpha-magnet [3], an S-band travelling wave linear accelerator (linac), and various beam diagnostic components. Electron beams with a bunch charge of about 16-96 pC and an rms bunch length as short as 70 fs were experimentally measured.

When the electron bunches with the above mentioned bunch length pass through an undulator, the radiation with a frequency of about 0.3 to 3 THz is emitted in phase resulting in an intense coherent radiation. However, the intensity of the coherent radiation falls off at the frequency higher than 3 THz or at the wavelength shorter than 100 μm. When the radiation wavelength is shorter than the electron bunch length, the incoherent radiation part dominates the coherent radiation part. To increase the radiation intensity, an external electric field can be used to stimulate the electrons to emit more coherent radiation via a microbunching process.The external field must have a frequency and phase such that the electrons loss their energy into the radiation. This mechanism is a basic principle in production of free-electron lasers, which can be achieved either using a long undulator, or an external seed laser, or a reclying spontaneous undulator radiation. The later principle is commonly used in a compact, low energy, and long radiation wavelength FEL.

*Corresponding author (S. Rimjaem):
Tel +66 53 943 379, Fax +66 53 222 776
Email address: sakhorn.rimjaem@cmu.ac.th

A possibility to develop an infrared free-electron laser (IR FEL) facility is studied at Chiang Mai University. The project focuses on the production and utilization of the mid-infrared (MIR) and far-infrared (FIR) or THz radiation based on a linac injector and free-electron laser technology [4]. The goal of the project is to produce the intense coherent radiation with tunable wavelengths covering from 2.5-20 μm (MIR) to 20-200 μm (THz).

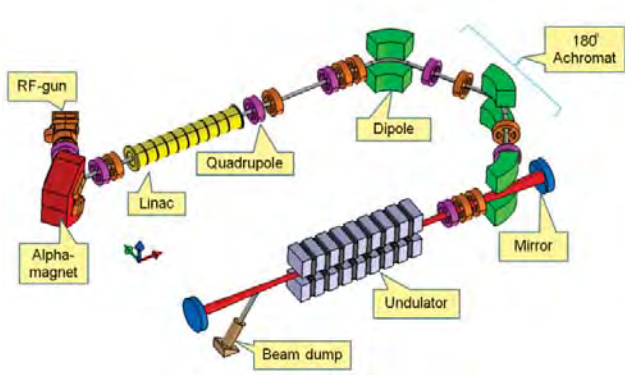

Fig.1. Schematic layout and components of the possible IR FEL system at Chiang Mai University, Thailand

A plan to upgrade the existing PBP linac system to be the injector for both coherent THz transition radiation experimental station and free-electron lasers is proposed. The foreseen FEL facility will consist of a thermionic cathode RF-gun, an alpha-magnet, an S-band SLAC-type linac, a 180° achromat section, a planar type undulator, and an optical resonator (Figure 1). Details of the components in the current PBP linac system were already reported in [1]. The 180° achromat section, the undulator magnet, and the optical cavity are new components which are under detailed consideration. The undulator magnet is a planar type with 22 periods and a total length of 1.67 m. The optical cavity composes of two symmetric spherical mirrors with a coupling hole on one of the mirrors. To design and optimize the 180° achromat section, we adopt the magnet lattice of the Kyoto University Free-Electron Lasers (KU-FEL) for initial study. The achromat section

consists of three 60° bending magnets and two sets of doublet quadrupole magnets. Details of the KU-FEL achromatic system have been described in [5]. Schematic layout of the proposed IR FEL at Chiang Mai University is shown in Figure 1.

For benchmark, we have investigated the injector parameters of the MARK-III FEL of Duke University, USA [6] and the FEL–SUT of Tokyo University, Japan [7]. Both facilities use the same type of the electron source, the magnetic bunch compressor and the accelerating section as the current PBP linac system. Electron beam and undulator parameters of the MARK-III FEL and the FEL-SUT are shown in Table 1.

Table 1. Parameters of electron beam, undulator, and FEL wavelengths at MARK-III and FEL-SUT

Parameters	MARK-III	FEL-SUT
Electron beam		
Average energy (MeV)	25-45	40
Energy spread (%)	0.3	1.0
Peak current (A)	15.45	>20
Bunch length (ps)	0.5-3	2-3
Bunch charge (pC)	140	-
Undulator & FELs		
Period length (mm)	23	32
Number of period	47	43
Deflecting parameter	-	0.6-2.5
Radiation wavelength (μm)	2-9	4-46

Based on the parameters in Table 1, the beam dynamics study and optimization of the proposed injector system are performed to achieved the proper electron beam parameters for driving the IR FEL. The computer code PARMELA (Phase And Radial Motion in Electron Linear Accelerator) [8] has been used to investigate multi-particle beam dynamics from the RF-gun to the exit of the 180° achromat and to optimize the electron beam lattice parameters. For the FEL radiation due to the interaction between optical fields and electron beams, the study has been studied using the numerical code GENESIS 1.3 [9]. Some preliminary results of the FEL simulation are presented and discussed in the last section of this paper.

2. ELECTRON BEAM OPTIMIZATION

The FEL performance depends greatly on electron beam characteristics. Generally, the injector system for the FEL facility should produce electron beams with high peak current, small transverse emittance, and low energy spread in order to generate intense coherent FEL light in an undulator. In this study, we focus on optimization of longitudinal electron beam properties by adjusting the parameters of three main components; the RF-gun, the linac, and the 180° achromatic system.

PARMELA simulations were performed to study electron beam dynamics in all components, except the alpha magnet. Since the goal of the optimization aims to produce electron beams with a very low energy spread (<1%), the electrons with high energy level have been optimized to form a quasi-monogenetic beam at the head of the bunch. Therefore, the compression in the alpha-magnet for this useful part of the bunch can be neglect. In this case, the alpha-magnet will serve only as the energy filter element. Some small energy spread will be induced during the post acceleration of the electron beam through the linac leading to the electron distribution suitable for the bunch compression downstream the linac. In our case, the 180° achromat is used as both turn around section and as the magnetic bunch compressor. For the simulation of multi-particle beam dynamics, we assume that the cathode emits a uniform stream of 30,000 (macro) particles per 2856 MHz with a current of 2.9 A. Thus, a single particle represents a charge of 33.85 fC, which equivalents to 2.12×10^5 electrons.

Beam Dynamics Simulation of the RF-gun

The RF-gun at the PBP facility is a one and a half-cell S-band resonant cavity with a thermionic cathode and a side coupling cavity. To simulate the RF field distribution inside the RF-gun, the code SUPERFISH is used [10]. Then, the particle-in-cell code PARMELA is utilized to track multi-particles through the fields obtained from the SUPERFISH simulation.

The accelerating field gradients of both half- and full-cell cavities were adjusted to produce an electron bunch with low energy spread, especially at the head of the bunch. These concentrated electrons at the head of the bunch will be the main contribution in the FEL lasing. The field ratio of the RF-gun is defined as a ratio of the accelerating field amplitudes at the cathode plane and at the center of the full-cell. For the field ratio of 1:2 with the accelerating field gradients of 35 and 70 MV/m, the RF-gun provides an electron beam with low energy spread at the head of the bunch. The three dimensional electron beam distributions at the RF-gun exit are shown in Figure 2. The distributions for transverse and logitudinal phase spaces are shown in Figures 3 and 4, respectively.

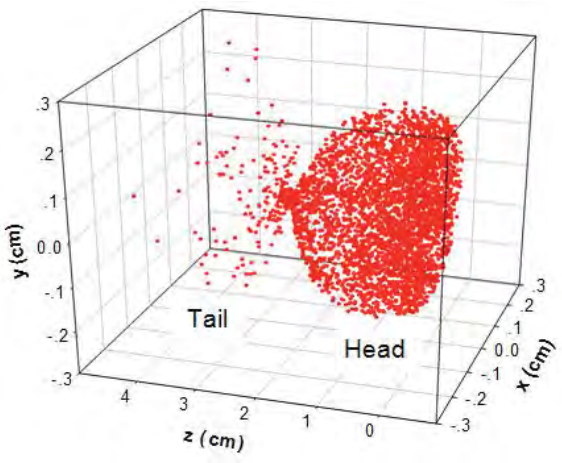

Fig.2. Three dimensional particle distributions at the RF-gun exit for the field ratio of 1:2 and the accelerating field amplitudes of 35 and 70 MV/m

The electron bunch that actually exits the RF-gun is about 100 ps long (Figure 4). The high energy electrons with small energy spread are accumulated at the head of

the bunch of about 10-15 ps, which is the most useful fraction of the bunch. Then, the electron bunches are filtered by the energy slits inside the vacuum chamber of the alpha-magnet to remove low energy electrons. For the RF-gun condition noted above, we set the energy filter level at 3.81 MeV. This leads to the output electron beams with the maximum electron energy of 3.91 MeV and the rms energy spread of 0.82%. Parameters of the electron beam after energy filtering using the alpha-magnet energy slits are listed in Table 2.

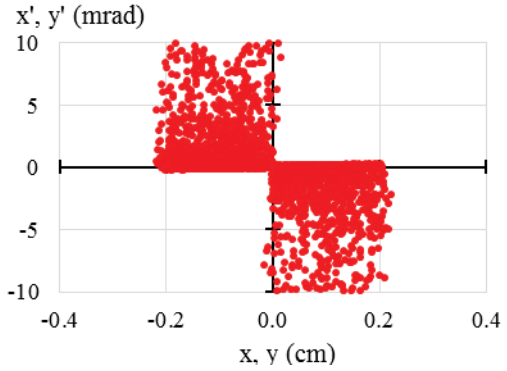

Fig.3. Particle distributions in the transverse phase space (x-x′ and y-y′ plane) at the RF-gun exit

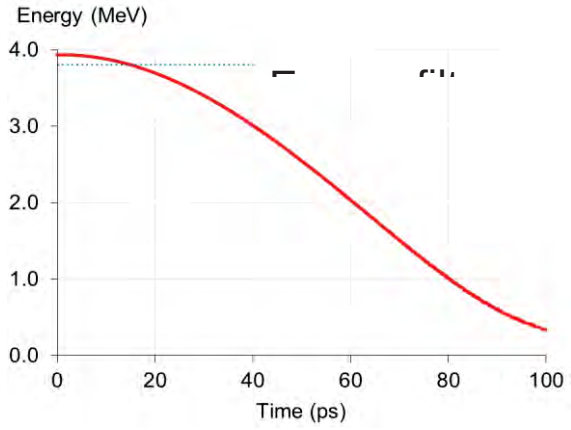

Fig.4. Particle distributions in longitudinal phase space (energy-time) at the RF-gun exit

Table 2. Parameters of RF-gun and its output electron beam

Parameters	Value
Field ratio	1 : 2
Accelerating field	Half-cell: 35 MV/m Full-cell: 70 MV/m
Beam output energy - Average - Maximum - Minimum	 3.91 MeV 3.94 MeV 3.81 MeV
Energy spread	0.82 %
Energy filter level	3.81 MeV
Bunch length (FWHM)	15 ps
Bunch charge	33 pC

Beam Dynamics Simulation of the Linac

The linac at the PBP facility is an S-band SLAC-type travelling wave linear accelerator. It can be used to accelerate an electron beam to reach a maximum energy of about 30 MeV. In this study, we consider that the electron beam is accelerated through the linac to reach an average energy of about 15 MeV. In order to achieve an electron bunch with low energy spread, the linac initial phase is varied between 0^o and -90^o relative to the reference particle phase at the entrance of the linac. Then, the number of particles is counted within the desired energy bin (1% in this study). Figure 5 shows the number of particles within 1% energy spread normalized to the total number of the particles entering the linac for different linac phases.

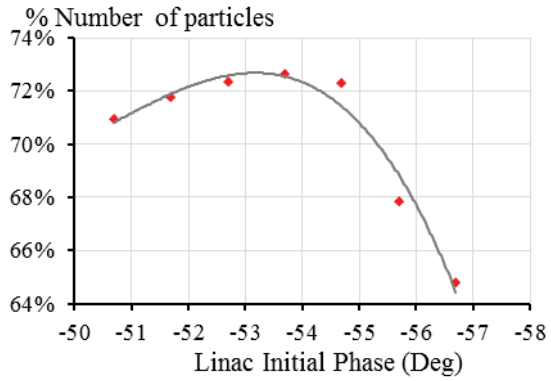

Fig.5. Number of particles within 1% energy spread normalized to the total number of the particles entering the linac as a function of the linac initial phase respect to the reference particle phase entering the linac

The energy gain from the linac can be adjusted by optimizing the product of the accelerating field (E_0) and the transit time factor (T). This product is linearly proportional to the electron energy at the linac exit. The product of accelerating field and transit time factor (E_0T) has been optimized to achieve the electron beam with low energy spread and short bunch length at the exit of the 180^o achromat section. The optimized value of E_0T is 4 MV/m, which provides the final maximum and average electron energies of 15.6 and 15.4 MeV, respectively. The longitudinal phase space distributions of the particles at the exit of the RF-gun and at the exit of the linac for the linac initial phase of -53.7^o are illustrated in Figure 4. Parameters of the electron bunch after exiting the linac are shown in Table 3.

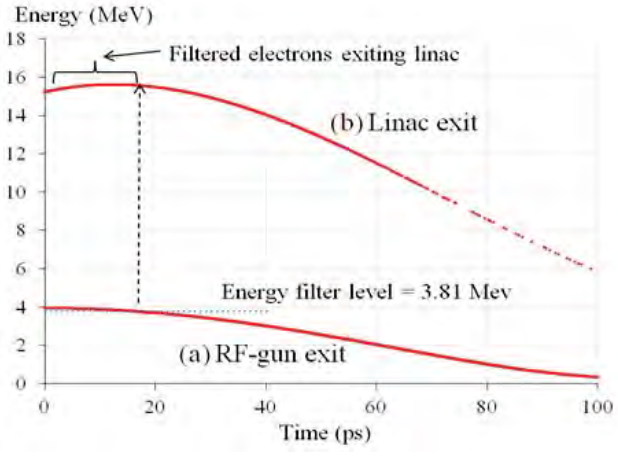

Fig.5. Particle distributions in longitudinal phase space of all particles at (a) the RF-gun exit for the field ratio of 1:2 and the accelerating field amplitudes of 35/70 MV/m and (b) the linac exit with the linac accelerating initial phase of -53.7^o and the product between the accelerating field gradient and the transit time factor (E_0T) of 4 MV/m

Table 3. Parameters of linac and the electron beam exiting the linac

Parameters	Values
Accelerating length	3 m
Initial phase	-53.7° w.r.t. reference particle entering linac
Beam output energy - Average - Maximum - Minimum	 15.4 MeV 15.6 MeV 15.2 MeV
Energy spread	0.78 %
Bunch length (FWHM)	10.1 ps
Bunch charge	33 pC

180° Achromat and Bunch Compressor

In this study, we consider the 180° achromat as a turn-around element and a magnetic bunch compressor. It is an triple bend type consisting of three dipole magnets and two sets of quadrupole magnet, which are placed at the straight section between the dipoles (see Figure 1). The goal of the optimization of this section is to establish the parameters of the dipole and the quadrupole magnets as well as the drift lengths for transporting the electron beam through and exit the section with a shorter bunch length and no change of energy spread.

The dipole magnets have the deflecting angle of 60° and the effective length of 35 cm. The electron bunch length can be adjusted by changing the gradient of the doublet quadrupoles to have the minimum bunch compression condition. At the electron beam energy of 15.4 MeV, the simulated shortest electron bunch length of 0.85 ps is achieved with the doublet quadrupoles' strengths of 56.4 m^{-2} and -44.6 m^{-2}, respectively. The particle distributions and energy spectrum of the electron bunch at the exit of the 180° achromat section with the optimized condition are shown in Figure 6. Optimized specifications of the components in the 180° acromat and the electron beam parameters at the exit of the acromat section are listed in Table 4.

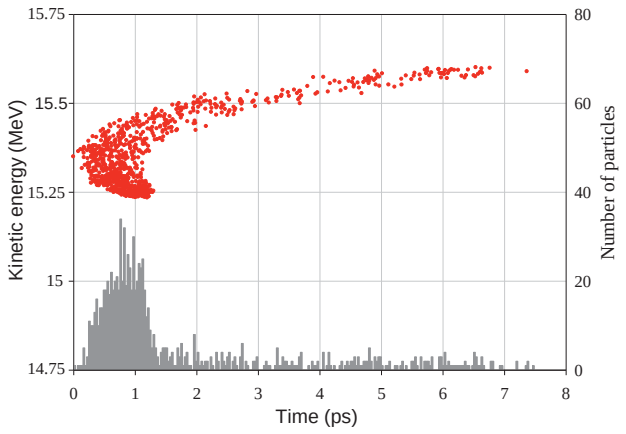

Fig.6. Particle distributions in longitudinal phase space at the 180° achromat exit

Table 4. Specifications of the components in the 180° achromat and the electron beam parameters at the achromat exit

Parameters	Values
Bending magnet - Defection angle - Effective length - Curvature	 60° 35 cm 2.99 m^{-1}
Quadrupole - Focusing strength - Defocusing strength	 56.4 m^{-2} - 44.6 m^{-2}
Beam output energy - Average - Maximum - Minimum	 15.4 MeV 15.6 MeV 15.2 MeV
Energy spread	0.74 %
Bunch length (FWHM)	0.85 ps
Bunch charge	33 pC
Peak current	38.8 A

3. FEL SIMULATIONS

The code GENESIS 1.3 is used to simulate the FEL radiation due to the interaction between optical fields and an electron beam inside the undulator. At this early stage the simulations have been performed in the time-independent mode. The undulator considered for the IR FEL at CMU is a planar type undulator with a period length of 77 mm and a number of periods of 22. The undulator gab is adjustable to vary the deflection parameter (K) between 0.4 and 2.6 in order to provide the radiation wavelengths of 50- 200 μm. As an example, the electron beam with an average energy of 15 MeV and an rms bunch length of 1 ps is used in the initial simulations. The undulator specifications and some preliminary required beam parameters used in the simulations are listed in Table 5. The optical cavity length is set to be 5 m with the diffraction and out coupling losses in the cavity of 5%.

Figure 7 shows the time evolution of the simulated FEL radiation peak power at radiation wavelengths of 200, 100, 75 and 50 μ m for the electron beam with the average energy of 15 MeV, rms energy spread of 0.5%, and peak current of 30A. It can be seen that the longer FEL radiation wavelength reaches the power saturation faster than the shorter one. The numbers of round trips needed to accumulate the radiation amplification until reaching the saturation condition are within 60 turns for the radiation wavelengths of 200, 100 and 75 μm, while it needs 120 turns for the case of 50 μm. It seems that GENESIS simulation in the time-independent mode has a limit of the simulation for the case of electron bunch length shorter than the radiation wavelength. Further study using the code GENESIS in time-dependent mode together with the Optical Propagation Code (OPC) [11] will be performed.

Table 5. Undulator and electron beam parameters used in FEL simulations

Parameters	Value
Undulator type	Planar
Undulator period length	7.7 cm
Number of undulator period	22
Undulator deflecting parameter	0.036 - 3.39
Beam energy	15 MeV
Energy spread	0.5%
Bunch length (RMS)	1 ps
Peak current	30 A
Normalized emittance (ε_x, ε_y)	3 mm-mrad
Beam transverse size (σ_x, σ_y)	0.42 mm
Twiss parameters (β_o, α_o)	0.72, 0

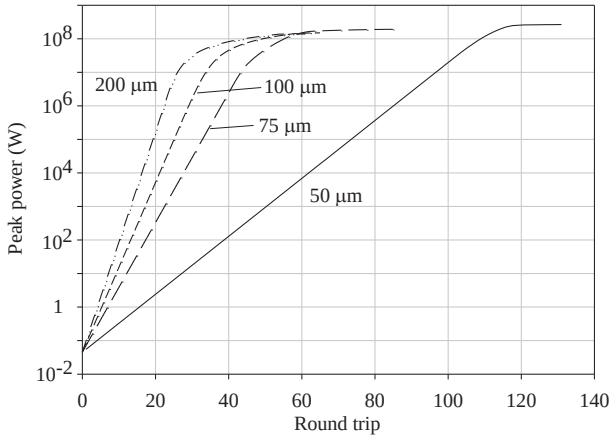

Fig.7. Calculated time evolution of the peak power at the radiation wavelengths of 200, 100, 75 and 50 μm for the electron beam with an average energy of 15 MeV, an energy spread of 0.5 %, and a peak current of 30 A

4. CONCLUSION

The longitudinal beam dynamics of the injector system for an IR FEL at Chiang Mai University has been studied using numerical simulations. The results have achieved the parameters suitable for the IR FEL lasing requirements. By properly adjusting the machine parameters, the electron bunches exiting the 180° achromat section have an average energy of 15.4 MeV, an rms energy spread of 0.74%, a bunch length of 0.85 ps, and a bunch charge of 33 pC. Further studies and optimization will be proceeded to investigate both transverse and longitudinal electron beam dynamics. The initial study of the FEL radiation with wavelengths of 50 to 200 μm has been performed for the electron beam energy of 15 MeV and the bunch length of 1 ps without considering the slippage effect. The total FEL peak power in the optical cavity of about 10^8 W can be achieved. However, the time-dependent simulation including optical cavity parameters will be conducted to investigate the realistic loss in the cavity and the slippage effect.

ACKNOWLEDGMENT

Authors would like to acknowledge the support of the Department of Physics and Materials Science, Chiang Mai University, the Thailand center of Excellence in Physics (ThEP-center), the (Thailand) Commission on Higher Education (CHE), and the Thailand Research Fund (TRF). We would like to express our gratitude to Prof. H. Ohgaki from Kyoto University for the very useful discussion and suggestion in the beam dynamic simulations.

REFERENCES

[1] Thongbai, C.; et al. 2008. Femtosecond Electron Bunches, Source and Characterization. *Nuclear Instruments and Method A* 587: 130-135.

[2] Rimjaem, S. 2006. *Generation of Far Infra-red Radiation from Relativistic Electron Beam*. Ph.D. Thesis. Chiang Mai University.

[3] Saisut, J.; et al. 2010. Construction and Performance of the Magnetic Compressor for the THz Facility at Chiang Mai University. *Nuclear Instruments and Method A* 637: S99-S106.

[4] Vilaithong, T.; Singkarat, S.; Yu, L.D.; Kamwannaa, T.; Thongbai, C.; and Songsiriritthigul, P. 2011. The Accelerators and Related R & D Activities in Thailand. *Journal of the Korean Physical Society* 59: 534-541.

[5] Zen, H.; et al. 2007. Numerical study on the optimum cavity voltage of RF gun and bunch compression experiment in KU-FEL. In *Proceeding of the 2007 Free-Electron Laser Conference*. Novosibirsk, Russia, 26-31 August.

[6] Retrieved October 1, 2012 from the World Wide Web: http://www.fel.duke.edu/lightsources/mk3.html.

[7] Retrieved October 1, 2012 from the World Wide Web: http://www.rs.noda.tus.ac.jp/fel-tus/.

[8] Young, L.M.; and Billen, J.H. (2002). PARMELA (Technical Note No. LA-UR-96-1835). Los Alamos National Laboratory.

[9] Reiche, S. 1999. GENESIS 1.3: a fully 3D time-dependent FEL simulation code. *Nuclear Instruments and Method A* 429: 243-248.

[10] Young, L.M.; and Billen, J.H. (1999). POISSON/ SUPERFISH (Technical Note No. LA-UR-96-1834). Los Alamos National Laboratory.

[11] Retrieved October 1, 2012 from the World Wide Web: http://lf.tnw.utwente.nl/opc.html

Linac-based THz Radiation Sources at Chiang Mai University

S. Rimjaem[1,2], P. Boonpornprasert[1,2], S. Chunjarean[2], K. Kusoljariyakul[1,2], M. Rhodes[2], J. Saisut [1,2], S. Suphakul[1,2], P. Thamboon[3], and C. Thongbai [1, 2]*

[1]Department of Physics and Materials Science, Faculty of Science,
Chiang Mai University, Chiang Mai 50200, Thailand
[2]Thailand Center of Excellence in Physics, CHE, Bangkok 10400, Thailand
[3]Science and Technology Research Institute, Chiang Mai University, Chiangmai 50200, Thailand

***Abstract*— *A THz radiation source based on RF-linear accelerator had been constructed at the Plasma and Beam Physics (PBP) research facility, Chiang Mai University. The accelerator system consists of an RF-gun with a thermionic cathode, an alpha-magnet as a magnetic bunch compressor, and a linear accelerator as a post acceleration section. Coherent transition radiation emitted from short electron bunches is used as the THz radiation source. This THz radiation can be used as a source of the THz imaging system and THz or far-infrared spectroscopy. The generation and characterization of the THz is presented. Recent experimental results on THz spectroscopy and THz imaging are presented and discussed. A plan for extension to accommodate infrared Free Electron Lasers (FEL) is also presented.*

***Keywords*— coherent transition radiation, femtosecond electron bunches, FEL, THz radiation**

1. INTRODUCTION

THz radiation is electromagnetic radiation spectrum covering wavelengths of 1000 μm to 100 μm (0.3 x 10^{12} – 3 x 10^{12} THz) and lies in the gap between Microwave and Infrared. In the past, this gap was an unexplored region but nowadays THz technologies and applications have been developed rapidly and were reviewed in [1-4]. An RF-linac-based THz facility has been established at the Plasma and Beam Physics (PBP) research facility, formerly the Fast Neutron Research Facility (FNRF), Chiang Mai University. Figure 1 shows a schematic layout of the system. The main components of the system are a thermionic cathode RF-gun, an alpha-magnet as a magnetic bunch compressor, a SLAC-type linear accelerator (linac), beam steering and focusing elements, and beam diagnostic instruments.

The RF electron gun is a 1-1/2 cell S-band (2856 MHz) with a side coupling cavity and was specially designed and optimized [5] for bunch compression using an alpha-magnet. The gun produces an electron bunch of 2.0-2.5 MeV maximum kinetic energy with a well-defined correlation between energy and time such that later electrons gain less and less energy. Electron bunches of 20-30 ps from the RF-gun are compressed in the alpha-magnet, where the particle path length increases with energy. This allows the lower energy particles, at later times in each bunch, to catch up with the front for effective bunch compression. The optimized and compressed part of the electron bunch is filtered by energy slits located in the alpha-magnet vacuum chamber and then transported to the linac. The electron beams are then accelerated through the linac to 10 -15 MeV. At the experimental station, the bunches are compressed to be less than 1 ps [6,7]. These short electron bunches can be used to produce high intensity THz radiation in the form of coherent transition radiation [8].

* Corresponding author. E-mail: chitrlada.t@cmu.ac.th
Tel: +66 53 943379, Fax: +66 53 222776

2. GENERATION OF THz RADIATION

Total electromagnetic radiation emitted from a bunch of N electrons at radiation frequency ω is

$$I(\omega) = NI_e(\omega)[1+(N-1)f(\omega)], \quad (1)$$

where $I_e(\omega)$ is the radiation intensity from a single electron and the bunch *form factor* $f(\omega)$ is the Fourier transformation of the longitudinal bunch distribution squared. Since the radiation spectrum is proportional to the Fourier transform of the bunch distribution, the short bunch is therefore desired for production of broadband radiation spectrum. At a wavelength about or longer than the bunch length, the radiation from an electron bunch becomes coherent and the intensity of coherent radiation, proportional to the number of radiating electrons squared, exceeds greatly that of incoherent radiation at the same wavelength. The radiation brightness in Figure 2 shows that electron bunches of 100 fs can provide broadband radiation covering from 5 cm^{-1} to 200 cm^{-1} wavenumber. This intense coherent transition radiation greatly exceeds that of a black body as well as that of synchrotron radiation.

At the PBP facility, the THz radiation is generated in the form of transition radiation by placing an aluminium foil (Al-foil) in the electron path, representing a transition between vacuum and Al-foil. When electron passes through an interface between two media of different dielectric constants, it emits electromagnetic fields. In the case of a normal incidence, the radiation energy W per unit angular frequency $d\omega$ per unit solid angle $d\Omega$ for the backward transition radiation from vacuum-conductor interfaces is given by [8]

$$\frac{dW}{d\omega\, d\Omega} = \frac{e^2\beta^2 \sin^2\theta}{\pi^2 c(1-\beta^2\cos^2\theta)^2}, \quad (2)$$

where θ is the angle between the emitted radiation direction and the inverse direction of electron trajectory (-z axis). For relativistic electrons ($\gamma >> 1$ and $\beta \to 1$), the maximum intensity can be obtained at $\theta \approx \pm 1/\gamma$.

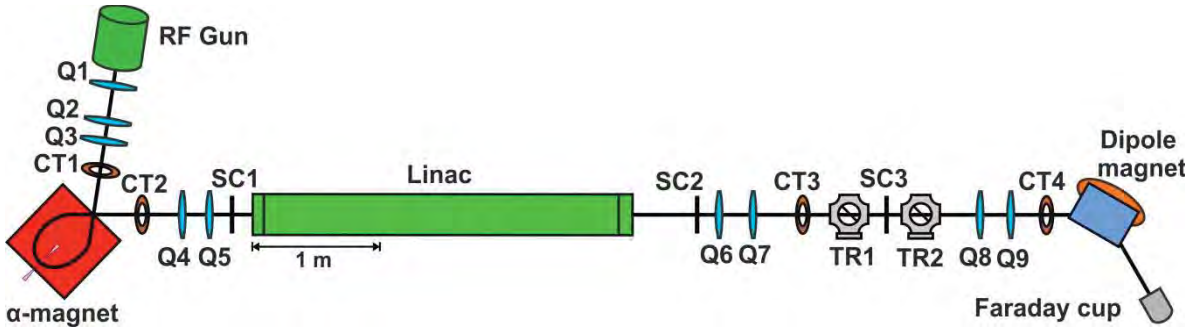

Fig.1. Schematic diagram of the accelerator system at Chiang Mai University to generate short electron bunches and THz radiation [Q:quadrupole magnet, CT:current monitor, SC:screen, TR: transition radiation]

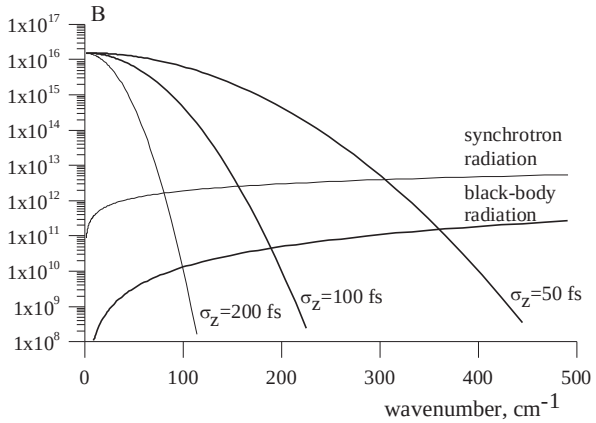

Fig.2. Radiation brightness B (ph/s/mm^2/100%BW) for coherent transition radiation from electron bunches of σ_z = 50, 100, and 200 fs compared to black body radiation and synchrotron radiation

In case of a 45^o incidence, the backward radiation emitted at 90^o with respect to the beam axis with its spectral-angular distribution given by the contribution of parallel and perpendicular polarization radiation.

$$\frac{dW^{II}}{d\Omega d\omega} = \frac{e^2\beta^2}{2\pi^2 c}\left[\frac{2\sin\theta - \sqrt{2}\beta\cos\phi}{(\sqrt{2} - \beta\sin\theta\cos\phi)^2 - \beta^2\cos^2\theta}\right]^2 \quad (3)$$

$$\frac{dW^{\perp}}{d\Omega d\omega} = \frac{e^2\beta^2}{2\pi^2 c}\left[\frac{\sqrt{2}\beta\cos\theta\sin\phi}{(\sqrt{2} - \beta\sin\theta\cos\phi)^2 - \beta^2\cos^2\theta}\right]^2, \quad (4)$$

where θ is the emission angle between the direction of emitted radiation and the -z axis, while ϕ is the azimuthal angle defined in the xy-plane with respect to the -x axis.

At the experimental station, the Al-foil radiator is 25.4 μm thick and 24 mm in diameter. The radiator is tilted by 45^o facing the electron beam direction. The backward transition radiation, described by equation (3) and (4), is emitted perpendicular to the beam axis and transmits through a high density polyethylene (HDPE) window of 1.25-mm-thick and 32-mm diameter.

A copper light cone or a THz lens are used to collect the THz radiation into a room-temperature pyroelectric detector. The radiation energy of 19 μJ per macropulse or a peak power of 24 W was measured by collecting over an acceptance angle of 160 mrad. Experimentally, the transition radiation spatial distributions as well as horizontal and vertical polarizations of radiation were observed using a PYROCAM and a wire-grid polarizer from Graseby-Spec (Model IGP223). The results are shown in Figure 3. An asymmetry shown up in horizontally polarized beam was a result of the Al-foil orientation which is tilted 45° horizontally as predicted theoretically [8].

The radiation spectrum measured using a Michelson interferometer is shown in Figure 4 (dashed-line). The available THz radiation covers from 5 cm^{-1} to around 80 cm^{-1} wavenumber (0.15 THz – 2.4 THz). At low frequency (< 5 cm^{-1}), the spectrum was suppressed by effects of the beam splitter and the periodic response is the effect of the pyroelectric detector [7]. The spectrum seems to extend to above 80 cm^{-1} (2.4 THz) where the noise becomes dominate. These can be further minimized with better detection and amplification system.

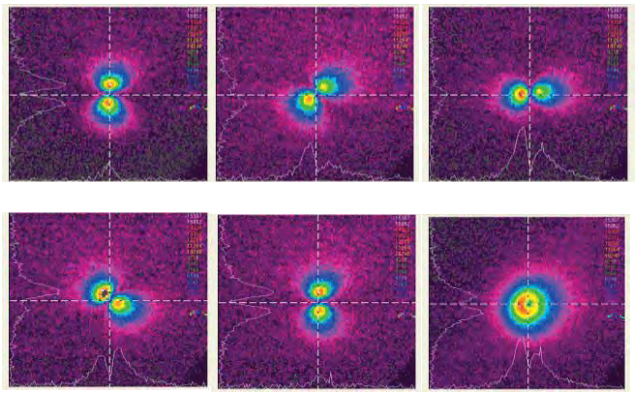

Fig. 3. THz transition radiation profiles taken with a polarizer rotated 0, 45, 90, 135, 180 degree respectively. The last profile is taken without any polarizer.

3. THz SPECTROSCOPY AND IMAGING

THz spectroscopy can be done easily by measuring power transmission or power absorption of a sample via a Michelson interferometer and the Fourier Transformation. As shown in Figure 4 (solid line), the radiation spectrum taken in humid-air reveals several water absorption lines. Although phase information has been lost in the measurement, optical constants of the sample can be obtained by some modeling or by Kramers-Kronig calculation [9]. Dispersive Fourier Transform Spectro-

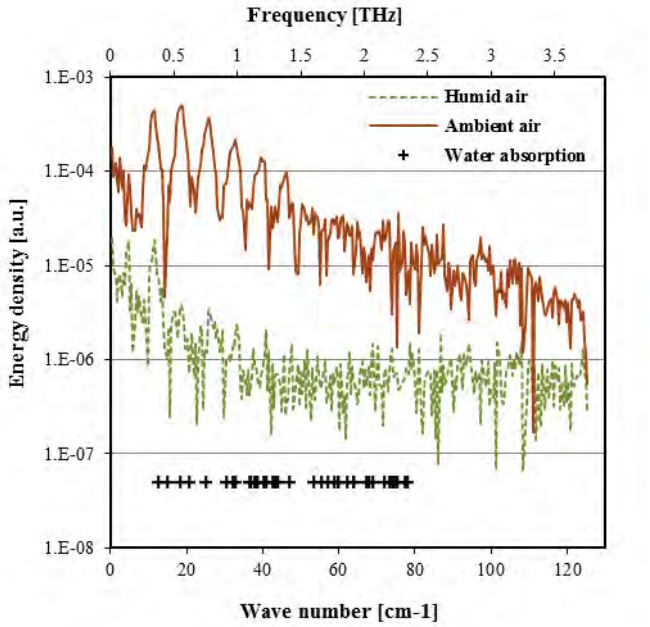

Fig.4. The radiation power spectra taken in humid air (solid) and in ambient air (dashed-line)

scopy (DFTS) [10] may also be used for direct determination of optical constants of a sample. In a DFTS setup, a sample is inserted in one arm of the interferometer, causing attenuation and dispersion of theradiation pulse. The attenuated and dispersed pulse can be recorded and its attenuation factor and phase shift can then be recovered. The attenuation and dispersion can be related to optical constants of the sample depending on the optical configuration of the measurements. With the DFTS technique, the phase information can be recovered in measurements using a Michelson interferometer. A THz imaging system has been setup and tested at the PBP facility. For transmission measurement, THz radiation is focused on a sample which is scanned using an xy-translation stage controlled by a computer interface. The transmission intensity is detected by a room-temperature pyroelectric detector. Computer program is employed to calculate and analyze intensity at difference points on the sample for THz image construction. Figure 5 shows an example of THz imaging obtained from the leaf concealed in an envelope.

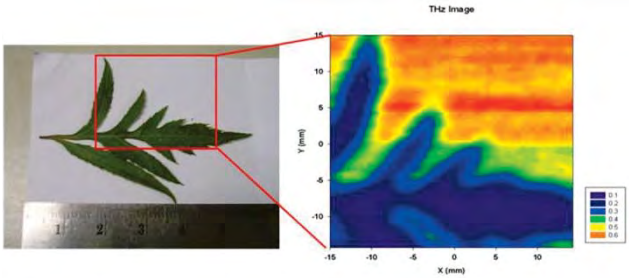

Fig. 5. Leaf and its THz image.

4. FUTURE EXPANSION

As a plan to become a research facility centered on the production and utilization of femtosecond electron pulses, accelerator-based light sources covering the mid and far-infrared regime to wavelengths up to the THz regime have beem studied. Preliminary designs of the extension are shown in the diagrams in Figure 6. A planar undulator can be added to the beamline as in Figure 6(a). With short electron bunches from the current PBP accelerator system, coherent undulator radiation can be produced. The existing beamline can also be extended and turned around by a 180^{o} achromatic system to let the electron beam pass through an undulator and an optical cavity as an IR-THz FEL (Figure 6(b)) .

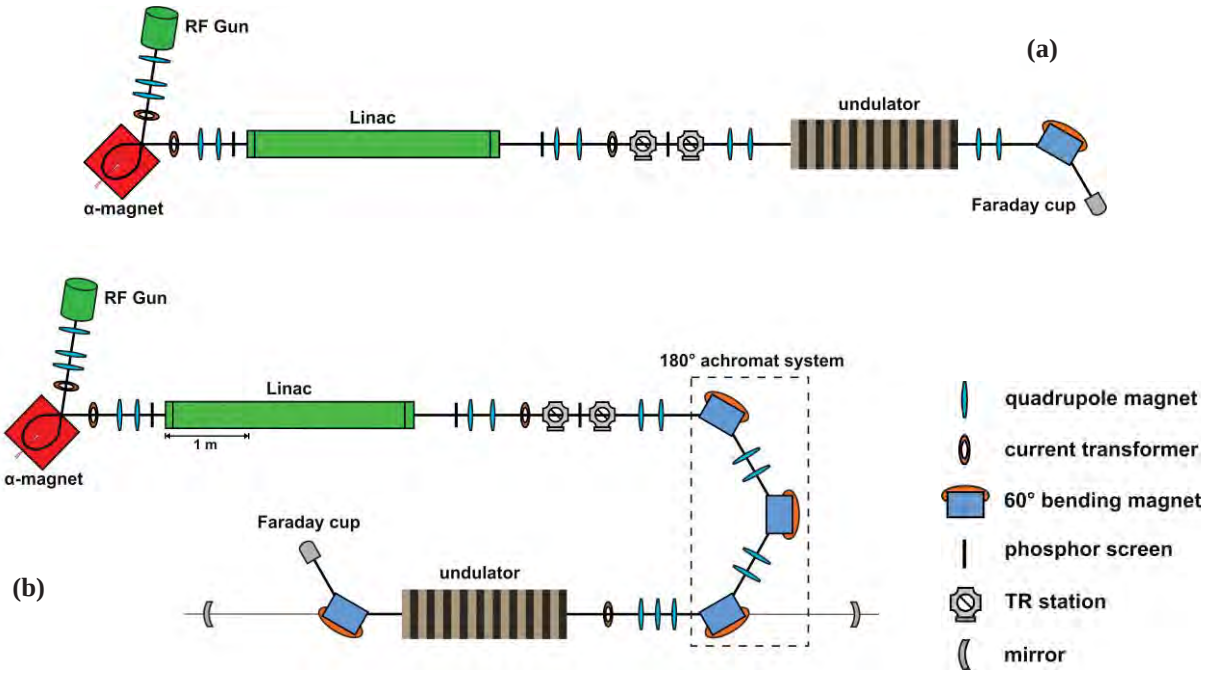

Fig. 5. Diagrams for future expansion of the accelerator system (a) without and (b) with an FEL cavity.

Generally, an electron trajectory as a pure sine wave in the undulator produces the radiation in the forward direction with a fundamental wavelength (λ_r) of

$$\lambda_r = \frac{\lambda_p}{2\gamma^2}(1+\frac{1}{2}K^2), \quad (5)$$

where λ_p is an undulator period length. To achieve the radiation at a desired wavelength, either K of the undulator or the beam energy can be varied.

Results of the preliminary study of

The radiation output from the undulator with 22 periods of 0.077 m period length are investigated and shown in Figure 7. The beam and the undulator parameters used for the study are listed in table 2. The effect of electron bunch length on the coherent undulator radiation from the setup in Figure 6(a) is clearly seen. The preliminary simulation study on the radiation from an FEL optical cavity (oscillator) as the setup shown in Figure 6(b) has been numerically investigated using the FEL code GENESIS 1.3 [11] in the time-independent mode. The FEL radiation outputs cover well beyond 6 THz spectral range.

Table 2. Parameters used for calculation and simulation

Parameters	Value
Beam	
Beam energy, E	15 MeV
Longitudinal rms bunch length, σ_b	0.1,1,2 ps
Peak current, I_p	30 A
Undulator	
Undulator type, material	Planar, $SmCo_5$
Undulator period length, λ_p	7.7 cm
Deflecting parameter, K	0.036-3.39
Undulator length	1.694 m

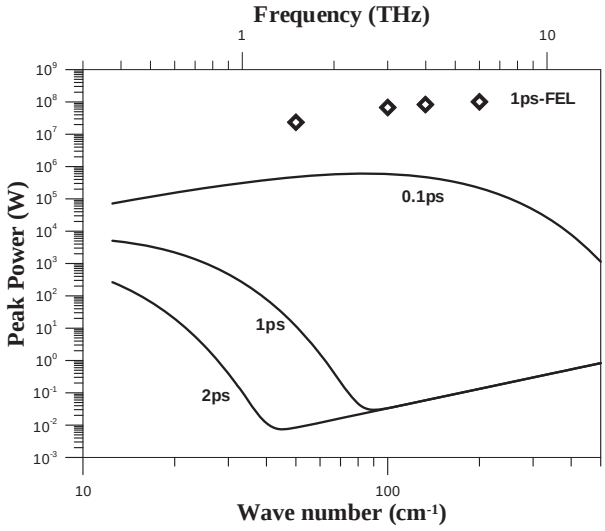

Fig. 7. Radiation output from 0.1 ,1 and 2 ps electron bunch lengths and an undulator (22 periods of 0.077 m period length) with (◊) and without (solid lines) FEL optical cavity

5. CONCLUSION

Intense THz radiation can be generated in the form of coherent transition radiation by using short electron bunches which are available at the Plasma and Beam Physics Research Facility, Department of Physics and Materials Science, Chiang Mai University. The available coherent THz transition radiation covers from 5 cm^{-1} to 80 cm^{-1} wavenumber (0.15 – 2.4 THz). This THz radiation can be used as a source of the THz imaging system and far-infrared or THz spectroscopy. The plan for future expansion with a planar undulator with and without the FEL optical cavity will allow more coverage of the IR-THz spectrum regime.

ACKNOWLEDGMENT

We would like to thank Mr. P. Wichaisirimongkol, Mr. N. Kangrang and Mr. V. Jinamoon for their technical support. We would like to acknowledge the support from the National Research Council of Thailand (NRCT), the Thailand Research Fund (TRF), the Thailand center of Excellence in Physics (ThEP-Center), the (Thailand) Commission on Higher Education (CHE) and Chiang Mai University.

REFERENCES

[1] Siegel, P. H. 2001. Terahertz Technology, *IEEETrans. Microwave. Theory & Tech*. 55: 910-928.

[2] Ferguson, B.; and Zhang, X. C. 2002. Materials for terahertz science and technology, *Nature materials* 1: 26-33.

[3] Gallerano. G. P. et al., "Overview of terahertz radiation sources", in the 2004 FEL conference, 2002, pp. 216-221.

[4] Tonouchi, M. 2007 Cutting-edge terahertz technology, *Nature photonics*, 1: 97-105.

[5] Rimjeam, S.; et al. 2004. Femtosecond electron bunches from an RF-gun. *Nuclear Instruments and Method A* 533: 258-269.

[6] Thongbai, C.; et al. 2008. Femtosecond Electron Bunches, Source and Characterization. *Nuclear Instruments and Method A* 587: 130-135.

[7] Thongbai, C.; and Wiedemann, H. 2006. Review and analysis of autocorrelation electron bunch length measurements. *Nuclear Instruments and Method A* 568: 923 -932.

[8] Thongbai, C. S.; and Vilaithong, T. 2007. Coherent transition radiation from short electron bunches. *Nuclear Instruments and Method A* 581: 874-881.

[9] Bell, R. J. 1972. *Introductory Fourier Transform Spectroscopy*, (London: Academic Press).

[10] Birch, J.R. ; and Parker, T.J. 1979. Dispersive fourier transform spectroscopy. In *Infrared and Millimeter Waves V.2: Instrumentation*, Button, K.J. Ed. (NewYork: Academics Press).

[11] Reiche, S. 1999. GENESIS 1.3: a fully 3D time-dependent FEL simulation code. *Nuclear Instruments and Method A* 429: 243-248.